

UNIVERSITY OF SOUTHAMPTON

**Disc Winds Matter: Modelling
Accretion and Outflow on All Scales**

by

James Matthews

A thesis submitted in partial fulfillment for the
degree of Doctor of Philosophy

in the
Faculty of Physical Sciences and Engineering
Department of Physics & Astronomy

May 2016

“Here, on the edge of what we know, in contact with the ocean of the unknown, shines the mystery and the beauty of the world.

And it’s breathtaking.”

Seven Brief Lessons on Physics, Carlo Rovelli

“Good enough for government work.”

Christian Knigge

UNIVERSITY OF SOUTHAMPTON

Abstract

Faculty of Physical Sciences and Engineering
Department of Physics & Astronomy

Doctor of Philosophy

by James Matthews

Outflows are ubiquitous in accreting systems across 10 orders of magnitude in mass. They can take the form of highly collimated radio jets, or less collimated, mass loaded winds emanating from the accretion disc. Perhaps the most spectacular evidence for accretion disc winds is the blue-shifted, broad absorption lines (BALs) in UV resonance lines, seen in cataclysmic variables (CVs) and approximately 20% of quasars. In addition to directly producing absorption in the spectrum, it is possible that accretion disc winds may significantly affect the line and continuum *emission* from CVs and quasars – as a result, they may even dominate the spectral appearance of such objects. When one considers that disc winds are also a possible mechanism for AGN feedback, it becomes clear that understanding the physics and true spectral imprint of these winds is of wide-ranging astrophysical significance.

In this thesis I use the confusingly named Monte Carlo radiative transfer (MCRT) code, PYTHON, to conduct a series of MCRT and photoionization simulations designed to test simple biconical disc wind models. I provide a detailed description of these methods, focusing particularly on the macro-atom implementation developed by Leon Lucy. First, I apply them to the optical spectra of CVs. Second, I conduct tests of quasar unification models. Finally, informed by the previous study, I use Sloan Digital Sky Survey and Hubble Space Telescope data to test the models in an empirical way, by using emission line equivalent widths as a probe of unification geometries.

Overall, the work presented here suggests that *disc winds matter*. They not only act as a spectral ‘filter’ for the underlying accretion continuum, but may actually dominate the emergent spectrum from accreting objects. As a result, unveiling their driving mechanisms, mass-loss rates, and ionization structure is an important goal for the astronomical community.

Contents

Abstract	ii
List of Figures	viii
List of Tables	xii
1 Introduction	1
1.1 The Physics of Accretion	3
1.1.1 Spherical Accretion and The Eddington Limit	4
1.1.2 Accretion Discs	5
1.1.2.1 Steady-state Accretion Discs: the α -prescription	6
1.1.3 Boundary Layers, Black Hole Spin and the ISCO	8
1.1.4 The Emergent Spectrum	10
1.2 Accreting Compact Binaries	12
1.2.1 Roche Lobe-Overflow	14
1.2.2 Cataclysmic Variables	15
1.2.2.1 Dwarf Novae and the Disc-instability Model	15
1.2.2.2 Nova-like Variables	16
1.2.3 Low Mass X-ray Binaries	20
1.3 Quasars and Active Galactic Nuclei	20
1.3.1 AGN Unification and the Dusty Torus	21
1.3.2 X-ray Properties of AGN	24
1.3.2.1 The Soft X-ray Excess	26
1.3.3 The Broad Line Region: Connection to Winds and Unification . .	26
1.4 The Current Understanding of the Disc Continuum	27
1.4.1 The Spectral shape of CV discs	27
1.4.2 The Big Blue Bump in AGN	29
1.4.2.1 The Accretion Disc Size Problem	29
1.4.2.2 Fitting AGN Spectra and the 1000Å Break	29
1.5 The Universality of Accretion	30
1.5.1 The RMS-flux relation	30
1.5.2 Accretion states and disc-jet coupling	31
1.5.3 A Global Picture	32
2 Accretion Disc Winds	34

2.1	Observational Evidence	34
2.1.1	Cataclysmic Variables	35
2.1.2	X-ray Binaries	38
2.1.3	AGN and Quasars	39
2.1.3.1	Broad Absorption Line Quasars	39
2.1.3.2	Warm Absorbers	43
2.1.3.3	Ultra-fast Outflows	44
2.1.4	Stellar Winds	45
2.1.4.1	Clumping in Stellar Winds	46
2.1.5	Outflow Physics	47
2.2	Driving Mechanisms	47
2.2.1	Thermal Winds	48
2.2.2	Radiatively Driven Winds	49
2.2.3	Line-driven Winds	49
2.2.4	Magnetic Winds	51
2.3	Accretion Disc Wind Models	52
2.3.1	MCGV95: A Line-driven Wind Model for AGN	52
2.3.2	De Kool & Begelman: A Radiatively Driven, Magnetically Confined Wind	53
2.3.3	Elvis 2000: A Structure for Quasars	54
2.3.4	Proga et al.: Line-driven Hydrodynamic Models for AGN and CVs	54
2.4	A Kinematic Prescription for a Biconical Wind	57
2.5	The big picture: AGN Feedback	59
2.5.1	Observational evidence for feedback	61
2.5.2	Alternative Explanations	64
3	Monte Carlo Radiative Transfer and Ionization	65
3.1	Fundamentals of Radiative Transfer	66
3.1.1	Spectral Line Formation	67
3.1.2	Local thermodynamic equilibrium	68
3.1.2.1	Dilute approximation	69
3.1.3	The Two Level Atom	69
3.1.3.1	Einstein coefficients	70
3.1.4	The Sobolev Approximation	71
3.1.4.1	Two-level Atom with Escape Probabilities	72
3.1.5	Monte Carlo approaches	73
3.2	PYTHON: A Monte Carlo Ionization and Radiative Transfer Code	73
3.2.1	Basics	73
3.2.2	Radiation Packets	75
3.2.3	Radiative Transfer procedure	76
3.2.3.1	Continuum opacities	77
3.2.3.2	Doppler Shifts	78
3.2.3.3	Choosing packet directions	79
3.3	Macro-atoms	80
3.3.1	Transition Probabilities	81
3.3.2	Rate equations	82
3.3.2.1	Collision strengths	83

3.3.3	Macro-atom estimators	84
3.3.3.1	Bound-free estimators	85
3.3.3.2	Bound-bound estimators	86
3.3.3.3	Other heating and cooling estimators	86
3.3.4	k -packets	88
3.3.5	Putting it all together	88
3.3.6	Ionization Fractions and Level Populations	88
3.3.7	Numerical Issues and Population Inversions	90
3.4	A hybrid line transfer scheme: including simple-atoms	91
3.4.1	Line Transfer	92
3.4.2	Heating and Cooling Estimators	92
3.4.2.1	Radiation Field Estimators, Ionization and Excitation . .	93
3.5	Heating And Cooling Balance	96
3.5.1	Convergence	96
3.6	Spectral Cycles	97
3.6.1	Macro-atom Emissivity Calculation	98
3.7	Atomic Data	100
3.7.1	Macro-atom Level and Line Data	100
3.7.2	Photoionization Cross-sections	101
3.8	Code Validation	102
3.8.1	Testing against CLOUDY	102
3.8.2	Macro-atom testing against TARDIS and theory	104
3.8.3	Testing line transfer modes	108
3.9	Code Maintenance and Version Control	109
3.9.1	Parallelisation	110
4	The Impact of Accretion Disc Winds on the Optical Spectra of Cataclysmic Variables	112
4.1	Introduction	112
4.1.1	Sources and Sinks of Radiation	113
4.1.1.1	Accretion disc	114
4.1.1.2	White Dwarf	114
4.1.1.3	Boundary Layer	114
4.1.1.4	Secondary Star	115
4.2	A Benchmark disc Wind Model	115
4.2.1	Physical Structure and Ionization State	116
4.2.2	Synthetic Spectra	118
4.3	A Revised Model Optimized for Optical Wavelengths	122
4.3.1	Synthetic Spectra	123
4.3.2	Continuum Shape and the Balmer Jump	126
4.3.3	Line Profile Shapes: Producing Single-Peaked Emission . .	128
4.3.4	Sensitivity to Model Parameters	130
4.3.5	Comparison to RW Tri	130
4.4	Discussion: Collision Strengths and Boundary Layers	132
4.4.1	Model Sensitivity to Collision Strengths	132
4.4.1.1	Collisions Between Radiatively Forbidden Transitions .	132
4.4.1.2	Line Heating and Cooling	132

4.4.2	Improving Collision Strengths	133
4.4.3	Introducing a Boundary Layer	133
4.5	Conclusions	133
5	Testing Quasar Unification: Radiative Transfer In Clumpy Winds	135
5.1	Introduction	135
5.2	A Clumpy Biconical Disk Wind Model for Quasars	136
5.2.1	Photon Sources	136
5.2.2	A Simple Approximation for Clumping	138
5.2.3	The Simulation Grid	141
5.3	Results and Analysis From A Fiducial Model	142
5.3.1	Physical Conditions and Ionization State	142
5.3.2	Synthetic Spectra: Comparison to Observations	145
5.3.2.1	Broad absorption lines ('BALQSO-like' angles)	147
5.3.2.2	Broad emission lines ('quasar-like' angles)	150
5.3.3	X-ray Properties	151
5.3.4	LoBALs and Ionization Stratification	152
5.4	Discussion	154
5.4.1	Parameter Sensitivity	154
5.4.2	Inclination Trends: FWHM and EW	154
5.4.2.1	FWHM and Black Hole Mass Estimates	157
5.5	Summary And Conclusions	158
6	Quasar Emission Lines as Probes of Orientation and Unification	160
6.1	Introduction	160
6.2	Data Sample	161
6.3	The Angular Distribution of Emission from an Accretion Disc	165
6.3.1	Standard Thin Disc Models	165
6.3.2	Including GR, Comptonisation and Opacity Effects	166
6.4	Predicted EW Distributions Compared to Observations	166
6.4.1	Fitting the Quasar Distribution	166
6.4.2	Comparing non-BAL and LoBAL Distributions	171
6.4.3	Broad Emission Lines in HiBAL quasars	174
6.5	Discussion	174
6.5.1	Eigenvector 1	174
6.5.2	Radio Observations	176
6.5.3	Polarisation	178
6.5.4	Theoretical Considerations	178
6.6	Conclusions	178
7	Conclusions and Future Work	181
7.1	Suggestions for Future Work	184
7.1.1	CVs as Accretion and Outflow Laboratories	184
7.1.2	Improving the Treatment of Clumping	185
7.1.3	Improving Atomic Models	186
7.1.4	Using Radiative Transfer to Test	186
7.1.5	Obtaining Reliable Orientation Indicators	186

7.1.6	Placing BAL Quasars on the Eigenvector 1 Parameter Space . . .	186
7.2	Closing Remarks	186
 Bibliography		 188

List of Figures

1.1	The temperature profile of an accretion disc for three different classes of compact object.	8
1.2	Angular velocity as a function of radius in an accretion disc around a rotating compact object.	9
1.3	The radius of the ISCO, R_{ISCO} , and the horizon, R_H , is as a function of the BH spin parameter, a_*	10
1.4	Accretion disc SEDs for three different compact objects.	11
1.5	A comparison between an accretion disc spectrum computed with black-body and stellar atmosphere spectra.	12
1.6	Artists impression of an LMXB and CV.	13
1.7	The Roche potential in a binary system	14
1.8	A year in the life of SS Cyg.	16
1.9	Spectra of SS Cyg during an outburst cycle	17
1.10	Optical spectra of three nova-like variables.	18
1.11	UV spectrum of RW Tri in and out of eclipse.	19
1.12	Template spectra, from the AGN atlas, for four common types of AGN. .	22
1.13	A unified scheme for AGN.	24
1.14	Broadband SEDs for different AGN SEDs	25
1.15	Occam's quasar	28
1.16	Hardness-intensity diagrams for three types of accreting objects.	32
2.1	A disagram showing how P-Cygni profiles form.	35
2.2	UV spectrum of the DN TW Vir during outburst.	36
2.3	UV spectrum of Z Cam, compared to a synthetic spectrum from MCRT simulations.	36
2.4	The effect of a disc wind on a double-peaked line profile.	37
2.5	A cartoon illustrating the expected geometry of soft-state LMXB winds. .	38
2.6	Hardness-intensity diagram for four dipping LMXBs.	39
2.7	Top Panel: A comparison between the SDSS non-BAL, HiBAL and LoBAL composite spectra as presented in Reichard et al. (2003). Bottom Two Panels: Two individual examples of a HiBAL and LoBAL quasar spectrum, respectively. In all panels some of the more prominent lines are labeled and shaded, and the object name is given in the bottom two plots. .	40
2.8	X-ray spectrum of PDS 456 fitted with a P-Cygni profile.	45
2.9	UV spectrum of one of the O4 supergiant ζ Puppis.	46
2.10	Cartoon showing the geometry of the MCGV95 model.	52
2.11	A cartoon showing the components in the De Kool & Begelman model. .	53
2.12	A schematic showing the main features of the Elvis model.	55

2.13	Density snapshot of the PK04 model.	56
2.14	A schematic showing the geometry and kinematics of the SV93 model	58
2.15	The SV93 velocity law for various values of the acceleration exponent, α .	60
2.16	The $M_{BH} - \sigma_*$ correlation.	61
2.17	The $M_{BH} - M_{bulge}$ correlation.	62
2.18	<i>Figure adapted from Fabian 2012.</i> Chandra X-ray images showing two examples of X-ray cavities, illustrating how a radio jet from an AGN can have a dramatic impact on its environment. a) The RBS 797 Cluster (Cavagnolo et al. 2011). b) elliptical galaxy NGC 5813 (Randall et al. 2011).	63
2.19	Results of Gaussian line profile fitting to integral field spectroscopy of Mrk 231.	64
3.1	A schematic showing a ray obliquely incident on a surface of area dA . The labeled quantities are used in the definition of specific intensity.	66
3.2	A flowchart showing the basic operation of PYTHON.	74
3.3	The process of choosing a scattering location in a cell.	77
3.4	The decision tree traversed by an energy packet in macro-atom mode.	89
3.5	An example of a modeled spectrum in PYTHON compared to the recorded MC spectrum, from an individual cell in an AGN model.	95
3.6	The average temperature and fraction of converged cells in a typical CV model, shown as a function of the number of ionization cycles completed.	97
3.7	A comparison of synthetic spectra produced in extract and live or die modes.	99
3.8	The effect of extrapolated cross-sections on the soft X-ray spectrum	102
3.9	Relative ion fractions for Hydrogen in CLOUDY, PYTHON in standard mode and PYTHON in hybrid mode.	104
3.10	As figure 3.9, but for Helium.	105
3.11	As figure 3.9, but for Carbon.	105
3.12	As figure 3.9, but for Nitrogen.	106
3.13	As figure 3.9, but for Oxygen.	106
3.14	As figure 3.9, but for the first 11 ionization stages of Iron.	107
3.15	Balmer decrements in PYTHON compared to Seaton (1959), and He level populations compared to TARDIS.	108
3.16	Comparison between TARDIS and PYTHON synthetic spectra from a simple 1D supernova model.	109
3.17	A comparison between weight reduction and line transfer mode.	110
3.18	Github commit history for PYTHON from 2013-2016.	110
3.19	Total runtime per cycle for an AGN run as a function of the number of processors.	111
4.1	Cartoon illustrating the geometry and kinematics of the benchmark CV wind model.	113
4.2	The spectral energy distribution of the accretion disc and white dwarf used in the ionization cycles for the CV modelling.	115
4.3	The physical properties of the wind in the benchmark CV model.	117
4.4	UV and optical synthetic spectra from the benchmark CV model	119

4.5	Optical synthetic spectra from the benchmark CV model divided by the continuum.	121
4.6	Total packet-binned spectra across all viewing angles from the benchmark CV model.	122
4.7	UV and optical synthetic spectra from CV model B	124
4.8	Optical synthetic spectra from CV model B divided by the continuum.	127
4.9	Total packet-binned spectra across all viewing angles from CV model B.	128
4.10	$H\alpha$ line profiles from CV models A, B and X	129
4.11	In and out of eclipse spectra from model B compared to the high inclination NL RW Tri	131
5.1	A cartoon showing the geometry and some key parameters of the biconical quasar wind model.	137
5.2	The input spectrum used for the quasar modelling.	138
5.3	Some typical length scales for the fiducial model.	140
5.4	Contour plots showing the logarithm of some important physical properties of the quasar outflow.	143
5.5	The electron density in the fiducial model on linear axes.	144
5.6	Synthetic spectra at four viewing angles for the fiducial quasar model.	146
5.7	A schematic showing the broad classes of sightline in the fiducial model.	147
5.8	Synthetic spectra at two viewing angles compared to the non-BAL SDSS quasar composite.	148
5.9	X-ray properties of the clumped quasar model compared to H13 and samples from the literature.	151
5.10	$C\,\text{IV}$, $Mg\,\text{II}$, $Al\,\text{III}$ and $Fe\,\text{II}$ line profiles for wind viewing angles.	153
5.11	Equivalent widths and BALnicities of some important lines for the quasar wind grid.	155
5.12	$W_{\lambda,RW}$ as a function of inclination in the fiducial model.	156
5.13	f_{FWHM} as a function of inclination	158
6.1	BH mass and Eddington fraction for the BAL samples plotted over the overall quasar sample from S11.	162
6.2	Histograms of equivalent widths for three emission lines from the two different samples.	163
6.3	Monochromatic continuum luminosities from AGNSPEC and classical thin disc models.	167
6.4	Theoretical Ew distributions from the numerical experiment described in section 6.4.1 for a few different maximum angles. The results in the top panel use the same intrinsic distribution as Model 1 from R11 (shown in black), whereas the bottom panel shows the distributions obtained from a narrower intrinsic Gaussian. By the time the maximum angle is limited to around 70° the cutoff is clear even at moderate values of EW.	169
6.5	The EW distribution of quasars in the R11 sample (red errorbars) and the best fit model with a maximum viewing angle of 84°	170
6.6	χ^2/dof as a function of maximum angle, θ_1 , calculated in steps of 0.1° . The choice for μ_* and σ_* is left free in each case.	171
6.7	The geometry of the toy model used to carry out the Monte Carlo simulations	172

6.8	Heat map showing the results of the MC simulation described in section 6.4.2. The quantities shown are discussed further in the text, but correspond to (clockwise from top left): the p_{KS} value from a comparison between the mock BAL dataset and the observed BAL dataset, the reduced χ^2 from the fit to the non-BAL EW distribution, the difference in mean EW between the mock BAL and mock non-BAL datasets, and the BAL fraction expected for the geometry in question.	173
6.9	Heat map showing the results of the MC simulation described in section 6.4.3. The top panel shows the expected BAL fraction for the geometry in question, and the	175
6.10	Eigenvector 1 for BAL and non-BAL quasars.	177
6.11	LoBAL fraction compared to mean LoBAL fraction in Eigenvector 1 space.	177
6.12	<i>Top:</i> Polarisation percentages as a function of measured inclination from Marin et al. (2015) for Type I and Type II AGN. <i>Bottom:</i> Histograms of polarisation percentages for BAL quasars from Schmidt et al. (1999) together with the Marin et al. (2015) AGN sample.	179

List of Tables

1.1	Approximate values of compactness for four different compact objects. . .	4
4.1	Model parameters for the CV wind models	116
5.1	The grid points used in the parameter search for quasar wind models . .	142
5.2	Model parameters for the fiducial quasar model.	144
5.3	Some derived spectral properties of the fiducial model compared to ob- servations.	149
6.1	Eigenvector 1 correlation coefficients	174

Dedicated to my family. Thanks for being awesome....

Chapter 1

Introduction

“And now you’re asking, I don’t know where to begin”

Mike Vennart, Silent/Transparent

The release of gravitational potential energy as mass falls towards a compact object is the most efficient energetic process in the universe, even more efficient than nuclear fusion. This *accretion* process is thought to power the huge radiative engines at the centres of many galaxies – accreting supermassive black holes known as active galactic nuclei (AGN). As the matter falls into the potential well of the black hole it often forms an accretion disc. This disc is an efficient radiator of the gravitational potential energy released. and can sometimes outshine the entire stellar population of the galaxy, appearing as a quasi-stellar object (QSO) or *quasar*. As well as powering, AGN, accretion discs are present in X-ray binaries (XRBs), young-stellar objects (YSOs) and cataclysmic variables (CVs). Accretion is a universal process; broadly speaking, the physics is similar regardless of whether matter is falling on to a $\sim 1 M_{\odot}$ neutron star or white dwarf, or a $\sim 10^{10} M_{\odot}$ black hole.

Outflows are ubiquitous in accreting systems. We see collimated radio jets in AGN (Hazard et al. 1963; Potash & Wardle 1980; Perley et al. 1984; Marscher 2006) and XRBs (Belloni 2010), and there is even evidence of radio emission in CVs (Benz et al. 1983; Coppejans et al. 2015). These radio jets tend to appear in specific accretion states (Fender 2001; Fender et al. 2004; Körding et al. 2008), implying an intrinsic connection to the accretion process. Even more intriguing, in XRBs less collimated, mass-loaded

outflows or *winds* are observed in the opposite accretion state, possibly emanating from the accretion disc. Evidence for disc winds is widespread across the mass range, but perhaps the most spectacular indication is the blue-shifted, broad absorption lines (BALs) in the rest-frame ultraviolet (UV) seen in high-state CVs (Heap et al. 1978; Greenstein & Oke 1982; Cordova & Mason 1982) and the so-called broad absorption line quasars (BALQSOs) that make up 20 – 40% of quasars (Weymann et al. 1991; Knigge et al. 2008; Allen et al. 2011). BALs and ‘P-Cygni’ profiles (Struve 1935; Rottenberg 1952) are also seen in stellar winds (e.g. Cassinelli 1979) and sometimes even in the optical spectra of CVs (Patterson et al. 1996; Ringwald & Naylor 1998; Kafka & Honeycutt 2004). Broad, blue-shifted absorption is also observed in the Fe K α line in some AGN (Reeves et al. 2003; Pounds & Reeves 2009; Tombesi et al. 2010) – these are known as ultra-fast outflows or UFOs.

The astrophysical significance of disc winds extends, quite literally, far beyond the accretion environment. They offer a potential mechanism by which the central accretion engine can interact with the host galaxy and interstellar medium via a ‘feedback’ mechanism (King 2003; Fabian 2012). Feedback is required in models of galaxy evolution (Springel et al. 2005) and may explain the famous ‘ $M_{BH} - \sigma$ ’ (Silk & Rees 1998; Häring & Rix 2004) and ‘ $M_{BH} - M_{bulge}$ ’ (Magorrian et al. 1998) relations. Winds also offer a natural way to *unify* much of the diverse phenomenology of AGN, CVs and XRBs. This principle of unification can be applied along more than one ‘axis’ of parameter space. For example, there exist elegant models that attempt to explain *all* of the behaviour of quasars with only a central black hole, a jet, an accretion disc, and an associated outflow, just by varying the viewing angle (Elvis 2000). Similarly elegantly, it has been shown that much of the behaviour of XRBs is directly applicable to AGN (McHardy et al. 2006), and models of outflows in CVs have been successfully ‘scaled-up’ and applied to quasars and AGN (e.g. Higginbottom et al. 2013).

Despite their clear importance and ubiquity, there are still many unanswered questions relating to the true impact of winds and their underlying physical origins. Here, I aim to address some of these questions, and take steps towards building a more holistic picture of the impact of winds on the spectral appearance and accretion physics of disc systems. This thesis is structured as follows. In the remainder of this chapter, I will give the background accretion theory and detail the successes and failures of accretion disc models when compared to observations, as well as describing the different classes

of accreting objects in more detail. In chapter 2, I dedicate some time to specifically discussing the theory of, and observational evidence for, accretion disc winds. In chapter 3, I outline the Monte Carlo radiative transfer (MCRT) and photoionization methods I have used in order to investigate the impact of disc winds on the spectra of accreting systems. The next three chapters contain three separate submitted papers, in which I discuss the impact of disc winds on the spectra of CVs (Chapter 4), and test disc wind quasar unification models (Chapters 5 and 6). In chapter 8, I summarise my findings and their astrophysical significance, and discuss potential avenues for future work.

1.1 The Physics of Accretion

The basic phenomenon of accretion- matter falling into a gravitational potential well- is ubiquitous in astrophysics. The energy, ΔE , released by a parcel of mass, Δm , falling from infinity onto an object of mass M and radius R_* is given by

$$\Delta E = \frac{GM\Delta m}{R_*}, \quad (1.1)$$

meaning that the power by mass accreting at a rate \dot{M} is given by

$$L_{acc} = \frac{GM\dot{M}}{R}. \quad (1.2)$$

We can also characterise the efficiency of any energetic process by relating the energy released to the rest mass energy of the parcel of mass, such that

$$\Delta E = \eta\Delta Mc^2, \quad (1.3)$$

where η is the radiative efficiency. Similarly, in terms of luminosity, L ,

$$L = \eta\dot{M}c^2, \quad (1.4)$$

Nuclear fusion is one of the more efficient energetic processes in the universe, with an efficiency of $\eta = 0.007$. If we rearrange the above equations in terms of η we find

$$\eta = \frac{G}{c^2} \frac{M}{R_*}. \quad (1.5)$$

Object	$M(M_\odot)$	R_* (cm)	$M/R_*(M_\odot/R_J)$	
White Dwarf	0.8	0.01	79.4	1.6×10^{-4}
Neutron Star	1.4	1.4×10^{-5}	10^5	0.2
Black Hole	10	$2GM/c^2 = 4.2 \times 10^{-6}$	2.4×10^5	0.48
SMBH	10^9	$2GM/c^2 = 4244$	2.4×10^5	0.48

TABLE 1.1: Approximate values of compactness for four different compact objects with typical parameters. Note that here R_* for black holes is set to the event horizon for a Schwarzschild black hole.

In other words, the efficiency of accretion is directly related to the *compactness*, M/R_* , of the central object. Values of compactness and the associated radiative efficiencies for four different compact objects are shown in table ??.

1.1.1 Spherical Accretion and The Eddington Limit

The simplest geometry one might propose for accretion would be one in which a central mass accretes matter from an all-encompassing cloud. The process of spherical accretion has come to be known as Bondi-Hoyle-Lyttleton accretion ([Hoyle & Lyttleton 1939](#); [Bondi & Hoyle 1944](#)). In particular, [Bondi \(1952\)](#) studied spherically symmetric accretion onto a point mass and derived the Bondi radius,

$$r_B = \frac{GM}{c_S^2}, \quad (1.6)$$

where $c_S = c_S(r_B)$ is the sound speed as a function of radius. The Bondi radius represents a critical point inside which the material is supersonic and will accrete on the free-fall timescale.

When this timescale is long enough, the accreting matter can radiate away its potential energy, generating a luminosity L . This radiation will induce a force on electrons, given by

$$F_{rad} = \frac{L\sigma_T}{4\pi r^2 c}, \quad (1.7)$$

where $\sigma_T = 6.65 \times 10^{-25} \text{ cm}^2$ is the Thomson cross-section. If this radiation force term dominates over the gravitational force, then the material will no longer fall inwards. Consider radiation pressure acting on ionized hydrogen, for which the gravitational force

is approximately given by GMm_p/r^2 . Combining this expression with equation 1.7 gives a natural maximum accretion luminosity, known as the *Eddington limit*, of

$$L_{Edd} = \frac{4\pi GMm_p c}{\sigma_T}, \quad (1.8)$$

with an associated Eddington accretion rate of

$$\dot{M}_{Edd} = \frac{L_{Edd}}{\eta c^2}. \quad (1.9)$$

The Eddington limit makes a number of assumptions, namely that the accretion flow is steady, spherically symmetric, ionized, and has its opacities dominated by electron scattering. Clearly, there are many astrophysical situations where this does not hold. For example, the recent outburst of V404 Cyg showed wildly variable luminosities on short timescales (see, e.g., [Kuulkers et al. 2015](#); [Motta et al. 2015](#), among many, many ATels), and in any binary system or disc dominated system the assumption of spherical symmetry will break down. Nevertheless, the Eddington limit provides a good order of magnitude estimate of the maximum luminosity of an accreting object, and also provides a useful way of parameterising accretion rate, as it scales linearly with mass. It can also be used to characterise the *state* of an accretion disc. In general, sources above $\sim 0.1 L_{Edd}$ find themselves in a ‘soft’ or thin-disc state, whereas for much lower Eddington fractions, sources will possess advection-dominated accretion flows (ADAFs; [Narayan & Yi 1994, 1995](#)) or, more generally, radiatively inefficient accretion flows (RIAFs). It is also clear that around the Eddington limit radiation pressure must play a major role in determining the disc morphology (see section 2.2.2).

1.1.2 Accretion Discs

In many astrophysical situations – for example, in binary systems and gas clouds orbiting BHs – any accreting matter will possess some net angular momentum. If the medium is dense enough, collisions between particles will be frequent, but the total angular momentum vector of two colliding particles will always be conserved. This provides a mechanism for a gas cloud to relax to its minimum energy state – an accretion disc.

As well as losing gravitational potential energy as it falls towards the central mass, a parcel of matter must also lose its angular momentum. Crucially, accretion discs

provide a way for this to happen. If the disc overall maintains the same total angular momentum, it follows that angular momentum must therefore be transported outwards. The mechanism for transporting angular momentum outwards is unknown, and is one of the biggest weaknesses of current accretion disc theory. Traditional molecular viscosity is inefficient in this regard (?). The reasons for this are readily apparent when we consider that molecular viscosity operates over the Debye length, λ_D , and at the sound speed, c_s . The viscous force density is therefore much less than the inertial force density (or in other words the Reynolds number is much greater than 1); the consequence being that molecular viscosity is dynamically unimportant in accretion flows.

An alternative mechanism for angular momentum transport is therefore necessary. The most commonly invoked candidate is the magnetorotational instability (MRI; [Balbus & Hawley 1991](#)), in which accretion discs are subject to a strong shearing instability even when the magnetic field is weak. Possible alternatives are that the angular momentum is lost via a magnetohydrodynamic outflow ([Blandford & Payne 1982](#)) or spiral shock waves ([Ju et al. 2016](#)), although the former cannot be the main angular momentum loss mechanism if the disc is to remain intact (e.g. ?). Given the uncertainty about the angular momentum transport mechanism, it is convenient to simply parameterise the unknown physics in an *effective* viscosity.

1.1.2.1 Steady-state Accretion Discs: the α -prescription

The so-called α -disc model developed by [Shakura & Sunyaev \(1973\)](#), hereafter SS73) and [Lynden-Bell \(1969\)](#) is a simple approximation for how energy and angular momentum is transported in an accretion disc, and provides useful insights into the expected observational appearance. The starting point for this model is the parameterisation of viscosity, ν' , using the simple form

$$\nu' = \alpha c_s H, \quad (1.10)$$

where H is the scale height of the disc, α is a parameter ≤ 1 and c_s is the sound speed. Viscous torques then allow the conversion of orbital kinetic energy into heat, which can be radiated away. If we make one further assumption, that the accretion rate is constant throughout the disc, we can write down a mass continuity equation valid at all radii, given by

$$\dot{M} \equiv 2\pi R V_R \Sigma = \text{constant}, \quad (1.11)$$

where Σ is the surface density at that point. The angular momentum equation then becomes

$$\nu'\Sigma = \frac{\dot{M}}{3\pi} \left[1 - \left(\frac{R}{R_*} \right)^{1/2} \right]. \quad (1.12)$$

The viscous torques throughout the disc cause a local loss of mechanical energy, allowing us to derive (see, e.g. Frank et al. 1992) a rate of viscous dissipation, per unit area, given by

$$D(R) = \frac{1}{2}\nu'\Sigma(R\Omega')^2. \quad (1.13)$$

Here, $D(R)$ is proportional to the derivative of the angular velocity, $\Omega' = d\Omega/dR$. By combining equations 1.13 and 1.12 we can show that the viscous dissipation rate is

$$D(R) = \frac{GMM}{8\pi R^3} \left[1 - \left(\frac{R}{R_*} \right)^{1/2} \right] \quad (1.14)$$

where we have also set the angular velocity to the Keplerian velocity. This expression is independent of viscosity – which is fortunate, because we do not know what value of α to use in equation 1.10. This result comes about because of the explicit assumption that the viscosity regulates the mass accretion rate so as to achieve a steady state.

We can now integrate across both sides of the whole disc to obtain the disc luminosity,

$$L_{disc} = 2 \int_{R_*}^{\infty} D(R) 2\pi R dR = \frac{GMM}{2R_*} = \frac{1}{2} L_{acc}. \quad (1.15)$$

This result can also be shown by considering the gravitational binding energy of gas in Keplerian rotation at R_* and infinity. From equation 1.14 an effective temperature distribution can be derived by setting

$$\sigma T_{eff}^4(R) = D(R), \quad (1.16)$$

which then gives

$$T_{eff}(R) = T_* \left[1 - \left(\frac{R}{R_*} \right)^{1/2} \right]^{1/4}, \quad (1.17)$$

where

$$T_* = \left(\frac{3GMM}{8\pi R_*^3 \sigma} \right)^{1/4}. \quad (1.18)$$

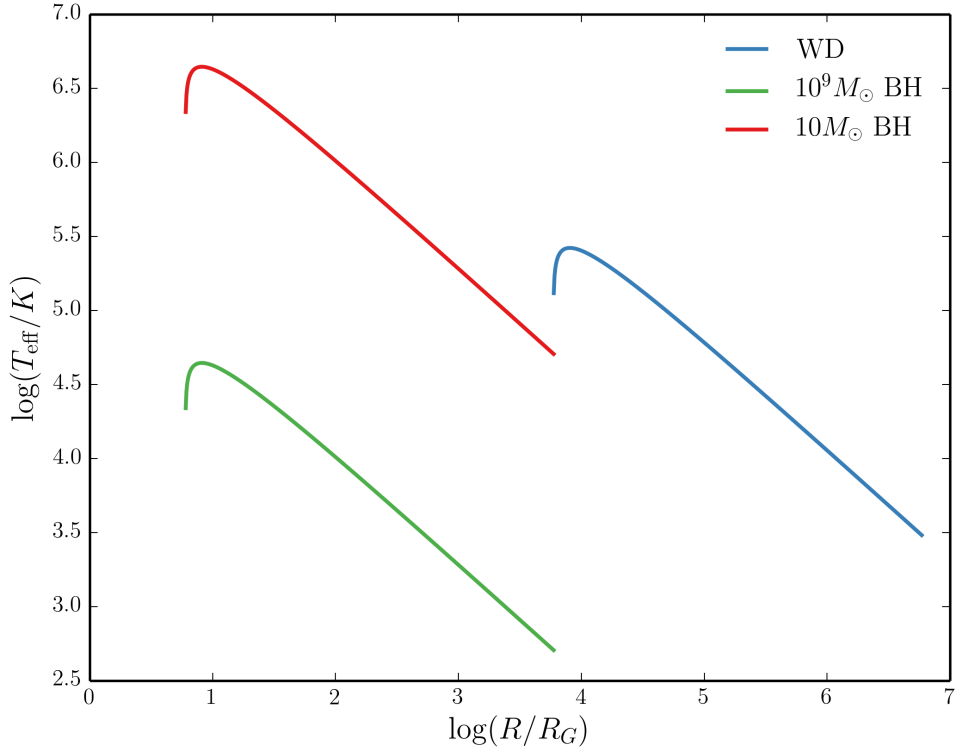


FIGURE 1.1: The temperature profile of an accretion disc for three different classes of compact object.

When $R \gg R_*$ this simplifies to

$$T_{\text{eff}}(R) = T_*(R/R_*)^{-3/4}. \quad (1.19)$$

Now I have not only derived the total luminosity of an accretion disc, but also the effective temperature profile which will govern the shape of the emergent SED. This temperature profile is shown in figure 1.1 for three different compact objects, assuming an Eddington fraction of 0.2.

1.1.3 Boundary Layers, Black Hole Spin and the ISCO

In equation 1.15, I showed that $L_{\text{disc}} = 1/2 L_{\text{acc}}$. One might then ask: where does the rest of the luminosity go? Alternatively, what happens to the kinetic energy the material has at the inner disc edge? The answer is dependent on the compact object in question. In an accreting WD, the rotating matter must eventually deposit itself on the surface of the WD. This is illustrated in figure 1.2, which shows the angular velocity as a

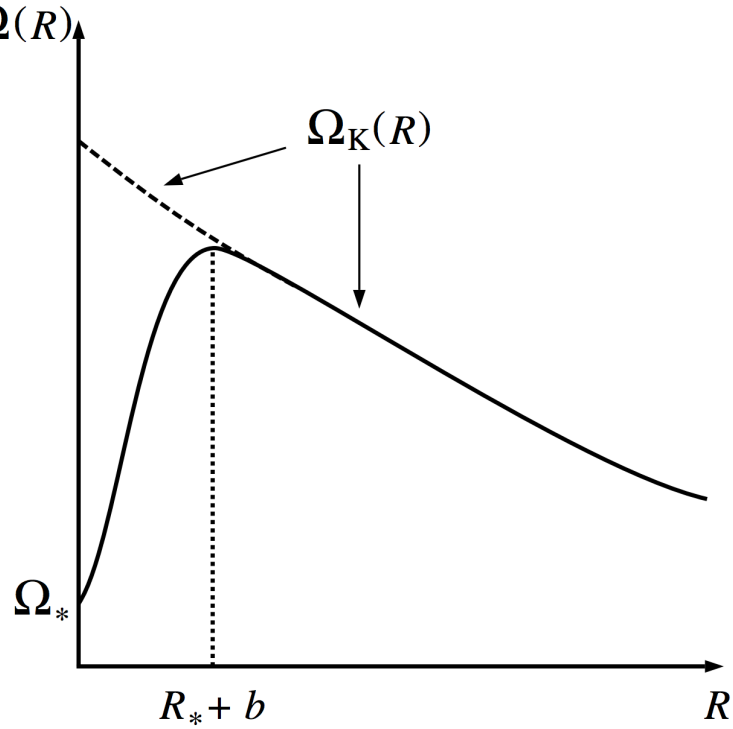


FIGURE 1.2: Credit: Frank et al. 2002. Angular velocity as a function of radius in an accretion disc around a rotating compact object with angular velocity Ω_* . Ω_K is the Keplerian angular velocity. This graph also helps explain why there is a turnover in the temperature-radius relation, as $D(R)$ is proportional to the square of the derivative of this quantity.

function of radius in a disc around a compact object rotating with angular velocity Ω_* . The boundary layer (BL) is the region to the left of the dotted line, inside the maximum of Ω_K , the Keplerian angular velocity. The luminosity of the boundary layer is ([Frank et al. 1992](#))

$$L_{BL} = \frac{1}{2} \frac{GM\dot{M}}{R} \left[1 - \left(\frac{\Omega_*}{\Omega_K(R_*)} \right) \right]^2, \quad (1.20)$$

where $\Omega_K(R_*)$ is the Keplerian angular velocity at R_* , assuming the thickness of the BL is small. When $\Omega_K(R_*) \gg \Omega_*$, this reduces to $L_{BL} = 1/2 L_{acc} = L_{disc}$

In cataclysmic variables, BLs can be approximated with blackbodies and their temperatures estimated indirectly via the [Zanstra \(1929\)](#) method (e.g. [Hoare & Drew 1991, 1993](#)). However, they likely exhibit a variety of atomic features ([Suleimanov et al. 2014](#)). Extreme-UV (EUV) datasets have confirmed the existence of boundary layer emission in non-magnetic CVs ([Mauche 1996](#)), although these observations are limited in number.

Clearly, in BH systems a boundary layer cannot exist in the same way, due to the lack of a physical surface. Instead, the energy must either go into growing the BH, contributing

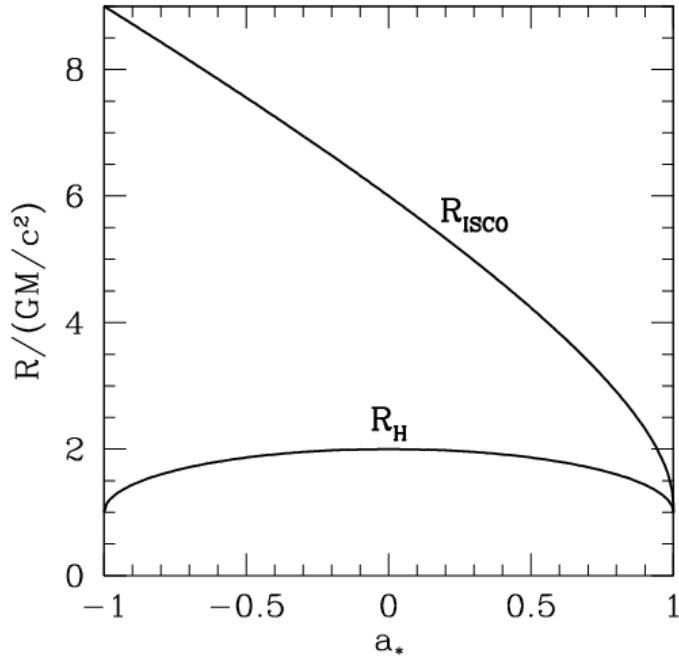


FIGURE 1.3: Credit: Narayan 2014. The radius of the ISCO, R_{ISCO} , and the horizon, R_H , is as a function of the BH spin parameter, a_* . $a_* = 0$ corresponds to a Schwarzschild BH, and $a_* = 1$ and $a_* = -1$ to prograde and retrograde Kerr BHs respectively. Note that this figure ignores the counteracting torque of photons swallowed by the BH, which actually limits a_* to a value of around 0.998 (Thorne 1974).

to its angular momentum or being channeled into a jet or other radiative source (see section 1.5.2). The question of what happens at the inner disc edge is complicated further by the fact that the disc cannot extend to the event horizon of the BH. Instead, there is an ‘innermost stable circular orbit’ (ISCO) beyond which the accreting matter will simply fall into the BH along nearly radial paths. The radius of this orbit, R_{ISCO} , and the horizon radius, R_H , is shown for different values of the BH spin parameter, a_* , in figure 1.3, showing how matter can orbit closer to a prograde spinning BH. In estimating the luminosity of a Keplerian disc around a BH, we should really set $R_* = R_{ISCO}$ in equation 1.5, giving the interesting result that rapidly spinning (Kerr) BHs ($\eta \approx 0.4$) are more radiatively efficient than Schwarzschild BHs ($\eta \approx 0.1$).

1.1.4 The Emergent Spectrum

It is important to recognise that the steady-state disc treatment *does not specify the exact shape of the disc SED*. What it does do is say where energy is originally released.

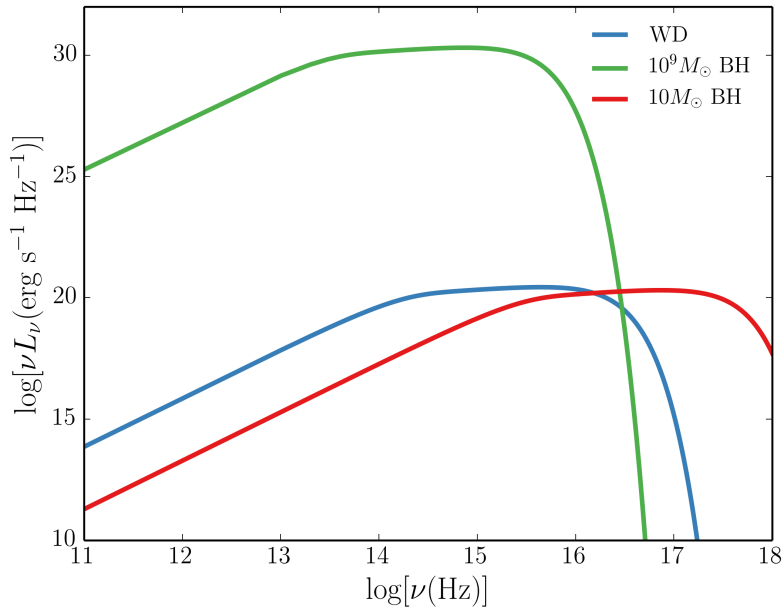


FIGURE 1.4: Accretion disc SEDs for three different compact objects, corresponding roughly to a quasar, an XRB and a CV. The SEDs are computed via an area-weighted sum of blackbodies with effective temperatures governed by equation 1.17, and the $\nu^{1/3}$ shape in the middle of the spectra can be seen.

The simplest assumption is that each annulus emits as a blackbody with temperature $T_{eff}(R)$, and the specific intensity through the emitting surface thus follows the Planck Law:

$$B_\nu(T) = \frac{2h\nu^3}{c^2} \frac{1}{\exp(h\nu/kT) - 1} \quad (1.21)$$

Under this assumption it is possible to show that at intermediate frequencies, where $kT(R_{max}) \ll h\nu \ll kT_*$, then the spectrum appears as a ‘stretched blackbody’ with the form

$$F_\nu \propto \nu^{1/3}. \quad (1.22)$$

Figure 1.4 shows the blackbody SEDs expected for the same objects as figure 1.1, in which the $\nu^{1/3}$ portion can be clearly seen. A disc atmosphere model with frequency-dependent opacity creates a somewhat different (and more realistic) spectrum. Figure 1.5 shows a comparison between a stellar atmosphere model and blackbody model for $T_{eff} = 50,000$ K, showing how an annulus at that temperature can have a significantly different spectral shape when one includes frequency-dependent opacities in the atmosphere. It is of course possible that *neither* blackbody or disc atmosphere treatments are realistic. I shall therefore devote a little time to discussing the observational

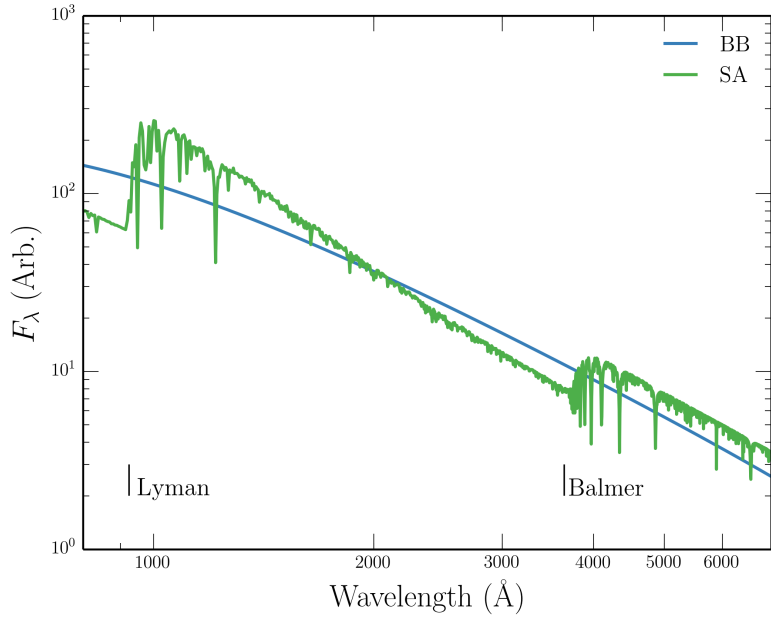


FIGURE 1.5: A comparison between a Planck curve and Kurucz (1991) stellar atmosphere model at $T_{eff} = 50,000\text{K}$ and surface gravity of $\log(g) = 5$. The major photoabsorption edges are marked. Flux is reprocessed into different wavelengths by bound-free opacities, and line blanketing also has a big effect on the spectrum. The Hydrogen and Helium lines also experience a degree of pressure broadening.

arguments for accretion discs and reviewing the different classes of accreting objects.

1.2 Accreting Compact Binaries

Accreting compact binaries form many different classes, but are all characterised by matter streaming from a donor onto a compact object. When the compact object is more massive than the donor then it is designated as the ‘primary’, and the companion as the ‘secondary’. In high-mass X-ray binaries (HMXBs), the opposite is formally true. There are only two ways by which matter can transfer from the secondary to the compact object. One is by Roche Lobe-overflow (RLOF), where the donor star expands to fill its Roche Lobe, the surface of equipotential around the star. The alternative is that the donor may expel material via a disc or radiatively driven stellar wind, allowing some of it to flow onto the compact object. Although accretion from a wind or circumstellar disc is common in HMXBs (Bartlett 2013), here I will focus on RLOF as it is more common in the systems that possess high-state accretion discs and associated outflows. Two examples of these are shown in figure 1.6

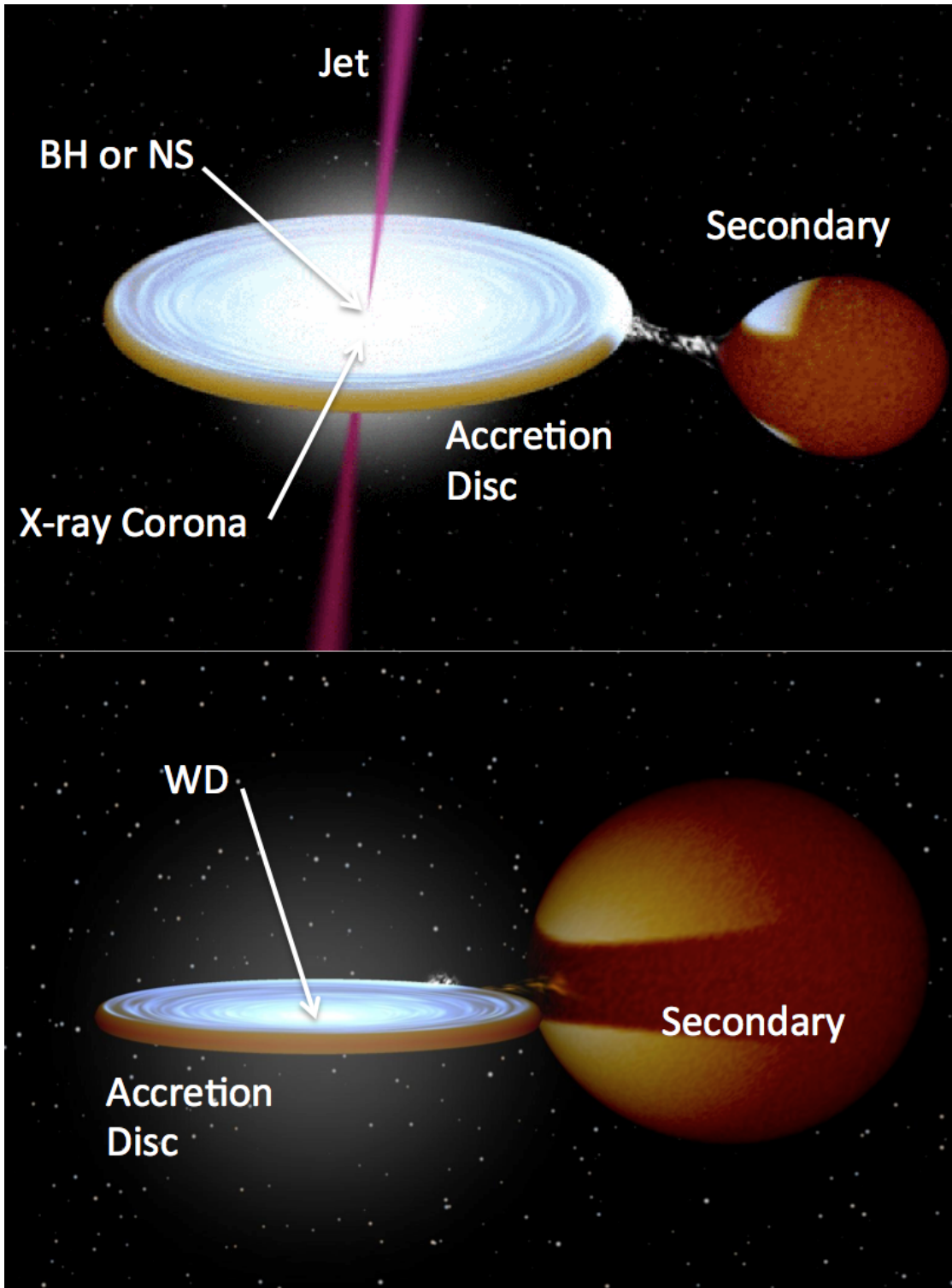


FIGURE 1.6: Credit: Rob Hynes. Artists impression of a low-mass X-ray binary (top) and cataclysmic variable (bottom). The key components are marked, and the clear similarity in overall structure is apparent.

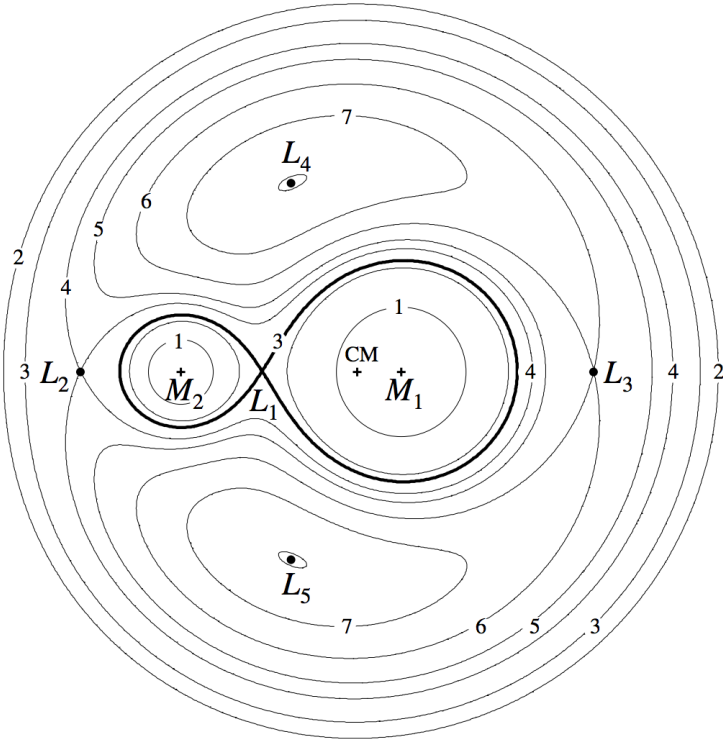


FIGURE 1.7: Credit: Frank et al. 2002. The Roche potential in a binary system for $q = M_2/M_1$ of 0.25. The Lagrangian points are marked, as are the locations of the individual and system centres of mass.

1.2.1 Roche Lobe-Overflow

Let us consider a binary system, with masses M_1 and M_2 , at positions \vec{r}_1 and \vec{r}_2 . The Roche potential, Φ_R , in this system is then

$$\Phi_R = -\frac{GM_1}{|\vec{r} - \vec{r}_1|} - \frac{GM_2}{|\vec{r} - \vec{r}_2|} - 1/2(\vec{\omega} \times \vec{r})^2, \quad (1.23)$$

where $\vec{\omega}$ is the angular velocity of the binary and is a vector normal to the orbital plane. This potential is plotted in figure 1.7 for a mass ratio, $q = M_2/M_1$ of 0.25.

In the context of semi-detached binary systems, the most important region of the potential is the dumbbell shaped region enclosing the masses. Each of these enclosed regions is known as the ‘Roche lobe’ of the object and can be expressed approximately in terms of the mass ratio and separation of the system. A good approximation for the size of the Roche lobe takes the form (Eggleton 1983)

$$\frac{R_2}{a} = \frac{0.49q^{2/3}}{0.6q^{2/3} + \ln(1 + q^{1/3})}. \quad (1.24)$$

Here R_2 is the radius of a sphere with the same volume as the Roche lobe for the secondary star, which we can see depends only on q and the orbital separation, a . If this secondary expands enough to fill its Roche lobe, then matter will fall onto the other object. This process is known as Roche Lobe overflow (RLOF), and is vitally important in astrophysics. Although caused by stellar evolution, any accretion from RLOF will affect the mass ratio of the binary system and thus itself affects the evolution of binary systems. This helps determine the orbital period distribution of binaries (e.g. Knigge et al. 2011) as well as affecting the delay time distribution of Type Ia Supernovae, for which CVs are one of the progenitor candidates (e.g. Wang & Han 2012). It is also worth noting that the existence of gravitational waves has been required in models to explain the orbital period evolution of CVs since the 1960s (Kraft et al. 1962).

1.2.2 Cataclysmic Variables

Cataclysmic variables (CVs) are systems in which a WD accretes matter from a donor star via Roche-lobe overflow (see the ‘CV bible’, Warner 2003). CVs are not always dominated by their accretion luminosity; classical novae and super soft sources (SSS) emit mostly due to nuclear burning or detonation on the WD surface. Accretion dominated CVs – the focus here – can be classified according to the magnetic field strength of the WD (B_{WD}) and photometric activity. Magnetic systems are classified as either ‘Polars’ ($B_{WD} \gtrsim 10^7$ G) or ‘Intermediate Polars’ ($10^6 \lesssim B_{WD} \gtrsim 10^7$ G); in these systems the accretion flow inside the some critical radius (related to the Alfvén radius) is dominated by the WDs magnetic field (e.g. Patterson 1994). In polars, this radius is large enough, due to the strong magnetic field, that no disc forms at all (Liebert & Stockman 1985). When $B_{WD} \lesssim 10^6$ G then the accreting material can fall onto the WD via a disc, and the CV is classified as non-magnetic. There are two main types of non-magnetic CVs; dwarf novae and nova-like variables.

1.2.2.1 Dwarf Novae and the Disc-instability Model

Dwarf novae (DNe) are CVs that are characterised by repeated periods of quiescence and dramatic outburst. One of the most famous DNe is SS Cyg, whose light curve is shown in figure 1.8. The repeated outbursts can be clearly seen, and SS Cyg itself has been undergoing this behaviour for the full century for which it has been observed. A

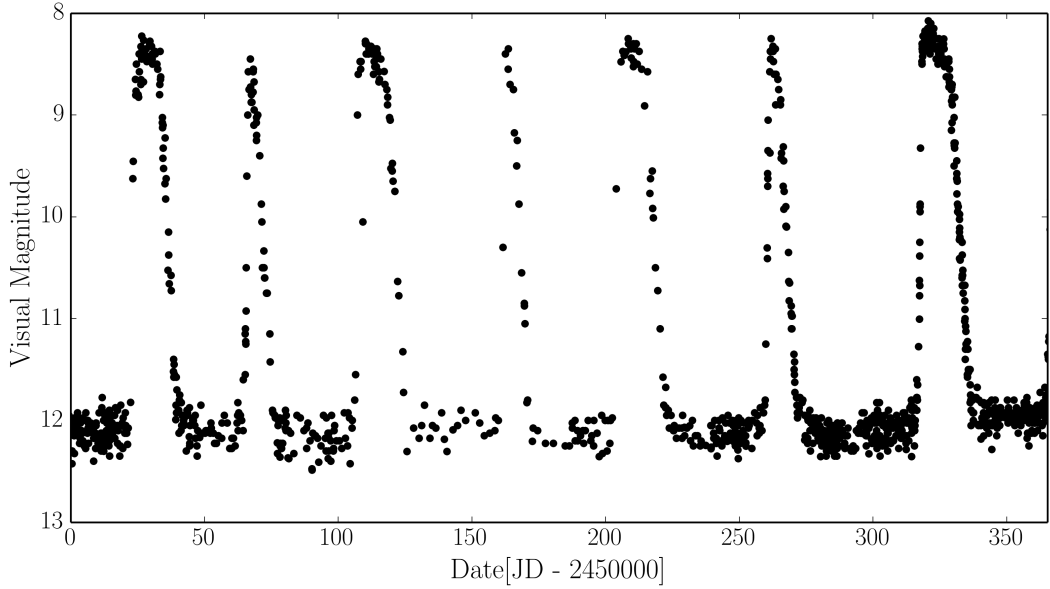


FIGURE 1.8: *Data: AAVSO.* A year in the life of SS Cyg, showing the characteristic repeated outbursts and periods of quiescence typical of a DN. SS Cyg has been undergoing this activity since it was first observed in 1896.

spectrum over the course of a typical outburst is shown in figure 1.9, and is characterised by the appearance of an optically thick accretion disc continuum – note the similarity to the stellar atmosphere disc spectrum computed in section 1.1.2.1, and to the intermediate inclination nova-like variables discussed in the next section.

The leading scenario for explaining DN outbursts, and in fact also the outbursts in low mass X-ray binaries or ‘soft X-ray transients’, is the disc-instability model (DIM; [Osaki 1974](#); [Lasota 2001](#)). In this model, a gradual increase in supply rate from the donor star (and hence surface density in the disc) causes the disc to heat up. Eventually, the disc hits a critical temperature, around 7000 K, and becomes ionized. Now the surface density in the disc can increase significantly, and the disc becomes geometrically thin and optically thick. Most importantly, it can undergo efficient radiative cooling, and a significant increase in brightness is observed.

1.2.2.2 Nova-like Variables

Nova-like variables (NLs) are similar to DNe, except that the disc is always in a relatively high-accretion-rate state ($\dot{M} \sim 10^{-8} M_{\odot} \text{ yr}^{-1}$). NLs are therefore one of the best ‘laboratories’ for testing the steady-state accretion disc theory described in section 1.1.2.1. In the optical, NLs generally exhibit a series of H and He emission lines superposed on a

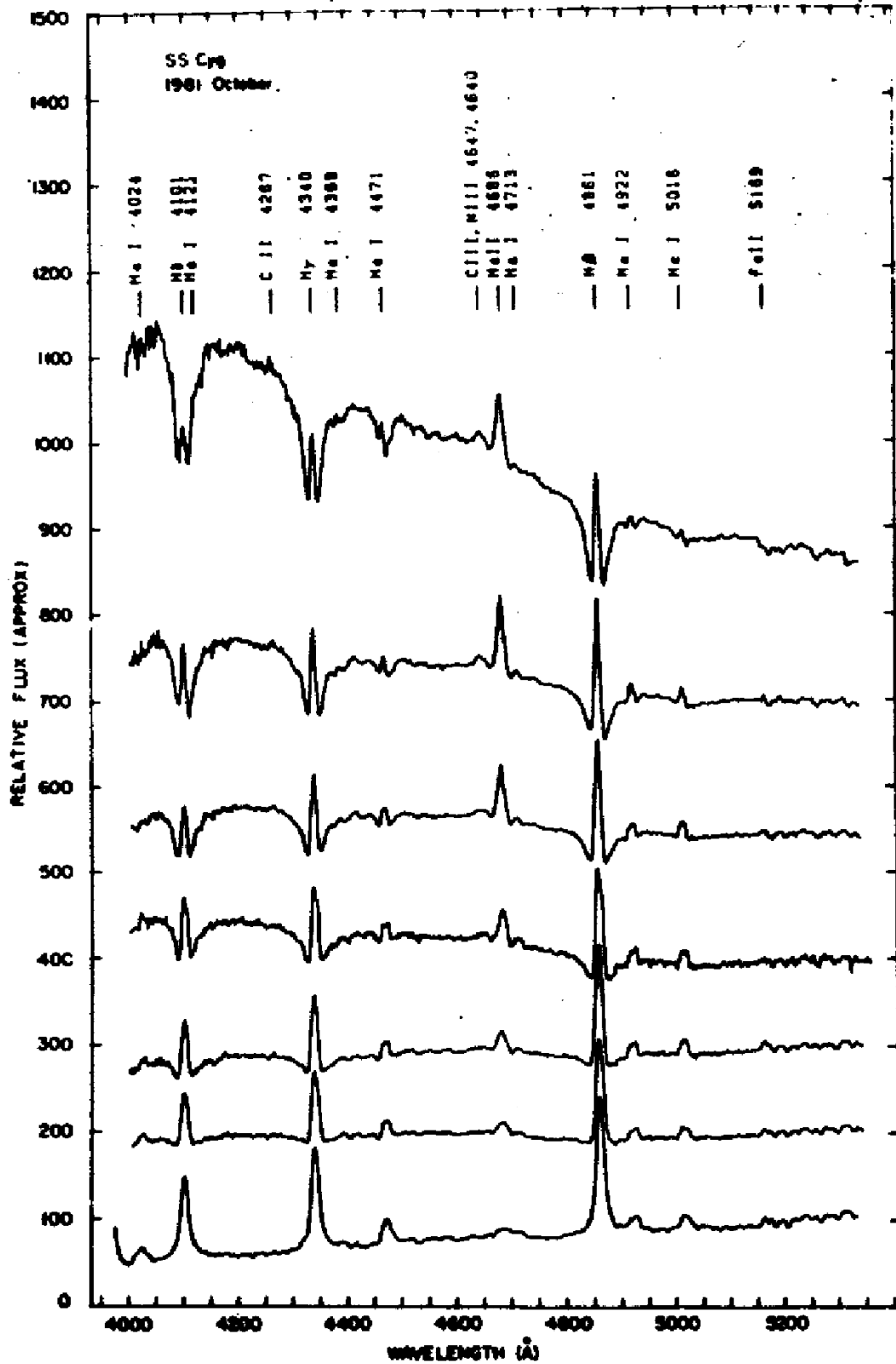


FIGURE 1.9: Credit: Hessman et al. 1984 / Dhillon et al. 1996. Spectra of SS Cyg during an outburst cycle, showing the evolution from minimum to maximum light. The rise is characterised by the appearance of an optically thick accretion disc spectrum. The flux scale is approximate.

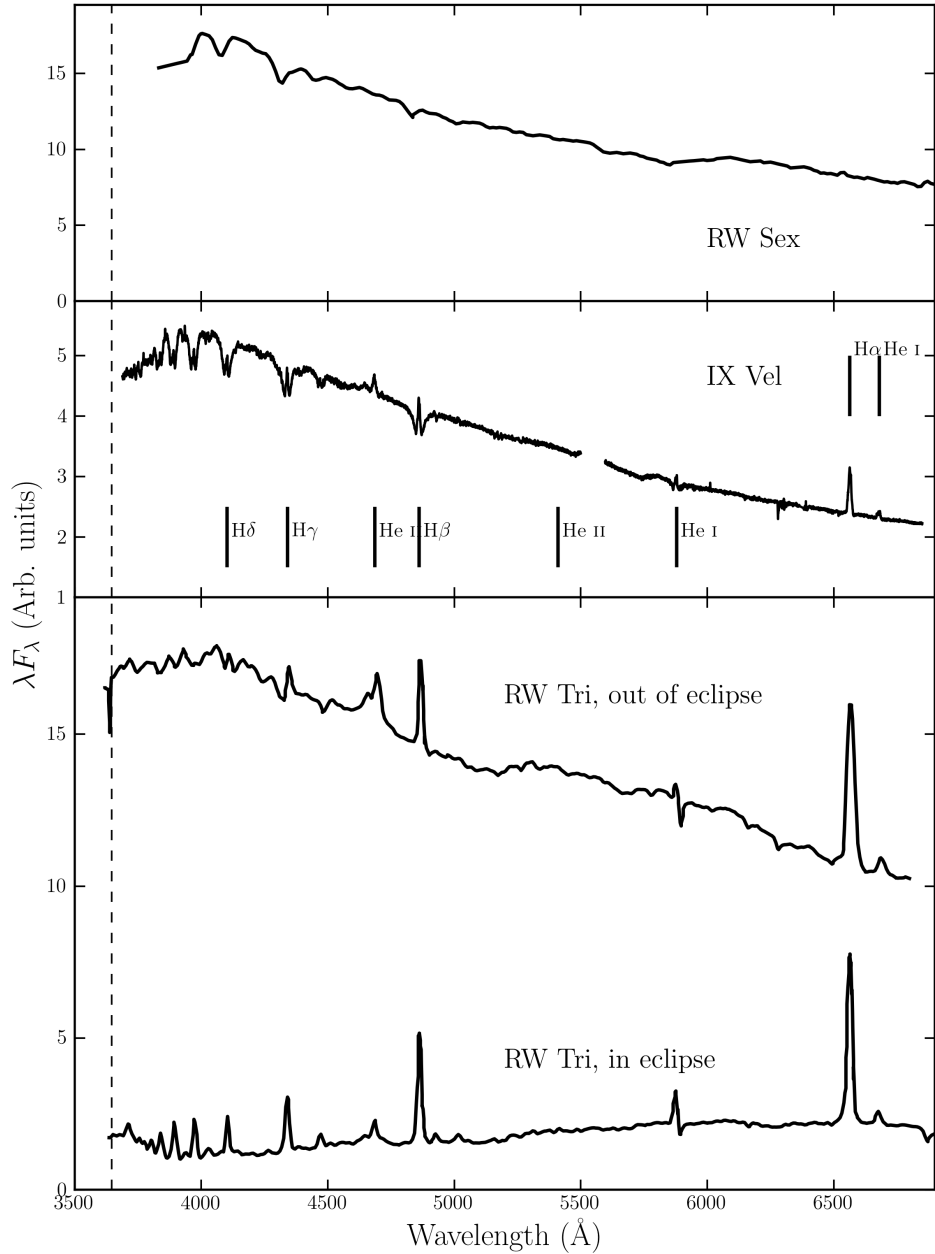


FIGURE 1.10: Optical spectra of three nova-like variables: RW Sex (top; Beuermann et al. 1992), IX Vel (top middle; A. F. Pala & B. T. Gaensicke, private communication) and RW Tri in and out of eclipse (bottom two panels; Groot et al. 2004). The data for RW Sex and RW Tri were digitized from the respective publications, and the IX Vel spectrum was obtained using the XSHOOTER spectrograph on the Very Large Telescope on 2014 October 10. These systems have approximate inclinations of 30° , 60° and 80° respectively. The trend of increasing Balmer line emission with inclination can be seen. In RW Tri strong single-peaked emission in the Balmer lines is seen even in eclipse, indicating that the lines may be formed in a spatially extensive disc wind, and there is even a suggestion of a (potentially wind-formed) recombination continuum in the eclipsed spectrum. I have attempted to show each spectrum over a similar dynamic range.

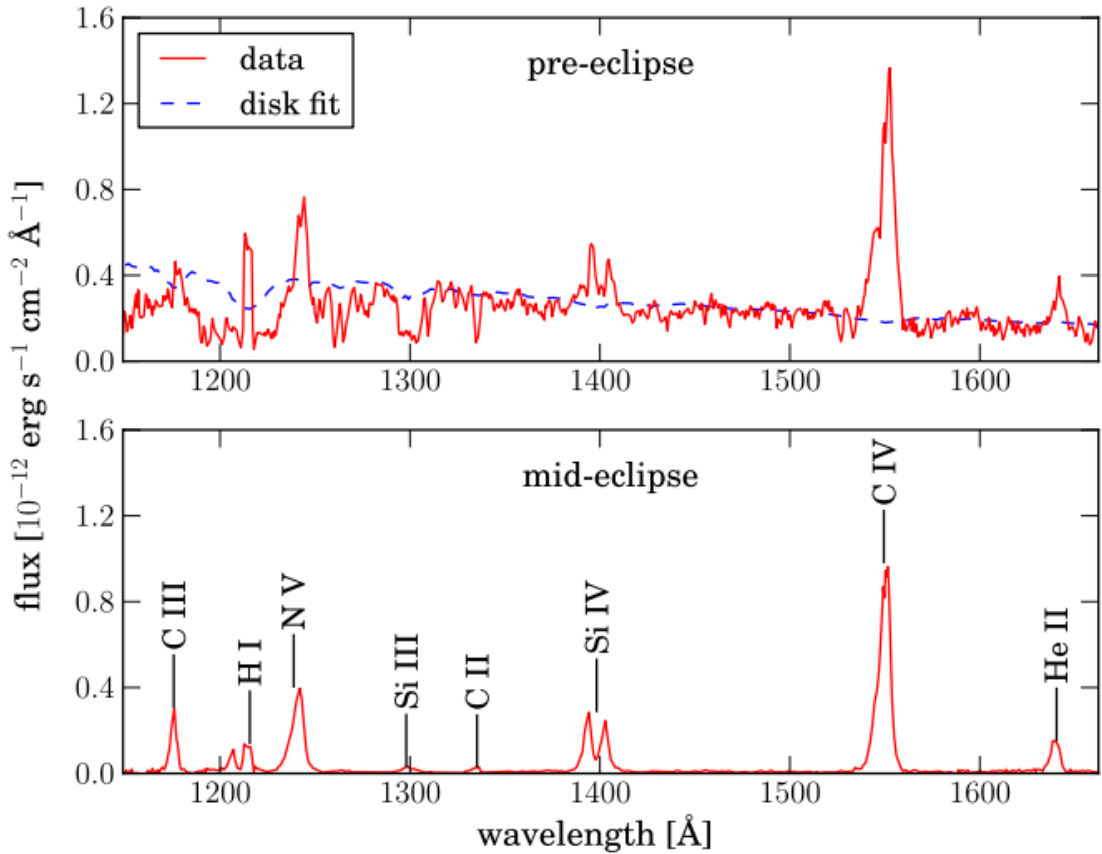


FIGURE 1.11: Credit: Noebauer et al. 2010. UV spectrum of RW Tri in and out of eclipse, showing strong lines in C IV 1550Å and Ly α , among others.

blue continuum. In many cases, and particularly in the SW Sex subclass of NLs (Honeycutt et al. 1986; Dhillon & Rutten 1995), these lines are single-peaked. This is contrary to theoretical expectations for lines formed in accretion discs, which are predicted to be double-peaked (Smak 1981; Horne & Marsh 1986). *Low-state* CVs (dwarf novae in quiescence) do, in fact, exhibit such double-peaked lines (Marsh & Horne 1990).

The UV spectra of NLs also show strong emission lines, and at low to intermediate inclinations dramatic blue-shifted absorption lines can be seen in some objects. The emission line equivalent widths in both the optical and the UV show clear correlations with inclination (Hessman et al. 1984; Echevarria 1988; Noebauer et al. 2010). This can be seen clearly in figure 1.11, and is connected to the correlation between line strength and absolute magnitude found by Patterson (1984); that is, the decrease in equivalent width at low inclination is caused by an *increase* in continuum flux. This is discussed further in chapters 4 and 6, but also has relevance to AGN and quasar unification schemes mentioned later in this introduction. The optical and UV spectra of NL CVs

are discussed further in the context of winds in chapter 2.

1.2.3 Low Mass X-ray Binaries

Low-mass X-ray binaries (LMXBs) are similar to CVs in structure (see figure 1.6), but the compact object is either a neutron star (NS) or black hole (BH). The accretion disc emits in the soft X-ray regime, and an additional hard X-ray power law is also seen in the spectrum. This hard component is normally attributed to Compton up-scattering of seed disc photons by some kind of ‘corona’ of hot electrons close to the BH (e.g. [White et al. 1988](#); [Mitsuda et al. 1989](#); [Uttley et al. 2014](#)). Although I do not study LMXBs directly in this thesis, it is instructive to briefly discuss of their observational appearance as it is relevant to the links between accretion and outflow. The discovery that XRBs and CVs follow similar tracks on a hardness-intensity diagram (HID; [Körding et al. 2008](#)) is particularly interesting in this regard, especially since [Ponti et al. \(2012\)](#) showed that broad Fe absorption lines are only seen in the soft-state high-inclination systems (see section 2.1.2). This implies that equatorial outflows are intrinsic to the accretion process. Although the driving mechanism is probably different to CVs (e.g. [Díaz Trigo & Boirin 2015](#)), the similarity in general structure to models for CVs and quasars is striking.

1.3 Quasars and Active Galactic Nuclei

Spectra of AGN have now been studied for over 100 years, and we have known that they exhibit strong, broad emission lines since the first spectrum was taken by [Fath \(1909\)](#). However, it wasn’t until the work of [Seyfert \(1943\)](#) that the systematic classification of AGN really began, leading to the phrase ‘Seyfert galaxy’. This label was applied to galaxies possessing a bright nucleus, spectroscopically characterised by a blue continuum and a series of strong emission lines. The first real physical insight into the extraordinary nature of AGN was provided by [Woltjer \(1959\)](#), who noted that (i) the nuclei must have sizes < 100 pc, based on the fact that they were unresolved, and (ii) the mass of the nucleus must be very high, based on virial estimates. While both of these observations were based on simple arguments, the fact that these ultra-luminous celestial objects are both *compact* and *supermassive* is perhaps the defining insight into the nature of AGN.

Although the study of AGN was established in the optical waveband, radio astronomy also significantly furthered our understanding of AGN in the mid-20th century. A number of surveys, such as the Cambridge (Edge et al. 1959), Parkes (Ekers 1969) and Ohio (Ehman et al. 1970) surveys discovered a great many bright radio point sources distributed isotropically across the sky. These sources eventually became known as ‘quasi-stellar radio sources’, or *quasars*, and were soon found to be coincident with bright optical sources or ‘quasi-stellar objects’ (QSOs) at high redshifts (Schmidt 1963, 1965a,b). Nowadays, the term quasar normally has very little to do with radio emission and is often used interchangeably with QSO. Indeed, throughout this thesis I shall refer to a quasar as simply a bright, massive AGN; one with sufficiently high luminosity that it dominates the emission from its host galaxy.

One of the main classification schemes for AGN is a spectroscopic one, based on whether an object possesses broad emission lines in its spectrum, such as C IV broad H β and Ly α , in addition to the narrow lines that are always present. If these broad lines are seen, then the AGN is classed as type I; if not, it is classed as type II (figure 1.12). These designations were originally applied to Seyfert galaxies (Seyfert 1943), but can also be used to classify the more luminous quasar class, despite the apparent difficulty in finding the expected number of type II sources (Zakamska et al. 2003). This classification scheme is complicated somewhat by the existence of two unusual types of AGN: narrow line Seyfert Is (NLSIs), which may be explained by super-Eddington accretion (Done & Jin 2015) or perhaps simply an orientation effect (Baldi et al. 2016), and so-called ‘true type II’ AGN, in which the broad line region is absent (Tran 2001; Shi et al. 2010) rather than obscured (see next section). Despite this muddying of the waters, what was originally a clear dichotomy in spectral type provided a profound motivation for attempting to *unify* AGN via geometric arguments.

1.3.1 AGN Unification and the Dusty Torus

Although Seyfert had identified type 1 and 2 AGN, a physical explanation for this dichotomy was not forthcoming until a study by Antonucci & Miller (1985, AM85). They showed unambiguously that the nearby Seyfert 2 NGC 1068 is simply an obscured type 1 AGN, by finding that broad emission lines appeared in the spectrum of *polarised* flux. This provided the basis for the first successful attempt to unify AGN behaviour, as

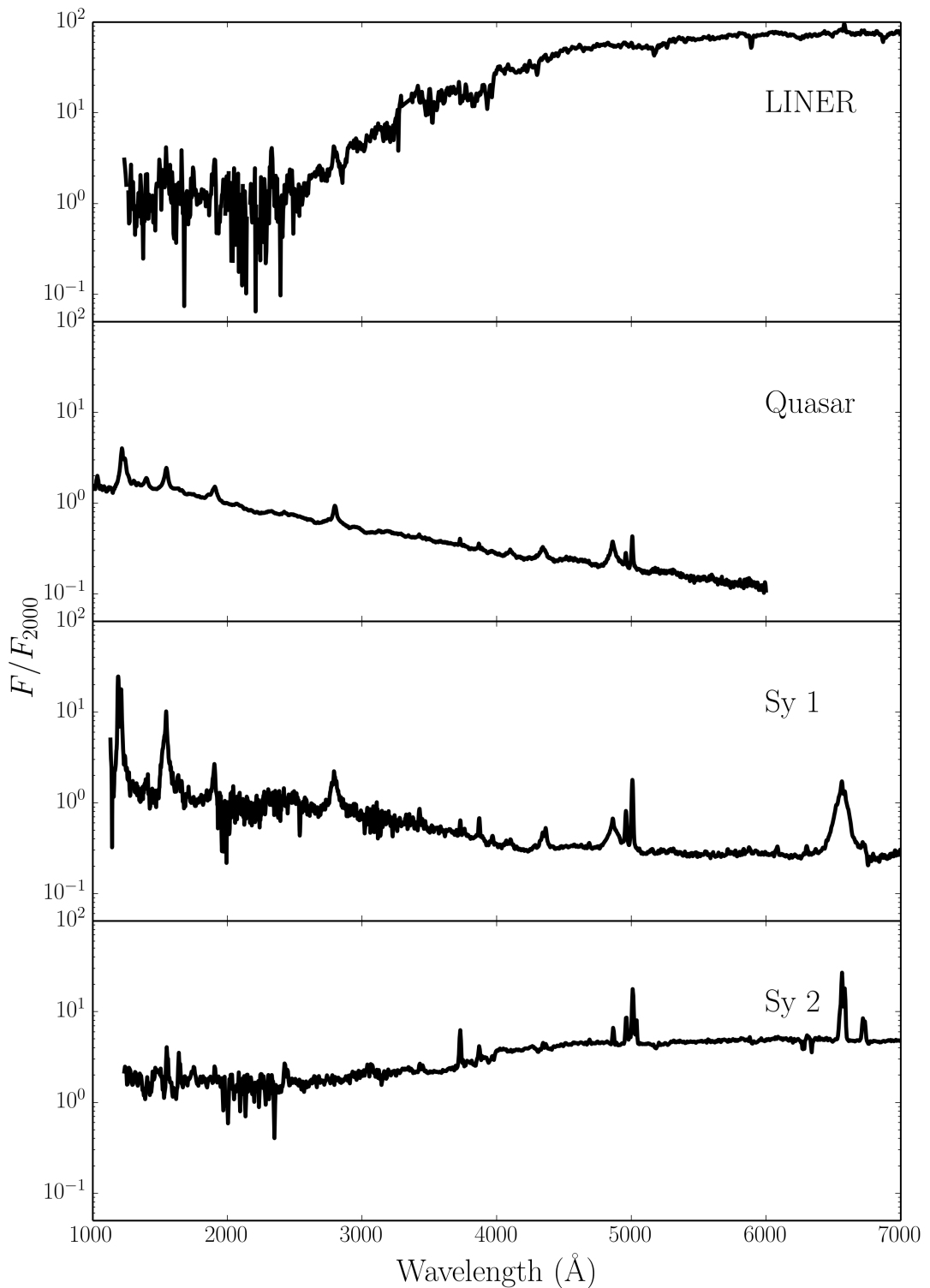


FIGURE 1.12: Template spectra, from the AGN atlas, for four common types of AGN.
Obtained from http://www.stsci.edu/hst/observatory/crds/cdbs_agn.html.

it elegantly explained the apparent disconnect between the two types of AGN as simply a viewing angle effect; at one angle, an observer could look directly into the broad line region (BLR) near the nucleus, but at Type 2 angles this region was hidden from view. The obscuring structure became known as the ‘torus’ (Krolik & Begelman 1986), due to its proposed geometry, and it was soon realised that this structure may be made of dust, in which case it could also be responsible for the infra-red (IR) bump in AGN (Neugebauer et al. 1979).

Urry & Padovani (1995, UP95) went further than the original unification model proposed by AM85, as they also tried to account for the dichotomy in AGN radio properties (radio-loud/radio-quiet). The picture they proposed is shown in figure 1.13. This model attempts to explain all of the types of AGN merely as a function of viewing angle and presence, or absence, of a radio jet. Models such as this also describe the series of ‘bumps’ observed in AGN – the portions of the spectrum that dominate the luminosity, shown in figure 1.14. In most models, the ‘Big Blue Bump (BBB)’ is ascribed to thermal emission from an accretion disc, and the ‘Small Blue Bump’ to optically thin Balmer continuum and Fe II emission from the BLR. The latter can just be seen between $\sim 2000\text{\AA}$ and $\sim 4000\text{\AA}$ in the Seyfert 1 and quasar templates in figure 1.12. Our understanding of the BBB is still unsatisfactory (see section 1.4).

Since the seminal works by AM85 and UP95, the picture has become somewhat more complicated. Variable X-ray absorption has been detected in so-called ‘changing look’ AGN (Matt et al. 2003; Puccetti et al. 2007), including even NGC 1068 itself (Marinucci et al. 2016). Changes in type have also been seen in the optical lines; the broad H β component in some AGN can dramatically disappear or reappear (e.g. Tohline & Osterbrock 1976; Cohen et al. 1986; Denney et al. 2014). The explanation for this could be variable absorption (Elitzur 2012) or a change in the accretion state of the disc. In the latter case, it has even been suggested that a disc wind could be directly responsible for this switch (Elitzur et al. 2014). Furthermore, dusty *polar* outflows have been found to be important IR emitters (Hönig et al. 2013), implying that, even when it comes to dust, the torus is not the whole picture. Despite these complications, the AGN torus unification picture still explains a lot of AGN phenomenology, and represents a useful framework that can be tested with observations.

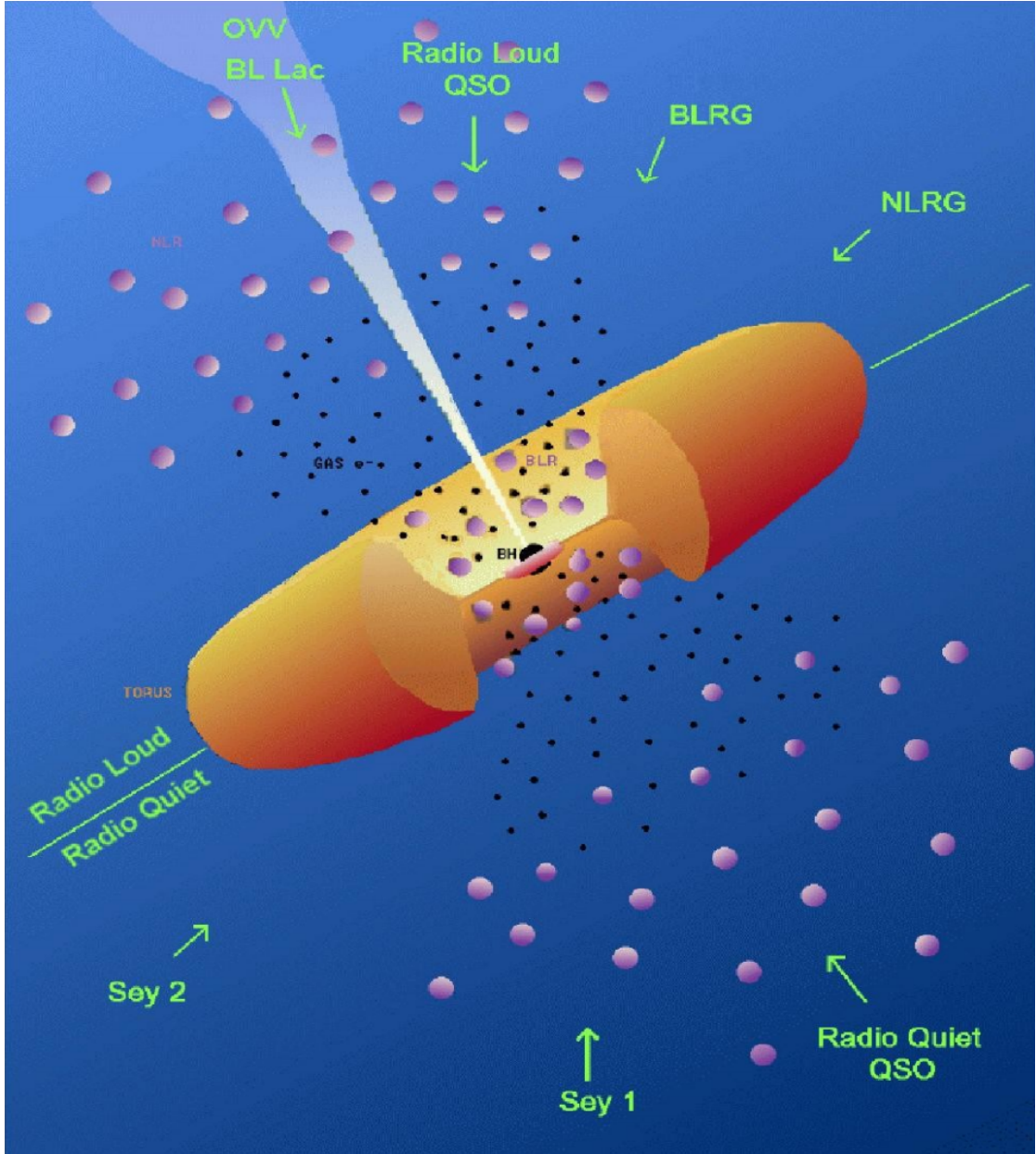


FIGURE 1.13: A unified scheme for AGN.

1.3.2 X-ray Properties of AGN

Approximately 10% of the bolometric luminosity of AGN comes out in the X-ray band, between ~ 0.1 and ~ 100 keV. Thus, AGN dominate the cosmic X-ray background (Madau et al. 1994). The hard X-ray emission typically follows a power law shape with spectral index -0.9 (e.g. Koratkar & Blaes 1999), widely considered, as in LMXBs, to come from a hot ‘corona’ of electrons close to the BH that upscatters disc seed photons (e.g. Haardt & Maraschi 1991). The compactness of this X-ray corona has been confirmed by microlensing (Chartas et al. 2009; Dai et al. 2010) and variability studies

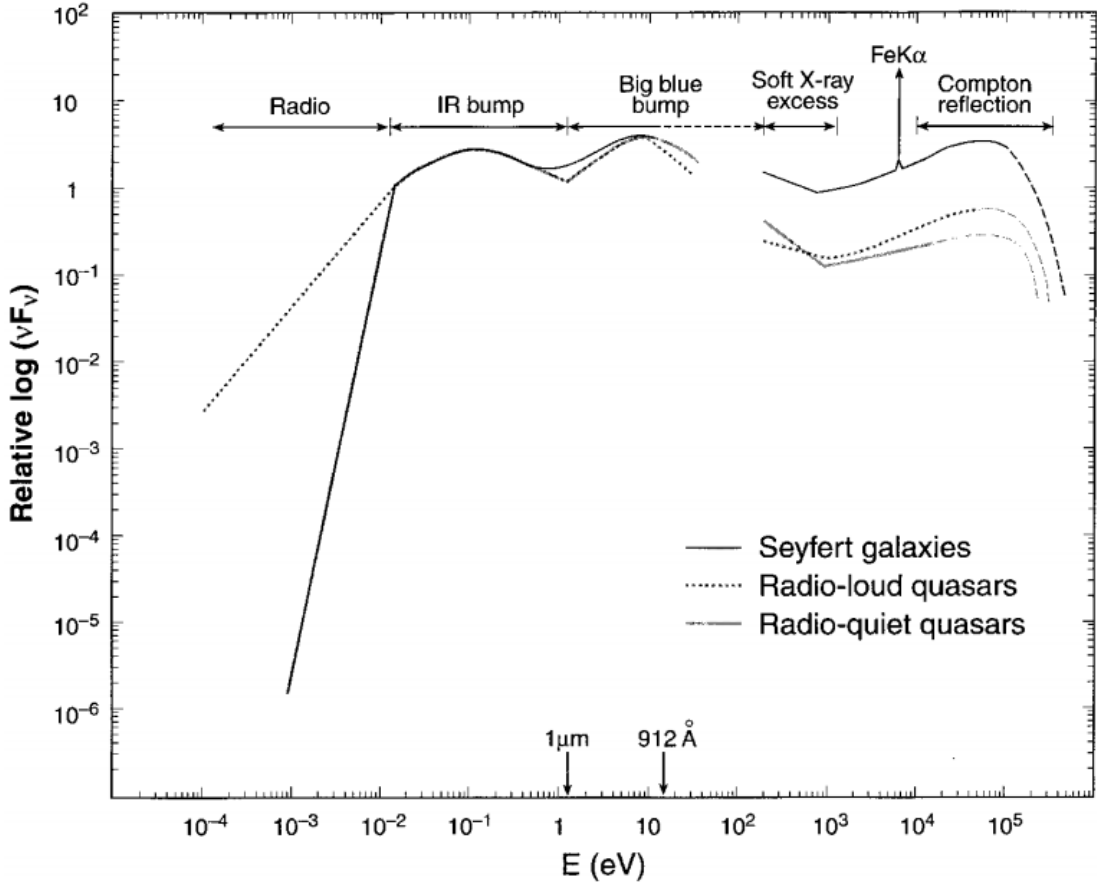


FIGURE 1.14: Credit: Koratkar & Blaes 1999 Approximate average broadband SEDs for a few types of AGN. The series of characteristic bumps can be clearly seen. The Soft-X-ray excess is also visible (see section 1.3.2.1).

(Green et al. 1993; Crenshaw et al. 1996; Risaliti et al. 2007; Emmanoulopoulos et al. 2014). Indeed, X-rays in AGN can be highly variable, both in terms of their intrinsic X-ray emission, but also due to changes in the absorption characteristics (Risaliti et al. 2002; Miller et al. 2008; Connolly et al. 2014). I discuss X-ray absorption in more detail, particularly with respect to disc winds, in chapter 2.

The hard X-ray spectra AGN also tend to exhibit a number of reflection features. Typically, these consist of a strong Fe K α emission line and a ‘Compton hump’ at high energies. The latter is produced by Compton down-scattering of high energy photons (Pounds et al. 1989; Nandra & Pounds 1994). It is still unclear exactly where these features originate, but a common interpretation is that they are caused by reflection off the inner parts of the accretion disc (Fabian et al. 1995; Iwasawa et al. 1996a; Reynolds 1999). If this is the case, and the broadening of the iron line is relativistic, this would allow for measurements of the BH spin (Laor 1991; Iwasawa et al. 1996b; Dabrowski et al.

1997). This hypothesis is somewhat controversial, as many of the relativistic features supposedly imprinted by BH spin can also be explained by Comptonisation or absorption (e.g. Misra & Kembhavi 1998; Miller & Turner 2013). In addition, an outflow can naturally produce the characteristic broad red Fe K α wing (Sim et al. 2010a).

In Compton-thick AGN, the intrinsic continuum is heavily absorbed with columns of $N_H \sim 10^{24}$ cm $^{-2}$ – this absorption is normally attributed to the dusty torus, but disc winds could also contribute. Compton-thick AGN are required in large numbers in order to explain the cosmic X-ray background (Setti & Woltjer 1989). In these sources, reflection features can actually dominate the X-ray spectrum (Alexander et al. 2011; Gandhi et al. 2013), but the Fe line is formed from low ionization stages of Fe on ~ 0.1 pc scales (Gandhi et al. 2015).

1.3.2.1 The Soft X-ray Excess

If one interpolates between the $\nu^{1/3}$ law from the BBB in the UV, and the power law in the hard X-rays, a curious excess of flux is often found in type 1 AGN (see figure 1.14, and Koratkar & Blaes 1999). This is known as the soft X-ray excess (SXES), which is too hot to be explained by thermal disc emission, as a thin disc around an AGN should never approach the temperatures required. Many models have been proposed to explain this excess, including relativistically smeared photoabsorption (Gierliński & Done 2004, 2006), relativistically smeared line and free-free emission (Ross & Fabian 2005; Crummy et al. 2006) and a variety of cool Comptonised component geometries such as an inner accretion flow (Magdziarz et al. 1998; Done et al. 2012) and geometrically thin layer on top of the disc (Janiuk et al. 2001). While the SXES poses a challenge to the simplest pictures of AGN, it may also solve some of the issues, as some of the geometries proposed may help to explain the accretion disc size problem discussed in section 1.4 (Gardner & Done 2016).

1.3.3 The Broad Line Region: Connection to Winds and Unification

In the UP95 unification model, the broad emission lines come from a series of virialised clouds close to the disc plane. As noted by Murray et al. (1995, hereafter MCGV95), there are a number of problems with the BLR ‘cloud’ model, perhaps most notably that

there is no obvious physical origin for such virialised clouds. Testing alternative models for the BLR is therefore important. Indeed, MCGV95 proposed a disc wind model in order to explain both BALs and BELs in quasars. A disc wind model was also discussed by [Elvis \(2000\)](#), who proposed a structure for quasars that attempted to explain much of the behaviour of luminous AGN merely as a function of viewing angle. It is worth noting that there is observational support for the unification paradigm; for example, it has been suggested that orientation is a key driver of the so-called ‘Eigenvector 1’ relationship in quasars ([Boroson & Green 1992](#); [Sulentic et al. 2000](#); [Marziani et al. 2001](#); [Shen & Ho 2014](#)). Disc wind unification models are discussed further in section 2. The philosophy of these models is that, before invoking additional degrees of freedom in a model, we should first test if known quasar phenomenology (disc winds) can explain other aspects of their observational appearance. I have illustrated this general principle with the ‘Occam’s quasar’ cartoon shown in figure 1.15. This is the picture that I will quantitatively test in the latter, quasar-focused sections of this thesis. The same general principle can also be applied to cataclysmic variables and other accreting objects.

1.4 The Current Understanding of the Disc Continuum

The SS73 model is still the most common way to fit accretion disc spectra and infer information about the underlying physics. However, a number of issues have been raised with the thin-disc model and its applicability to accreting systems.

1.4.1 The Spectral shape of CV discs

Attempts to fit the observed SEDs of high-state CVs with simple disc models have met with mixed success. In particular, the SEDs predicted by most stellar/disc atmosphere models are too blue in the UV ([Wade 1988](#); [Long et al. 1991, 1994](#); [Knigge et al. 1998a](#)) and exhibit stronger-than-observed Balmer jumps in absorption ([Wade 1984](#); [Haug 1987](#); [La Dous 1989a](#); [Knigge et al. 1998a](#)). One possible explanation for these problems is that these models fail to capture all of the relevant physics. Indeed, it has been argued that a self-consistent treatment can produce better agreement with observational data (e.g. [Shaviv et al. 1991](#); but see also [Idan et al. 2010](#)). However, an alternative explanation, suggested by [Knigge et al. \(1998b; see also Hassall et al. 1985\)](#), is that

OCCAM'S QUASAR: THE PRINCIPLE THAT IN EXPLAINING A QUASAR NO MORE ASSUMPTIONS SHOULD BE MADE THAN ARE NECESSARY.

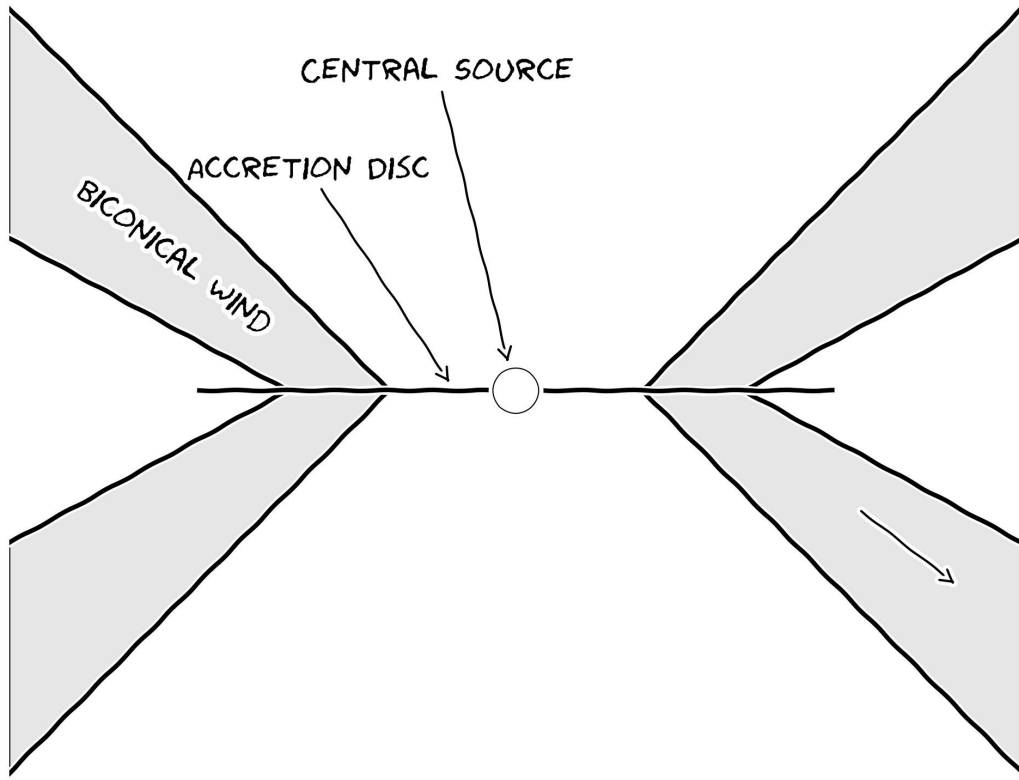


FIGURE 1.15: Occam's quasar. How far can this general picture take us when trying to explain the behaviour of quasars and other accreting compact objects?

recombination continuum emission from the base of the disc wind might fill in the disc's Balmer absorption edge and flatten the UV spectrum.

Alternatively, it may just be that CV disks are never really in a steady state, and so we should only expect the $R^{-3/4}$ temperature profile to hold in a limited portion of the disc. From eclipse mapping, it has been shown that the inferred accretion rate increases with radius in NLs (Rutten et al. 1992; Horne 1993). These results suggest that a non-radiative form of energy loss is present in the inner regions of the disc, of which potential forms may be advection or mass loss. This is yet another piece of evidence that the understanding of accretion and outflow are intertwined, although hopefully not inextricably.

1.4.2 The Big Blue Bump in AGN

Does the SS73 model apply well to AGN spectra? There are contrasting views on the matter. On the one hand, [Antonucci \(2013\)](#) claims that “most of the AGN community is mesmerized by unphysical models that have no predictive power”. Yet a recent spectral fitting study by [Capellupo et al. \(2015\)](#) concludes that “altogether, these results indicate that thin ADs are indeed the main power houses of AGN”. So, what are the current problems when confronting thin disc models with observation?

1.4.2.1 The Accretion Disc Size Problem

One of the most interesting results of recent years relating to AGN and accretion discs is the discovery that the continuum emission region size appears to be a factor ~ 3 larger than predicted by standard thin disc theory. This result has been found independently in both microlensing ([Morgan et al. 2010; Dai et al. 2010](#)) and reverberation ([Edelson et al. 2015](#)) studies, and poses a challenge to the current best-fit model for the big blue bump in AGN. One proposed solution is that the discs in AGN are inhomogeneous, consisting of individual clumps with independently varying temperatures ([Dexter & Agol 2011](#)), but this is very much still an active area of research. It is worth noting that the impact of winds on these results has not yet been properly quantified, something our team is currently trying to address ([Mangham et al. 2016](#)).

1.4.2.2 Fitting AGN Spectra and the 1000Å Break

One of the *successes* of the thin disc model, when applied to AGN, is that we do observe a slope in the UV of $\alpha_{UV} = 0.32$, confirming the theoretical prediction of $\nu^{1/3}$. However, AGN spectra do not exhibit the *overall* spectral shape (e.g. [Davis et al. 2007; Shankar et al. 2016](#)) or colour-mass scalings ([Bonning et al. 2007](#)) expected from theoretical predictions. This can be seen clearly in figure 1.12, where both the quasar and Seyfert spectra tend to peak in the UV, rather than the EUV. Furthermore, there is a characteristic break in AGN spectra at around 1000 Å ([Lusso et al. 2015](#)), which does not scale with BH mass or luminosity, as one might expect for a break associated with

an accretion disc. There is also no evidence in AGN of the expected polarisation signatures from an optically thick disc atmosphere (Stockman et al. 1979; Antonucci 1988; Antonucci et al. 1996).

Despite these problems, recent work suggests that the thin disc model still has some potential. Capellupo et al. (2015) were able to fit a number of AGN spectra in the UV and optical with thin disc models, although successful fits were only found once they included effects such as Comptonisation and mass-loss, as well as correcting for extinction. BH spin also had a reasonable effect on the spectral fits, although it is somewhat difficult to constrain from spectral fitting alone. The 1000 Å break has also been explained with a mass-losing disc (Laor & Davis 2014), and Lusso et al. (2015) suggested that incorrect IGM corrections may be exacerbating the effect. So, while many problems exist, it may not quite be time to abandon the Shakura-Sunyaev ship just yet.

1.5 The Universality of Accretion

Accretion appears to be an important physical processes across ~ 10 orders of magnitude in mass. But is this process the same on all scales? Does any behaviour manifest in all accreting systems?

1.5.1 The RMS-flux relation

Broad-band variability is common in all types of accretion disc. It has been known for some time that there exists a linear relationship between the flux and absolute root-mean-square (rms) amplitude of this variability. This was discovered first in XRBs and AGN (Uttley & McHardy 2001; Uttley et al. 2005; Heil et al. 2012), but it has been shown more recently that the relationship extends to CVs and even YSOs (Scaringi et al. 2012, 2015). The relationship is also not limited to just one type of CV but is present in both NLs and DNe (Van de Sande et al. 2015).

The model that best reproduces this behaviour is the so-called ‘fluctuating accretion disc’ model (Lyubarskii 1997; Kotov et al. 2001; Arévalo & Uttley 2006; Hogg & Reynolds

2015). More generally, additive processes cannot reproduce this behaviour, and a multiplicative mechanism is required (Uttley et al. 2005). Regardless of the mechanism, the rms-flux relation is one of the most clear-cut examples of a universal accretion phenomenon. It tells us that at least some of the behaviour in CV discs is also present in AGN and XRBs, strengthening the argument that CVs can be used as ‘accretion laboratories’.

1.5.2 Accretion states and disc-jet coupling

Variable and transient sources are common in astrophysics, particularly when the sources are accreting. I have already mentioned the DIM and its applicability to LMXBs and CVs; it turns out that when one plots the colour and luminosity evolution over the course of an outburst cycle then they follow very similar tracks (see figure 1.16, Körding et al. 2008). The detection of radio jets is also intrinsically linked to the accretion state of the system (disc-jet coupling), as jets only appear in the ‘hard’ accretion state, to the right of the so-called ‘jet line’ (Fender 2001; Fender et al. 2004). Körding et al. (2008) showed that this behaviour also occurs in CVs, as radio emission in the DN SS Cyg is also detected in the same region of colour-luminosity space. There is also a well-known correlation between radio and X-ray luminosities in low-hard states (Gallo et al. 2003).

Clear correlations between disc state and radio loudness have also been found in AGN. Perhaps the most obvious piece of evidence that disc-jet coupling is scale invariant is the so-called ‘fundamental plane of BH activity’ (Merloni et al. 2003), which extends from LMXBs right up to quasars. AGN have also been shown to occupy similar regions of colour-luminosity space to the LMXBs (Körding et al. 2006), and simulations involving scaled-up LMXB discs have been successful in reproducing AGN accretion states (Sobolewska et al. 2011). Correlations in X-ray photon index are also found in present AGN and LMXBs; ‘softer when brighter’ behaviour is found at relatively high Eddington ratios (McHardy et al. 1999; Gu & Cao 2009), while ‘harder when brighter’ is observed in low states (Gu & Cao 2009; Emmanoulopoulos et al. 2012; Connolly et al. 2016).

Despite this apparently universal behaviour, the jet production mechanism in BHs is not well known. Theoretical work suggests that radio jets should be correlated with BH spin (Penrose & Floyd 1971; Blandford & Znajek 1977), but whether such a correlation exists in LMXBs is controversial (Fender et al. 2010; Narayan & McClintock 2012). This has

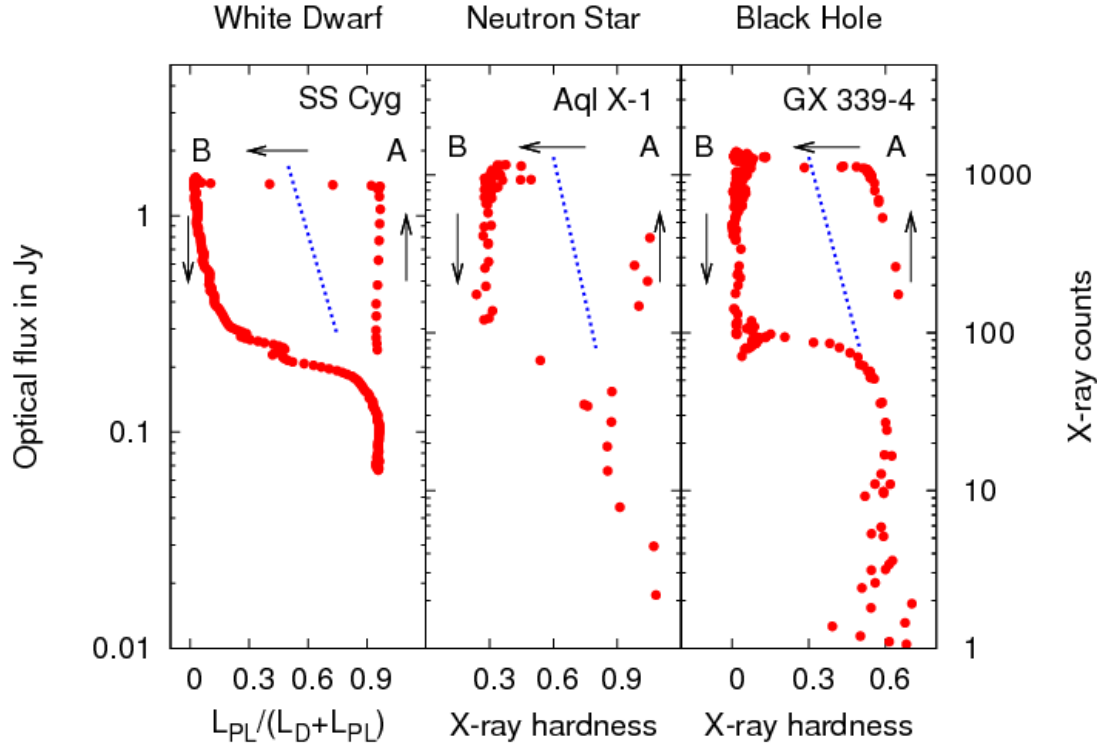


FIGURE 1.16: Credit: Kording et al. 2008. Caption.

significant implications for AGN; if powerful radio jets are associated exclusively with rotating BHs then the number of radio-loud AGN would imply a large fraction of them must be rapidly spinning, with high radiative efficiencies. Further evidence that radio jets are not simply produced by RIAFs onto spinning BHs is found when one considers that NLs show evidence of synchrotron radio emission (Coppejans et al. 2015). This important result suggests that our understanding of jets is incomplete, and that the links between accretion state and jet production are fundamental, but unsolved. Disc winds may complicate, or simplify, matters, depending on one's outlook (see chapter 2).

1.5.3 A Global Picture

Clearly, accretion physics is relevant to a plethora of astrophysical phenomena, and at least some of the physics of accretion is applicable to *all* classes of accreting object. It would also appear that the outflowing material observed in accreting systems has a profound effect on the accretion process itself, and possibly significantly affects the observational appearance of disc-accreting systems (c.f. Elvis unification model). Hence,

in the next chapter, I will review the evidence for winds and discuss some of the relevant background theory.

Chapter 2

Accretion Disc Winds

“A view of space, with an elephant
obstructing it”

Mike Vennart, Silent/Transparent

2.1 Observational Evidence

Observational evidence for mass-loaded outflows or winds is widespread across the entire astrophysical mass range and most of the electromagnetic spectrum. Before exploring this evidence, it is pertinent to briefly discuss the ‘smoking gun’ used to unambiguously detect winds – the presence of blue-shifted BALs or ‘P-Cygni’ profiles in an object’s spectrum.

Fig. 2.1 shows how a spherical outflow presenting significant line opacity will cause these characteristic profile shapes to form, as scattering out of the line of sight causes a dip in the blue wing of the line, while scattering into the line of sight from other portions of the outflow causes an increase in flux in the red wing of the line. The situation is much more complex in most astrophysical situations; for example, the geometry is rarely spherically symmetric, and the line is rarely a pure scattering case. Indeed, the potential for complicated radiative transfer effects and the variety in line formation mechanisms (e.g. recombination, collisionally excitation) is one of the reasons why 3D Monte Carlo radiative transfer simulations are necessary to effectively model disc winds (see chapter 3).

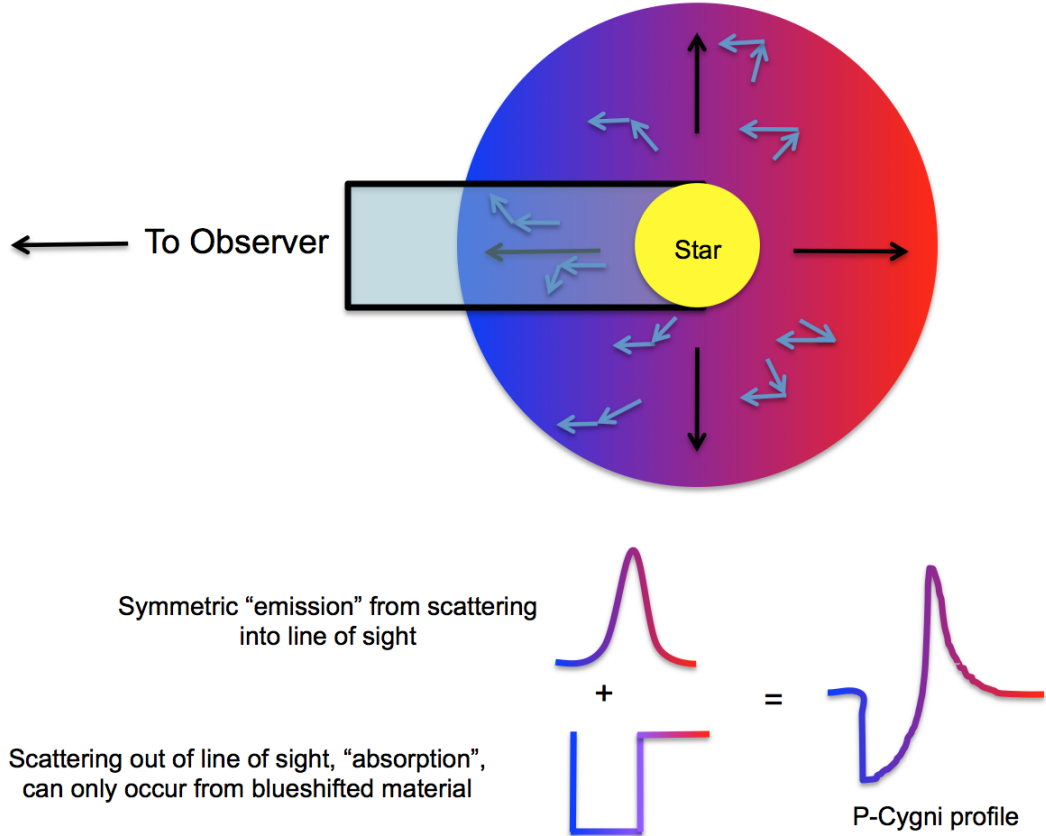


FIGURE 2.1: Diagram showing how an expanding envelope or wind presenting significant line opacity around a continuum source leads to the formation of P-Cygni profiles. The black arrows denote the outflow direction and the blue arrows typical scattering interactions.

2.1.1 Cataclysmic Variables

It has been known for a long time that winds emanating from accretion discs are important in shaping the ultraviolet (UV) spectra of high-state CVs (Heap et al. 1978; Greenstein & Oke 1982). The most spectacular evidence for such outflows are the P-Cygni-like profiles seen in UV resonance lines such as C IV 1550Å (e.g. Cordova & Mason 1982, see Fig. 2.2). Considerable effort has been spent over the years on understanding and modelling these UV features (e.g. Drew & Verbunt 1985; Mauche & Raymond 1987; Shlosman & Vitello 1993; Knigge et al. 1995; Knigge & Drew 1997; Knigge et al. 1997; Long & Knigge 2002; Noebauer et al. 2010; Puebla et al. 2011). The basic picture emerging from these efforts is of a slowly accelerating, moderately collimated bipolar outflow that carries away $\simeq 1\% - 10\%$ of the accreting material. State-of-the-art simulations of line formation in this type of disc wind can produce UV line profiles that are remarkably similar to observations, as shown in Fig. 2.3.

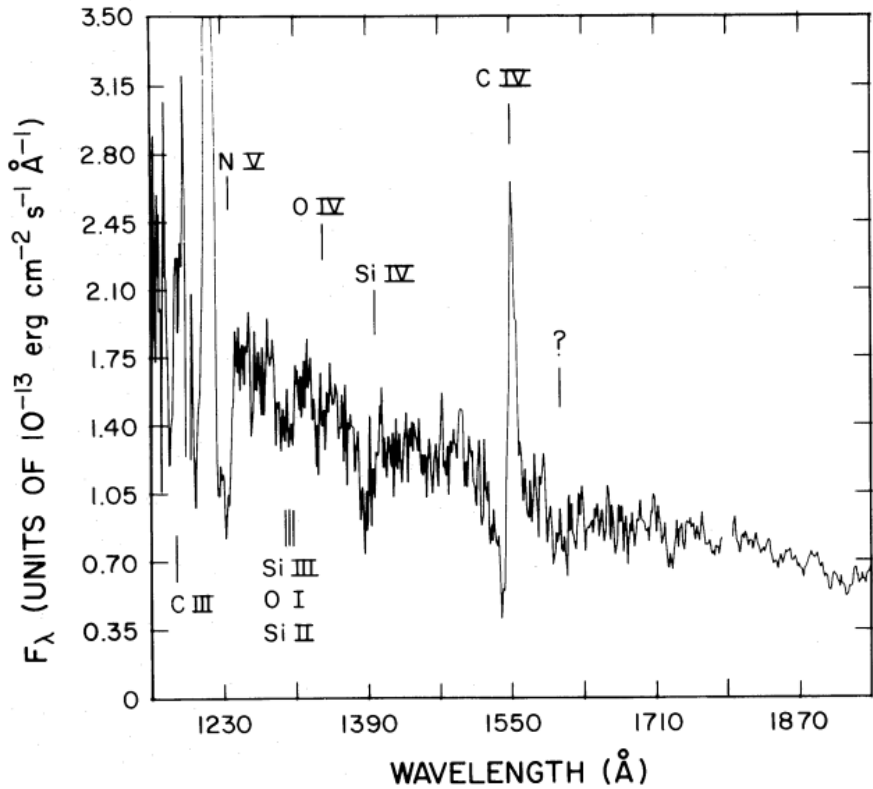


FIGURE 2.2: Credit: Cordova & Mason 1982. UV spectrum of the DN TW Vir during outburst. The P-Cygni profiles can be seen clearly, demonstrating that a strong, fast outflow is present in the system.

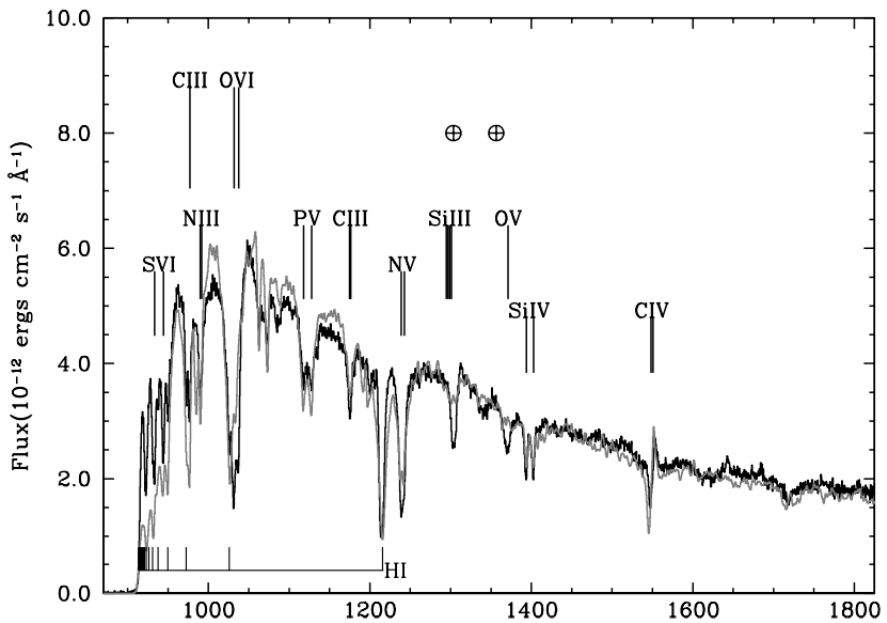


FIGURE 2.3: Credit: Long & Knigge 2002. UV spectrum of Z Cam, compared to a synthetic spectrum from MCRT simulations.

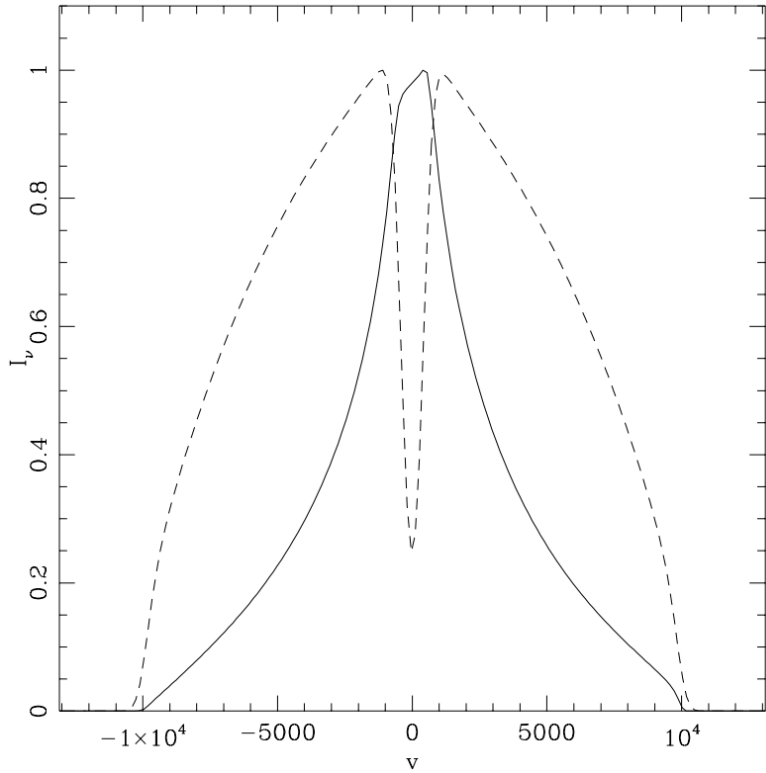


FIGURE 2.4: Credit: Murray & Chiang (1997). A comparison between a line profile, normalised to have peak intensity of 1, produced from a Keplerian disk (solid line) and the same model with an additional disc wind (dashed line). The radial velocity component of the disc wind modifies the escape probabilities across the disc, causing a single-peaked line to form.

Much less is known about the effect of these outflows on the optical spectra of high-state CVs. Direct evidence of wind-formed lines comes from isolated observations of P-Cygni-like line profiles in H α and He I λ 5876, ([Patterson et al. 1996](#); [Ringwald & Naylor 1998](#); [Kafka & Honeycutt 2004](#)). However, the effect of a wind on the *emission* lines in the optical spectrum is unclear. [Murray & Chiang \(1996, 1997\)](#) have shown that the presence of disc winds may offer a natural explanation for the single-peaked optical emission lines in high-state CVs, since they can strongly affect the radiative transfer of line photons (Fig. 2.4; also see [Flohic et al. 2012](#)). Stronger support for a significant wind contribution to the optical emission lines comes from observations of eclipsing systems. There, the single-peaked lines are often only weakly eclipsed, and a significant fraction of the line flux remains visible even near mid-eclipse (e.g. [Baptista et al. 2000](#); [Groot et al. 2004](#)). This points to line formation in a spatially extended region, such as a disc wind. It is also possible that a wind may affect the continuum emission of CVs, as described in section 1.4. The effect of an accretion disc wind on the optical line and continuum emission of CVs is addressed directly in chapter 4.

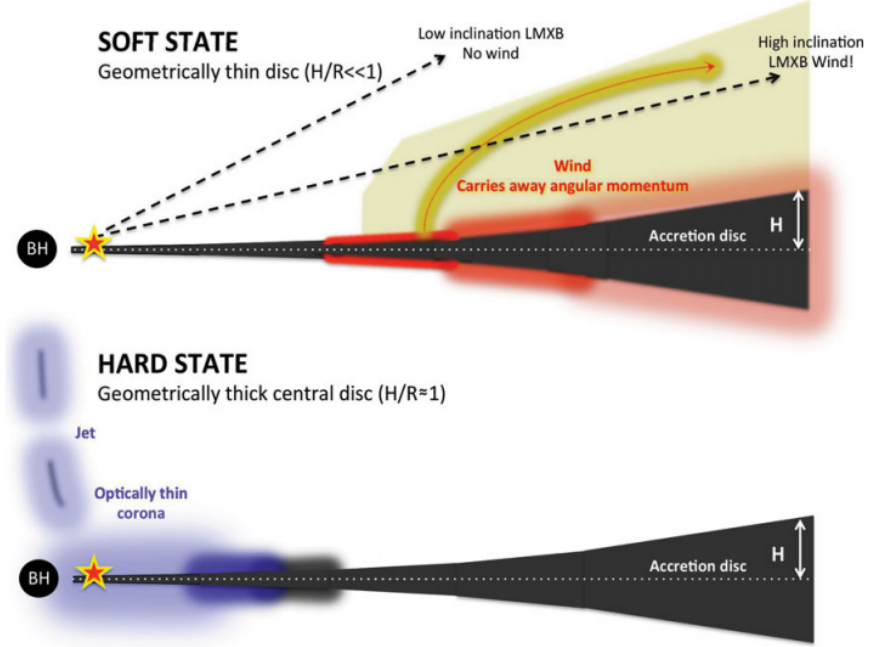


FIGURE 2.5: Credit: Ponti et al. 2012. A cartoon illustrating the expected geometry of soft-state LMXB winds.

2.1.2 X-ray Binaries

As in CVs, evidence for fast outflows in LMXBs is not constrained to a single waveband. UV absorption in outflows was detected when [Ioannou et al. \(2003\)](#) observed C IV 1550Å P-Cygni profiles with blueshifts of $\sim 1500 \text{ km s}^{-1}$ in the LMXB X2127+119. A series of studies also found X-ray absorption features in similar objects ([Ueda et al. 1998](#); [Kotani et al. 2000](#); [Parmar et al. 2002](#)). These absorption features appeared to be preferentially detected in high-inclination, ‘dipping’ LMXBs. This was confirmed by [Ponti et al. \(2012\)](#), who proposed an equatorial outflow geometry based on this association (see Fig. 2.5). The same study demonstrated that the winds only appeared in the soft, disc dominated accretion state, on the opposite side of the HID to the region where jets are common (Fig. 2.6). This exciting result illustrates how important winds are to our understanding of accretion, and requires that we expand the discussion of accretion states from ‘disc-jet’ coupling to also include winds.

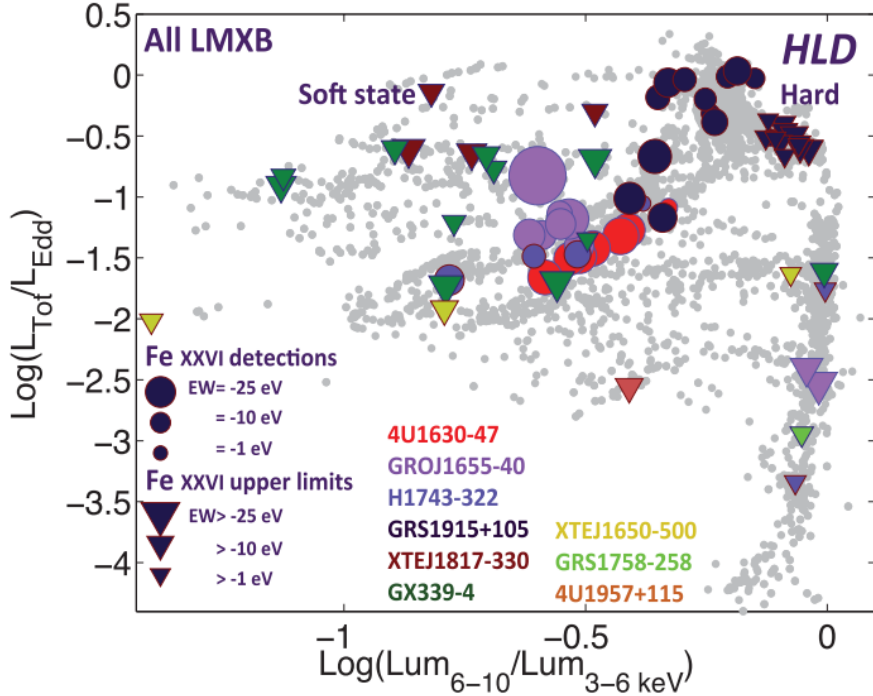


FIGURE 2.6: Credit: Ponti et al. 2012. Hardness-intensity diagram for four dipping LMXBs, demonstrating that winds appear only in the soft state.

2.1.3 AGN and Quasars

2.1.3.1 Broad Absorption Line Quasars

Perhaps the clearest evidence of outflows in AGN is provided by the blueshifted ($\sim 0.1 c$) ultraviolet BALs seen in approximately 20% of quasars (Weymann et al. 1991; Knigge et al. 2008; Dai et al. 2008; Allen et al. 2011). High-ionization BAL quasars (HiBALs) show only broad, blue-shifted absorption in species such as C IV, Si IV, N V and O VI, the most prominent BAL profile often being the C IV 1550Å line. In addition to the more common HiBALs, approximately 10% of BALQSOs show absorption in lower ionization species such as Mg II and Al III (LoBALs; Voit et al. 1993; Gibson et al. 2009) and an even smaller subset also show absorption in Fe II and III (FeLoBALs; Becker et al. 2000; Hall et al. 2002). Some example spectra of BAL quasars from the HST and SDSS archives are shown in Fig. 2.7, with important spectral lines marked.

The simplest explanation for the incidence of BAL quasars (BALQSOs) is in terms of an accretion disc wind viewed from different angles. This principle of geometric unification is very similar to the idea behind the UP95 and AM95 models discussed in Chapter 1. According to this paradigm, a biconical wind rises from the accretion disc so that the

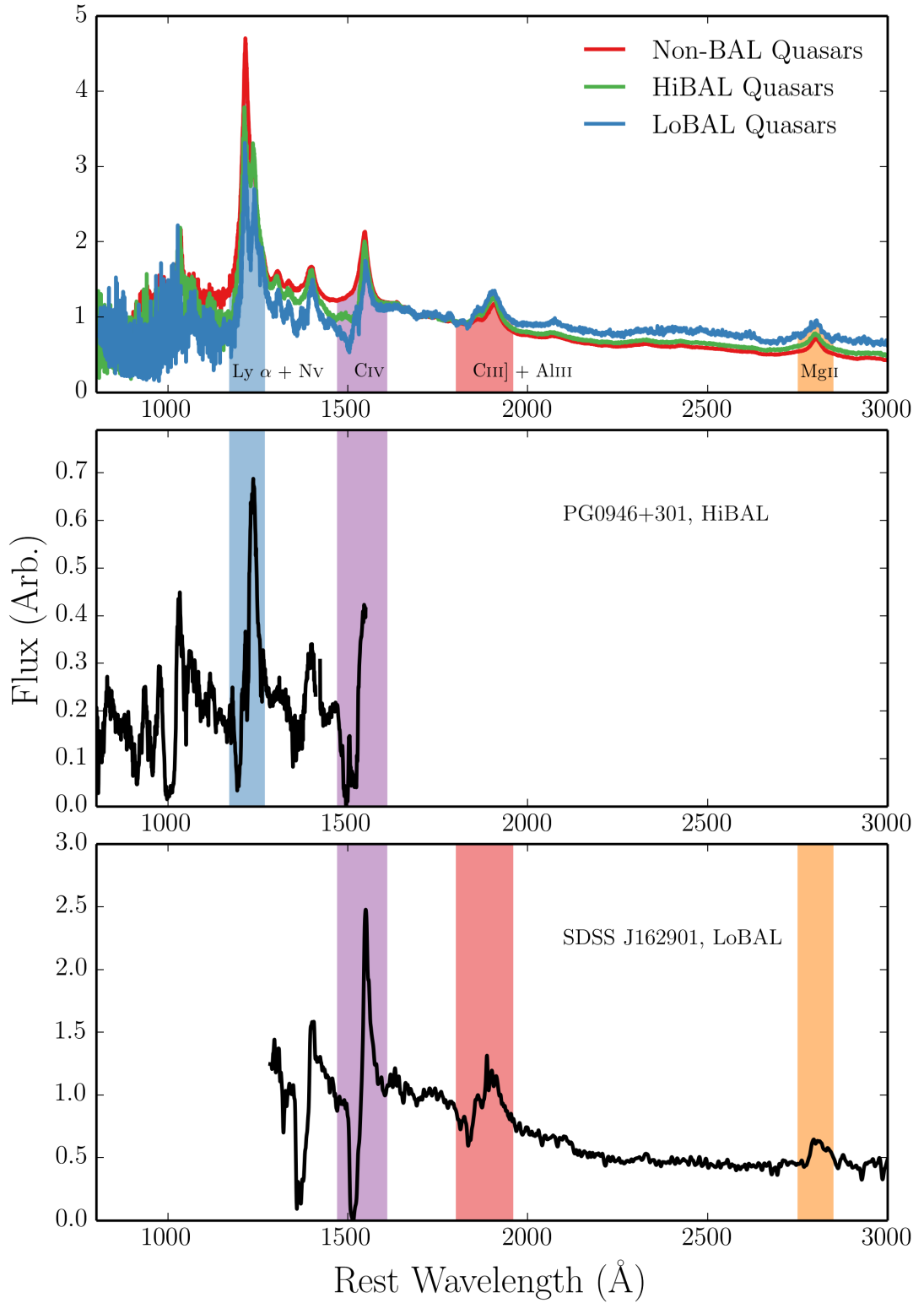


FIGURE 2.7: Top Panel: A comparison between the SDSS non-BAL, HiBAL and LoBAL composite spectra as presented in [Reichard et al. \(2003\)](#). Bottom Two Panels: Two individual examples of a HiBAL and LoBAL quasar spectrum, respectively. In all panels some of the more prominent lines are labeled and shaded, and the object name is given in the bottom two plots.

BALQSO fraction is associated with the covering factor of the outflow. This fraction has been estimated by various authors using different selection criteria, with values ranging between 10% and 40% depending on the treatment of selection effects and the classification scheme used (Weymann et al. 1991; Trump et al. 2006; Knigge et al. 2008; Dai et al. 2008; Allen et al. 2011)

BAL quasars can also be interpreted in an *evolutionary* context, in which quasars spend a certain proportion of their life in the ‘BAL phase’. Models generally put this phase near the start of the quasar lifetime (Hazard et al. 1984; Surdej & Hutsemekers 1987; Boroson & Meyers 1992; Zubovas & King 2013), after a dust-enshrouded phase, but before the main quasar period. It is perhaps more likely that *both* evolutionary and geometric effects are at work (Borguet & Hutsemékers 2010; Dai et al. 2012). One of the main problems with testing these two paradigms is that many of the properties of BAL quasars fit naturally into either picture, and so disentangling their true nature is challenging. The latter chapters of this thesis attempt to address this issue by testing the geometric unification model and seeing how close this simple picture can get to explaining the BAL phenomenon.

While the BAL fraction, f_{BAL} , is a very useful number and must be at least related to the covering factor of the outflow, continuum selection (Goodrich 1997; Krolik & Voit 1998) and reddening (Allen et al. 2011) effects could lead to significant underestimates of its true value. Unfortunately, accurate corrections for these effects are challenging. The degree of collimation of the BAL wind is also not well known. Polarisation studies suggest that the wind is roughly equatorial (Goodrich & Miller 1995; Cohen et al. 1995), as also found from hydrodynamical and radiative transfer simulations (Proga et al. 2000; Proga & Kallman 2004; Higginbottom et al. 2013), but there is also evidence for polar BAL outflows in radio-loud (RL) sources (Zhou et al. 2006; Ghosh & Punsly 2007). In addition to these uncertainties, the physical scale of the BAL phenomenon is also disputed and may vary from object to object. A common assumption is that the BAL region is roughly co-spatial with the BLR, which is reasonable considering the similar velocity widths and ionization states in BELs and BALs. In this case, the radius of the absorbing material can be estimated as $\sim 100r_G - 1000r_G$ from reverberation mapping and microlensing (e.g., for BLRs in BALQSOs, Sluse et al. 2015; O’Dowd et al. 2015). However, distances of ~ 0.1 pc ($\sim 10^4r_G$) have been estimated in at least some objects

from photoionization modelling, conducted using densities calculated from absorption line doublets (Borguet et al. 2013; Chamberlain et al. 2015).

BAL quasars display a wide variety of different trough shapes, as shown in Fig. 2.7. The line profiles themselves often show complex structure (Foltz et al. 1987; Ganguly et al. 2006; Simon & Hamann 2010) and can be time variable (Hall et al. 2011; Capellupo et al. 2011, 2012, 2014; Filiz Ak et al. 2012). Furthermore, there are a set of quasar absorption systems that show BAL-like absorption troughs with much smaller velocity widths. Depending on their width, these are known as narrow absorption lines (NALs) or ‘mini-BALs’ (Misawa et al. 2007, 2008; Nestor et al. 2008). While some of this behaviour can be explained once again as a viewing angle effect (e.g. Ganguly et al. 2001), the BAL profile variety and variability suggests that BALQSOs are far from a homogenous population, and may point towards dense substructures (clumps) in their flows. Clumpiness has been invoked in disc wind unification models for AGN and quasars (see section 2.3)

The X-ray properties of BAL quasars are particularly important due to the strong ionizing potential of the X-ray radiation. BALQSOs are X-ray weak when compared to non-BAL quasars (Gibson et al. 2009). The X-ray weakness of BALQSOs is often attributed to X-ray absorption with column densities of $N_H \sim 10^{22-24} \text{ cm}^{-2}$ (Gallagher et al. 1999, 2002; Green et al. 2001; Grupe et al. 2003a; Stalin et al. 2011), although there is also evidence that BALQSOs are *intrinsically* X-ray weak (Sabra & Hamann 2001; Clavel et al. 2006; Morabito et al. 2013). The X-ray properties of BAL quasars are fundamentally coupled to the properties of the wind – the X-ray absorption may be caused by the outflow, which in turn has its ionization state determined by the X-ray radiation. Furthermore, the true X-ray luminosities cannot be reliably inferred until the inclinations of BALQSOs are constrained, as gravitational lensing can significantly alter the emergent angular distribution of X-ray emission even for an intrinsically isotropic source (Chen et al. 2013a,b).

Although the X-rays in BALQSOs are weaker than in similar mass quasars, they still possess strong ionizing power. This leads to what has become known as the ‘over-ionization problem’ in BALQSOs: how is the moderate ionization state of the BAL gas maintained in the presence of ionizing X-rays? A number of potential solutions have been proposed, which can be broadly separated into ‘shielding’ models (Murray et al.

1995; Proga & Kallman 2004) and ‘clumpy’ models (de Kool & Begelman 1995; Hamann et al. 2013). Some of these models are discussed further in section 2.3 and chapter 5.

2.1.3.2 Warm Absorbers

Warm absorbers (WAs) are regions of photoionized plasma responsible for some of the characteristic absorption features seen in the X-ray spectra of AGN (Reynolds & Fabian 1995). In particular, they produce photoelectric continuum absorption (e.g. Halpern 1984; Cappi et al. 1996; Kriss et al. 1996) and a series of narrow absorption lines in H-like and He-like ions of C, N, O, Si, Ne, and Fe (Kaastra et al. 2000), that appear in the soft X-rays. A wind origin is a common hypothesis for WAs (e.g. Krolik & Kriss 2001). Clear evidence for this comes from the measured blueshifts of the lines, typically on the order of $\sim 100 \text{ km s}^{-1}$. X-ray absorption and WAs are often variable (Fabian et al. 1994; Otani et al. 1996), which may be interpreted in terms of changing kinematics of an accretion disc wind (Connolly et al. 2014). There is also evidence of contemporary and associated UV and X-ray absorption in NGC 5548 (Kaastra et al. 2014) and mini-BALS (Giustini et al. 2011), and, as mentioned above, BALQSOs often show strong X-ray absorption. This suggests the same outflow phenomenon produces observational signatures across a large range of ionization states and line energies.

Some WAs can be modelled well with single absorbers (Kaastra et al. 2000), but most require multiple absorption components with different ionization states (e.g. Kriss et al. 1996; Orr et al. 1997; Krolik & Kriss 2001; Connolly et al. 2014). If this is the case, then self-consistent ionization and radiative transfer models should really be used to model the spectrum (see e.g. chapter 3). This is because optically thin ionization parameter estimates will not properly capture the ionization physics in a complex geometry and radiation field. The overall body of observations points towards an outflow with a stratified ionization structure ranging from $\log \xi \sim 0 - 2$, and densities on the order of 10^8 cm^{-3} . These physical conditions or scales are not well constrained, and the connection to other outflows, such as the ultra-fast outflows introduced in the next section, is unknown. Timing observations may help to shed light on the properties of the mysterious, but ubiquitous, AGN WAs (Silva et al. 2015).

2.1.3.3 Ultra-fast Outflows

As well as acting as WAs, winds can also imprint clear absorption features in highly ionized Fe K α lines in AGN such as PDS 456 (Reeves et al. 2003; Gofford et al. 2014; Matzeu et al. 2016), MCG-5-23-16 (Braito et al. 2007) and PG 1211+143 (Pounds & Reeves 2009; Fukumura et al. 2015). These outflow signatures are fairly common in Seyfert galaxies (Tombesi et al. 2010; Gofford et al. 2013). One example of such a feature is shown in Fig. 2.8 along with a simple spherical outflow model fit (Nardini et al. 2015). The high velocities ($\sim 0.1c$) inferred from the line blueshifts have lead to these winds becoming known as ultra-fast outflows, or UFOs.

UFOs are characterised by ionization parameters in the range $\log \xi \sim 3 - 4$ and column densities $N_H > 10^{22} \text{ cm}^{-2}$. Their high mass-loss rates and large energy budgets mean that they are natural candidates for AGN feedback (see section 2.5). Measurements of their kinetic luminosities suggest that UFOs have sufficient energy to affect their host galaxy (Gofford et al. 2015). In fact, a large-scale molecular outflow has recently been detected in one UFO host, possibly driven by the UFO itself (Tombesi et al. 2015). As with WAs, many of the models used to constrain physical parameters are simplistic, and assume single ionization parameters, large covering factors and thin expanding shells of outflow. Under the assumption of a thin expanding shell, the mass-loss rate can be estimated using (e.g. Borguet et al. 2012)

$$\dot{M} \sim \Omega N_H m_p v_{out} R_{in}, \quad (2.1)$$

where Ω is the solid angle covered by the outflow, N_H is the column density, m_p is the proton mass, v_{out} is the outflow velocity and R_{in} is the launch radius of the outflow. In reality, the absorber is probably much more complex, and full RT and photoionization simulations are required to accurately model the expected spectrum. In a series of papers, Sim et al. (2008, 2010b,b) carried out such calculations and found that reasonable verisimilitude with Fe line profiles could be achieved. However, as with many models of AGN, a holistic, broad wavelength range fit is still required.

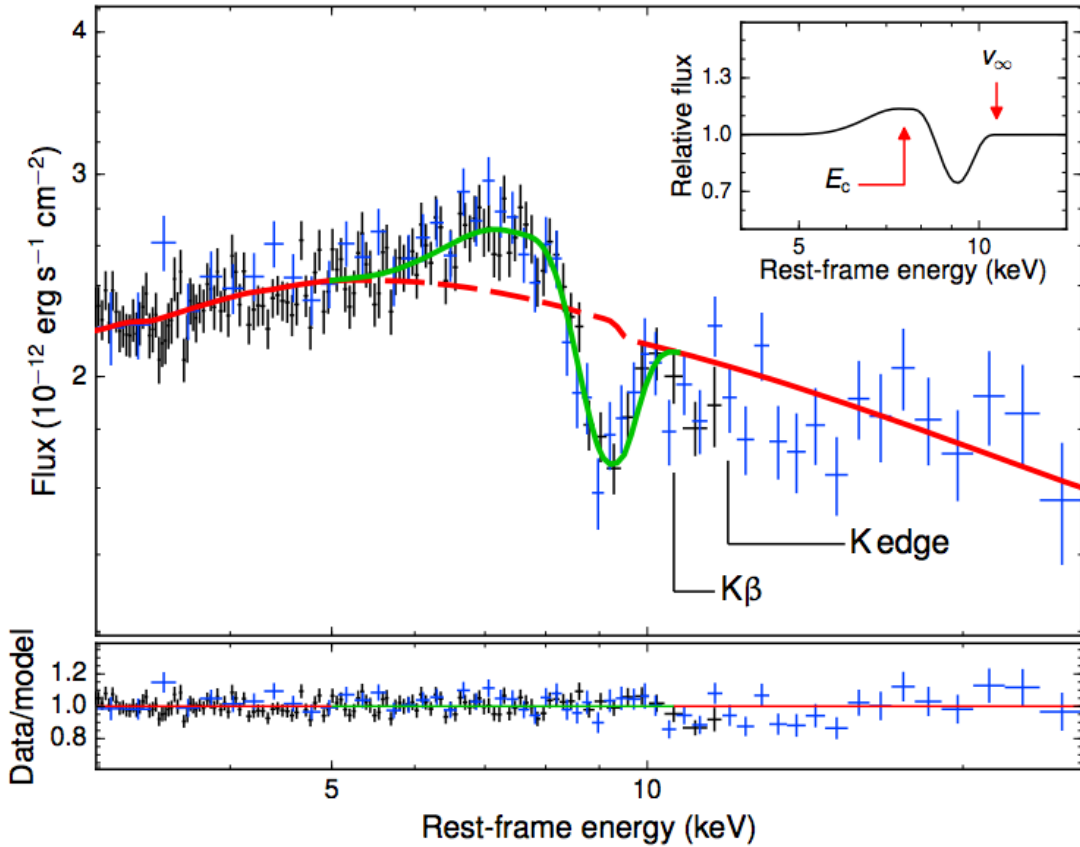


FIGURE 2.8: Credit: Nardini et al. 2015. X-ray spectrum of PDS 456 fitted with a P-Cygni profile from a spherical outflow model. XMM-Newton data is shown in black with two combined NuStar observations in blue.

2.1.4 Stellar Winds

Although stellar winds are clearly not accretion disc winds, they provide a useful, and better understood, testing ground for much of the physics of radiatively-driven outflows. Wolf-Rayet (WR) stars and O-stars possess strong outflows with mass-loss rates of up to $10^{-5} M_{\odot} \text{ yr}^{-1}$, thought to be driven by radiation pressure mediated by spectral lines (see section 2.2.3). Over the typical lifetime of a massive star ($\sim 10^6 \text{ yr}$), this can have a significant impact on the overall stellar mass, causing losses of around $10 M_{\odot}$ of material.

As with the systems described previously, the P-Cygni profiles in spectra from hot, massive stars are the main pieces of evidence that a strong wind is present (see Fig. 2.9). Mass-loaded winds are also thought to be responsible for the emission lines seen in hot star spectra (e.g. Pauldrach et al. 1994). Indeed, emission line diagnostics have been

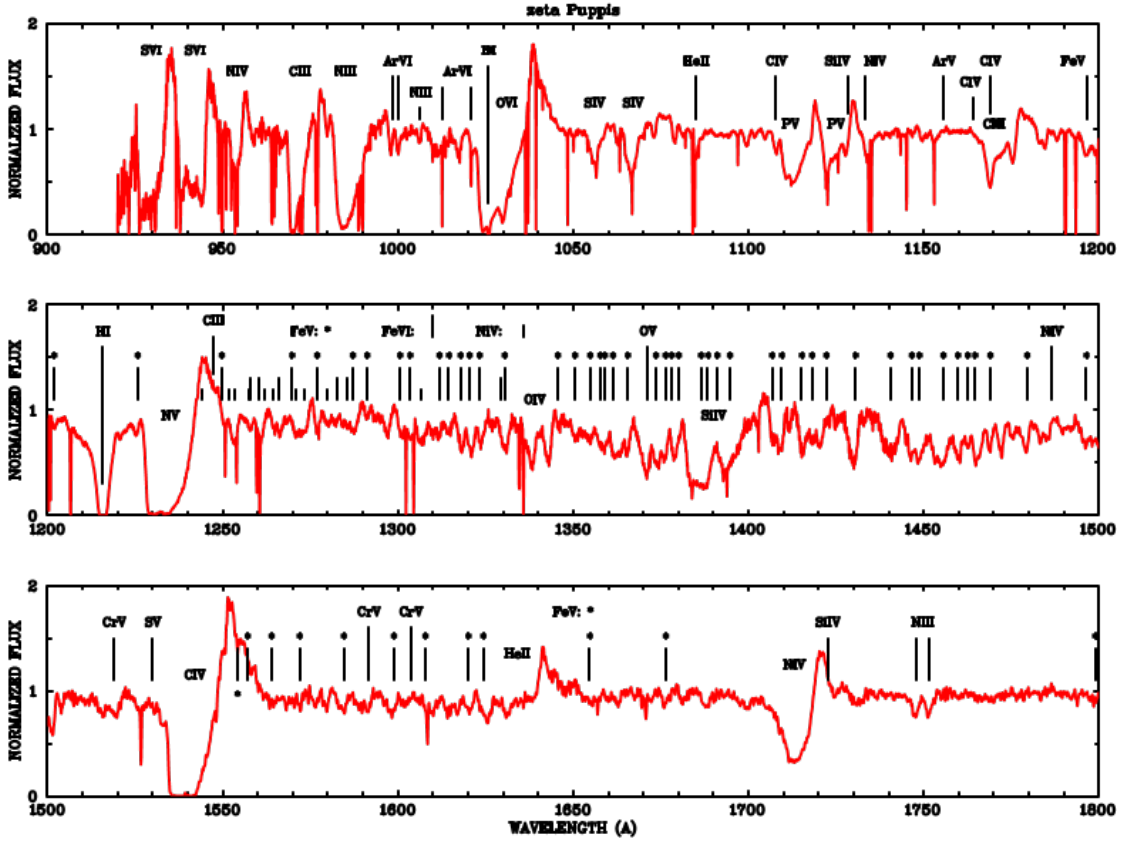


FIGURE 2.9: Credit: Pauldrach et al. 1994. UV spectrum of one of the brightest massive O stars, the O4 supergiant ζ Puppis. The spectrum is merged from Copernicus and IUE UV observations, and the prominent lines are marked.

particularly important in determining the mass-loss rates of stellar winds and have also been used to demonstrate that line-driven stellar winds are clumpy.

2.1.4.1 Clumping in Stellar Winds

Evidence for clumping in hot star winds comes from a range of sources. Perhaps the most conclusive is from electron scattering wings in emission lines; homogenous models overestimate the strength of these wings, whereas clumpy models produce good agreement with data (Hillier 1984, 1991; Hamann et al. 1992, 1994; Schmutz 1997). Further evidence for clumping comes from line variability (Prinja & Smith 1992) and polarisation (Brown et al. 1995). Clumping is theoretically expected in line-driven winds (see section 2.2.3 and the review by Owocki 2014), and is directly dealt with in this thesis. In chapter 5, I describe the treatment of clumping I have implemented in our radiative transfer code, before presenting results from a clumpy AGN wind model.

2.1.5 Outflow Physics

The spectra in figures 2.2, 2.7 and 2.9 show striking similarities – characteristic broad, P-Cygni-like absorption features in UV resonance lines extending to high blueward velocities – despite vast differences in mass, scale and the source of radiation. Furthermore, some of the phenomena observed in e.g. stellar winds may naturally solve some of the unanswered questions in other systems. For example, clumping may prevent over-ionization in AGN outflows. It would seem that at least some of the physics of outflows, like accretion physics, is universal, and that lessons learned from smaller scale systems may be scaleable to AGN and quasars. In order to understand if the similarity extends beyond a cosmetic one, I will discuss some of the underlying physical mechanisms that may be responsible for accelerating these outflows.

2.2 Driving Mechanisms

Let us consider a parcel of ideal gas. By imposing nothing more than conservation of mass, energy and momentum on that parcel, and using Maxwell's equations, we can write down three equations of magnetohydrodynamics (MHD):

$$\frac{D\rho}{Dt} + \rho \nabla \cdot \vec{v} = 0, \quad (2.2)$$

$$\rho \frac{D\vec{v}}{Dt} = -\nabla P + \frac{1}{4\pi} (\nabla \times \vec{B}) \times \vec{B} + \rho \vec{g}_{rad} + \rho \vec{g}, \quad (2.3)$$

$$\rho \frac{D}{Dt} \left(\frac{e}{\rho} \right) = P(\nabla \cdot \vec{v}) + \rho \mathcal{L}. \quad (2.4)$$

Here D denotes a derivative within the comoving frame of the gas parcel, \vec{v} is the velocity, ρ is the gas density, \vec{B} is the local magnetic field, \vec{F}_{rad} is the radiation force per unit mass, \mathcal{L} is the cooling rate of the gas and \vec{g} denotes the gravitational acceleration vector.

Equation 2.2 is the *continuity equation* and describes conservation of mass. Equation 2.3 is the *equation of motion* and describes conservation of momentum. Equation 2.4 is the *equation of energy conservation*. Equation 2.3 can be used to neatly demonstrate how

an outflow can be driven. I have deliberately written the equation so that all the force terms lie on the RHS. For an outflow to be driven from an accreting object, one of the terms on the RHS must dominate over gravity, $\rho\vec{g}$. These terms thus signify three potential driving mechanisms.

- Magnetic / Lorentz Forces, $\frac{1}{4\pi}(\nabla \times \vec{B}) \times \vec{B}$.
- Radiative Forces, $\rho\vec{g}_{rad}$.
- Thermal Pressure, $-\nabla P$.

We can now examine under what physical conditions (and in which corresponding astrophysical objects) we might expect these forces to overcome gravity and cause a parcel of mass to escape to infinity. In other words: *what might drive a wind?*

2.2.1 Thermal Winds

In a disc in hydrostatic equilibrium (HSE), thermal pressure balances gravity in the vertical direction. The equation of motion in this z direction can then be written as

$$\rho \frac{Dv_z}{Dt} = -\frac{\partial P}{\partial z} + \rho g_z = 0 \quad (2.5)$$

Clearly, if the thermal pressure is significantly increased, this equilibrium condition no longer holds. This can occur in accretion discs at temperatures in excess of $\sim 10^7$ K – where other forces are negligible compared to thermal pressure – and where the escape velocities are relatively low (i.e. far out in the disc). Due to the temperature and gravity scalings, this means that XRBs are natural candidates for showing evidence of thermally driven winds. The outer disc can be heated to the Compton temperature by the central X-ray source, potentially driving relatively high mass-loss rate outflows ([Begelman et al. 1983](#); [Woods et al. 1996](#)). This driving mechanism has been proposed as a natural explanation for the ever-present equatorial outflows in soft state XRBs ([Ponti et al. 2012](#)). However, they are much less likely candidates in CVs and AGN, because the escape velocity tends to greatly exceed the thermal velocity.

2.2.2 Radiatively Driven Winds

Under spherical symmetry, one simply obtains the Eddington limit discussed in section 1.1.1 when $\rho\vec{F}_{rad} = \rho\vec{g}$. Hence, sources must be fairly close to the Eddington luminosity in order to drive an outflow purely from radiation pressure on electrons. There are a number of accreting systems that may drive super-Eddington (or close to Eddington) outflows, such as AGN with UFOs (e.g. Reeves et al. 2002; Pounds et al. 2016), NLSIs (Done & Jin 2015) and ultra-luminous X-ray sources (ULXs; Walton et al. 2013). However, high-state CVs are significantly below the Eddington limit (Warner 2003), and at least some BALQSOs have low Eddington fractions ($\sim 25\%$ have $L/L_{Edd} < 0.1$; Grupe & Nousek 2015). These systems may nevertheless be capable of radiatively driving strong radiatively driven outflows due to the influence of line opacity.

2.2.3 Line-driven Winds

Under the right ionization conditions, radiation pressure mediated by spectral lines can be a significant acceleration term in a partially ionized plasma (Castor et al. 1975, hereafter CAK). The most common way to parameterise the cumulative effect of lines on the radiation force is via the *CAK force multiplier*, $\mathcal{M}(t)$, which modifies the equation for the acceleration due to radiation to give (Castor 1974, CAK)

$$\vec{g}_{rad} = \frac{\sigma_T F}{\mu c m_p} \mathcal{M}(t), \quad (2.6)$$

where F is the flux, and μ is the mean atomic weight. $\mathcal{M}(t)$ can be approximated by

$$\mathcal{M}(t) = t^{-\alpha} \left(\frac{n_e}{10^{11} \text{ cm}^{-3}} \right)^\delta W^{-\delta}, \quad (2.7)$$

where t is the dimensionless optical depth, given by

$$t = \frac{\sigma_T \rho v_{th}}{m_p |d(v_i)/ds|} \quad (2.8)$$

Here W is the dilution factor, and k , α and δ are constants with values of 0.28, 0.56 and 0.99 respectively in O-star winds (Abbott 1982). v_i is the component of the velocity field in the direction being considered, normally a line between the source of radiation and the wind. It is possible to show (CAK, Owocki et al. 1988) that the maximum force

multiplier is around $2000 - 4000$. This is already an interesting result, as it tells us that line-driven outflows can be accelerated when accretion rates / luminosities are much lower than the Eddington limit. Indeed, using equation 2.6 we can see that a radiatively driven wind can be accelerated when $L_{UV} > L_{Edd}/M_{UV}(t)$, where the UV subscript pertains to the UV region of the spectrum and $M_{UV}(t)$ will thus depend on the lines in this region and their relative ionization and excitation fractions. Line-driven winds are present in O-stars and Wolf-Rayet stars and the theory produces good matches with observations (e.g. Friend & Abbott 1986; Pauldrach et al. 1986, 1994; Hamann et al. 2008). It is also a strong candidate for driving the winds seen in high-state CVs when the accretion disc is UV bright (Pereyra et al. 1997; Proga et al. 1998; Proga 2005, see also section 2.3.4).

Line driving is also a promising mechanism to explain BAL outflows, as the strong UV resonance lines seen in absorption in O stars are also present in BALQSOs. The presence of ‘line-locked’ features (Bowler et al. 2014) and the ‘ghost of Ly α ’ (Arav et al. 1995; Arav 1996; North et al. 2006) in the spectra of some BALQSOs also suggests that line-driving is at least contributing to the acceleration of the wind (but see also Cottis et al. 2010). However, the presence of an X-ray source complicates matters. I have already briefly touched on the ‘over-ionization’ problem in AGN outflows, but it now has another consequence. Not only will strong X-rays prevent the right features forming in the spectrum, but, if the outflow is line-driven, they will prevent the wind existing in the first place. Despite these problems, hydrodynamic simulations have been successful in producing high mass-loss rates (see section 2.3.4).

Line-driving is subject to a strong instability known as the line deshadowing instability (LDI; Lucy & Solomon 1970; MacGregor et al. 1979; Owocki & Rybicki 1984, 1985). The basic idea is that any velocity perturbation in a line-driven flow can cause a ‘deshadowing’ effect, as the fluid element will now be in resonance with a region of the spectrum that is less absorbed. Thus, an increase in the line force will occur in proportion with this velocity perturbation, and the instability can grow. Time-dependent numerical modelling of the LDI has shown that it can produce a clumpy flow (Owocki et al. 1988; Feldmeier 1995; Šurlan et al. 2012; Owocki 2014) that may explain the observational characteristics of clumping in stellar winds (see section 2.1.4.1). The LDI is also of interest in CV and AGN winds, as it may affect the ionization state of the flow and possibly the inferred mass-loss rates.

2.2.4 Magnetic Winds

There is still great uncertainty over the magnetic fields in accretion discs and the physics of these magnetic processes. However, the MRI is one of the leading candidates for explaining angular momentum transport in accretion discs, implying that magnetic processes are important in their dynamics. Thus, in many senses, magnetic driving is an attractive wind driving mechanism. There are two main ways in which magnetic forces can drive an accretion disc wind, which are best explained by writing down an alternative form for the Lorentz force,

$$\vec{F}_m = \frac{1}{4\pi} \vec{B} \cdot \nabla \vec{B} - \nabla \frac{B^2}{8\pi}. \quad (2.9)$$

The first term can be thought of as a magnetic *tension* associated with the field lines and the second as an isotropic magnetic *pressure*.

Historically, the most popular magnetic wind model has been the ‘bead on a wire’ mechanism proposed by [Blandford & Payne \(1982\)](#) and [Pelletier & Pudritz \(1992\)](#). In these models, the poloidal magnetic field is dominant and is anchored in the accretion disc. A wind can then be driven by magnetic tension, as the first term in the above equation operates on fluid elements (‘beads’) on the surface of the accretion disc. This can accelerate a wind when the poloidal component of the field makes an angle of $> 30^\circ$ with the normal to the disc surface. These models are known as magnetocentrifugal winds as it is the interaction between a centrifugal force and a strong, large-scale, ordered magnetic field threading the disc that drives the wind. Magnetocentrifugal winds have been proposed in both AGN and YSOs ([Pelletier & Pudritz 1992](#); [Konigl & Kartje 1994](#); [Kudoh & Shibata 1997](#)), and numerical simulations have demonstrated that this mechanism can produce jets and outflows ([Romanova et al. 1997](#); [Ouyed & Pudritz 1997](#); [Ustyugova et al. 1999](#)).

In an alternative magnetohydrodynamic (MHD) model the isotropic magnetic pressure is responsible for driving the outflow ([Proga 2003](#)). In this case the toroidal component dominates over the poloidal component and drives a slow, dense outflow which behaves more like a thermally-driven wind (i.e. it conserves specific angular momentum rather than angular velocity).

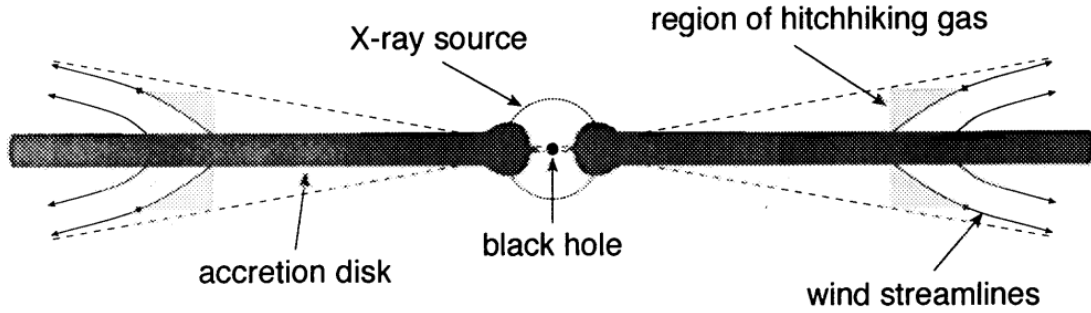


FIGURE 2.10: Credit: Murray et al. 1995. Cartoon showing the geometry of the MCGV95 model.

2.3 Accretion Disc Wind Models

A number of different wind models have appeared in the literature over the years, each attempting to explain the different observational characteristics of quasars with a mixture of conceptual frameworks and underlying physics. Typically, the models attempt to explain the origins of BLR and BAL gas, although some extend their remit into the infra-red, radio and X-ray regimes. I will briefly discuss a few examples that have gained traction over the years, before outlining the kinematic prescription I have used in the modelling that forms part of this thesis.

2.3.1 MCGV95: A Line-driven Wind Model for AGN

MCGV95 proposed a model in which a smooth wind rises from an accretion disc with a launch radius of around 10^{16} cm. The wind is equatorial, with an opening angle of 5° , and is accelerated by line forces up to a terminal velocity of $0.1c$. A sketch of the geometry is shown in Fig. 2.10. One of the key features of the model is the presence of a ‘shield’ of hitchhiking gas, which protects the outflow from X-ray over-ionization and allows radiation pressure on UV resonance lines to efficiently accelerate the flow.

MCGV95 found that BAL profiles were seen for an observer looking into the wind cone, and significant collisionally excited line *emission* emerged at low inclinations. This line emission came from a relatively small BLR ($r_{BLR} \sim 10^{16}$ cm) at the base of the wind, where densities were high ($n_e \approx 10^{10}$ cm $^{-3}$). The MCGV95 model was one of the first successful disc-wind unification models. It is especially impressive as it includes photoionization calculations and quantitative estimates of the resultant line

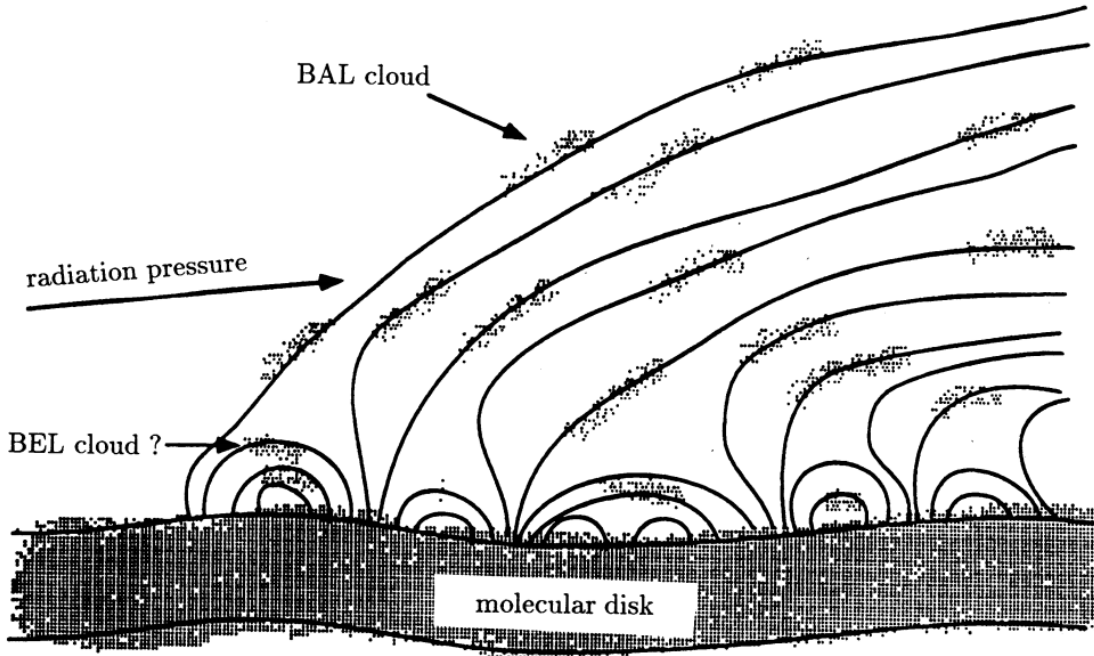


FIGURE 2.11: Credit: De Kool & Begelman 1995. A cartoon showing the components in the De Kool & Begelman model.

EWs. However, the effects of multiple scattering and complex radiative transfer effects could not be included in the calculations (see chapter 5).

2.3.2 De Kool & Begelman: A Radiatively Driven, Magnetically Confined Wind

It is, of course, possible that radiation and magnetic fields are both important in determining the outflow characteristics. In the [de Kool & Begelman \(1995\)](#) model, radiation pressure drives an outflow from an accretion disc and also compresses the magnetic field lines that are dragged along with the flow. This causes the magnetic field strength in certain regions to be comparable to the gas pressure, meaning that clouds can be magnetically confined in the flow. A diagram is shown in Fig. 2.11. The authors find that such a model would naturally emerge at a fairly equatorial angle with a covering factor of around 10%, and that lower ionization material would be intercepted when the system was viewed from higher inclinations, potentially explaining some of the properties of LoBALQSOs.

2.3.3 Elvis 2000: A Structure for Quasars

[Elvis \(2000\)](#) expanded on the work of MCGV95 by proposing a simple disc wind model, empirically derived to explain as much of quasar phenomenology as possible within one unifying framework. The geometry of the Elvis' is shown in Fig. 2.12. As in the two previous models, observers looking into the wind cone will see a BALQSO, whereas observers looking down onto the wind will see a type 1 quasar. Initially, the wind rises vertically, so that observers looking underneath the flow will see NALs due to the small range of velocities intercepted by their line of sight.

The flow conserves angular momentum, such that the initial Keplerian velocities determine the BEL widths, before accelerating to BAL-like velocities of $\sim 0.1c$. The wind is assumed to be two-phase, with BEL and BAL clouds embedded in a warm, highly ionized medium (WHIM). This WHIM is responsible for WA-like absorption and the X-ray scattering phenomena seen in AGN. It is also responsible for confining the BAL and BEL clouds, allowing high densities and cooler temperatures to exist within the flow. The ionization structure for the wind is stratified, such that the material further out along the disc plane is somewhat shielded from the inner disc and X-rays. This allows the lower ionization BEL profiles to form in the right locations, and also means that LoBAL profiles would be seen at a subset of inclinations.

2.3.4 Proga et al.: Line-driven Hydrodynamic Models for AGN and CVs

Around the turn of the century, Daniel Proga and collaborators published a series of important papers in which they conducted hydrodynamic simulations of line-driven disc winds in AGN and CVs. In the first of these, the problem considered was that of disc winds in CVs ([Proga et al. 1998](#)). In their model, the disc was assumed to radiate according to the α -disc model, and the central WD was also included as a radiating source. They found that when the disc had an Eddington fraction of greater than $\approx 1/\mathcal{M}_{max}(t) = 0.001$, then strong, line-driven outflows were driven from a few WD radii with bending angles of $\sim 45^\circ$. This result agreed qualitatively with outflows in CVs, and later efforts to compute synthetic line profiles produced promising results

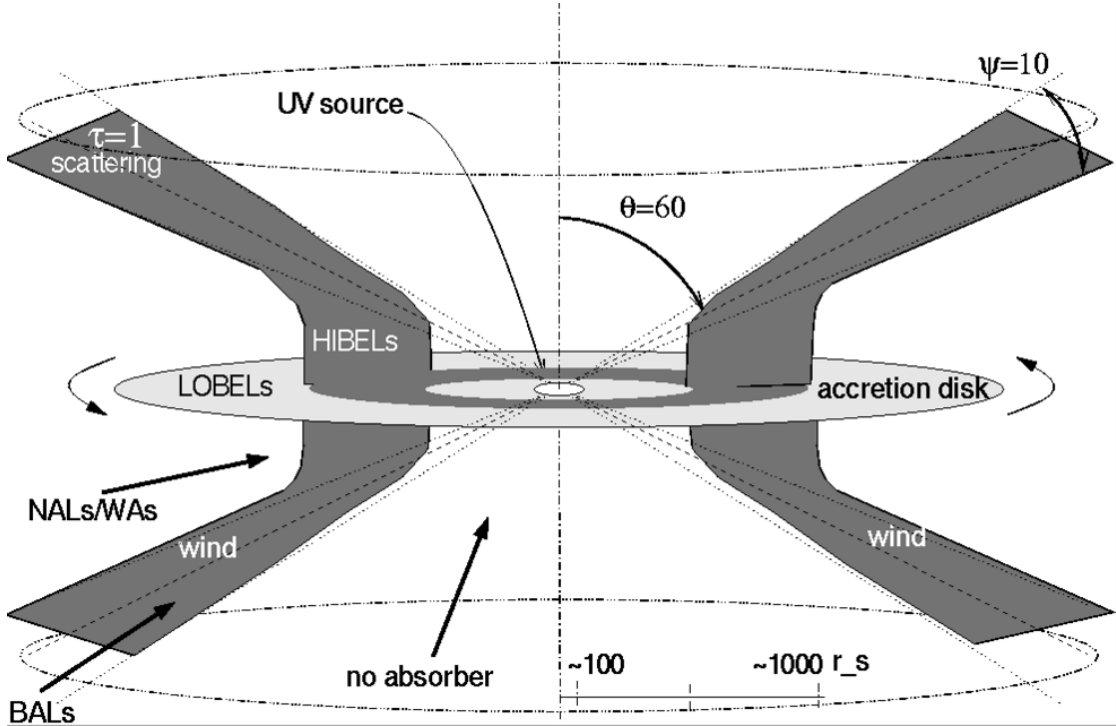


FIGURE 2.12: Credit: Martin Elvis. A schematic showing the main features of the Elvis model. A biconical wind rises from an accretion disc, and the observed spectrum is determined purely by the viewing angle of the observer.

(Proga et al. 2002a). This was the first successful demonstration of line driving in a full hydrodynamic simulation.

The same principle was then applied to the problem of AGN outflows, with the additional complication of an ionization X-ray source now included (Proga et al. 2000; Proga & Kallman 2004, hereafter PK04). A density snapshot from the PK04 model is shown in Fig. 2.13. An inner ‘failed’ wind formed in this simulation, which initially rose up from the disc before being over-ionized by the central X-rays. Crucially, this acted as a shield, similarly to the hitchhiking gas proposed by MCGV95, and allowed a line-driven wind to be accelerated further out in the disc. This outflow can be seen clearly in Fig. 2.13.

One of the interesting results of the Proga-led simulations is that they tended to produce somewhat unsteady, clumpy flows. In the CV case, this was caused by the interaction between the line force and gravity, as both force terms varied differently with height. In the AGN case, it was instead due to the critical importance of the ionization state on the line force. Parcels of gas can only be accelerated when if they have the ‘right’ ionization state, and this depends critically on their density and the radiation field they see. This causes an interplay between the dynamics of the flow and the path of ionizing

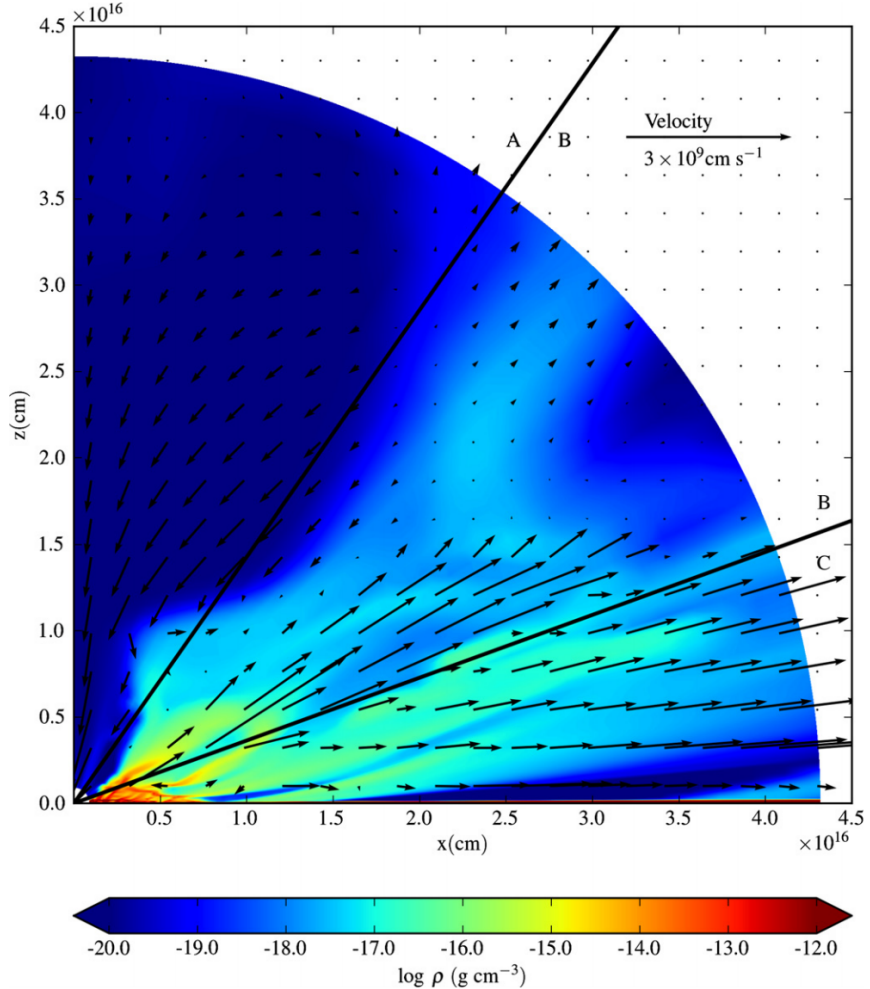


FIGURE 2.13: Credit: Higginbottom et al. 2014.. A snapshot of the PK04 model. Colours shows the density and arrows show the velocity of the flow. The radial lines separate three areas described by H14.

radiation, which are coupled. The radiation field also helped determine the geometry of the outflow, as increasing the strength of the radiation interior to the launch radius tends to flatten out the wind and lead to more equatorial outflows ([Proga 2005](#)). This is particularly important when considering quasar unification, as it means the viewing angles of BALQSOs can provide information about where the wind is launched.

It is worth noting that the smaller scale LDI could not be included in this model, partly for computational reasons and partly because of the approximations used to treat the radiation field. Treating the radiation transport is also important for other reasons. [Higginbottom et al. \(2014](#), hereafter H14) showed that, in this particular geometry, multiple scattering renders shielding region ineffective, and radiation will simply find its way around the failed wind to over-ionize the flow beyond. Ideally, full radiative

transfer and hydrodynamical simulations would be used to estimate the viability of line-driven winds. Our team is currently working on this problem (see H14 for the first step); however, much can also be learned from simpler, kinematic prescriptions for outflows, which can then be treated with full radiative transfer and ionization treatments.

2.4 A Kinematic Prescription for a Biconical Wind

[Shlosman & Vitello \(1993\)](#), hereafter SV93) expanded on the work of the stellar wind community (e.g. [Abbott & Lucy 1985](#)) in proposing a kinematic model for an accretion disc wind. Unlike hydrodynamical models, this model has no real predictive power in terms of velocities and mass-loss rates. Instead, one sets these quantities in advance and examines the resultant properties of the flow and emergent spectra. The SV93 prescription is the most common way of describing the outflow in the radiative transfer code PYTHON (see chapter 3) and has been used to simulate spectra for CVs ([Long & Knigge 2002](#); [Matthews et al. 2015](#), chapter 4), AM CVn systems ([Kusterer et al. 2014](#)) and AGN/quasars ([Higginbottom et al. 2013](#); [Matthews et al. 2016](#); [Yong et al. 2016](#), chapter 5). A similar philosophy applied to the model of [Knigge et al. \(1995\)](#), which has been used in similar applications ([Long & Knigge 2002](#); [Sim et al. 2008, 2010a](#)), as well as for young-stellar objects (YSOs; [Sim et al. 2005](#)). Kinematic prescriptions have thus been a useful tool in providing quantitative tests of conceptual models, and specifically for assessing their ability to reproduce the observed spectra of a variety of disc wind systems.

In the SV93 parametrization, a smooth, biconical disc wind emanates from the accretion disc between r_{min} and r_{max} . A schematic is shown in Fig. 2.14. The covering fraction of the outflow is also controlled by the inner and outer opening angles of the wind, θ_{min} and θ_{max} , and the launch angle of the other streamlines is given by

$$\theta(r_0) = \theta_{min} + (\theta_{max} - \theta_{min}) \left(\frac{r_0 - r_{min}}{r_{max} - r_{min}} \right)^\gamma, \quad (2.10)$$

where r_0 is the launch radius of the streamline.

The poloidal (non-rotational) velocity field of the wind, v_l , is given by

$$v_l = v_0 + [v_\infty(r_0) - v_0] \frac{(l/R_v)^\alpha}{(l/R_v)^\alpha + 1}, \quad (2.11)$$

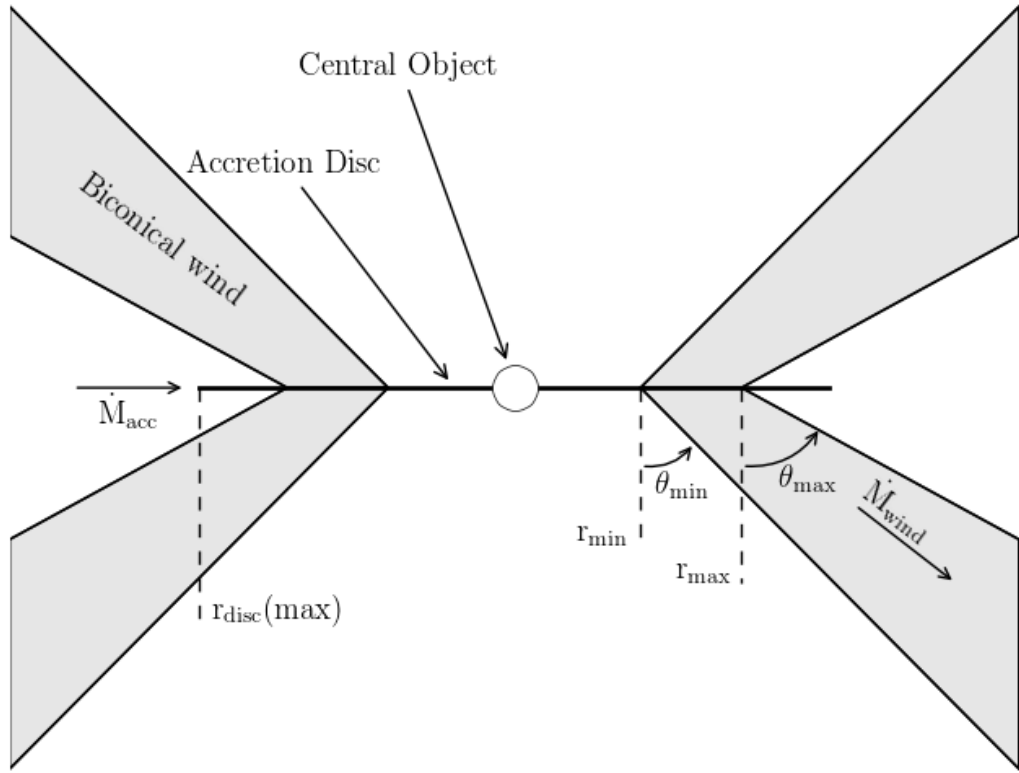


FIGURE 2.14: A schematic showing the geometry and kinematics of the SV93 model.

where l is the poloidal distance along a particular wind streamline. The terminal velocity along a streamline, v_∞ , is set to a fixed multiple of v_{esc} , the escape velocity at the launch point. The terminal velocity will therefore be higher for streamlines closer to the inner disc edge. The launch velocity from the disc surface, v_0 , is assumed to be constant (set to 6 km s^{-1}). Once the wind is launched, it accelerates, reaching half of its terminal velocity at $l = R_v$. The velocity law exponent α controls how quickly the wind accelerates. Larger values of α cause the main region of acceleration to occur close to R_v , whereas smaller values correspond to fast acceleration close to the disc (see Fig. 2.15). The rotational velocity v_ϕ is Keplerian at the base of the streamline and the wind conserves specific angular momentum, such that

$$v_\phi r = v_k r_0, \quad (2.12)$$

where $v_k = (GM_{WD}/r_0)^{1/2}$.

The mass-loss rate per unit surface area, \dot{m}' , can be controlled by a free parameter λ_m such that

$$\dot{m}' \propto \dot{M}_W r_0^{\lambda_m} \cos[\theta(r_0)], \quad (2.13)$$

where \dot{M}_W is the total mass loss rate in the wind. This equation is normalised so that when integrated over both sides of the disc the correct \dot{M}_W emerges. I have adopted $\lambda = 0$ throughout this thesis, which corresponds to uniform mass loss across the disc. The density at a given point can then be calculated by imposing mass conservation and using the velocity law. At the base of the wind, the density is given by

$$\rho(r_0) = \frac{\dot{m}'(r_0)}{v_z(r_0)}. \quad (2.14)$$

At a coordinate (r, z) in the wind, the density is then

$$\rho(r, z) = \frac{r_0}{r} \frac{dr_0}{dr} \frac{\dot{m}'(r_0)}{v_z(r, z)} \quad (2.15)$$

where the corresponding r_0 is found by considering the streamline that passes through (r, z) . These equations govern the kinematics and densities in the wind in the SV93 prescription, which is used extensively throughout this thesis.

2.5 The big picture: AGN Feedback

The event horizon of a $10^9 M_\odot$ BH is approximately 10^{15} cm, a billionth of the radius of a typical galactic bulge. This is roughly the ratio in size between a small coin and the Earth. Even the sphere of gravitational influence of the BH is roughly 1000 times smaller than the size of the galactic bulge. Despite this vast difference in scale, there is strong evidence that the physics on the scale of the gravitational radius of the BH affects the evolution and dynamics of its host galaxy. This becomes less surprising when considering the *energetics* of accretion. The binding energy of a galactic bulge, with mass M_{bulge} and velocity dispersion σ_* , is

$$E_{bulge} \approx M_{bulge} \sigma_*^2, \quad (2.16)$$

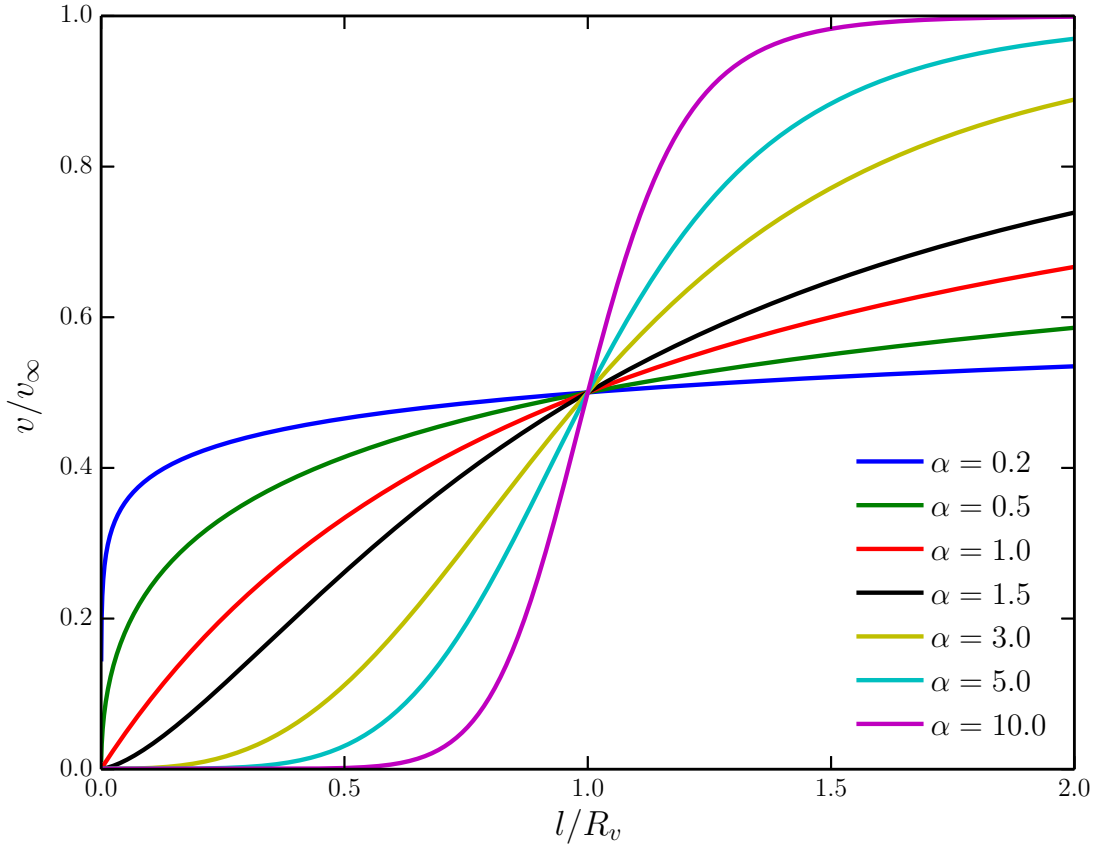


FIGURE 2.15: The SV93 velocity law for various values of the acceleration exponent, α .

while the energy released in growing a black hole to a mass M'_{BH} is (equation 1.3, assuming $\eta = 0.1$)

$$E_{BH} \approx 0.1 M'_{BH} c^2. \quad (2.17)$$

By combining these two equations, and substituting in typical numbers ($\sigma_* = 0.001c$, $M'_{BH}/M_{bulge} = 10^{-3}$), we can show that

$$\frac{E_{BH}}{E_{bulge}} \approx 10^{-4} \left(\frac{c}{\sigma_*} \right)^2 \sim 10. \quad (2.18)$$

In other words, the energy released when growing a BH can significantly exceed the binding energy of the galactic bulge. This energetic argument is, of course, not sufficient to claim that the accreting BH must affect its host. For example, if the radiated energy never experienced an optical depth of ~ 1 , it could not couple to the galactic bulge. However, we have already seen that many outflows in AGN possess kinetic luminosities that are significant compared to the bolometric luminosity. Thus, outflows (and jets) may provide a mechanism by which the vast accretion energies can be transferred to the

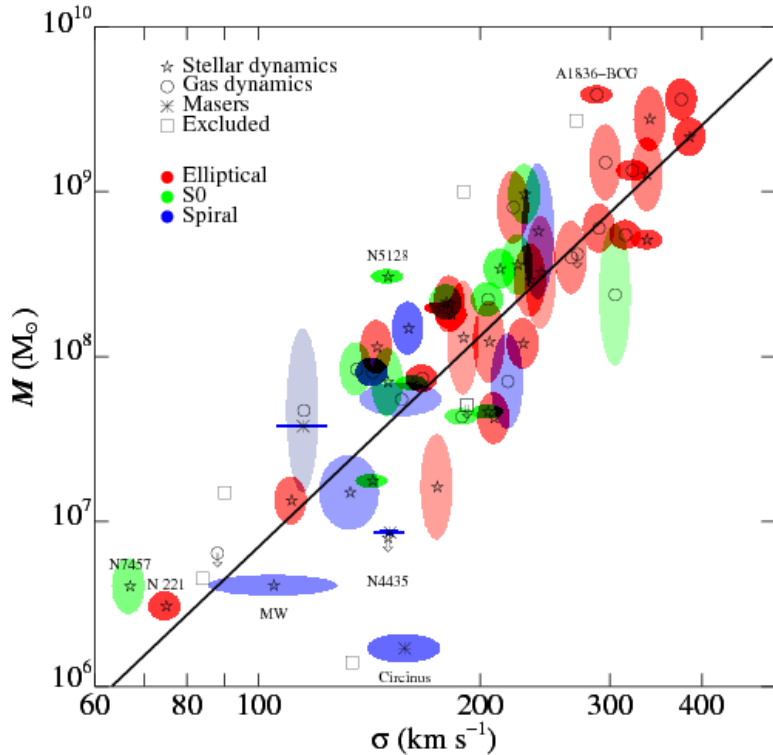


FIGURE 2.16: Credit: Gultekin et al. 2009. The $M_{BH} - \sigma_*$ correlation.

BH environment.

2.5.1 Observational evidence for feedback

Perhaps the most famous pieces of evidence for some kind of long-distance relationship between a central BH and its host galaxy are the $M_{BH} - \sigma_*$ (Ferrarese & Merritt 2000; Gebhardt et al. 2000; Gultekin et al. 2009) and $M_{BH} - M_{bulge}$ (Magorrian et al. 1998; Häring & Rix 2004; McConnell & Ma 2013) correlations, shown in Fig. 2.16 and Fig. 2.17, respectively. By themselves, these correlations would not necessarily imply that the AGN is having an impact on its environment. Indeed, there are many different theoretical models for the origin of these relations (e.g Somerville et al. 2001; Adams et al. 2001; Burkert & Silk 2001; King 2003; Croton et al. 2006; Kormendy & Ho 2013). However, there are many other clues that outflows and jets from AGN can affect the host galaxy evolution and morphology.

The galaxy luminosity function describes the number of galaxies as a function of luminosity and is generally modelled with the Schechter (1976) function. Theories of galaxy evolution tend to overpredict the number of galaxies at the high luminosity end, which

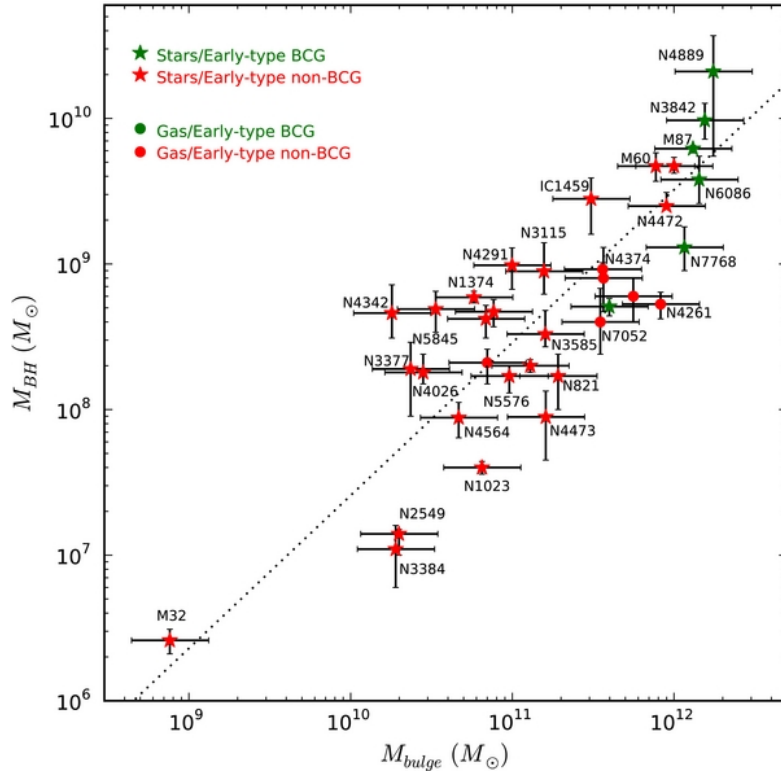


FIGURE 2.17: Credit: McConell & Ma 2013. The $M_{BH} - M_{bulge}$ correlation.

can be avoided by invoking quenching of star formation by the central AGN (e.g. [Read & Trentham 2005](#); [Bongiorno et al. 2016](#)). Galaxies also show bimodality in their colour distributions ([Strateva et al. 2001](#); [Bell et al. 2003](#); [Baldry et al. 2004](#)), with a clear separation between a blue, star-forming main sequence, and a red sequence with lower specific star formation rate (sSFR). Furthermore, these two sequences tend to lie in the same regions of colour space as the host galaxies of high and low Eddington fraction AGN respectively, implying that the AGN may be directly responsible for quenching the star formation and moving a galaxy onto the ‘red and dead’ branch. This has been demonstrated in several numerical simulations (e.g. [Springel et al. 2005](#); [Croton et al. 2006](#)).

There is also evidence that AGN are energetically significant on scales larger than the galactic bulge. X-ray observations of cool core clusters and elliptical galaxies can show dramatic X-ray cavities or bubbles up to 50 kpc across, with a radio-loud AGN at the centre ([Randall et al. 2011](#); [Cavagnolo et al. 2011](#); [Fabian 2012](#), Fig. 2.18). This shows how radio jets can significantly impact the surrounding gas, a flavour of feedback known as ‘radio’ or ‘kinetic’ mode. These cavities also provide an estimate of the kinetic power of a radio jet, as the volume of the bubble and surrounding gas pressure gives a rough

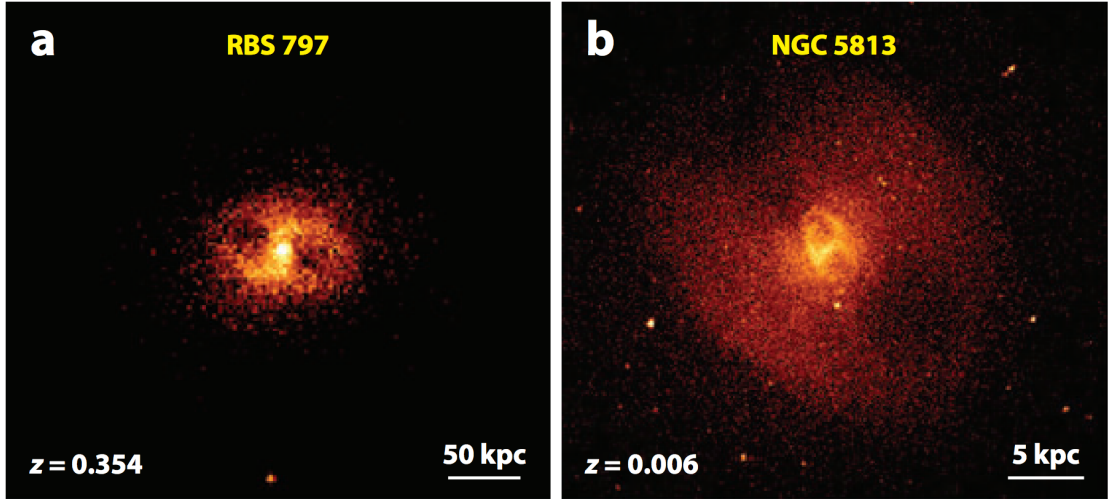


FIGURE 2.18: Figure adapted from Fabian 2012. Chandra X-ray images showing two examples of X-ray cavities, illustrating how a radio jet from an AGN can have a dramatic impact on its environment. a) The RBS 797 Cluster (Cavagnolo et al. 2011). b) elliptical galaxy NGC 5813 (Randall et al. 2011).

estimate of the PV work done by the jet. This can be divided by an age estimate for the cavity, giving powers of up to $10^{46} \text{ erg s}^{-1}$, which are weakly correlated with the radio luminosity of the source, and can be large for modest radio power (Bîrzan et al. 2008).

However, jets are not the only way for AGN to interact with their environment. I have already briefly discussed in section 2.1.3.3 how fast AGN winds can drive larger-scale molecular outflows. This can be seen spectacularly in the FeLoBALQSO Mrk231, where integrated field spectroscopy shows kiloparsec-scale neutral gas outflows (see Fig. 2.19; Rupke & Veilleux 2011). Furthermore, King (2003) expanded on the ideas of Silk & Rees (1998) and considered a super-Eddington, momentum-driven outflow expanding into the surrounding gas. This model naturally reproduces the observed slope of the $M_{BH} - \sigma_*$ relation. This line of argument was used to suggest that super-Eddington accretion must be common near the end of a quasar cycle, although it is worth noting that line-driving, or non-radiative driving, would mean that super-Eddington accretion rates are not required to drive such an outflow. Intriguingly, this means that understanding outflow physics has implications for the Soltan (1982) argument, SMBH spin and the accretion history of the Universe.

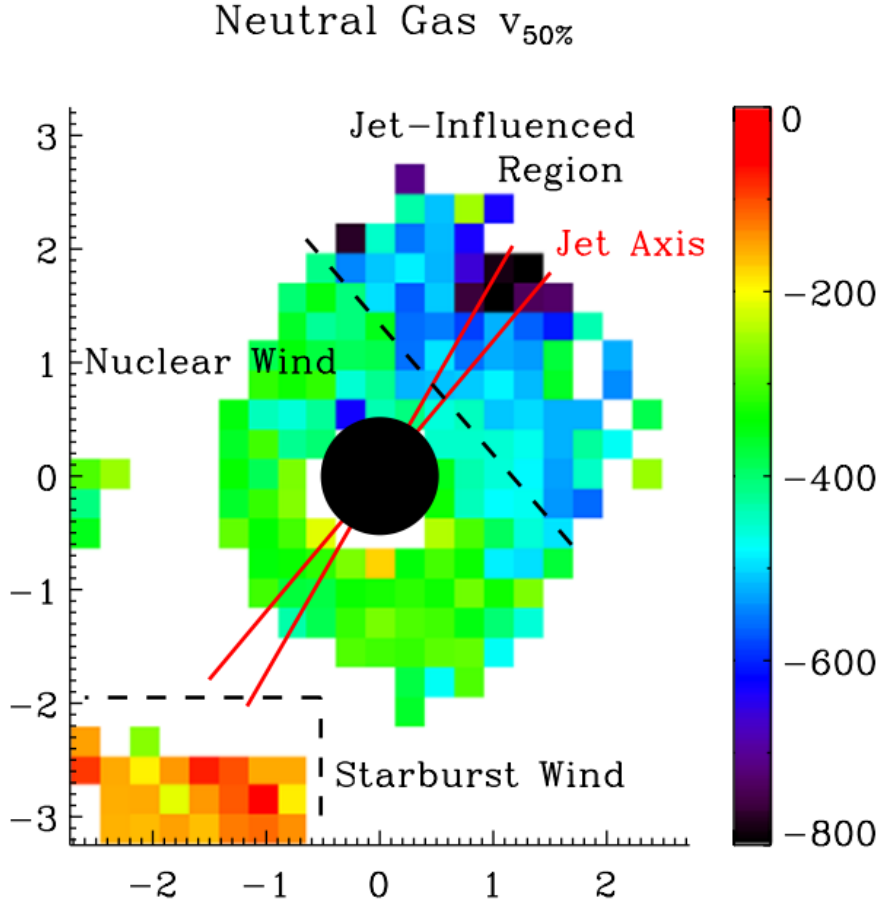


FIGURE 2.19: Credit: Rupke & Veilleux 2011. Results of Gaussian line profile fitting to integral field spectroscopy of Mrk 231. The quantity shown, $v_{50\%}$, corresponds to the centre of the fitted Gaussian profile and indicates that high outflow velocities are present in the neutral gas.

2.5.2 Alternative Explanations

It cannot yet be proven that AGN are the drivers of the observed galaxy colour evolution, high-end luminosity function discrepancy or BH-bulge correlations. In particular, it is also possible that mergers are responsible for these phenomena. For example, major galaxy mergers may explain the ‘red and dead’ branch of the galaxy colour bimodality (e.g. Somerville et al. 2001; Baldry et al. 2004). However, AGN winds and jets are clearly energetically significant with respect to their host galaxies, so estimating their kinetic powers accurately is important in discriminating between in-situ and ex-situ scenarios.

Having established the astrophysical importance of outflows, I will now move on to discussing how we might go about accurately modelling the ionization states of accretion disc winds, and their emergent spectra.

Chapter 3

Monte Carlo Radiative Transfer and Ionization

“I’m splashing greys where once was
glowing white”

Mike Vennart, *Silent/Transparent*

In the previous chapters I have given an introduction to the field and some relevant background relating to accretion discs and their associated outflows. Now it proves useful to discuss some of the specific *methods* I will use in order to answer some of the questions raised in the previous sections. In particular, I will discuss radiative transfer techniques and their potential applications.

Notation: This section contains a lot of algebraic quantities and sums over ions, levels, and so on. Throughout, I use N to denote fractional populations of ions and n to denote fractional populations of levels. The primed quantities ℓ' and u' follow the convention of Lucy (2002) in that they denote sums over all lower/upper levels. The symbol \mathcal{R} denotes a total rate (radiative + collisional), and the symbol C is a collisional rate, whereas \mathcal{C} is a cooling rate. Starred quantities are evaluated at the stated temperature but in local thermodynamic equilibrium, following Mihalas (1978). An S superscript denotes that the estimator pertains to simple-atoms.

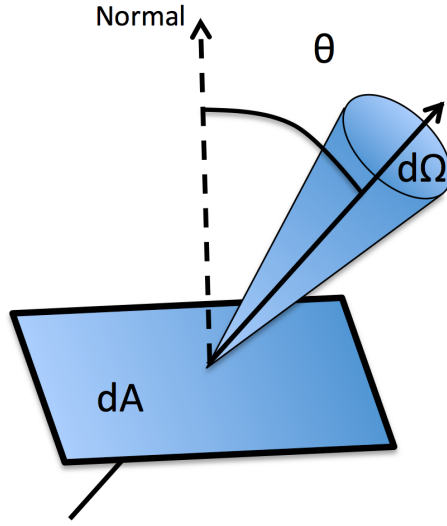


FIGURE 3.1: A schematic showing a ray obliquely incident on a surface of area dA . The labeled quantities are used in the definition of specific intensity.

3.1 Fundamentals of Radiative Transfer

Let us consider a ray passing through a reference surface dA and making an angle θ with the normal to this surface. The energy flow can then be related to the *specific intensity*, I_ν , by

$$I_\nu = \frac{dE}{d\Omega dt dA d\nu}, \quad (3.1)$$

which has CGS units of $\text{erg s}^{-1} \text{Hz}^{-1} \text{sr}^{-1} \text{cm}^{-2}$. The specific intensity is the most fundamental quantity of radiative transfer as it describes everything about the radiation field; its time, angular, spatial and frequency dependence. By successively multiplying by $\cos \theta$ and integrating over solid angle we can obtain the first and second ‘moments’ of the radiation field. These are the flux, F_ν and momentum flux, p_ν , respectively, given by

$$F_\nu = \int I_\nu \cos \theta d\Omega, \quad (3.2)$$

$$p_\nu = \frac{1}{c} \int I_\nu \cos^2 \theta d\Omega \quad (3.3)$$

We can also define the *mean intensity*, J_ν , as

$$J_\nu = \frac{1}{4\pi} \int I_\nu d\Omega \quad (3.4)$$

The mean intensity is particularly useful when one wants to ignore the solid angle dependence of the radiation, for example when considering the impact of an ionizing radiation field.

The equation describing the specific intensity change along a path element ds is the radiative transfer equation,

$$\frac{dI_\nu}{ds} = -\kappa_\nu I_\nu + j_\nu, \quad (3.5)$$

where κ_ν and j_ν are the absorption and emission coefficients respectively. If we define the optical depth $d\tau_\nu = \kappa_\nu ds$ we can recast this as

$$\frac{dI_\nu}{d\tau_\nu} = -I_\nu + S_\nu \quad (3.6)$$

where $S_\nu = j_\nu / \kappa_\nu$ is the source function. This equation can be solved to give the *formal solution to the radiative transfer equation*:

$$I_\nu = I_{\nu,0} e^{-\tau_\nu} + \int_0^{\tau_\nu} S_\nu(\tau'_\nu) e^{\tau'_\nu - \tau_\nu} d\tau'_\nu. \quad (3.7)$$

A useful limit is when the source function is constant in the absorbing medium, in which case the integral can be easily evaluated to give

$$I_\nu = I_{\nu,0} e^{-\tau_\nu} + S_\nu(1 - e^{-\tau_\nu}). \quad (3.8)$$

3.1.1 Spectral Line Formation

From the above equations, it is trivial to show how emission and absorption lines form when the source function is approximately constant. Say we have a plasma illuminated by a blackbody of temperature T_0 , such that $I_{\nu,0} = B_\nu(T_0)$. The plasma layer then has a different temperature, T , such that $S_\nu = B_\nu(T)$ in that medium. By inspecting

equation 3.8 we can see that if we are optically thick within the line, but optically thin in the continuum, then inside the line the source term is dominant and outside the line the first $I_{\nu,0} e^{-\tau_\nu}$ term dominates. Therefore, if $T > T_0$ we will see an emission line, and if $T < T_0$ we will see an absorption line.

3.1.2 Local thermodynamic equilibrium

An important physical limit is that of local thermodynamic equilibrium (LTE). This is a first-order way to describe the physical conditions of a plasma, and assumes that all the properties of the plasma, such as the level populations and source function, are the same as those in thermodynamic equilibrium for local values of temperature and density. For this to be the case, the principle of *detailed balance* must also apply, in which every process by which electrons transition in state must be exactly balanced by its inverse process. LTE also assumes that $T_e = T_R$, and that the source function is given by a blackbody, i.e. $S_\nu = B_\nu(T_R)$. Three *microscopic* requirements of LTE also follow (Mihalas 1978):

- a) The velocities of the electrons and ions in the plasma obey Maxwellian distributions, such that

$$f(v) = 4\pi \left(\frac{m_e}{2\pi k T_e} \right)^{3/2} v^2 \exp \left(-\frac{m_e v^2}{2k T_e} \right), \quad (3.9)$$

where m_e is the mass of an electron and T_e is the electron temperature.

- b) the ionization state of the plasma is governed by the *Saha equation*, which states that two adjacent ions have relative populations given by

$$\frac{N_{i+1} n_e}{N_i} = \frac{2g_{i+1}}{g_i} \left(\frac{2\pi m_e k T_e}{h^2} \right)^{3/2} \exp(-h\nu_0/kT), \quad (3.10)$$

where g_i is the multiplicity of ion i and ν_0 is the threshold frequency.

- c) the excitation state of the plasma is governed by *Boltzmann statistics*. A level j then has a population relative to ground governed by

$$\frac{n_j}{n_1} = \frac{g_j}{g_1} \exp(-E_j/k T_e), \quad (3.11)$$

where E_j is the energy difference between the two levels and g_j is the statistical weight of level j .

Although these three assumptions are sometimes valid, in many astrophysical situations there can be large departures from LTE. A good example of these departures is when the SED is not a blackbody and is affected by absorption – as is the case in AGN and other accreting systems. The Maxwellian assumption is probably the most reliable, but even this may break down when high-energy photons create suprathermal electron distributions ([Humphrey & Binette 2014](#)).

3.1.2.1 Dilute approximation

A first step away from LTE is to introduce the dilute approximation. In this case, we relax the assumption that $T_R = T_e$, and assume that the mean intensity is given by a dilute blackbody, i.e.

$$J_\nu = WB_\nu(T_R), \quad (3.12)$$

where W is the dilution factor. We can then approximate the ionization state with a modified Saha equation ([Abbott & Lucy 1985; Mazzali & Lucy 1993](#)),

$$\frac{N_{i+1}n_e}{N_i} = W[\xi + W(1 - \xi)] \left(\frac{T_e}{T_R}\right)^{1/2} \left(\frac{N_{i+1}n_e}{N_i}\right)_{T_R}^*, \quad (3.13)$$

where ξ is the fraction of recombinations that go directly to the ground state. The excitation state can be approximated (fairly poorly) with a dilute Boltzmann equation ([Abbott & Lucy 1985; Lucy 1999b](#))

$$\frac{n_j}{n_1} = W \frac{g_j}{g_1} \exp(-E_j/kT_R). \quad (3.14)$$

3.1.3 The Two Level Atom

The two level atom formalism is well described by [Mihalas \(1978\)](#). Let us consider an atomic model consisting of two levels that are linked by radiative and collisional transitions, that can also interact with the continuum. Whilst this model is clearly a simplification, it nonetheless allows for a first step into non-LTE line transfer and proves useful for modelling the resonance lines briefly touched on in chapter 2.

To construct our simple model we must make a few assumptions. The first is the assumption of *statistical equilibrium*. This is the principle that the total rate into a given atomic level/state is equal to the total rate out of said state. This is clearly true whenever the timescale to establish this equilibrium is shorter than the timescale on which the ambient conditions change. The second is the assumption of *complete redistribution (CRD)*, which states that the emission and absorption line profiles are identical for a given transition. This assumption is somewhat analogous to the Sobolev approximation (see section 3.1.4). These assumptions allow us to formulate rate equations and derive the Einstein relations.

3.1.3.1 Einstein coefficients

Within a two level atom, the rate equation between the two levels in LTE can be written by invoking detailed balance, such that

$$B_{lu}\bar{J}_{ul}n_l = B_{ul}\bar{J}_{ul}n_u + A_{ul}n_u, \quad (3.15)$$

where B_{ul} , B_{lu} and A_{ul} are the *Einstein coefficients* for absorption, stimulated emission and spontaneous emission respectively. The ‘mean intensity in the line’, \bar{J}_{ul} , is given by

$$\bar{J}_{ul} = \int \phi(\nu) J_\nu d\nu. \quad (3.16)$$

We can then rearrange equation 3.15 in terms of the mean intensity, giving

$$\bar{J}_{ul} = \frac{A_{ul}/B_{ul}}{(n_l/n_u)(B_{ul}/B_{lu}) - 1}. \quad (3.17)$$

In LTE, $\bar{J}_{ul} = B_\nu(T)$ and the level populations obey Boltzmann statistics, so we can combine equations 1.21, 3.11 and 3.17 to write

$$\frac{2h\nu^3}{c^2} \frac{1}{\exp(h\nu/kT) - 1} = \frac{A_{ul}}{B_{ul}} \frac{1}{(g_l/g_u)(B_{ul}/B_{lu}) \exp(h\nu/kT) - 1}. \quad (3.18)$$

This must be true at all values of T , so we can simply equate coefficients to show that

$$\frac{A_{ul}}{B_{ul}} = 2h\nu_{ul}^3/c^2, \quad (3.19)$$

$$\frac{B_{lu}}{B_{ul}} = g_u/g_l. \quad (3.20)$$

These two equations are known as the *Einstein relations*, and have no dependence on temperature. They are therefore purely atomic properties.

3.1.4 The Sobolev Approximation

The Sobolev approximation (SA) is a useful limit used to treat line transfer in fast-moving flows. Originally the theory was mostly applied to stellar winds, although since then a wide variety of astrophysical objects have been modelled using Sobolev treatments, such as accreting systems (this work) and supernovae. The underlying theory of Sobolev optical depths and the associated escape probability formalism was originally developed by Sobolev (1957, 1960), but has since been expanded on by multiple authors (e.g. Rybicki 1970; Rybicki & Hummer 1978; Hubeny 2001).

The Sobolev limit is when the local bulk velocity gradients in a flow dominate other any thermal broadening. In the presence of these steep velocity gradients, one can assume that the interaction of a ray with a bound-bound transition takes place over a small resonant zone, known as a ‘Sobolev surface’. The length of this zone is defined by

$$l_s = \frac{v_{th}}{dv/ds}. \quad (3.21)$$

It is important that the physical conditions of the c do not change on this scale. If this is the case, then we can assume that all line interactions for a given frequency will occur at a single ‘resonant’ point. The location at which a given photon will interact with a line of frequency ν_{ul} is then given, in velocity space, by

$$v = c \left(1 - \frac{\nu_{ul}}{\nu} \right), \quad (3.22)$$

where the scalar velocity here is $v = \vec{v} \cdot \vec{n}$, the dot product of the bulk velocity of the plasma and the unit vector of the photon direction. The Sobolev optical depth is then

$$\tau_S = \frac{\pi e^2}{mc} \left(n_l - n_u \frac{g_l}{g_u} \right) \frac{f_{lu} \lambda_{lu}}{c |dv/ds|}. \quad (3.23)$$

We can see that the physical quantities determining line opacity are therefore the level populations in the plasma, the velocity gradient and the atomic physics associated with the bound-bound transition. An obvious consequence of line opacities in a resonant

zone is that many line interactions may occur if the line is optically thick. The more line interactions that occur, the higher the chance that an electron will collisionally de-excite and the photon will be absorbed. It thus becomes useful to introduce the angle-averaged Sobolev escape probability, given by

$$\beta_{ul} = \int \frac{1 - \exp(\tau_S)}{\tau_S} d\Omega, \quad (3.24)$$

where here I will use the approximate form by taking an appropriate average, $\langle \tau_S \rangle$, for the Sobolev optical depth, giving

$$\beta_{ul} = \frac{1 - \exp(-\langle \tau_S \rangle)}{\langle \tau_S \rangle}. \quad (3.25)$$

3.1.4.1 Two-level Atom with Escape Probabilities

Let us now write down the rate equation linking our two-level atom,

$$B_{lu}\bar{J}_{ul}n_l + C_{lu}n_l = B_{ul}\bar{J}_{ul}n_u + \beta_{ul}A_{ul}n_u + C_{ul}n_u, \quad (3.26)$$

where I have now introduced collisional rates C_{ul} and C_{lu} , and included the effect of line trapping via the angle-averaged Sobolev escape probability. We now seek to find a relation between the source function in the line and the intensity that will simplify the coupled problem of radiative transfer and statistical equilibrium. When we consider a two-level atom plus continuum this can be written as ([Mihalas 1978](#))

$$S_{ul} = (1 - q)\bar{J}_{ul} + qB(\nu_{ul}), \quad (3.27)$$

where $B(\nu_{ul})$ is the Planck function at line centre and q is the ‘absorption fraction’. This form can be obtained by splitting equation 3.5 into scattering and absorption components, and then substituting in approximate forms for the opacities and emissivities. If we now consider that the emissivity in the line is simply given by $n_u A_{ul} h \nu_{ul} / 4\pi$, then it is possible to show that the absorption fraction is given by

$$q = \frac{C_{ul}(1 - e^{-h\nu/kT_e})}{\beta_{ul}A_{ul} + C_{ul}(1 - e^{-h\nu/kT_e})}. \quad (3.28)$$

This quantity is approximately equal to the probability that an excited bound electron will collisionally de-excite, and is used in the formulation of two-level atom estimators in section 3.4.2.

3.1.5 Monte Carlo approaches

Simple radiation transfer problems can be solved analytically, but with more complicated geometries it is necessary to use Monte Carlo techniques, which are easily solved with modern computing approaches and are intuitively parallelisable problems. I will describe one specific Monte Carlo radiative transfer (MCRT) code, which has been used for the majority of the work in this thesis.

3.2 PYTHON: A Monte Carlo Ionization and Radiative Transfer Code

PYTHON¹ is a confusingly named Monte Carlo ionization and radiative transfer code. The general philosophy of the code is to be able to produce synthetic spectra for astrophysical objects with outflows in 2.5D, using a self-consistent ionization treatment. The code is written in C, and has been in development since the mid-1990s. Throughout this time it has been used with application to CVs (Long & Knigge 2002, hereafter LK02), YSOs (hereafter SDL05 Sim et al. 2005), supernovae (Kerzendorf & Sim 2014) and AGN/quasars (Higginbottom et al. 2013, 2014, hereafter H13 and H14). It is also capable of producing spectra for stellar winds and conducting simple photoionization balance calculations for comparison with codes such as CLOUDY. Some more detail on code testing and development can be found in sections 3.8 and 3.9 respectively. Although the operation of PYTHON is well-described by the above authors, it is central to this Thesis and I will thus provide substantial detail on its operation.

3.2.1 Basics

PYTHON operates in three distinct stages, shown in figure 3.2. First, the user specifies the photon sources, geometry and kinematics of the system, normally with a similar

¹Named c. 1995, predating the inexorable rise of a certain widely used programming language.

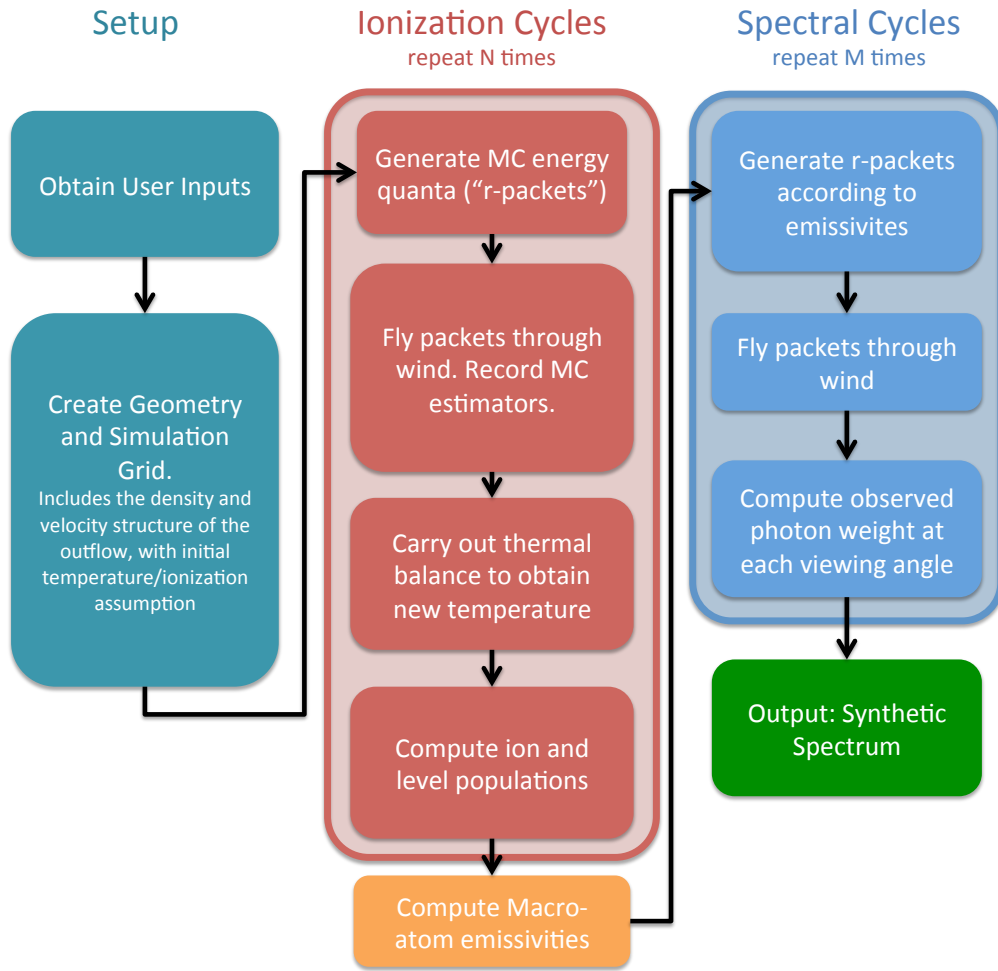


FIGURE 3.2: A flowchart showing the basic operation of PYTHON.

parameterisation to the SV93 model described in section 2.4. The code can operate with multiple coordinate systems (1D, spherical polar, cylindrical), but in this work I use cylindrical coordinates. In this case, the outflow is discretised into a $n_x \times n_y$ logarithmic grid with user-specified dimensions. The co-ordinates, (x_i, z_i) , of the corner of the i th cell are then given by

$$x_i = L_x 10^{(i-1)\frac{\log(R_{max}/L_x)}{n_x}}, \quad (3.29)$$

$$z_i = L_z 10^{(i-1)\frac{\log(R_{max}/L_z)}{n_z}}, \quad (3.30)$$

where L_x and L_z are appropriately chosen (but hardwired) scale lengths. From these co-ordinates the poloidal distance can be calculated and the velocity set according to equation 2.11. The density is then calculated from equation 2.15. An initial temperature,

T_{init} is set by the user. The ionization fractions throughout the wind are then to Saha (LTE) abundances at T_{init} , and the level populations are set according to the Boltzmann formula.

Once the basic setup process has been carried out, the ionization state, level populations and temperature structure are calculated. This is done via an iterative process, by transporting several populations of Monte Carlo energy quanta ('photons' or 'r-packets) through the outflow. This process is repeated until the code converges. In each of these iterations ('ionization cycles'), the code records estimators that characterize the radiation field in each grid cell. At the end of each ionization cycle, a new electron temperature is calculated that more closely balances heating and cooling in the plasma. The radiative estimators and updated electron temperature are then used to revise the ionization state of the wind, and a new ionization cycle is started. The process is repeated until heating and cooling are balanced throughout the wind (see sections 3.5 and 3.5.1).

This converged model as the basis for the second set of iterations ('spectral cycles'; section 3.6), in order to compute the synthetic spectrum based on the MC estimators record during the ionization cycles. The emergent spectrum over the desired spectral range is synthesized by tracking populations of energy packets through the wind and computing the emergent spectra at a number of user-specified viewing angles. In the ensuing sections, I will describe each of the above steps in more detail, particularly with regards to the macro-atom mode of operation.

3.2.2 Radiation Packets

Every energy packet in the simulation starts out as a radiation packet generated from one of N_S photon sources. To ensure that the frequency distribution of photons is adequately sampled in important frequency regimes, *stratified sampling* is used. A specified fraction, f_i , of photons must then emerge each band i , whose frequency boundaries can be adapted for the astrophysical situation considered. The weight, w_i , of the radiation packets in a given energy band i , with boundaries ν_i and ν_{i+1} is then given by

$$w_i = \frac{\sum_j^{N_S} \int_{\nu_i}^{\nu_{i+1}} L_{\nu,j} d\nu}{f_i N_p}, \quad (3.31)$$

where N_p is the *total* number of photons desired and $L_{\nu,j}$ is the monochromatic luminosity of photon source j . The frequency of photons is calculated by constructing a cumulative distribution function (CDF), $f_{C,i}(\nu)$ from the spectral energy distribution in each band i :

$$f_{C,i}(\nu) = \frac{\int_{\nu_i}^{\nu} L_{\nu} d\nu}{\int_{\nu_i}^{\nu_{i+1}} L_{\nu} d\nu}. \quad (3.32)$$

A photon frequency can then be generated by cycling through the bands. In each band, a random number is chosen between 0 and 1, and then the frequency is selected by interpolating on the sampled CDF. This process is repeated until each band has the specified number of photons, with the packet weights adjusted accordingly.

PYTHON can operate in two modes concerning the approach to energy packets. In the original mode described by LK02, continuum processes attenuate the weight of the radiation packets. This attenuation is accounted for by including the wind as an additional photon source. In the second mode, energy packets are indivisible and strict radiative equilibrium is enforced. From here on I will only be discussing this indivisible packet scheme, as it is required in order to be able to use macro-atoms to accurately treat recombination in H and He.

3.2.3 Radiative Transfer procedure

As a photon travels through a plasma, it has a finite probability of interacting with the free or bound electrons and undergoing a scattering or absorption event. To deal with this in a Monte Carlo sense, a random optical depth is generated before an r -packet is moved,

$$\tau_R = -\ln(1 - \mathcal{Z}), \quad (3.33)$$

where \mathcal{Z} is a random number between 0 and 1. The r -packet is then gradually transported through a given cell. As it moves, the optical depth, τ' , it experiences is incremented continuously, representing continuum processes. When the r -packet comes into resonance with a line, according to equation 3.22, then the Sobolev optical depth is calculated from equation 3.23 and added to τ' . This process is shown in Fig. 3.3, and continues until $\tau' \geq \tau_R$ or the r -packet leaves the cell. If the photon leaves the cell then the values of τ_R and τ' are preserved, and the process continues using the conditions in the new cell. If $\tau' \geq \tau_R$, then an interaction with the plasma has occurred, and the

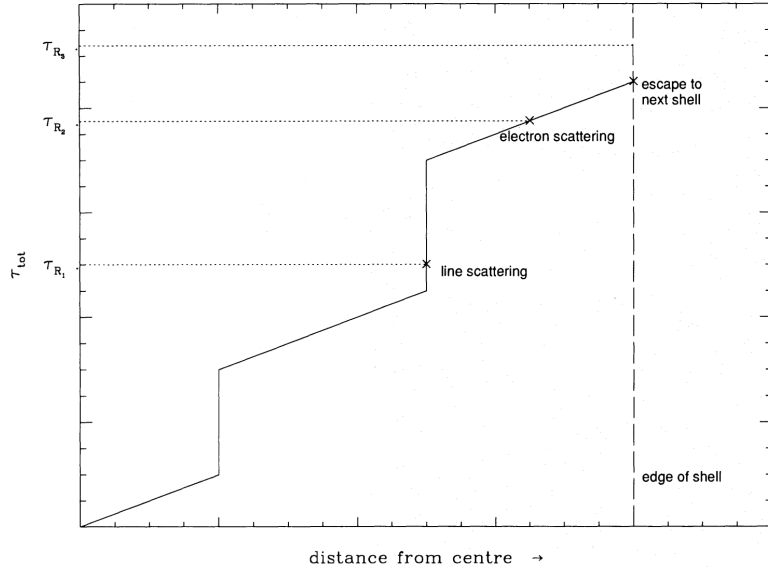


FIGURE 3.3: Credit: Mazzali & Lucy 1993. The process of choosing a scattering location in a cell.

process governing this interaction must be identified. This is done by randomly picking an interaction process in proportion with their contributions to τ' . If the process is an electron scatter then a new, isotropic direction is generated for the r -packet. Otherwise, the packet must interact with either the thermal pool or the excitation energy of the plasma.

3.2.3.1 Continuum opacities

In order to calculate τ' in the above approach, we need to know the opacities that will contribute to it. An opacity at a given frequency, $\kappa(\nu)$, is related to an optical depth, $\tau(\nu)$, by

$$\tau(\nu) = \kappa(\nu) \Delta s, \quad (3.34)$$

where Δs is the distance moved by the photon. The bound-free opacity is calculated from a sum over photoionization cross-section, such that

$$\kappa_{bf} = \sum_{j\kappa}^{bf jumps} \sigma_{j\kappa}(\nu) n_j. \quad (3.35)$$

The free-free emission coefficient for an individual ion i is (Gayet 1970)

$$j_{ff,i}(\nu) = \bar{g}_{ff} \frac{8Z_i^2 e^6}{3m_e c^2} \frac{2\pi m_e}{3kT_e}^{1/2} N_i n_e \exp(-h\nu/kT_e). \quad (3.36)$$

The free-free opacity is then calculated from Kirchhoff's law,

$$\kappa_{ff,i}(\nu) = \frac{B_\nu(T_e)}{j_{ff,i}(\nu)}, \quad (3.37)$$

which gives

$$\kappa_{ff,i}(\nu) = n_e N_i \frac{4}{3} \left(\frac{2\pi}{3} \right)^{1/2} \frac{Z_i^2}{e^6 m_e^2 h c} \left(\frac{m_e}{k T_e} \right)^{1/2} g_{ff} \nu^{-3} [1 - \exp(-h\nu/kT_e)]. \quad (3.38)$$

The electron scattering opacity is

$$\kappa_{es} = \sigma_T n_e. \quad (3.39)$$

These opacities are all used in the heating and cooling estimators introduced in section 3.3.3. In addition the Compton opacity is required in order to estimate the Compton heating effect on the plasma. The Compton opacity is given by

$$\kappa_C = \sigma_{KN}(\nu) n_e, \quad (3.40)$$

where $\sigma_{KN}(\nu)$ is the cross-section computed from the Klein-Nishina formula (Klein & Nishina 1929), and unlike σ_T is frequency dependent. This opacity is not included in the actual radiative transfer in the simulations presented in this Thesis, but is included in the heating and cooling balance (see section 3.3.3).

3.2.3.2 Doppler Shifts

To calculate the opacities correctly, the frequency must be shifted from the co-moving frame of the photon into the co-moving frame of the cell. This shift depends on the before and after direction of the photon. Let us denote these two directions with unit vectors \vec{n}_i and \vec{n}_f respectively, and consider a situation when a photon scatters off an electron in a region of the wind moving at velocity \vec{v} . The final frequency of the photon with initial frequency ν_i is then

$$\nu_f = \nu_i \frac{1 - (\vec{v} \cdot \vec{n}_i)/c}{1 - (\vec{v} \cdot \vec{n}_f)/c}. \quad (3.41)$$

In the case of a resonance scatter with line transition $u \rightarrow j$, the new frequency is

$$\nu_f = \frac{\nu_{uj}}{1 - (\vec{v} \cdot \vec{n}_f)/c}. \quad (3.42)$$

when we consider that the resonant point is chosen according to equation 3.22 and that $v = \vec{v} \cdot \vec{n}_f$ in this case, it is clear that the above two equations are equivalent.

3.2.3.3 Choosing packet directions

The last variable, in addition to w_i and ν , needed to define a radiation packet is the direction of travel. In the case of isotropic emission the direction of a photon packet is chosen so that the probability of emission in each bin of solid angle is the same. It follows that

$$P(\Omega)d\Omega \propto \cos\theta \sin\theta d\theta d\phi, \quad (3.43)$$

where the angles are in polar coordinates and relative to the local outward normal. For a spherical emitting source such as a star then one must first generate a location on the star's surface, and then calculate the photon direction relative to the normal at the point. For emission from solid surfaces the above equation is modified to include linear limb darkening, $\eta(\theta)$:

$$p(\theta\phi)d\theta d\phi = \eta(\theta) \cos\theta \sin\theta d\theta d\phi, \quad (3.44)$$

where, under the Eddington approximation use in the code, $\eta(\theta)$ is given by

$$\eta(\theta) = a(1 - \frac{3}{2}\cos\theta). \quad (3.45)$$

The constant a is simply normalised such that the total probability sums to 1. Whenever a radiation packet undergoes an electron scatter, the new direction is chosen to be isotropic. However, when the photon is a line photon then the new direction is chosen according to a line trapping model, which samples a probability distribution according to the Sobolev escape probability in different directions.

3.3 Macro-atoms

The macro-atom scheme was created by Leon Lucy and is outlined in his 2002/03 papers. It was implemented in PYTHON by Stuart Sim, initially for the study of recombination lines in YSOs (SDL05).

(Lucy 2002, 2003, hereafter L02, L03) has shown that it is possible to calculate the emissivity of a gas in statistical equilibrium without approximation for problems with large departures from LTE. His macro-atom scheme allows for all possible transition paths from a given level, dispensing with the two-level approximation, and provides a full non-LTE solution for the level populations based on Monte Carlo estimators. The macro-atom technique has already been used to model Wolf-Rayet star winds (Sim 2004), AGN disc winds (Sim et al. 2008; Tatum et al. 2012), supernovae (Kromer & Sim 2009; Kerzendorf & Sim 2014) and YSOs (SDL05). A full description of the approach can be found in L02 and L03.

The fundamental approach here requires somewhat of a philosophical shift. Normally MCRT is described in the most intuitive way- that is, we imagine real photons striking atoms and scattering, or photoionizing and depositing energy in a plasma. With Lucy's scheme we should instead reimagine the MC quanta as a packets of quantised energy flow, and the scheme as a *statistical* one. The amount of time a given energy quanta spends in a specific atomic level or thermal pool is then somewhat analogous to the absolute energy contained therein.

Following L02, let us consider an atomic species interacting with a radiation field. If the quantity ϵ_j represents the ionization plus excitation energy of a level i then the rates at which the level j absorbs and emits radiant energy are given by

$$\dot{A}_j^R = R_{\ell j} \epsilon_{j\ell'} \quad \text{and} \quad \dot{E}_i^R = R_{j\ell'} \epsilon_{j\ell'} , \quad (3.46)$$

Where I have adopted Lucy's convention in which the subscript ℓ' denotes a summation over all lower states ($\ell' < j$), and u' will thus denote a summation over all states ($u' > j$). Similarly, the rates corresponding to *kinetic* (collisional) energy transport can then be written as

$$\dot{A}_j^C = C_{\ell' j} \epsilon_{j\ell'} \quad \text{and} \quad \dot{E}_j^C = C_{j\ell'} \epsilon_{j\ell'} , \quad (3.47)$$

Let us define \mathcal{R} as a total rate, such that $\mathcal{R}_{\ell'j} = R_{\ell'j} + C_{\ell'j}$. If we now impose statistical equilibrium

$$(\mathcal{R}_{\ell'j} - \mathcal{R}_{j\ell'}) + (\mathcal{R}_{u'j} - \mathcal{R}_{ju'}) = 0 . \quad (3.48)$$

we can then obtain

$$\begin{aligned} & \dot{E}_j^R + \dot{E}_j^C + \mathcal{R}_{ju'}\epsilon_j + \mathcal{R}_{j\ell'}\epsilon_{\ell'} \\ &= \dot{A}_j^R + \dot{A}_j^C + \mathcal{R}_{u'j}\epsilon_j + \mathcal{R}_{\ell'j}\epsilon_{\ell'} . \end{aligned} \quad (3.49)$$

This equation is the starting point for the macro-atom scheme. It shows that, when assuming only radiative equilibrium, the energy flows through a system depend only on the transition probabilities and atomic physics associated with the levels the energy flow interacts with. By quantising this energy flow into radiant (r -) and kinetic (k -) packets, we can simulate the energy transport through a plasma discretised into volume elements (“macro-atoms”), whose associated transition probabilities govern the interaction of radiant and kinetic energy with the ionization and excitation energy associated with the ions of the plasma.

Although equation 3.49 assumes strict radiative equilibrium, it is trivial to adjust it to include non-radiative source and sink terms. For example, in an expanding parcel of plasma, adiabatic cooling may be included with a simple modification to the RHS of equation 3.49.

3.3.1 Transition Probabilities

Having interpreted equation 3.49 in a *stochastic* way, we can now construct our Monte Carlo scheme, following L02. A macro-atom in state j always has a finite probability of deactivating radiatively or collisionally:

$$p_j^R = \dot{E}_j^R / D_j \quad \text{and} \quad p_j^C = \dot{E}_j^C / D_j , \quad (3.50)$$

where I have defined

$$D_j = \dot{E}_j^R + \dot{E}_j^C + \mathcal{R}_{ju'}\epsilon_j + \mathcal{R}_{j\ell'}\epsilon_{\ell'} = (\mathcal{R}_{j\ell'} + \mathcal{R}_{ju'})\epsilon_j . \quad (3.51)$$

The corresponding jumping probabilities, which describe the probability that the macro-atom transitions to a different state while remaining active, are given by

$$p_{ju'} = \mathcal{R}_{ju}\epsilon_j/D_j \quad \text{and} \quad p_{j\ell'} = \mathcal{R}_{j\ell'}\epsilon_{\ell'}/D_j. \quad (3.52)$$

Note that the jumping probability is always proportional to the energy of the lower level, whereas the emission probability is proportional to the energy *difference* between the levels, as $\dot{E}_j^R = R_{j\ell'}(\epsilon_j - \epsilon_{\ell'})$. We can also trivially show that the probabilities are correctly normalised, as

$$\begin{aligned} p_j^R + p_j^C + p_{j\ell'} + p_{ju'} &= (1/D_j)(\mathcal{R}_{ju'}\epsilon_j + \mathcal{R}_{j\ell'}\epsilon_{\ell'} + \dot{E}_j^R + \dot{E}_j^C) \\ &= 1. \end{aligned} \quad (3.53)$$

With these transition probabilities identified, a Monte Carlo calculation can proceed by formulating the normal statistical equilibrium rate equations that will depend on the ambient conditions of the plasma. The effect of these ambient conditions is expressed through the use of Monte Carlo *estimators*.

3.3.2 Rate equations

The macroscopic transition probabilities above depend on the traditional rate equations formulated according to statistical equilibrium. In the framework of the Sobolev escape probability formalism (Rybicki & Hummer 1978; L02; Sim 2004), the bound-bound excitation rate, \mathcal{R}_{ju} , in an ion is given by

$$\mathcal{R}_{ju} = B_{ju}n_j J_{est} + q_{ju}n_j n_e, \quad (3.54)$$

where u is now a specific upper level and q_{ju} is the collisional rate coefficient (see section 3.3.2.1). J_{est} is the Monte Carlo estimator for the mean intensity impinging on the Sobolev region, weighted by an angle-dependent escape probability, given by (Sim 2004)

$$J_{est} = \frac{c}{4\pi\nu_0 V} \sum_i w_i \frac{1 - e^{-\tau_{s,i}}}{\tau_{s,i}} \frac{1}{(dv/ds)_i}. \quad (3.55)$$

Here w is the photon weight (in luminosity units), ν_0 is the line frequency, dv/ds is the velocity gradient and τ_s is the Sobolev optical depth. The sum is over all photons

that come into resonance with the line, and thus represents an integral over solid angle. This is essentially the MC estimator form of $\beta_{uj}\bar{J}_{uj}$, and differs from the estimator in equation (20) of L02 as there is no assumption of homologous flow or symmetric escape probabilities. The corresponding de-excitation rate is then

$$\mathcal{R}_{uj} = \beta_{ju}A_{uj}n_u + B_{uj}n_uJ_{est} + q_{uj}n_u n_e. \quad (3.56)$$

In practice, the stimulated emission term is included as a negative contribution to the radiative excitation rate, requiring no population inversions (see section 3.3.7). The photoionization and collisional ionization rates between a lower level, l , and the continuum level κ (or, in the case of ions with more than one bound electron, the ground state of the upper ion), κ , are

$$\mathcal{R}_{j\kappa} = n_j(\gamma_{j\kappa} - \alpha_{\kappa j}^{st}) + q_{j\kappa}n_j n_e. \quad (3.57)$$

Here, $q_{j\kappa}$ is the collisional ionization rate coefficient, $\gamma_{j\kappa}$ is the photoionization rate from $j \rightarrow \kappa$ and $\alpha_{\kappa j}^{st}$ is the stimulated recombination coefficient. This is included as a negative photoionization term rather than a positive recombination term as in L03, which requires that there are no population inversions (see section 3.3.7). The corresponding recombination rate is given by

$$\mathcal{R}_{\kappa j} = \alpha_{\kappa j}n_\kappa n_e + q_{\kappa j}n_\kappa n_e, \quad (3.58)$$

where $\alpha_{\kappa l}$ is the radiative recombination coefficient to level l , and is given by

$$\alpha_{\kappa j} = 4\pi\Phi_{j\kappa}^* \int_{\nu_0}^{\infty} \frac{\sigma_{j\kappa}(\nu)}{h\nu} \frac{2h\nu^3}{c^2} \exp\left(\frac{-h\nu}{kT_e}\right) d\nu. \quad (3.59)$$

This treatment means that radiative and collisional rates to and from all levels can be considered when calculating the ionization state, level populations and transition probabilities, although ionization directly to excited levels of the upper ion is neglected.

3.3.2.1 Collision strengths

The bound-bound collisional rate coefficient q_{lu} is calculated from the van Regemorter (1962) approximation, given by

$$q_{ju} = 2.388 \times 10^{-6} \lambda_{uj}^3 A_{uj} g_u \bar{g}, \quad (3.60)$$

where λ_{uj}^3 is the wavelength of the transition and \bar{g} is an effective gaunt factor of order unity. The inverse rate can just be calculated by considering detailed balance, such that

$$q_{uj} = q_{ju} \frac{g_u}{g_j} \exp\left(\frac{h\nu_{uj}}{kT_e}\right) \quad (3.61)$$

Using equation 3.60 means that collisions between radiatively forbidden transitions are not taken into account when one splits levels into l - and s -subshells, as well as principal quantum number, n (as done with He I; see chapter 4). Although this approximation is, in general, a poor one, the effect is second order in the physical regime where recombination lines are formed in our models. This is because bound-free processes are dominant in determining level populations and emissivities. I have verified that this is indeed the case in the He I emission regions in the models presented here.

The bound-free collision strengths are calculated using equation (5.79) of [Mihalas \(1978\)](#). The collisional ionization rate is

$$q_{j\kappa} = 1.55 \times 10^{-13} n_e \bar{g}_i \sigma_{j\kappa}(\nu_0) \frac{h\nu_{uj}}{kT_e^{3/2}} \exp\left(\frac{-h\nu_{kj}}{kT_e}\right), \quad (3.62)$$

where $\sigma_{j\kappa}(\nu_0)$ is the photoionization cross-section at the threshold energy. \bar{g}_i is an effective gaunt factor for ion i and is approximately equal to 0.1, 0.2, 0.3 for $Z = 1, 2$ and > 2 respectively, where Z is the atomic number. Note that the use of this estimator implies a ν^{-3} shape to the photoionization cross-section, which is only strictly true for hydrogenic ions. The collisional (three-body) recombination rate is found using the Saha equation and given by

$$q_{kj} = q_{j\kappa} \left(\frac{n_j}{n_e n_\kappa} \right)_{T_e}^*. \quad (3.63)$$

For numerical reasons, the above two expressions are combined in PYTHON where possible, to avoid multiplying two exponentials together.

3.3.3 Macro-atom estimators

To be able to solve the above rate equations and compute the transition probabilities, it is necessary to construct estimators for the various properties of the radiation field that appear in said equations. This is done by converting integrals over the radiation field into summations over r -packets passing through a cell. This represents the stochastic

nature of a MC simulation, and is by no means unique to the macro-atom formalism. The first step is to apply the energy-density argument of Lucy (1999a), which gives, for a time-independent code

$$J_\nu \, d\nu = \frac{1}{4\pi} \frac{1}{V} \sum_{d\nu} w_i \Delta s, \quad (3.64)$$

where the summation is over all photons between $(\nu, \nu + d\nu)$. This allows us to formulate estimators in a MC sense, rather than in integral form.

3.3.3.1 Bound-free estimators

The estimator for the photoionization rate is

$$\gamma_{j\kappa} = \frac{1}{V} \sum_i^{photons} \frac{w_i \sigma_{j\kappa}(\nu)}{h\nu} \Delta s \quad (3.65)$$

and for the stimulated recombination rate is

$$\alpha_{\kappa j}^{st} = \left(\frac{n_j}{n_e n_\kappa} \right)_{T_e}^* \frac{1}{V} \sum_i^{photons} \frac{w_i \sigma_{j\kappa}(\nu)}{h\nu} \exp(-h\nu/kT_e) \Delta s, \quad (3.66)$$

where $\sigma_{l\kappa}(\nu)$ is the photoionization cross-section for this transition. We also need to define modified rate coefficients which are the rates at which bound-free transitions add energy to and remove energy from the radiation field. These are required for photoionization, spontaneous recombination and stimulated recombination, and are given by

$$\gamma_{j\kappa}^E = \frac{1}{V} \sum_i^{photons} \frac{w_i \sigma_{j\kappa} \kappa j}{h\nu_{\kappa j}} \Delta s, \quad (3.67)$$

$$\alpha_{\kappa j}^E = 4\pi \left(\frac{n_j}{n_e n_\kappa} \right)_{T_e}^* \int_{\nu_{\kappa j}}^\infty \frac{\sigma_{j\kappa}(\nu)}{h\nu_{\kappa j}} \frac{2h\nu^3}{c^2} \exp\left(\frac{-h\nu}{kT_e}\right) d\nu, \quad (3.68)$$

$$\alpha_{\kappa j}^{st,E} = \left(\frac{n_j}{n_e n_\kappa} \right)_{T_e}^* \frac{1}{V} \sum_i^{photons} \frac{w_i \sigma_{j\kappa}(\nu)}{h\nu_{\kappa j}} \exp(-h\nu/kT_e) \Delta s. \quad (3.69)$$

The rate at which recombinations convert thermal *and* ionization energy into radiant energy is then $\alpha^E h\nu_{\kappa j} n_\kappa n_e$, where $h\nu_{\kappa j}$ is the potential of the bound-free transition, or the energy difference between continuum κ and the level j the electron is recombining

too. The amount of this energy which is removed from the thermal pool therefore needs a quantity $\alpha_{\kappa j} h\nu_{\kappa j} n_{\kappa} n_e$ subtracted from it, giving the bound-free cooling estimator

$$\mathcal{C}_{bf} = \sum_{j\kappa}^{bf jumps} (\alpha_{\kappa j}^E - \alpha_{\kappa j}) n_e n_{\kappa} h\nu_{\kappa j} V, \quad (3.70)$$

where the sum is over all the macro-atom bound-free transitions ($j \rightarrow \kappa$) in the simulation, set by the number of photoionization cross-sections. For bound-free heating, we write a similar expression. The rate at which a level l absorbs energy by bound-free transitions is given by $\gamma_{j\kappa}^E h\nu_{\kappa j} n_{\kappa} n_e$, but the amount $\gamma_{j\kappa} h\nu_{\kappa j} n_l$ goes into ionization energy, giving

$$\mathcal{H}_{bf} = \sum_{j\kappa}^{bf jumps} (\gamma_{\kappa j}^E - \gamma_{\kappa j} - \alpha_{\kappa j}^{st,E} + \alpha_{\kappa j}^{st}) n_j h\nu_{\kappa j} V \quad (3.71)$$

as the rate at which radiant energy heats the plasma via bound-free transitions.

3.3.3.2 Bound-bound estimators

The heating and cooling rates for macro-atom bound-bound transitions are the rates of collisional excitations and de-excitations - i.e. the rate at which thermal energy is converted into bound-bound excitation energy and vice versa. These heating and cooling rate estimators are:

$$\mathcal{H}_{bb} = \sum_{ju}^{lines} q_{uj} n_u n_e h\nu_{uj} V, \quad (3.72)$$

$$\mathcal{C}_{bb} = \sum_{ju}^{lines} q_{ju} n_j n_e h\nu_{uj} V. \quad (3.73)$$

3.3.3.3 Other heating and cooling estimators

Although we have now formulated the estimators required to calculate the transition probabilities, level populations, heating rates and cooling rates in macro-atoms, there are still a number of heating and cooling mechanisms that do not involve macro-atoms.

The free-free cooling estimator is calculated from the emission coefficient in equation 3.36

$$\mathcal{C}_{ff} = V \sum_i^{ions} \int \frac{j_{ff,i}(\nu)}{4\pi} d\nu, \quad (3.74)$$

where the integral is over all frequencies included in the simulation, and the sum is also over all ions included in the simulation. The corresponding heating rate is then

$$\mathcal{H}_{ff} = \sum_i^{photons} w_i \kappa_{ff} \Delta s. \quad (3.75)$$

Compton heating and cooling is included in the thermal balance and as ($r \rightarrow k$) and ($k \rightarrow r$) transitions:

$$\mathcal{C}_{comp} = 16\pi\sigma_T V J \frac{kT_e}{m_e c^2}, \quad (3.76)$$

$$\mathcal{H}_{comp} = n_e \sum_i^{photons} \frac{h\nu}{m_e c^2} w_i \kappa_C \Delta s, \quad (3.77)$$

where the estimator for the frequency-integrated mean intensity is

$$J = \frac{1}{4\pi V} \sum_i^{photons} w_i \Delta s. \quad (3.78)$$

Induced Compton heating is then given by (Ferland et al. 2013)

$$\mathcal{H}_{ind\ comp} = n_e \sum_i^{photons} \frac{J_\nu c^2}{h\nu^3} \frac{h\nu}{m_e c^2} w_i \kappa_C \Delta s, \quad (3.79)$$

where the first $J_\nu c^2/h\nu^3$ term represents the photon occupation number, and J_ν is either calculated from the spectral model described in section 3.4.2.1 or a dilute blackbody.

The adiabatic cooling rate is derived from PdV work and is given by

$$\mathcal{C}_a = kT_e V (\nabla \cdot v) \left(n_e + \sum_{i=1}^{ions} N_i \right), \quad (3.80)$$

where $\nabla \cdot v$ is the divergence of the velocity field at the centre of the cell. The sum is over all ions included in the simulation.

3.3.4 k -packets

k -packets represent quantised kinetic or thermal energy, and any interaction chain involving a k -packet thus represents interaction with the thermal pool of ions and electrons. k -packets can be produced either directly via a continuum heating process ($r \rightarrow k$), or by the collisional de-activation of a macro-atom ($r \dots \rightarrow A^* \rightarrow k$) according to equation 3.50.

Once they are produced, k -packets never move, as they represent the quantised thermal energy flow in a finite volume element. Hence, when they are produced, their destruction path is decided according to the different cooling mechanisms in the plasma. A k -packet then has a probability of being destroyed by process i of

$$p_{i,destruct} = \mathcal{C}_i / (\mathcal{C}_{bf} + \mathcal{C}_{ff} + \mathcal{C}_{bb} + \mathcal{C}_{comp} + \mathcal{C}_a). \quad (3.81)$$

Note that only adiabatic cooling leads to an actual destruction of the energy packet, as a departure from radiative equilibrium. All other processes will lead to the creation of an active macro-atom or an r -packet.

3.3.5 Putting it all together

I have now defined all quantities needed to write down the transition probabilities in a macro-atom simulation. Fig. 3.4 shows the decision tree traversed by an energy packet in the simulation, showing the complicated set of interactions it can undergo each time it scatters.

3.3.6 Ionization Fractions and Level Populations

In section 3.1.2 I described how it is possible to calculate the ionization and excitation of a plasma under LTE or dilute approximations. Macro-atoms are not approximated – their level and ion populations are calculated by solving the rate equations formulated in section ???. This is done via matrix inversion. For an element with n ions and m_i levels in each ion, we construct a square matrix with dimensions $m = \sum_i^n m_i$. This element then has a total number density of $N_{elem} = \sum_i^n N_i$. To turn the system of rate equations for this element into matrix form, we populate the j th diagonal of the matrix with the

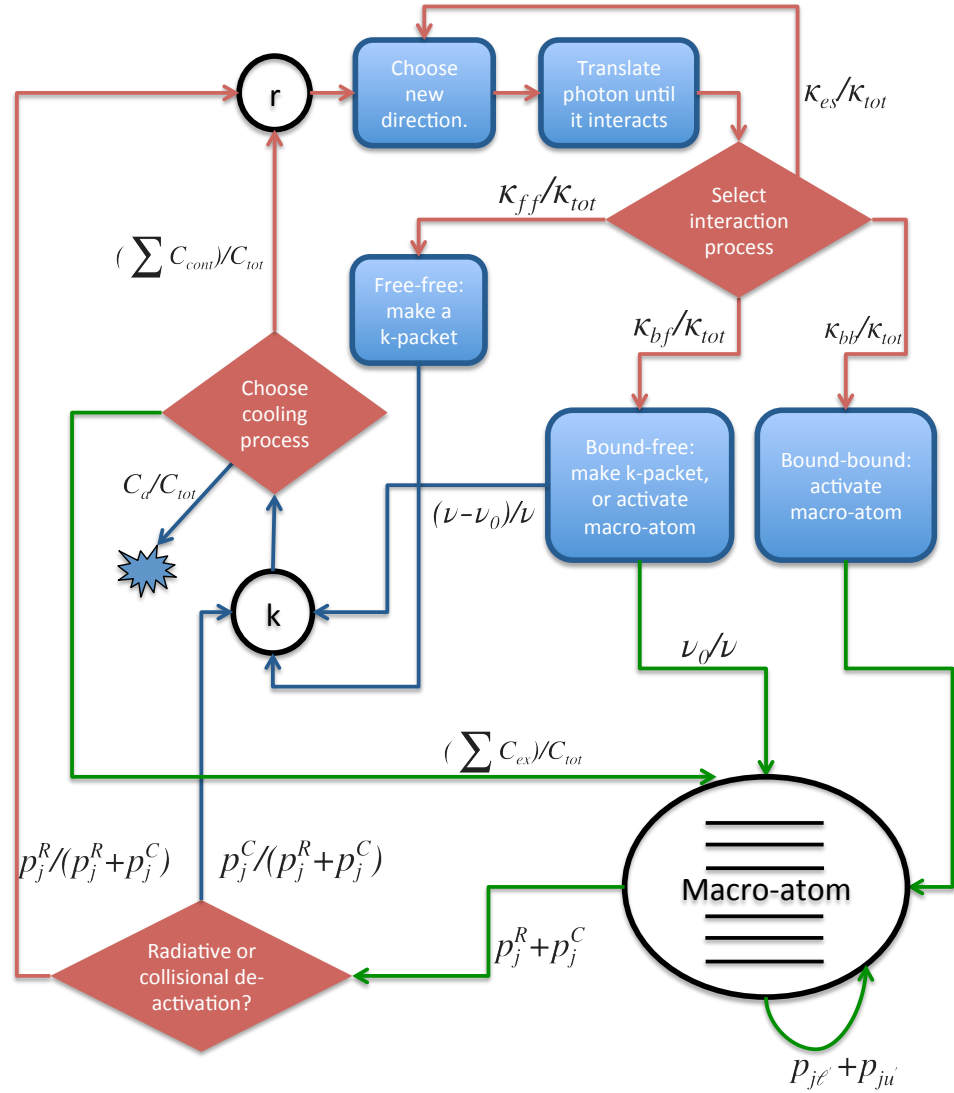


FIGURE 3.4: The decision tree traversed by an energy packet in macro-atom mode, depicting the interaction between radiation (r -packets), the thermal pool (k -packets), and ionization and excitation energy (macro-atoms). The probabilities at each decision point are marked, and are defined in the text. The red, blue and green coloured arrows represent radiant, kinetic and ionization/excitation energy respectively. The symbols are defined in the text, except \mathcal{C}_{cont} and \mathcal{C}_{ex} which refer to cooling contributions to radiative and excitation energy respectively.

negative of the rate out of level j , $-(\mathcal{R}_{j\ell'} + \mathcal{R}_{ju'})$, and populate the off-diagonals (j, k) with the positive rate \mathcal{R}_{jk} . These are then multiplied by a vector of the fractional level populations, and must equal a vector of zeros, due to statistical equilibrium. Our matrix equation is then

$$\begin{bmatrix} -\mathcal{R}_{1u'} & \mathcal{R}_{21} & \mathcal{R}_{31} & \dots & \mathcal{R}_{m1} \\ \mathcal{R}_{12} & -(\mathcal{R}_{2\ell'} + \mathcal{R}_{2u'}) & \mathcal{R}_{32} & \dots & \mathcal{R}_{m2} \\ \mathcal{R}_{13} & \mathcal{R}_{23} & -(\mathcal{R}_{3\ell'} + \mathcal{R}_{3u'}) & \dots & \mathcal{R}_{m3} \\ \vdots & \vdots & \vdots & \ddots & \vdots \\ \mathcal{R}_{1m} & \mathcal{R}_{2m} & \mathcal{R}_{3m} & \dots & -\mathcal{R}_{m\ell'} \end{bmatrix} \begin{bmatrix} n_1/N_{elem} \\ n_2/N_{elem} \\ n_3/N_{elem} \\ \vdots \\ n_m/N_{elem} \end{bmatrix} = \begin{bmatrix} 0 \\ 0 \\ 0 \\ \vdots \\ 0 \end{bmatrix}. \quad (3.82)$$

This problem is not yet soluble, as a valid solution is that all levels could simply have occupation numbers of 0. To close the problem, we must impose the boundary condition, that the sum of the fractional populations is 1, i.e.

$$\sum_i \frac{N_i}{N_{elem}} = 1. \quad (3.83)$$

In matrix form, this is equivalent to replacing the entire first row of the rate matrix with 1, and the first entry of the RHS vector with a 1, so that we have

$$\begin{bmatrix} 1 & 1 & 1 & \dots & 1 \\ \mathcal{R}_{12} & -(\mathcal{R}_{2\ell'} + \mathcal{R}_{2u'}) & \mathcal{R}_{32} & \dots & \mathcal{R}_{m2} \\ \mathcal{R}_{13} & \mathcal{R}_{23} & -(\mathcal{R}_{3\ell'} + \mathcal{R}_{3u'}) & \dots & \mathcal{R}_{m3} \\ \vdots & \vdots & \vdots & \ddots & \vdots \\ \mathcal{R}_{1m} & \mathcal{R}_{2m} & \mathcal{R}_{3m} & \dots & -\mathcal{R}_{m\ell'} \end{bmatrix} \begin{bmatrix} n_1/N_{elem} \\ n_2/N_{elem} \\ n_3/N_{elem} \\ \vdots \\ n_m/N_{elem} \end{bmatrix} = \begin{bmatrix} 1 \\ 0 \\ 0 \\ \vdots \\ 0 \end{bmatrix} \quad (3.84)$$

This matrix equation can now be solved. To do the actual matrix manipulation, the code uses the GNU scientific libraries (GSL; [Gough 2009](#)) implementation of LU decomposition ([Turing 1948](#)). This is a fast and reliable way of inverting large matrices that includes error handling and enables checking of, for example, singular rate matrices.

3.3.7 Numerical Issues and Population Inversions

An inherent problem in MC simulations is noise, particularly when the MC estimators involved rely on specific frequencies of photons in order to be incremented. One of the

side effects of this is that population inversions can occur. A population inversion is present when

$$n_u > n_l \frac{g_u}{g_l}. \quad (3.85)$$

This can cause clear problems, for example, with the inclusion of the stimulated recombination rate as a negative photoionization term. Inspection of equations 3.20 and 3.56 reveals that a negative excitation rate would be obtained in this situation.

To prevent this problem, we can simply ‘clean’ our level populations after calculation, as suggested by L03. This is done by cycling through the levels after the above calculation has been carried out and checking if condition 3.85 is ever satisfied. If it is, then the upper population is simply set to a value just below this limit. This is only necessary when there is a permitted dipole transition between the two levels being compared.

In addition to the population inversion problem, it is also possible to produce singular rate matrixes when photon statistics are poor, particularly in heavily absorbed portions of the wind where photons which come into resonance with lines, or are above threshold frequencies, may be rare. To deal with this issue, I have written a routine in PYTHON that checks if the rate matrix is singular and if any anomalous (negative or non-finite) populations exist in the solution found. If either of these conditions are met, then the calculation is redone using dilute estimators. This procedure is also carried out for the simple-atom ionization calculation when the rate matrix approach is in use (see section 3.4.2.1).

3.4 A hybrid line transfer scheme: including simple-atoms

I have now described in detail how the macro-atom approach is implemented in PYTHON. A pure macro-atom approach can be easily used for some situations – for example, in the YSO application described by SDL05, which uses a H-only model. However, in accretion disc winds the densities can be very high and higher Z elements must be included. To include all these elements as macro-atoms is not currently computationally feasible in PYTHON for anything but the simplest models. I will thus describe a ‘hybrid scheme’, which treats H and He under the macro-atom approach but models all other atoms as ‘simple-atoms’.

3.4.1 Line Transfer

Simple-atoms still interact with r - and k -packets, but do not possess internal transition probabilities. As a result, they are analogous to the two-level atom treatment, as any excitation is immediately followed by a deactivation into an r - or k -packet. The choice of radiative or kinetic deactivation is made according to the relative rates in the two-level atom formalism. For a bound-bound transition $u \rightarrow j$, these two probabilities are then

$$p_{uj}^{S,R} = \frac{A_{uj}\beta_{uj}}{A_{uj}\beta_{uj} + C_{uj} \exp(-h\nu_{uj}/kT_e)} = 1 - q \quad (3.86)$$

and

$$p_{uj}^{S,C} = \frac{C_{uj} \exp(-h\nu_{uj}/kT_e)}{A_{uj}\beta_{uj} + C_{uj} \exp(-h\nu_{uj}/kT_e)} = q. \quad (3.87)$$

For a bound-free transition we assume radiative recombination and thus any bound-free simple-atom activation is immediately followed by the creation of r -packet. This approximates the bound-free continuum, even when compared to other two-level atom radiative transfer schemes. This is discussed further and tested in section 3.8.3.

This hybrid approach allows us to preserve the fast treatment of, for example, UV resonance lines, while accurately modelling the recombination cascades that populate the levels responsible for H and He line emission. As a result of this hybrid scheme, a separate set of estimators must be recorded for simple-atoms, and the ionization and excitation of these elements is calculated with a different, approximate approach. In order to include simple-atoms, we must add in a few extra pathways to Fig. 3.4, so that energy packets can also undergo excite simple-atoms, through either bound-free or bound-bound processes. This is done in proportion with the simple-atom opacities.

3.4.2 Heating and Cooling Estimators

The bound-bound heating rate is computed during the photon propagation and is a sum over photons which come into resonance with each line, given by

$$\mathcal{H}_{bb}^S = \sum_i \sum_{ju}^{\text{photons lines}} (1 - q)(1 - e^{-\tau_{S,ju}}) w_i, \quad (3.88)$$

And our bound bound cooling rate is given by

$$\mathcal{C}_{bb}^S = \sum_{ju}^{lines} q \left(n_j \frac{g_u}{g_j} - n_u \right) q_{uj} n_e \frac{(1 - e^{-h\nu_{ju}/kT_e})}{(e^{h\nu_{ju}/kT_e} - 1)} h\nu_{ju}. \quad (3.89)$$

These estimators are fundamentally different quantities and are not used to calculate k-packet probabilities. Instead, they represent the amount of energy transferred to and from the plasma as a whole by the radiation field, whereas in the macro-atom case they represent that rate of collisional excitations and de-excitations. The bound-free heating rate is given by

$$\mathcal{H}_{bf}^S = \sum_i^{photons} \sum_{j\kappa}^{bf jumps} w_i e^{-\tau} \frac{\nu - \nu_{j\kappa}}{\nu} \quad (3.90)$$

where ν here is the frequency of the photon in question, and ν_0 . The bound-free cooling rate is then

$$\mathcal{C}_{bf}^S = \sum_{j\kappa}^{bf jumps} \int_{\nu_{j\kappa}}^{\infty} h\nu \left(\frac{2\pi m_e k T_e}{h^2} \right)^{-3/2} \frac{2h\nu^3}{c^2} \frac{g_j}{g_\kappa g_e} T_e^{-3/2} \sigma_{j\kappa}(\nu) \exp(-h(\nu - \nu_{j\kappa})/kT_e) \quad (3.91)$$

3.4.2.1 Radiation Field Estimators, Ionization and Excitation

For simple-atoms we do not record radiation field estimators for discrete transitions, as for macro-atoms. Instead, we record estimators to give us a model of the radiation field. The estimators needed depend on the ionization mode employed (see section 3.4.2.1). The radiation temperature, T_R , is estimated by first recording the mean frequency, $\bar{\nu}$, of the photons passing through a cell:

$$\bar{\nu} = \frac{\sum_{photons} w_i \nu_i \Delta s}{\sum_{photons} w_i \Delta s}. \quad (3.92)$$

This is then used to calculate the radiation temperature by considering the value expected from a blackbody (Mazzali & Lucy 1993):

$$T_r = \frac{h\bar{\nu}}{3.832 k} \quad (3.93)$$

The dilution factor can be calculated by comparing the estimator for the mean intensity (equation 3.78) to the Stefan-Boltzmann law:

$$W = \frac{\pi J}{\sigma T_r^4}, \quad (3.94)$$

This set of estimators is sufficient to describe the radiation field if one is adopting the dilute approximation (section 3.1.2.1). H13 improved on this by developing a method for modelling the SED in the cell using a series of band-limited radiation field estimators. In this scheme, a series of bands is defined in which to record these estimators. These bands are different to those discussed in section 3.2.2 as those instead govern photon generation. In H13, the band limited estimators were used to construct a correction factor that could be used in a modified Saha equation (similar in form to equation 3.13). However, the code has now been improved so that the ion populations are computed by solving the rate equations. Thus, we now simply need to calculate photoionization rate estimators for simple ions, which rely on being able to integrate a modelled form of the mean intensity.

The mean intensity is modelled in each band i using either a power law or exponential with respective forms of

$$J_{\nu,i} = K_{PL} \nu^{\alpha_{PL}} \quad (3.95)$$

$$J_{\nu,i} = K_{exp} \exp(-h\nu/kT_{exp}) \quad (3.96)$$

where T_{exp} and α_{PL} are the fit parameters and K_{PL} and K_{exp} are the normalisation constants, which are obtained by ensuring that the model reproduces the band limited mean intensity from equation 3.78. An example of a modeled spectrum compared to the recorded MC spectrum from the summed photons is shown in figure 3.5, showing how this scheme faithfully reproduces the SED in situations where there are large departures from a blackbody.

Once the model for the mean intensity has been calculated it is possible to formulate a photoionization rate estimator from ion i to $i + 1$ for simple-atoms:

$$\gamma_{i,i+1}^S = \sum_i^{bands} \int_{\nu_i}^{\nu_{i+1}} \sum_j^{levels} \frac{J_{\nu,i} \sigma_{jk}(\nu)}{h\nu} d\nu \quad (3.97)$$

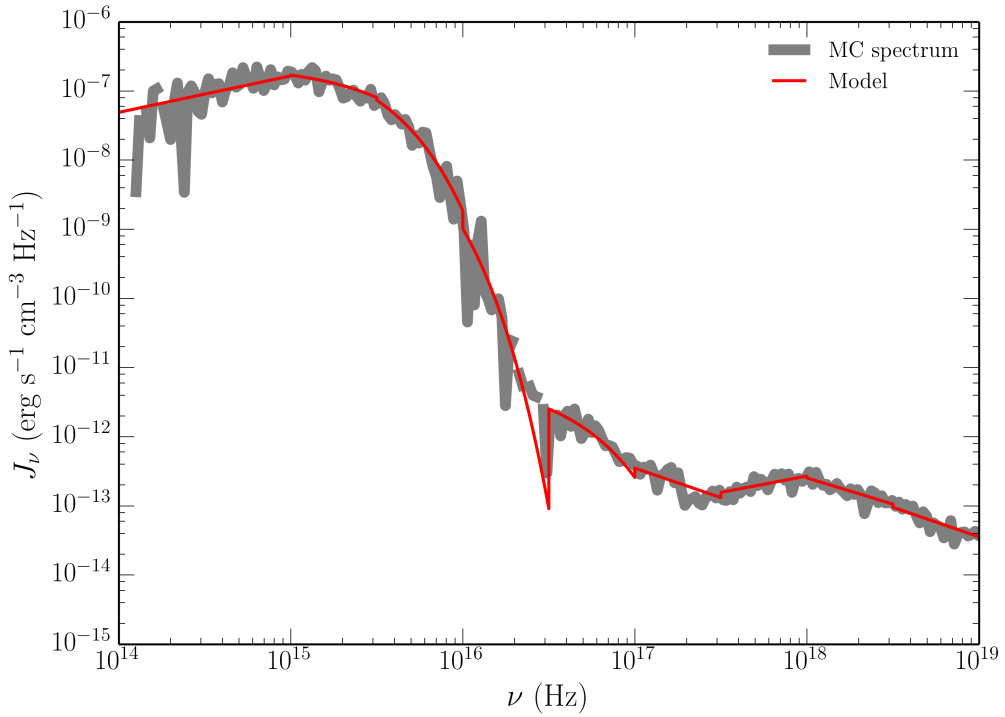


FIGURE 3.5: An example of a modeled spectrum in PYTHON compared to the recorded MC spectrum, from an individual cell in an AGN model.

Recombination rate coefficients are then obtained from either tabulated data (see section 3.7) or, failing that, the Milne relation (equation 3.59).

The rate matrix used to calculate the ionization state of simple-atoms can now be populated. An example rate matrix for H and He would be

$$\begin{bmatrix} 1 & 1 & 0 & 0 & 0 \\ \gamma_{H\text{I},H\text{II}}^S & -n_e \alpha_{H\text{II},H\text{I}} & 0 & 0 & 0 \\ 0 & 0 & 1 & 1 & 1 \\ 0 & 0 & \gamma_{He\text{I},He\text{II}}^S & -n_e \alpha_{He\text{II},He\text{I}} - \gamma_{He\text{II},He\text{III}}^S & 0 \\ 0 & 0 & 0 & \gamma_{He\text{II},He\text{III}}^S & -n_e \alpha_{He\text{III},He\text{II}} \end{bmatrix} = \begin{bmatrix} N_{H\text{I}} \\ N_{H\text{II}} \\ N_{He\text{I}} \\ N_{He\text{II}} \\ N_{He\text{III}} \end{bmatrix} = \begin{bmatrix} n_H \\ 0 \\ n_{He} \\ 0 \\ 0 \end{bmatrix}. \quad (3.98)$$

Thus the problem is very similar to solving for level populations in macro-atoms, except that it is bounded differently.

The rate matrix method with spectral model for the mean intensity is used in chapter 5 of this thesis, whereas for chapter 4 the approximate ML93 scheme is used. Regardless of ion mode, the relative excitation fractions of simple-atoms within each ionization

stage of a given species are estimated via a modified (dilute) Boltzmann equation (equation 3.14). This equation is approximate, and in general this approximation is not good. We therefore endeavour to treat any species in which the excitation state of the ions is thought to be important in determining either the ionizing radiation field, or emergent spectrum, as macro-atoms.

3.5 Heating And Cooling Balance

I have already given the estimators used to calculate heating and cooling rates in the plasma. These are not only used in the creation and elimination of k -packets, but also in the heating and cooling balance carried out in PYTHON to achieve a self-consistent temperature structure in the wind.

At the end of each ionization cycle, the code has stored a new set of MC estimators for radiative heating of the plasma. We then assume that each cell is in thermal equilibrium then the appropriate electron temperature is simply the value of T_e that is a solution to the equation

$$\mathcal{H}_{tot} - \mathcal{C}_{tot}(T_e) = 0, \quad (3.99)$$

where \mathcal{H}_{tot} and \mathcal{C}_{tot} are the total heating and cooling rates in the plasma. A number of checks are in place to ensure numerical stability, namely a maximum temperature and a maximum change in temperature from cycle to cycle. This is especially important in cases where the initial guess at wind temperature is far from the true value.

3.5.1 Convergence

PYTHON always runs a fixed number of ionization cycles, rather than terminating when a convergence criterion is reached. As a result, it is up to the user to check that the simulation is converged. An individual cell is considered converged when a) the temperature stops changing significantly, i.e. both T_R and T_e satisfy

$$\frac{|T_{new} - T_{old}|}{T_{new} + T_{old}} < 0.05, \quad (3.100)$$

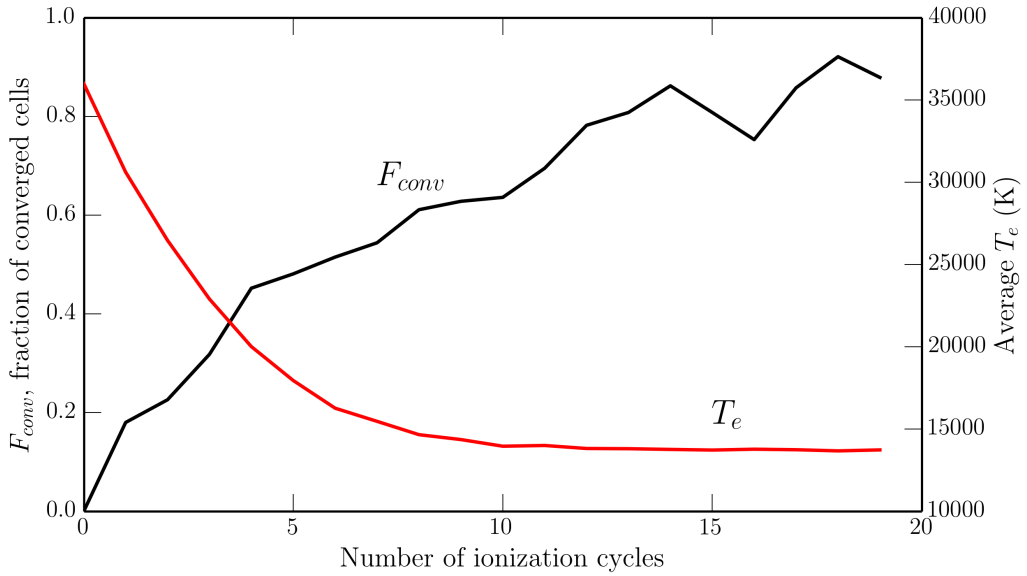


FIGURE 3.6: The average temperature and fraction of converged cells in a typical CV model, shown as a function of the number of ionization cycles completed.

and b) the heating and cooling rates are well balanced such that

$$\frac{|\mathcal{H}_{tot} - \mathcal{C}_{tot}|}{\mathcal{H}_{tot} + \mathcal{C}_{tot}} < 0.05. \quad (3.101)$$

These criteria could doubtless be improved, but they are nonetheless a good way of ensuring that thermal and radiative equilibrium holds in the plasma. An example of how the average temperature and fraction of converged cells changes over the course of the ionization cycles in a typical CV model is shown in Fig. 3.6.

3.6 Spectral Cycles

The primary output from PYTHON is a synthetic spectrum over a specific wavelength range produced at user-specified viewing angles. This spectrum is produced in a separate cycle from the calculation of the ionization state as it is concerned with producing detailed, high-resolution spectra in a specific wavelength regime that can then be compared to observations.

The code utilises a variance reduction technique in order to minimise the amount of time spent in the portion of the code. This technique is based on a similar method implemented by (Woods 1991) and is known in the code as the ‘extract’ method. This

method works by tracking photon packets until they scatter or interact with the plasma, according to the procedure described in section 3.2.3. At the scattering location, the optical depth the photon would experience were it to escape to infinity along each requested viewing angle, $\tau_{extract}(\theta_i)$, is calculated. The spectrum at each viewing angle θ_i is then incremented by an amount

$$\Delta L = w f(\theta_i) \exp(-\tau_{extract}(\theta_i)), \quad (3.102)$$

where w is the weight of the photon and $f(\theta_i)$ is a weighting proportional to the probability that the photon would have scattered in direction θ_i . Once this value has been added to the corresponding wavelength bin then the photon proceeds as normal in its new random direction.

In the alternative ‘live or die’ method this extraction procedure is not carried out and a user simply has to run enough escaping photons so that enough will happen to fall into the angle bins requested. This is clearly significantly less efficient. A comparison between the two methods is shown in figure 3.7 for a standard CV model, showing that the spectrum produced is identical in shape but with significantly higher signal-to-noise (for fixed number of cycles) in the ‘extract’ case.

3.6.1 Macro-atom Emissivity Calculation

In order to preserve the philosophy that a detailed spectrum is calculated in a limited wavelength regime, PYTHON carries out a macro-atom emissivity calculation before the spectral cycles. The aim of this step is to calculate the luminosity contributed by macro-atoms – equivalent to the total amount of reprocessed emission – in the wavelength range being considered. This process can be very computationally intensive, especially if the wavelength regime being simulated has very little emission from bound-free and line processes in the wind, but the overall broadband emissivity is high.

During the ionization cycles, the amount of energy absorbed into k -packets and every macro-atom level is recorded using MC estimators. Once the ionization cycles are finished and the model has converged, these absorption energies are split into a certain number of packets and tracked through the macro-atom machinery until a deactivation occurs. When this happens, the emissivity of the level the macro-atom de-activated

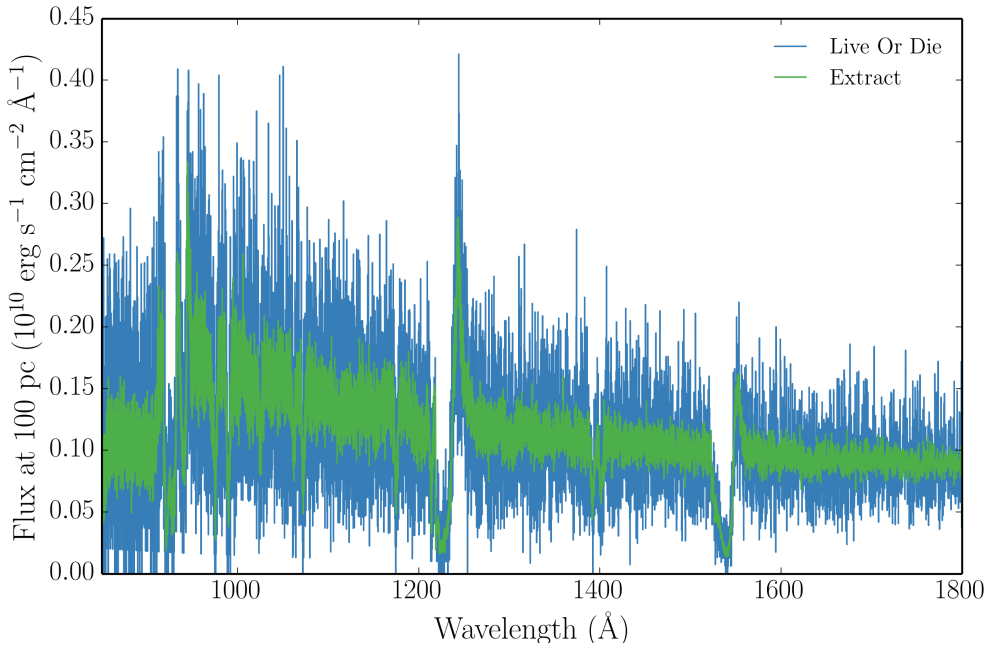


FIGURE 3.7: A synthetic spectrum after 30 spectral cycles with 100,000 photons from simple CV wind model at a 60° viewing angle. Spectra produced with both the extract and live or die modes are shown. The effectiveness of the extract variance reduction technique can be clearly seen, and we can see that the spectral shape is unaltered.

from is incremented if the packet lies in the requested wavelength range. If it does not, then the packet is thrown away. It is easy to see how what is essentially a MC rejection method can be an inefficient way of sampling this parameter space. Fortunately, this problem is parallelisable (see section 3.9.1).

Once the emissivities have been calculated then the spectral synthesis can proceed. This is done in a different way to the ionization cycles. Photons are generated from the specified photon sources over the required wavelength range, but are now also generated according to the calculated macro-atom and k -packet emissivities in each cell. These photons are ‘extracted’ according to the procedure outlined above. To now ensure that radiative equilibrium holds, any photon that interacts with a macro-atom or k -packet is immediately destroyed. The photons are tracked and extracted as normal until they escape the simulation, and resonant scatters are dealt with by a combination of macro-atom photon production and destruction.

3.7 Atomic Data

One of the big challenges in building reliable photoionization and radiative transfer lies in the acquisition of accurate and complete atomic datasets. All of the rates described so far contain a term, such as the oscillator strength or dimensionless collision strength, that is dependent purely on the atomic physics associated with the transition. These quantities can be measured in laboratory experiments, or predicted from atomic structure codes which derive the atomic physics from quantum theory.

Throughout this work, I have used very similar atomic data to that described by LK02 and H13. Elements included are H, He, C, N, O, Ne, Na, Mg, Al, Si, S, Ar, Ca and Fe, although this can be easily be adapted. Solar abundances from [Verner et al. \(1994\)](#) are adopted, and ionization potentials and ion multiplicities are from [Verner et al. \(1996b\)](#). Line information for simple-atoms is obtained from ([Verner et al. 1996b](#)) ($\sim 5,000$ lines) and ([Kurucz & Bell 1995](#)) ($\sim 55,000$ lines). The level information for simple-atoms is constructed from the line lists using the technique described by ?.

Radiative recombination rate coefficients are taken from the CHIANTI database version 7.0 ([Dere et al. 1997](#); [Landi et al. 2012](#)). Ground state recombination rates from [Badnell \(2006\)](#) are adopted where available, and otherwise the code defaults to calculating recombination rates from the Milne relation. Free-free Gaunt factors are from [Sutherland \(1998\)](#).

3.7.1 Macro-atom Level and Line Data

A 20-level model H atom was incorporated into PYTHON by SDL05, and includes line oscillator strengths from [Menzel & Pekeris \(1935\)](#). This model atom is only split according to principle quantum number n , and it is thus assumed that collisions in the plasma will cause the l -subshells to be populated according to statistical weights. This is known as *l-mixing* and is a good approximation for hydrogen in dense astrophysical plasmas due to the near degeneracy of the subshell energy levels.

In order to correctly model He recombination lines in CVs and AGN, such as the prominent He II 1640Å line, I expanded the atomic dataset such that PYTHON now contains all the atomic data needed for a He macro-atom. This data was obtained from TOPBASE,

with the exception that some of the line wavelengths were inaccurate and modified to the experimental values from the National Institute of Standards and Technology (NIST²). He I is split into l and s subshells so as to correctly model the singlet and triplet lines observed in many optical spectra. He II is assumed to be l -mixed, as it is hydrogenic.

For CV modelling (chapter 4), I used the full 20 level hydrogen atom, with 53 levels of He I up to principle quantum number 10, and 10 levels of He II. This can provide a performance hit in macro-atoms, but is necessary when modelling recombination lines from upper levels close to the continuum energy. In quasar models (chapter 5) this is not as important, and the plasma is generally more ionized. There, a 10 level hydrogen atom was used and He I was treated with only the ground state for stability – this simplification had no effect on the temperature structure of the wind or emergent spectrum.

3.7.2 Photoionization Cross-sections

Photoionization cross-sections are from TOPBASE ([Cunto et al. 1993](#)) and [Verner et al. \(1996a\)](#). Where possible, I use TOPBASE photoionization cross-sections. For macro-atoms, these cross-sections are partial and represent the cross-section for a photoionization from a given *level*. We neglect photoionizations to excited configurations of the upper ion. For simple-atoms they are from the ground state. The TOPBASE cross-sections have two major drawbacks in that they do not extend to particularly high energies

In order to improve the TOPBASE cross-sections, I extrapolated them to larger energies. This was done by finding the slope, in log-log space, of the cross-section at the maximum energy, and extrapolating to 100 keV. In some cases, the slope near the maximum energy was anomalous due to resonances or similar structure in the cross-section, or possibly simply due to unknown problems in the TOPBASE calculations. These cases were identified by eye, and instead a ν^{-3} extrapolation was applied. The results of this extrapolation on the soft X-rays in an AGN model are shown in figure 3.8. Where previously there was a sharp, unphysical edge, there is now a smooth recovery to an X-ray power law we expect. I also manually adjusted the threshold energies in some cases to match the more accurate values from [Verner et al. \(1996a\)](#).

²<http://www.nist.gov/>

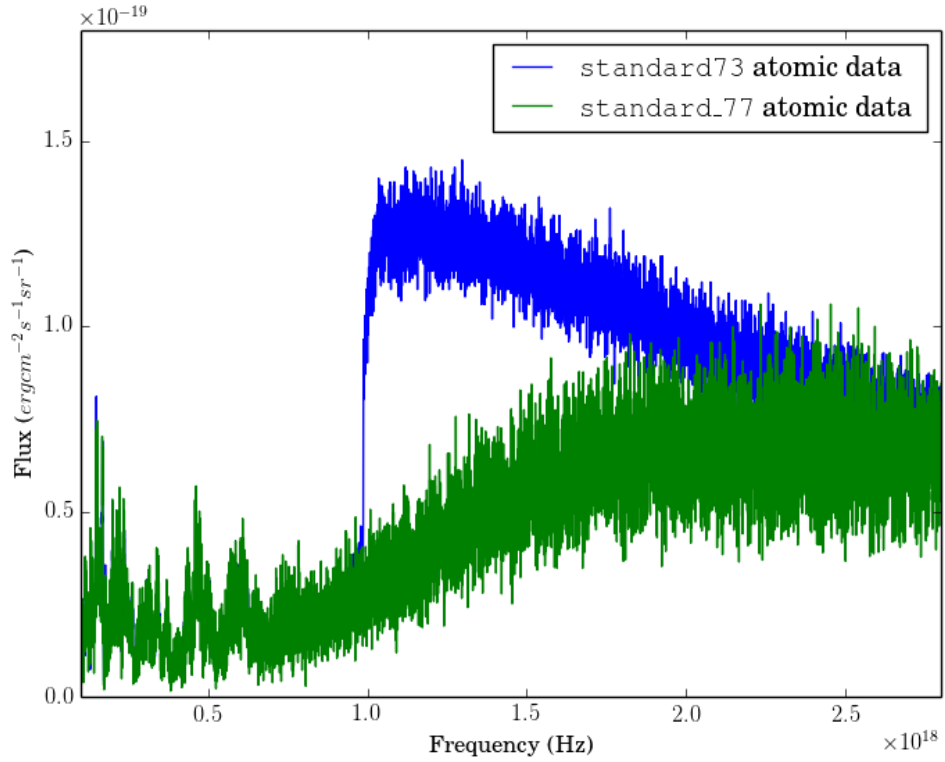


FIGURE 3.8: A comparison of the soft X-ray regime of the H13 model, with two different datasets. standard73 is the dataset with old, unextrapolated cross-sections and standard77 instead includes extrapolated cross-sections as described in the text.

3.8 Code Validation

The main challenge for high performance scientific computing can be elegantly summarised by Ferland’s (2002) epitaph, ‘*Reliability in the face of complexity*’. I have already delved into some of the complexity in this case, so it is important to assess whether the code is also reliable before I present results.

3.8.1 Testing against Cloudy

CLOUDY is a spectral synthesis and photoionization code used to simulate the emergent spectrum and ionization conditions in nebulae and other plasma environments. As a result, it uses many of the same techniques as PYTHON in order to compute ionization states, level populations and heating and cooling rates, and represents an excellent comparison tool. PYTHON has been tested extensively against CLOUDY in the past; some of these successful tests can be found in H13 and LK02.

Figs. 3.9 to 3.14 show a series of ionization plots with relative ion fractions plotted as a function of ionization parameter, U . The ionization parameter is a useful way to parameterise the ionization state of a plasma, and is given by

$$U = \frac{4\pi}{n_H c} \int_{13.6\text{eV}/h}^{\infty} \frac{J_{\nu} d\nu}{h\nu}. \quad (3.103)$$

In PYTHON, the ionization parameter in a cell is calculated via a MC estimator, such that

$$U_{\text{PYTHON}} = \frac{1}{c V n_H} \sum_i^{photons} \frac{w_i \Delta s}{h\nu}. \quad (3.104)$$

This test is designed to check that PYTHON still agrees well with CLOUDY when we turn on the full macro-atom machinery. The calculations are conducted using the same incident SEDs, densities and abundances, and PYTHON is operated in 1D, thin shell mode to simulate an optically thin plasma and facilitate comparison with CLOUDY. I have shown two separate ionization modes from PYTHON: standard mode, in which nothing is treated as a macro-atom and the spectral model ionization scheme of H13 is used to calculate ion fractions, and hybrid mode in which H and He are treated as macro-atoms and their level populations and ion fractions are solved using MC estimators according to the routine described in section 3.3.6. Thus, in both cases the simple-atoms have their populations calculated using the H13 scheme.

In general, the calculated fractions are in excellent agreement, with a few exceptions. The first problem is with He at low ionization parameters (see Fig. 3.10), where there is a discrepancy between the macro-atom solution and the standard mode solution. This is due to differences in the calculated recombination rate. In macro-atom mode, this is done using the Milne relation for all the bound-free jumps that have been identified, which currently includes all transitions from the lower ion but ignores transitions to excited states of the upper ion. However, in standard mode PYTHON uses the recombination rates from Chianti, which represent a weighted sum over all the possible bound-free transitions, and are thus in some ways more complete. Nevertheless, the macro-atom scheme is self-consistent, in that all photoionization pathways have a matching recombination pathway, and the level populations are calculated much more accurately. Furthermore, the models presented later generally have $\log U \gtrsim -2$, where the calculation agrees well with CLOUDY and standard mode. The second problem lies in Fe, where there can be quite large differences between PYTHON and CLOUDY. This is mainly due to Auger

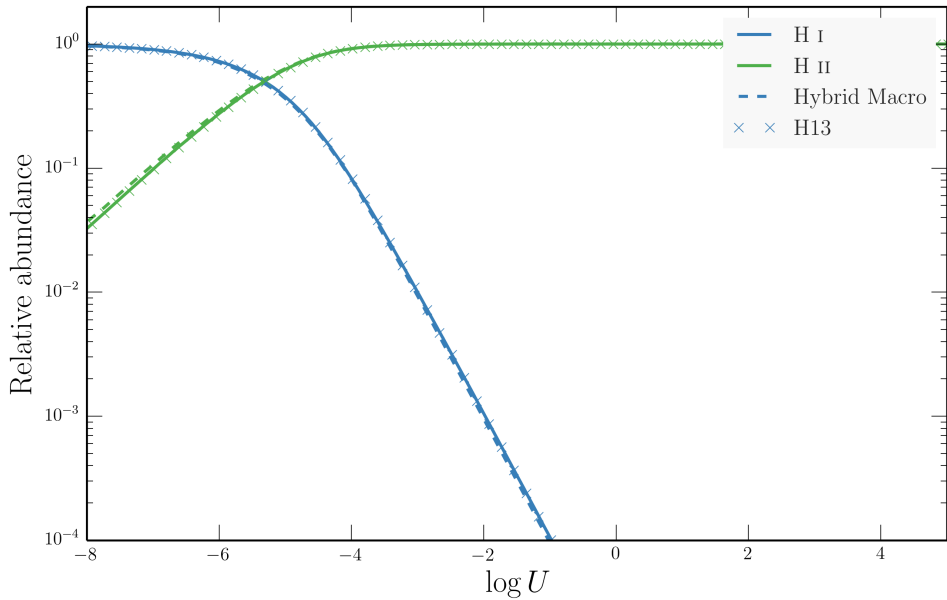


FIGURE 3.9: Relative ion fractions as a function of ionization parameter from the hybrid macro-atom scheme, with Hydrogen and Helium treated as a full macro-atom, compared to both CLOUDY and PYTHON in simple-atom only mode.

ionization and charge exchange and has recently been improved in PYTHON. The effect on quasar models is discussed in chapter 5.

3.8.2 Macro-atom testing against Tardis and theory

TARDIS is a 1D photoionization and radiative transfer designed to model SNe in a quick and easy python package, and is described in detail by [Kerzendorf & Sim \(2014\)](#). Although TARDIS is simpler in terms of geometry, it has many of the same capabilities of PYTHON and thus makes for an excellent comparison.

Fig. 3.15 shows the results of two code tests. In the top panel, I show a comparison of the Balmer series emissivities as predicted by PYTHON in the l-mixed Case B limit against the analytical calculations by [Seaton \(1959\)](#). Both calculations are calculated at $T_e = 10,000\text{K}$. Case B is an approximation commonly used in nebular astrophysics (see e.g. [Osterbrock 1989](#)) in which one assumes that all line transitions are optically thin, except for the Ly α transition, which is taken as optically thick. Thus, this test comparison is carried out using a thin shell of plasma in which the escape probabilities, β_{uj} are artificially set to 1 in all transitions except Ly α , which has its β_{uj} set to 0.

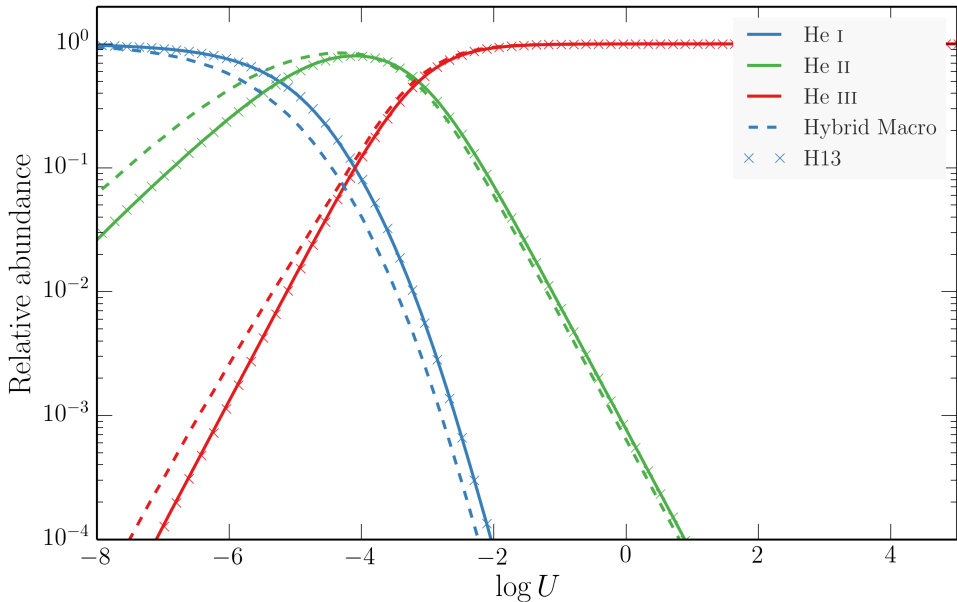


FIGURE 3.10: As figure 3.9, but for Helium.

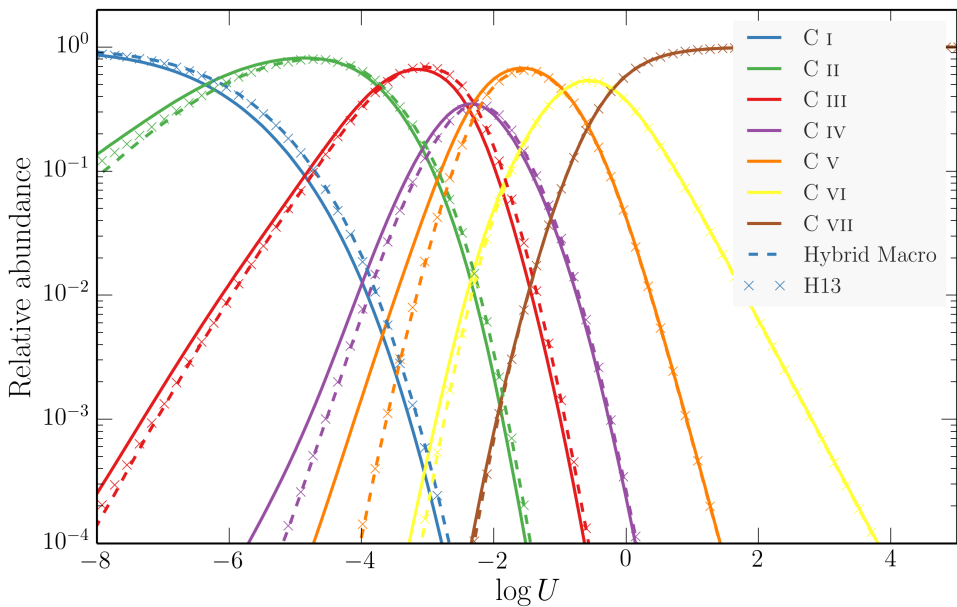


FIGURE 3.11: As figure 3.9, but for Carbon.

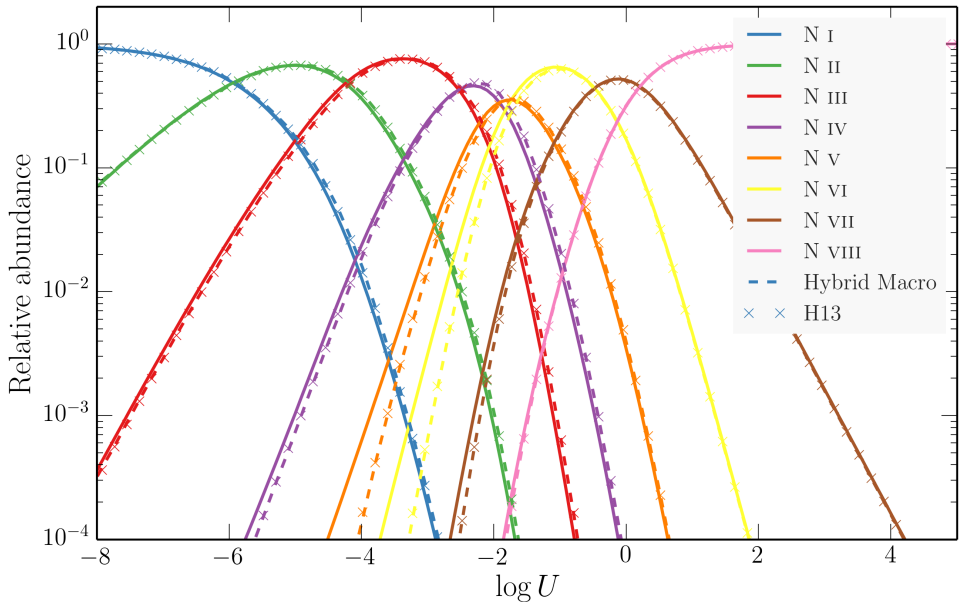


FIGURE 3.12: As figure 3.9, but for Nitrogen.

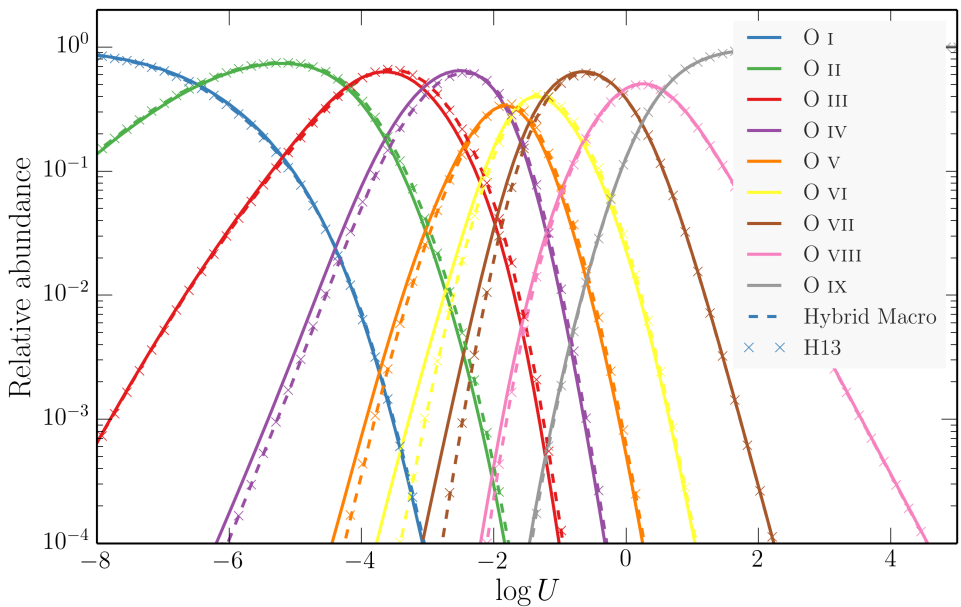


FIGURE 3.13: As figure 3.9, but for Oxygen.

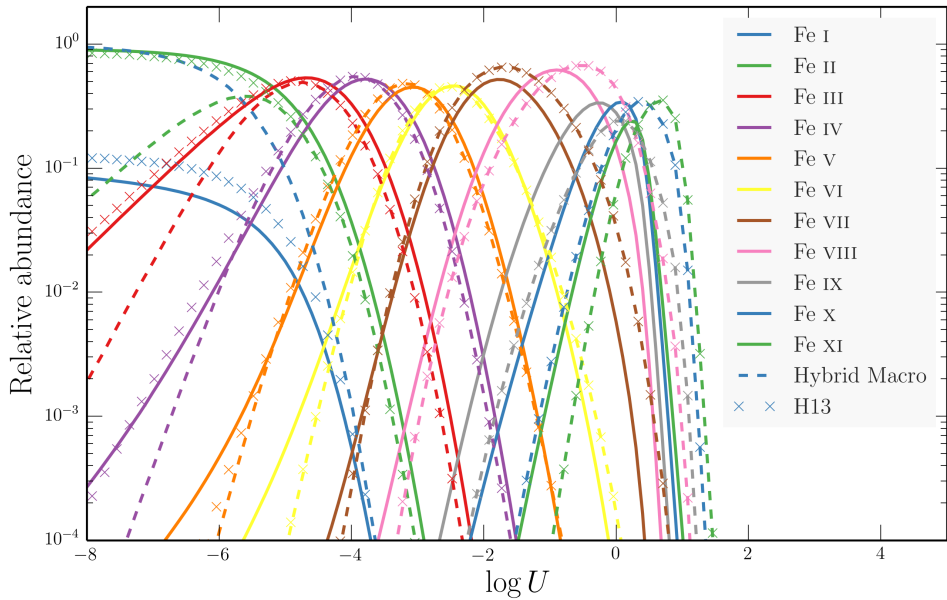


FIGURE 3.14: As figure 3.9, but for the first 11 ionization stages of Iron.

The bottom panel shows a comparison of He I level populations (the most complex ion currently treated as a macro-atom) between PYTHON and TARDIS models. The calculation is conducted with physical parameters of $n_e = 5.96 \times 10^4 \text{ cm}^{-3}$, $T_e = 30,600\text{K}$, $T_R = 43,482\text{K}$ and $W = 9.65 \times 10^{-5}$. Considering the two codes use different atomic data and TARDIS, unlike PYTHON, currently has a complete treatment of collisions between radiatively forbidden transitions, the factor of < 2 agreement is encouraging.

Fig. 3.16 shows a comparison between TARDIS and PYTHON synthetic spectra from a simple 1D SN model. This comparison was originally presented by Kerzendorf & Sim (2014), but I have since then discovered a bug in the Doppler shifting routine in PYTHON, introduced around PYTHON 76, which was present in this test. Fixing this issue leads to slightly better agreement between the two codes. The model involves a full computation of the ionization state in the ML93 mode, and, although run in 1D, still tests most of the radiative transfer machinery of the code. The spectra are in good agreement, considering there are differences in their excitation treatments and atomic data. This comparison is particular encouraging when we consider that Kerzendorf & Sim (2014) also show comparisons with other SN codes such as ARTIS (Kromer & Sim 2009).

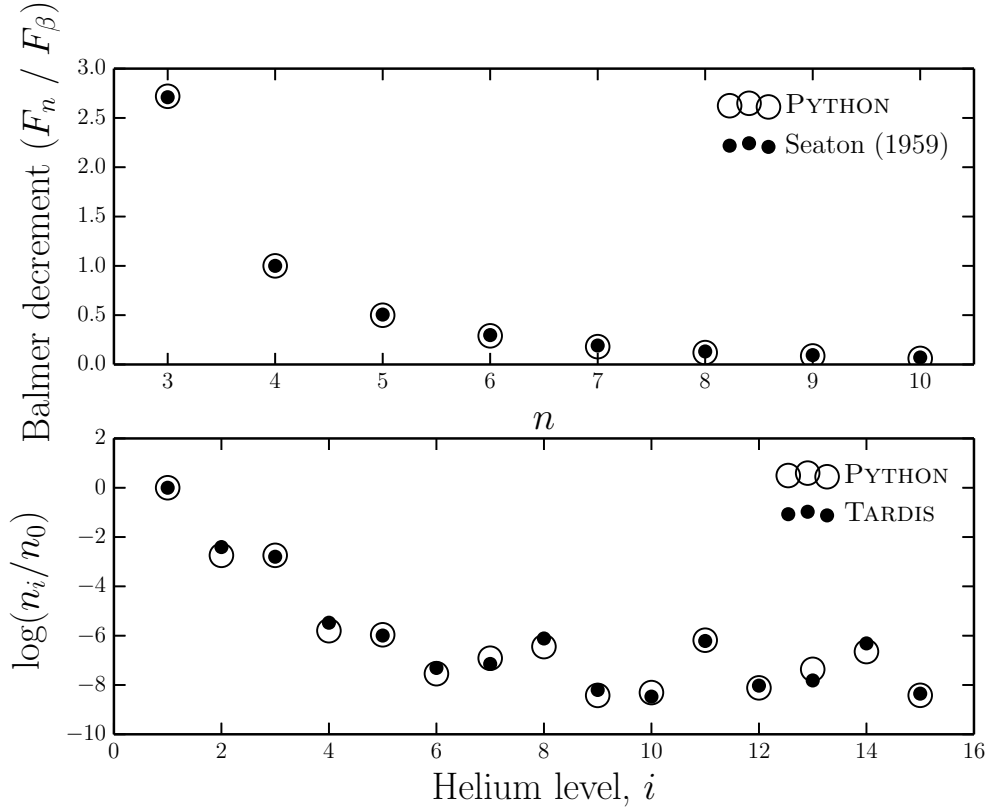


FIGURE 3.15: *Top Panel:* ‘Case B’ Balmer decrements computed with PYTHON compared to analytic calculations by Seaton (1959). Both calculations are calculated at $T_e = 10,000\text{K}$. *Bottom Panel:* a comparison of He I level populations (the most complex ion we currently treat as a macro-atom) between PYTHON and TARDIS models. The calculation is conducted in thin shell mode with physical parameters of $n_e = 5.96 \times 10^4 \text{ cm}^{-3}$, $T_e = 30,600\text{K}$, $T_R = 43,482\text{K}$ and $W = 9.65 \times 10^{-5}$.

3.8.3 Testing line transfer modes

The simple-atom approach has a few drawbacks. The first is that it cannot deal well with lines in which the lower level is an excited state, such as the Balmer lines. This means that it is important to treat recombination lines using the macro-atom approach. The second is that a bound-free continuum activation, in normal terms a photoionization, is followed by a radiative deactivation with the frequency chosen assuming a hydrogenic cross-section. This does not well represent reality where recombining electrons tend to do so to a variety of levels and so there is a gradual redshifting of the radiation field, and also atoms are in general not hydrogenic. This problem has wider implications than the first, as it could mean that the global ionization and temperature structure of the wind was affected, if, for example, opacities due to elements such as C, N and O were important in determining the ionizing radiation field.

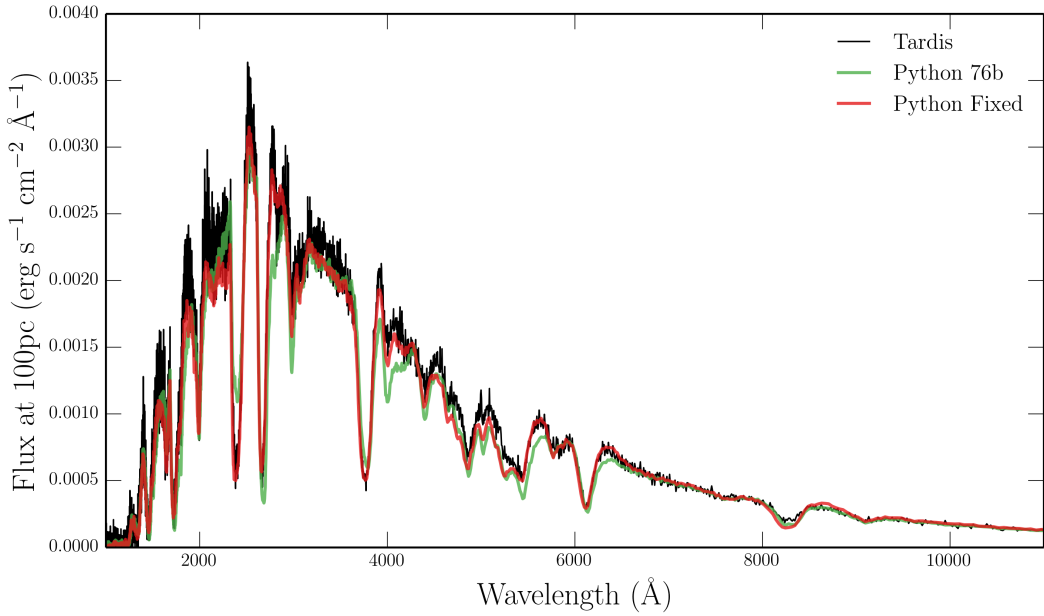


FIGURE 3.16: Comparison between TARDIS and PYTHON synthetic spectra from a simple 1D supernova model. A bug in Doppler shifting of photons was discovered around PYTHON 76, meaning that the code now gives even better agreement than presented in Kerzendorf & Sim 2014.

To verify that this is a second order effect, I have shown a test in Fig. 3.17 in I have tested the indivisible line transfer mode against weight reduction mode, which does not make this approximation. The model shown is the fiducial BAL quasar model from H13, where modelling the absorption effect on the ionizing radiation field properly is important due to the stratified and self-shielding flow. As long as H and He are treated as macro-atoms, the agreement between the modes is good and the ionization structure in the flow is very similar. Many of the differences in the ionization structure in the flow are actually caused by the improved treatment of the Balmer and Lyman continua.

3.9 Code Maintenance and Version Control

As part of the expansion of the team working on PYTHON I was responsible for bringing the code under the auspices of a robust version control system. Thanks to these efforts, the code is now hosted on GitHub at <https://github.com/agnwinds/python/>. Our team uses a Pull & Fork model for collaborative code development, in which major changes are made in a forked repository before the developer submits a ‘Pull request’ to the main repository. To test the code, we use a combination of Travis CI build tests –

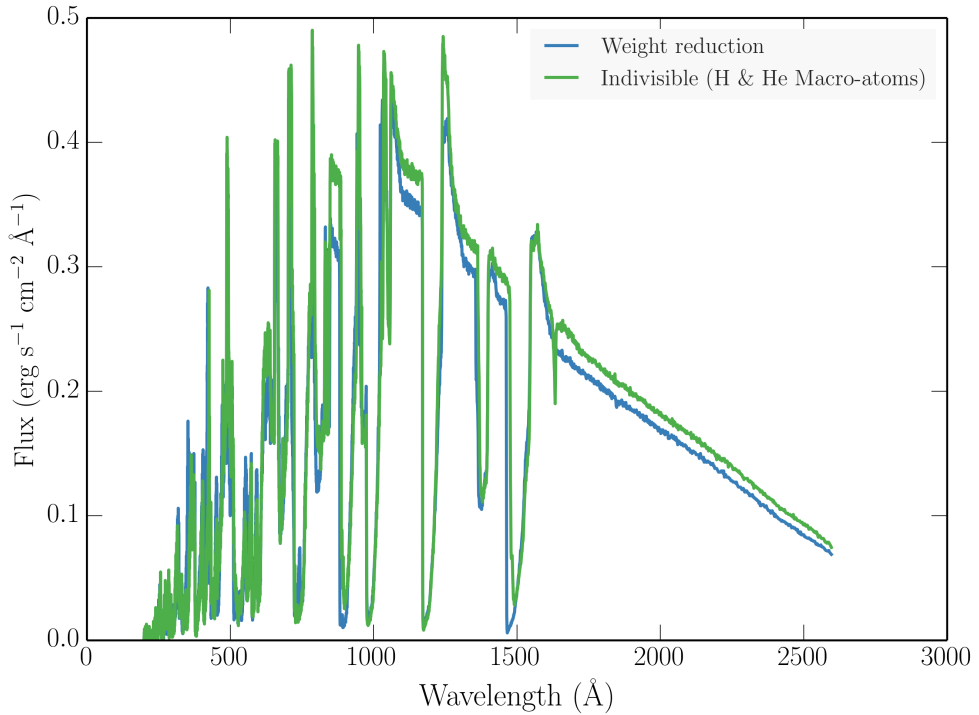


FIGURE 3.17: A comparison between weight reduction and line transfer mode. The model



FIGURE 3.18: Commit history from Feb 3, 2013 to Feb 29, 2016, showing the regular code development that makes version control such a necessity to a collaborative code project. Produced using the Github API and plotting capability.

run per commit to the upstream repository – and our own test suite which is run every night on a multi-core server.

3.9.1 Parallelisation

Including macro-atoms in a simulation can have a significant impact on runtime, especially when simulating dense regions of plasma. By way of example, the CV model presented by LK02 takes approximately 118s to run one ionization cycle with 10^6 photons. One of the macro-atom models presented in chapter 4 takes 5651s to complete the same task.

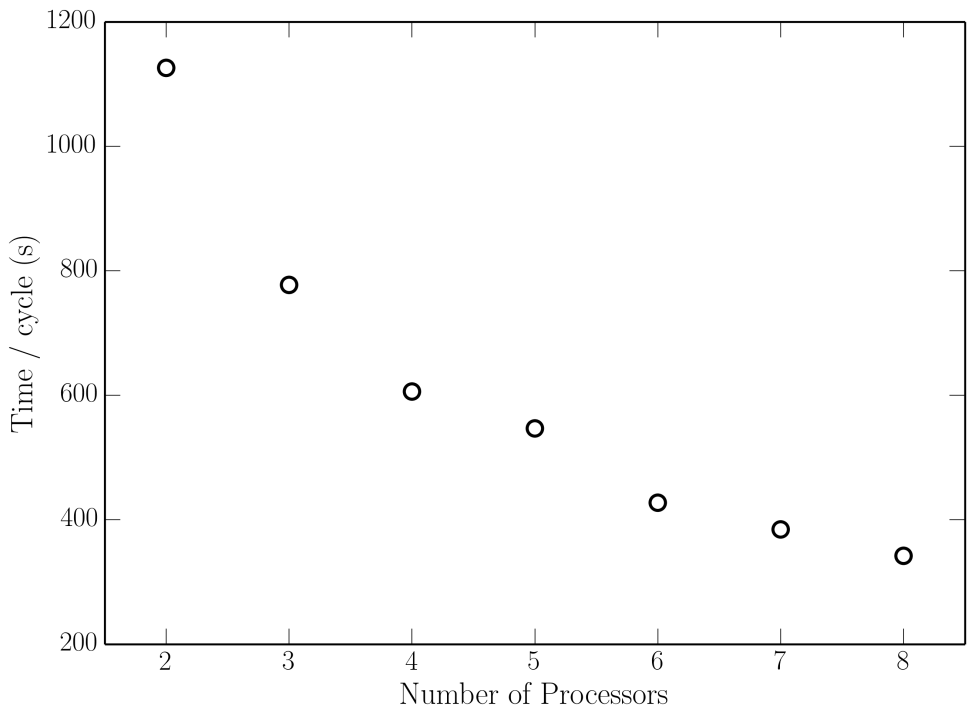


FIGURE 3.19: Total runtime per cycle for an AGN run as a function of the number of processors.

Fortunately, MCRT codes are intuitively parallelisable, as is the macro-atom emissivity calculation described above, as operations on cells or photons can simply be divided up between processors. PYTHON is parallelised using an open source Message Passing Interface (MPI) implementation known as Open MPI ([Gabriel et al. 2004](#)). This library provides the core functions needed in order to share out computing tasks among a series of parallel processors with distributed memory. The parallelised elements of PYTHON include the photon propagation, updating of wind ionization and temperature structure and calculation of macro-atom emissivities. As a result, this involves a reasonable amount of book-keeping in that the radiation field estimators must be communicated between threads so as to correctly account for all the photons that have interacted with a given cell. I have been responsible for all of the parallelisation implemented that is specific to the macro-atom routines.

[Fig. 3.19](#) shows the effect of parallelising a run. Due to the nature of MCRT, it is possible to achieve significant decrease in overall runtime. This improvement was crucial in order to be able to run the simulation grids used for chapters 4 and 5.

Chapter 4

The Impact of Accretion Disc Winds on the Optical Spectra of Cataclysmic Variables

This chapter is based on the publication:

Matthews J. H., Knigge C., Long K. S., Sim S. A., Higginbottom N., ‘The impact of accretion disc winds on the optical spectra of cataclysmic variables’, 2015, MNRAS, 450, 3331.

4.1 Introduction

Here, I present Monte Carlo radiative transfer simulations designed to assess the likely impact of accretion disc winds on the optical spectra of high-state CVs. More specifically, the goal is to test whether disc winds of the type developed to account for the UV resonance lines would also naturally produce significant amounts of optical line and/or continuum emission. In order to achieve this, I use the ‘macro-atom’ approach described in chapter 3. With this method, PYTHON is able to deal correctly with processes involving excited levels, such as the recombination emission observed in CV spectra.

The remainder of this paper is organized as follows. I begin by describing the photon sources and input SED used in this modelling. In section 4.2, I present spectra simulated

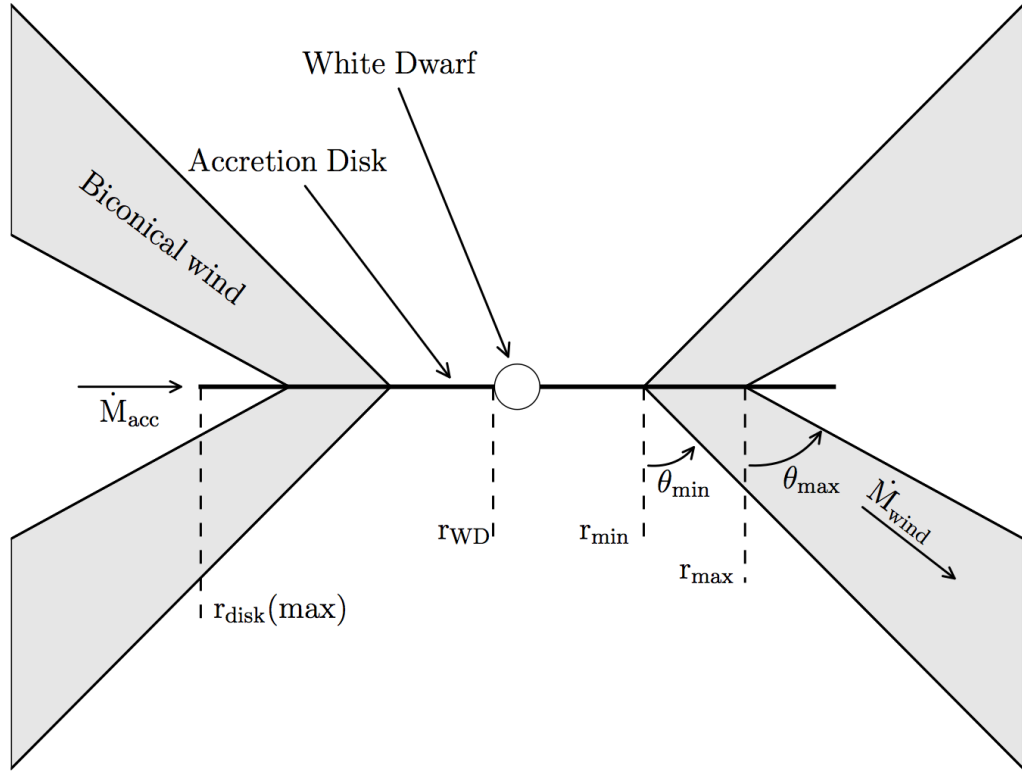


FIGURE 4.1: Cartoon illustrating the geometry and kinematics of the benchmark CV wind model.

from the benchmark model employed by LK02. In section ??, I present a revised model optimized for the optical waveband, before sum summarising the findings in section 4.5.

4.1.1 Sources and Sinks of Radiation

The net photon sources in our CV model are the accretion disc, the WD and, in principle, a boundary layer with user-defined temperature and luminosity. All of these radiating bodies are taken to be optically thick, and photons striking them are assumed to be destroyed instantaneously. The secondary star is not included as a radiation source, but is included as an occulting body. This allows us to model eclipses. Finally, emission from the wind itself is also accounted for, but note that this assumes the outflow is in radiative equilibrium. Thus all of the heating of the wind, as well as its emission, is ultimately powered by the radiation field of the net photon sources in the simulation. In the following sections, I will describe the treatment of these system components in slightly more detail.

4.1.1.1 Accretion disc

PYTHON has some flexibility when treating the accretion disc as a source of photons. The disc is broken down into annuli such that each annulus contributes an equal amount to the bolometric luminosity. We take the disc to be geometrically thin, but optically thick, and thus adopt the temperature profile of a standard [Shakura & Sunyaev \(1973\)](#) α -disc. An annulus can then be treated either as a blackbody with the corresponding effective temperature or as a stellar atmosphere model with the appropriate surface gravity and effective temperature. Here, blackbodies are used during the ionization cycles and to compute our Monte Carlo estimators. The input SED for the ionization cycles is shown in Fig. ?? However, during the spectral synthesis stage of the simulation stellar atmosphere models are used. This produces more realistic model spectra and allows us to test if recombination emission from the wind base can fill in the Balmer jump, which is always in absorption in these models. Our synthetic stellar atmosphere spectra are calculated with SYNSPEC¹ from either Kurucz ([Kurucz 1991](#)) atmospheres (for $T_{eff} \leq 50,000$ K) or from TLUSTY ([Hubeny & Lanz 1995](#)) models (for $T_{eff} > 50,000$ K).

4.1.1.2 White Dwarf

The WD at the center of the disc is always present as a spherical occulting body with radius R_{WD} in PYTHON CV models, but it can also be included as a source of radiation. In the models presented here, the WD is treated as a blackbody radiator with temperature T_{WD} and luminosity $L_{WD} = 4\pi R_{WD}^2 \sigma T_{WD}^4$.

4.1.1.3 Boundary Layer

It is possible to include radiation from a boundary layer (BL) between the disc and the WD. In PYTHON, the BL is described as a blackbody with a user-specified effective temperature and luminosity. The models presented here initially follow LK02 in setting the BL luminosity to zero. However, the influence of the BL on the heating and cooling balance in the wind, as well as the emergent spectrum, is discussed further in section 4.4.

¹<http://nova.astro.umd.edu/Synspec43/synspec.html>

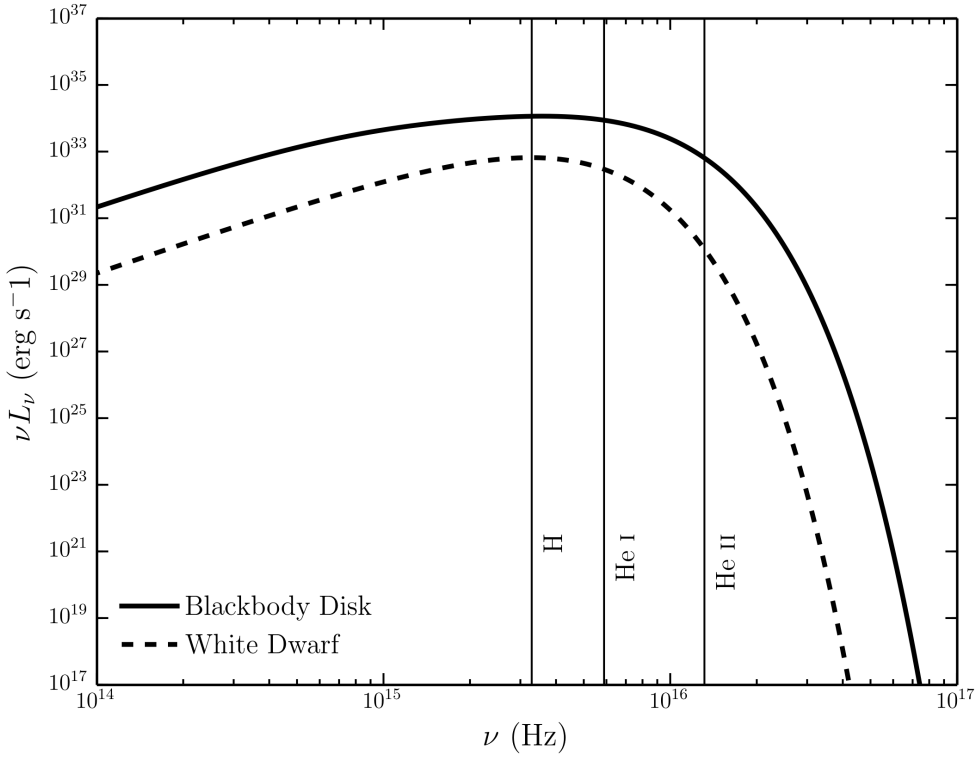


FIGURE 4.2: The spectral energy distribution of the accretion disc and white dwarf used in the ionization cycles for the CV modelling.

4.1.1.4 Secondary Star

The donor star is included in the system as a pure radiation sink, i.e. it does not emit photons, but absorbs any photons that strike its surface. The secondary is assumed to be Roche-lobe filling, so its shape and relative size are defined by setting the mass ratio of the system, $q = M_2/M_{WD}$. The inclusion of the donor star as an occulting body allows us to model eclipses of the disc and the wind. For this purpose, we assume a circular orbit with a semi-major axis a and specify orbital phase such that $\Phi_{orb} = 0$ is the inferior conjunction of the secondary (i.e. mid-eclipse for $i \simeq 90^\circ$).

4.2 A Benchmark disc Wind Model

Our main goal is to test whether the type of disc wind model that has been successful in explaining the UV spectra of CVs could also have a significant impact on the optical continuum and emission line spectra of these systems. In order to set a benchmark,

Parameter	Model Parameters	
	Model A	Model B
M_{WD}	$0.8 M_{\odot}$	
R_{WD}	7×10^8 cm	
T_{WD}	40,000 K	
M_2	-	$0.6 M_{\odot}$
q	-	0.75
P_{orb}	-	5.57 hr
a	-	$194.4 R_{WD}$
R_2	-	$69.0 R_{WD}$
\dot{M}_{acc}	$10^{-8} M_{\odot} yr^{-1}$	
\dot{M}_{wind}	$10^{-9} M_{\odot} yr^{-1}$	
r_{min}	$4 R_{WD}$	
r_{max}	$12 R_{WD}$	
$r_{disc}(\text{max})$	$34.3 R_{WD}$	
θ_{min}	20.0°	
θ_{max}	65.0°	
γ	1	
v_{∞}	$3 v_{esc}$	
R_v	$100 R_{WD}$	$142.9 R_{WD}$
α	1.5	4

TABLE 4.1: Parameters used for the geometry and kinematics of the benchmark CV model (model A), which is optimized for the UV band, and a model which is optimized for the optical band and described in section ?? (model B). For model B, only parameters which are altered are given - otherwise the model A parameter is used. P_{orb} is the orbital period (the value for RW Tri from Walker 1963 is adopted, see section 4.3.5) and R_2 is the radius of a sphere with the volume of the secondary's Roche lobe. Other quantities are defined in the text or Fig. 4.2. Secondary star parameters are only quoted for model B as we do not show eclipses with the benchmark model (see section 4.3.5).

we therefore begin by investigating one of the fiducial CV wind models that was used by SV93 and LK02 to simulate the UV spectrum of a typical high-state system. The specific parameters for this model (model A) are listed in Table 1. A key point is that the wind mass-loss rate in this model is set to 10% of the accretion rate through the disc. We follow SV93 in setting the inner edge of the wind (r_{min}) to $4 R_{WD}$. The sensitivity to some of these parameters is briefly discussed in section 4.3.4.

4.2.1 Physical Structure and Ionization State

Fig. 4.3 shows the physical and ionization structure of the benchmark disc wind model. The ionization parameter shown in the bottom right panel is given by equation 3.103. The ionization parameter is a useful measure of the ionization state of a plasma, as it evaluates the ratio of the number density of ionizing photons to the local H density.

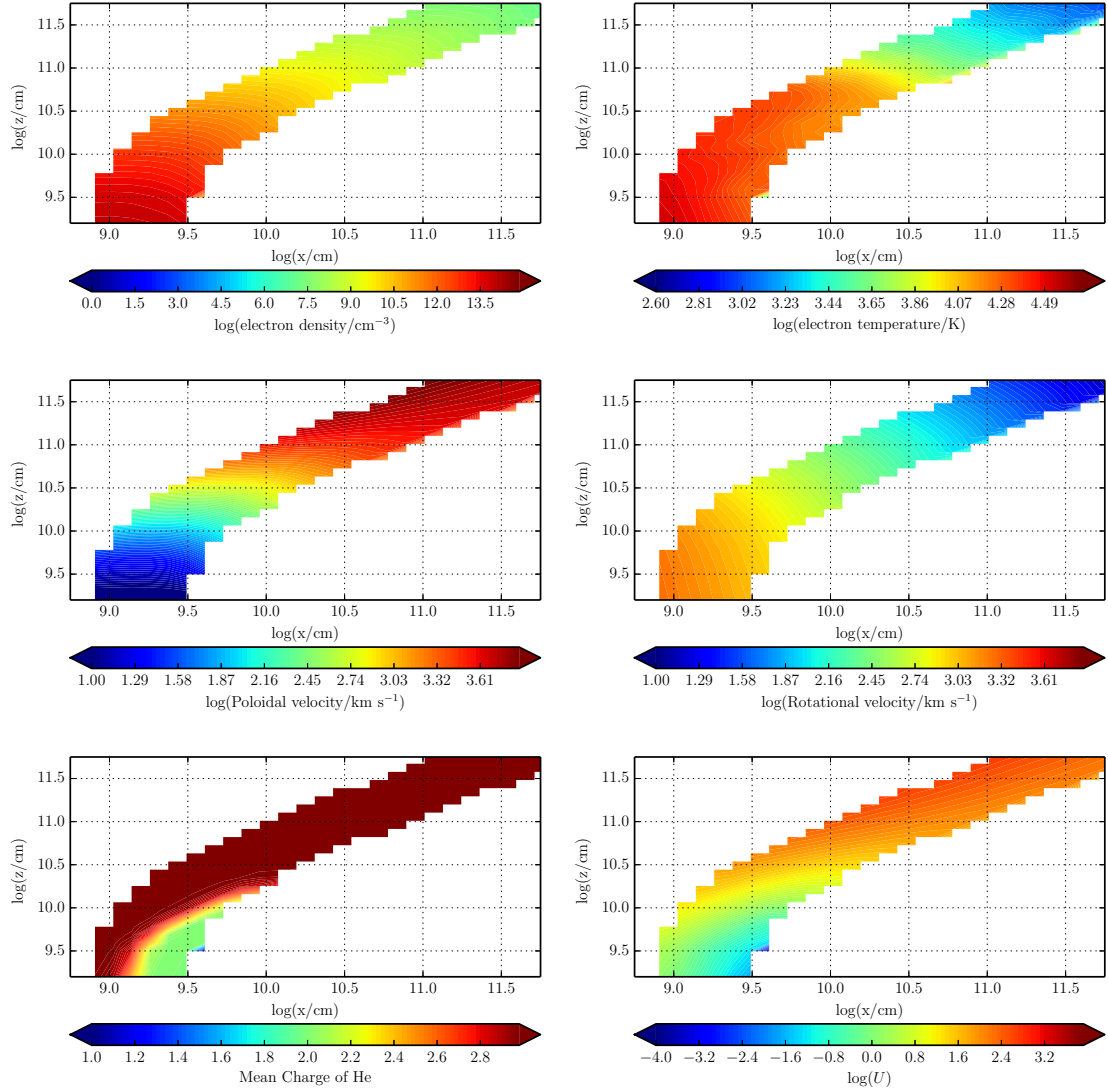


FIGURE 4.3: The physical properties of the wind – note the logarithmic scale. Near the disc plane the wind is dense, with low poloidal velocities. As the wind accelerates it becomes less dense and more highly ionized. The dominant He ion is almost always He III, apart from in a small portion of the wind at the base, which is partially shielded from the inner disc.

There is an obvious drop-off in density and temperature with distance away from the disc, so any line formation process that scales as ρ^2 – i.e. recombination and collisionally excited emission – should be expected to operate primarily in the dense base of the outflow. Moreover, a comparison of the rotational and poloidal velocity fields shows that rotation dominates in the near-disc regime, while outflow dominates further out in the wind.

The ionization equation used in the ‘simple atom’ approach used by LK02 (see section ??) should be a reasonable approximation to the photoionization equilibrium in the

benchmark wind model. Even though the macro-atom treatment of H and He does affect the computation of the overall ionization equilibrium, we would expect the resulting ionization state of the wind to be quite similar to that found by LK02. The bottom panels in Fig. 4.3 confirm that this is the case. In particular, He is fully ionized throughout most of the outflow, except for a small region near the base of the wind, which is shielded from the photons produced by the hot inner disc. In line with the results of LK02, CIV is the dominant C ion throughout the wind, resulting in a substantial absorbing column across a large range of velocities. As we shall see, this produces the broad, deep and blue-shifted CIV $\lambda 1550$ absorption line that is usually the most prominent wind-formed feature in the UV spectra of low-inclination nova-like CVs.

4.2.2 Synthetic Spectra

We begin by verifying that the benchmark model still produces UV spectra that resemble those observed in CVs. We do expect this to be the case, since the ionization state of the wind has not changed significantly from that computed by LK02 (see section 4.2.1). The left column of panels in Fig. 4.4 shows that this expectation is met: all of the strong metal resonance lines – notably N V $\lambda 1240$, Si IV $\lambda 1400$ and C IV $\lambda 1550$ – are present and exhibit clear P-Cygni profiles at intermediate inclinations. In addition, however, we now also find that the wind produces significant Ly α and He II $\lambda 1640$ emission lines.

Fig. 4.4 (right-hand panel) and Fig. 4.5 show the corresponding optical spectra produced for the benchmark model, and these do exhibit some emission lines associated with H and He. We see a general trend from absorption lines to emission lines with increasing inclination, as one might expect from our wind geometry. This trend is consistent with observations, as can be seen in Fig. 1. However, it is clear that this particular model does not produce all of the lines seen in observations of high-state CVs. The higher-order Balmer series lines are too weak to overcome the intrinsic absorption from the disc atmosphere, and the wind fails to produce any observable emission at low and intermediate inclinations. This contrasts with the fact that emission lines are seen in the optical spectra of (for example) V3885 Sgr (Hartley et al. 2005) and IX Vel (Beuermann & Thomas 1990, see also Fig. 1).

The emissivity of these recombination features scales as ρ^2 , meaning that they form almost entirely in the dense base of the wind, just above the accretion disc. Here,

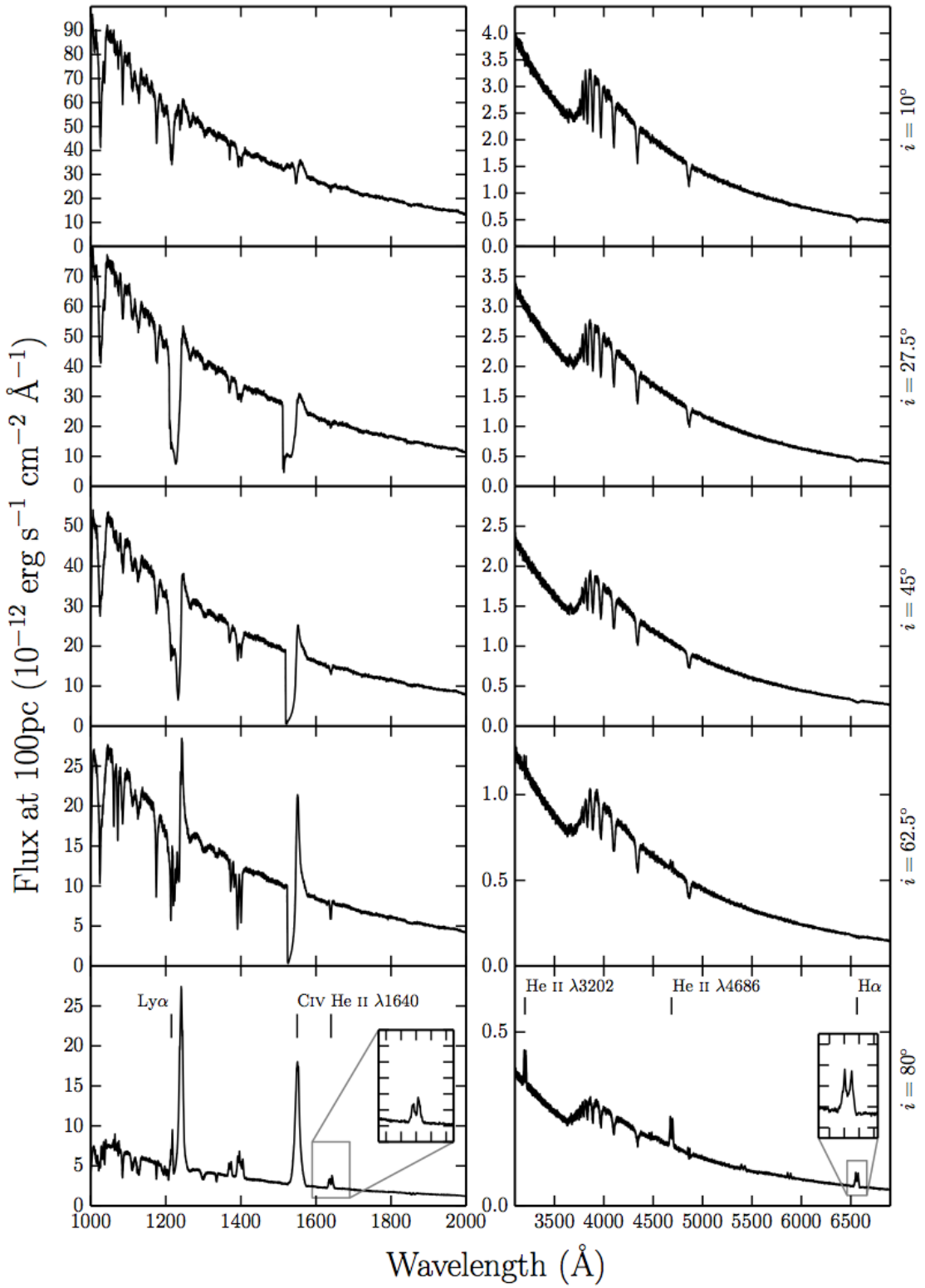


FIGURE 4.4: UV (left) and optical (right) synthetic spectra for model A, our benchmark model, computed at sightlines of 10, 27.5, 45, 62.5 and 80 degrees. The inset plots show zoomed-in line profiles for He II 1640Å and H α . Double-peaked line emission can be seen in He II 1640Å, He II 4686Å, H α and some He I lines, but the line emission is not always sufficient to overcome the absorption cores from the stellar atmosphere models.

The model also produces a prominent He II 3202Å line at high inclinations.

the velocity field of the wind is still dominated by rotation, rather than outflow, which accounts for the double-peaked shape of the lines. In principle, lines formed in this region can still be single peaked, since the existence of a poloidal velocity *gradient* changes the local escape probabilities (MC96). However, as discussed further in section 4.3.3, the radial velocity shear in our models is not high enough for this radiative transfer effect to dominate the line shapes.

The Balmer jump is in absorption at all inclinations for our benchmark model. This is due to the stellar atmospheres used to model the disc spectrum; it is not a result of photoabsorption in the wind. In fact, the wind spectrum exhibits the Balmer jump in *emission*, but this is not strong enough to overcome the intrinsic absorption edge in the disc spectrum. This is illustrated in Fig. 4.6, which shows the angle-integrated spectrum of the system, i.e. the spectrum formed by all escaping photons, separated into the disc and wind contributions. Even though the wind-formed Balmer recombination continuum does not completely fill in the Balmer absorption edge in this model, it does already contribute significantly to the total spectrum. This suggests that modest changes to the outflow kinematics might boost the wind continuum and produce emergent spectra with weak or absent Balmer absorption edges.

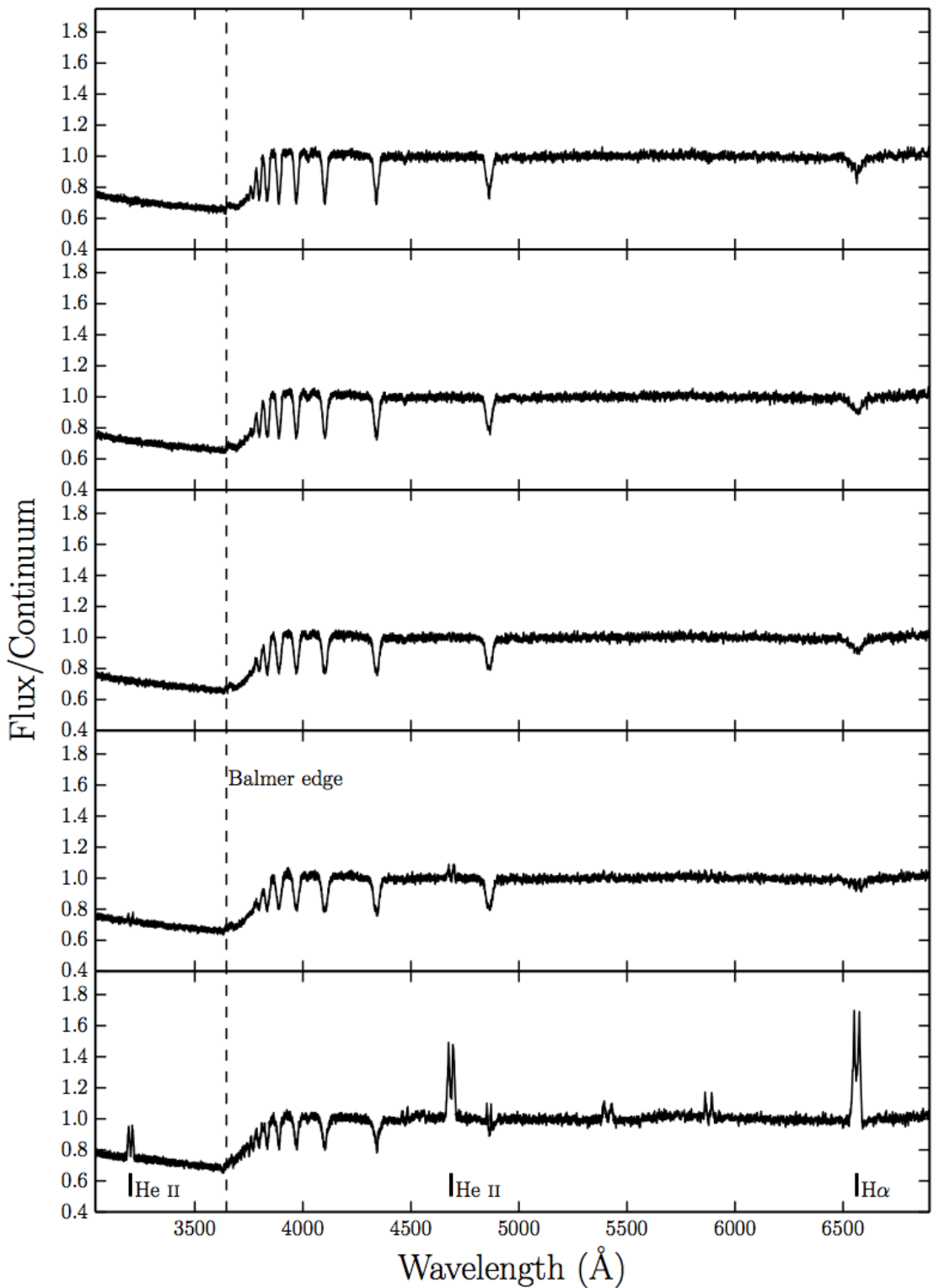


FIGURE 4.5: Synthetic optical spectra from model A computed for sightlines of 10, 27.5, 45, 62.5 and 80 degrees. In these plots the flux is divided by a polynomial fit to the underlying continuum redward of the Balmer edge, so that line-to-continuum ratios and the true depth of the Balmer jump can be shown.

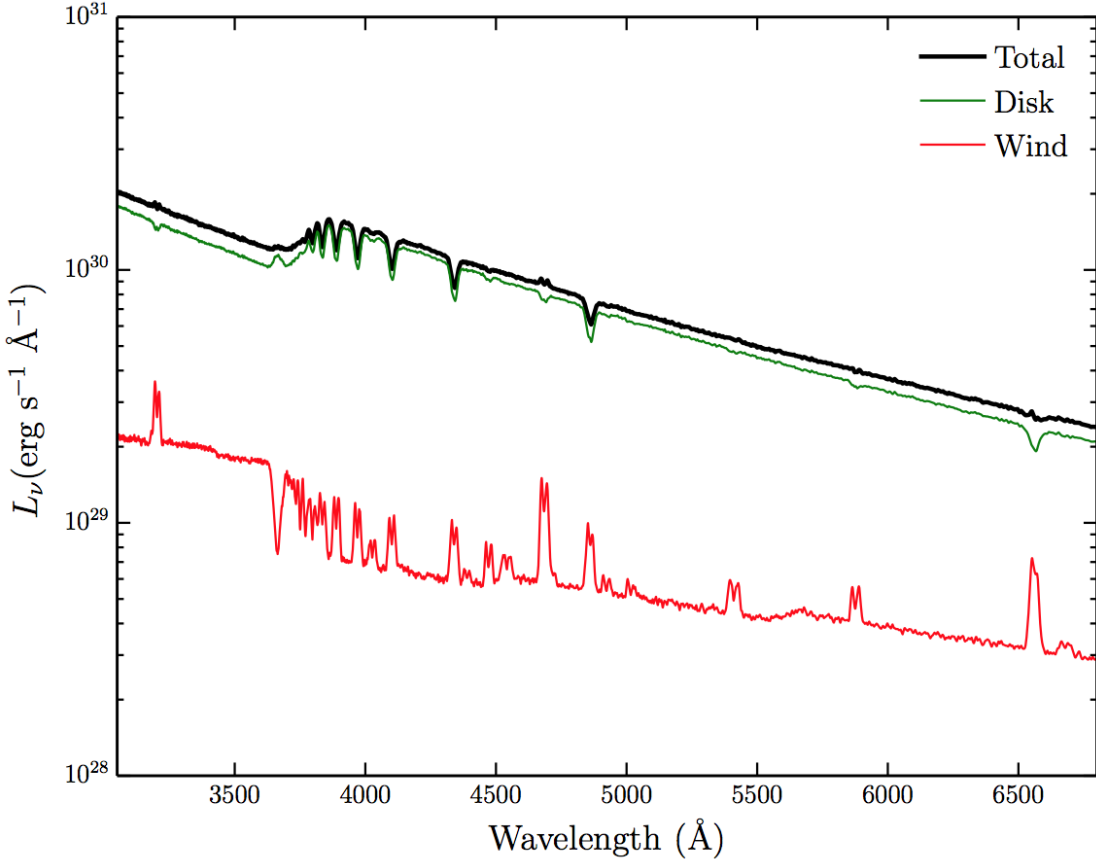


FIGURE 4.6: Total packet-binned spectra across all viewing angles, in units of monochromatic luminosity. The thick black line shows the total integrated escaping spectrum, while the green line shows disc photons which escape without being reprocessed by the wind. The red line show the contributions from reprocessed photons. Recombination continuum emission blueward of the Balmer edge is already prominent relative to other wind continuum processes, but is not sufficient to fill in the Balmer jump in this specific model

4.3 A Revised Model Optimized for Optical Wavelengths

The benchmark model discussed in section 4.2 was originally designed to reproduce the wind-formed lines seen in the UV spectra of high-state CVs. This model does produce some observable optical emission, but we can now attempt to construct a model that more closely matches the observed optical spectra of CVs.

Specifically, we aim to assess whether a revised model can:

- account for all of the lines seen in optical spectra of CVs while preserving the UV behaviour;
- produce single-peaked Balmer emission lines;

- generate enough of a wind-formed recombination continuum to completely fill in the disc's Balmer absorption edge for reasonable outflow parameters.

The emission measure of a plasma is directly proportional to its density. The simplest way to simultaneously affect the density in the wind (for fixed mass-loss rate), as well as the velocity gradients, is by modifying the poloidal velocity law. Therefore, we focus on just two kinematic variables:

- the acceleration length, R_v , which controls the distance over which the wind accelerates to $\frac{1}{2} v_\infty$;
- the acceleration exponent, α , which controls the rate at which the poloidal velocity changes near R_v .

The general behaviour we might expect is that outflows with denser regions near the wind base – i.e. winds with larger R_v and/or larger α – will produce stronger optical emission signatures. However, this behaviour may be moderated by the effect of the increasing optical depth through this region, which can also affect the line profile shapes. In addition, modifying R_v also increases the emission *volume*. Based on a preliminary exploration of models with different kinematics, we adopt the parameters listed in table 4.1 for our ‘optically optimized’ model (model B).

4.3.1 Synthetic Spectra

Fig. 4.7 shows the UV and optical spectra for the optically optimized model for the full range of inclinations. As expected, the trend from absorption to emission in the optical is again present, but in this revised model emission lines in the entire Balmer series are produced at high inclinations, as well as the observed lines in He II and He I. This can be seen more clearly in the continuum-normalized spectrum in Fig. 4.8.

Two other features are worth noting in the optical spectrum. First, the collisionally excited Ca II emission line at 3934 Å becomes quite prominent in our densest models. Second, our model predicts a detectable He II recombination line at 3202 Å. This is the He equivalent of Paschen β and should be expected in all systems that feature a strong He II $\lambda 4686$ line (the He equivalent of Paschen α). This line is somewhat unfamiliar

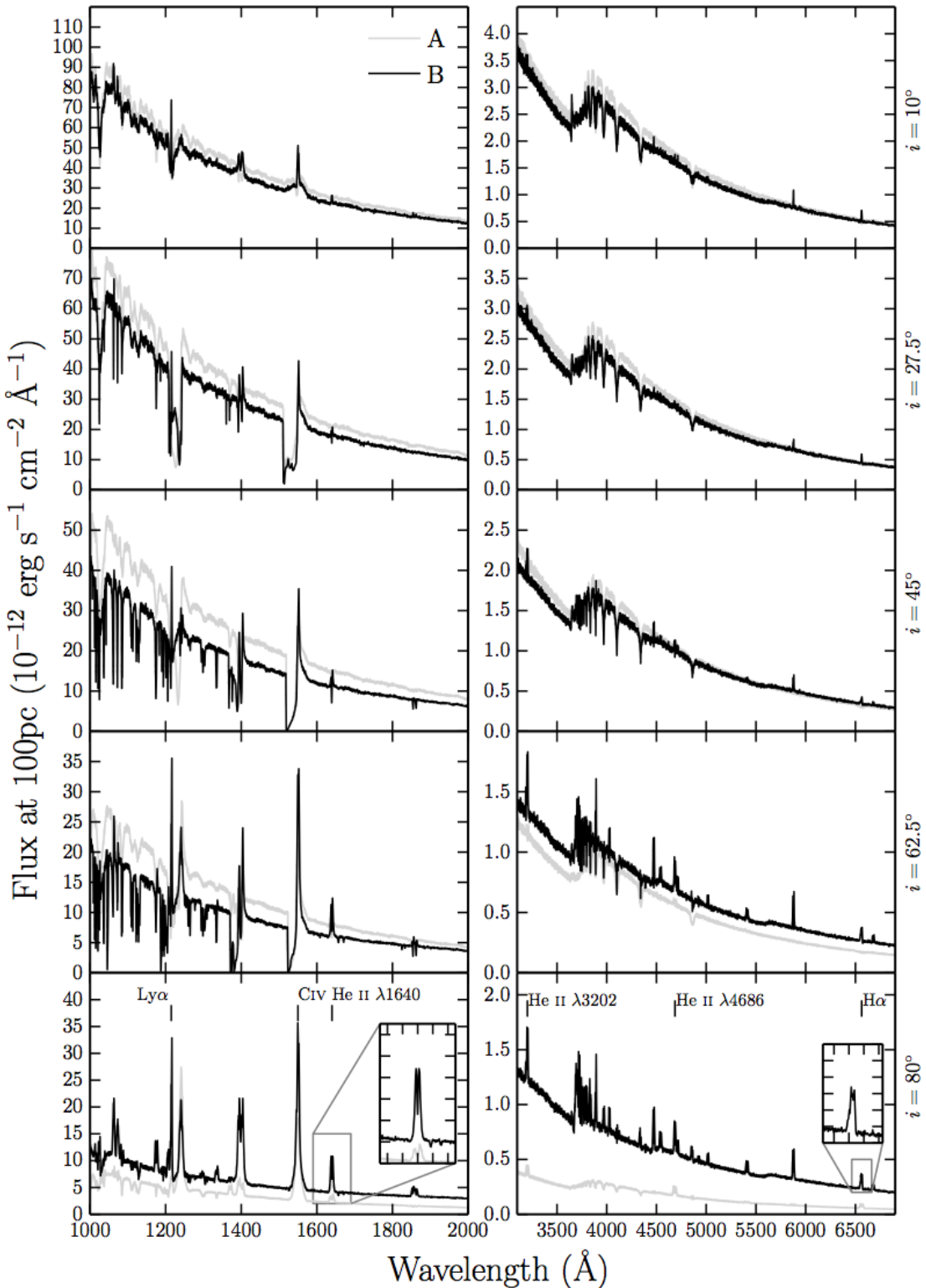


FIGURE 4.7: UV (left) and optical (right) synthetic spectra for model B computed at sightlines of 10, 27.5, 45, 62.5 and 80 degrees. Model A is shown in grey for comparison. The inset plots show zoomed-in line profiles for He II 1640Å and H α . The Balmer and He are double-peaked, albeit with narrower profiles. Strong He II 4686Å emission can be seen, as well as a trend of a deeper Balmer jump with decreasing inclination.

observationally, because it lies bluewards of the atmospheric cut-off, but also redwards of most ultraviolet spectra.

Our models do not exhibit P-Cygni profiles in the optical lines. This is perhaps not surprising. LK02 and SV93 originally designed such models to reproduce the UV line profiles. Thus, most of the wind has an ionization parameter of $\log U \sim 2$ (see Fig. 4.3). This means H and He are fully ionized throughout much of the wind and are successful in producing recombination features. However, the line opacity throughout the wind is too low to produce noticeable blue shifted absorption. We suspect that the systems that exhibit such profiles must possess a higher degree of ionization stratification, although the lack of contemporary observations means it is not known for certain if the P-Cygni profiles in UV resonance lines and optical H and He lines exist simultaneously. Ionization stratification could be caused by a clumpy flow, in which the ionization state changes due to small scale density fluctuations, or a stratification in density and ionizing radiation field over larger scales. Invoking clumpiness in these outflows is not an unreasonable hypothesis. Theories of line-driven winds predict an unstable flow (MacGregor et al. 1979; Owocki & Rybicki 1984, 1985), and simulations of CV disc winds also produce density inhomogeneities (Proga et al. 1998, 2002b). Tentative evidence for clumping being directly related to P-Cygni optical lines comes from the fact that Prinja et al. (2000) found the dwarf nova BZ Cam’s outflow to be unsteady and highly mass-loaded in outburst, based on observations of the UV resonance lines. This system has also exhibited P-Cygni profiles in He I $\lambda 5876$ and $H\alpha$ when in a high-state (Patterson et al. 1996; Ringwald & Naylor 1998). The degree of ionization and density variation and subsequent line opacities may be affected by our model parameters and the specific parameterisation adopted.

In the UV, the model still produces all the observed lines, and deep P-Cygni profiles are produced in the normal resonance lines, as discussed in section 4.2.2. However, the UV spectra also display what is perhaps the biggest problem with this revised model, namely the strength of resonance line emission at low and intermediate inclinations. In order to generate strong optical wind signatures, we have adopted wind parameters that lead to very high densities at the base of the wind ($n_e \sim 10^{13} - 10^{14} \text{ cm}^{-3}$). This produces the desired optical recombination emission, but also increases the role of collisional excitation in the formation of the UV resonance lines. This explains the pronounced increase in the emission component of the CIV $\lambda 1550$ resonance line, for example, relative to what

was seen in the benchmark model (compare Figures 4.4 and 4.7). The strength of this component in the revised model is probably somewhat too high to be consistent with UV observations of high-state CVs (see e.g. Long et al. 1991, 1994; Noebauer et al. 2010).

4.3.2 Continuum Shape and the Balmer Jump

The wind now also has a clear effect on the continuum shape, as shown by Fig. 4.9. In fact, the majority of the escaping spectrum has been reprocessed in some way by the wind, either by electron scattering (the wind is now moderately Thomson-thick), or by bound-free processes. This is demonstrated by the flatter spectral shape and the slight He photoabsorption edge present in the optical spectrum (marked in Fig. 4.8). This reprocessing is also responsible for the change in continuum level between models A and B. In addition, Figures 4.7, 4.8 and 4.9 clearly demonstrate that the wind produces a recombination continuum sufficient to completely fill in the Balmer jump at high inclinations.² This might suggest that Balmer continuum emission from a wind can be important in shaping the Balmer jump region, as originally suggested by Knigge et al. (1998b; see also Hassall et al. 1985).

It should be acknowledged, however, that the Balmer jump in high-state CVs would naturally weaken at high inclinations due to limb darkening effects (La Dous 1989b,a). Although simple limb darkening law which affects the emergent flux at each inclination is included, it is not a *frequency dependent* opacity in our model. As a result, the efficiency of filling in the Balmer jump should really be judged at low and medium inclinations, where, although prominent, the recombination continuum does not overcome the disc atmosphere absorption. In addition, this effect could mean that any model which successfully fills in the jump at low inclinations could lead to a Balmer jump in emission at high inclinations. In any case, to properly understand this phenomenon, a fully self-consistent radiative transfer calculation of both the disc atmosphere and connected wind is required.

²Note that the apparent absorption feature just redward of the Balmer jump in these models is artificial. It is caused by residual line blanketing in the stellar atmospheres, which our models cannot fill in since they employ a 20-level H atom.

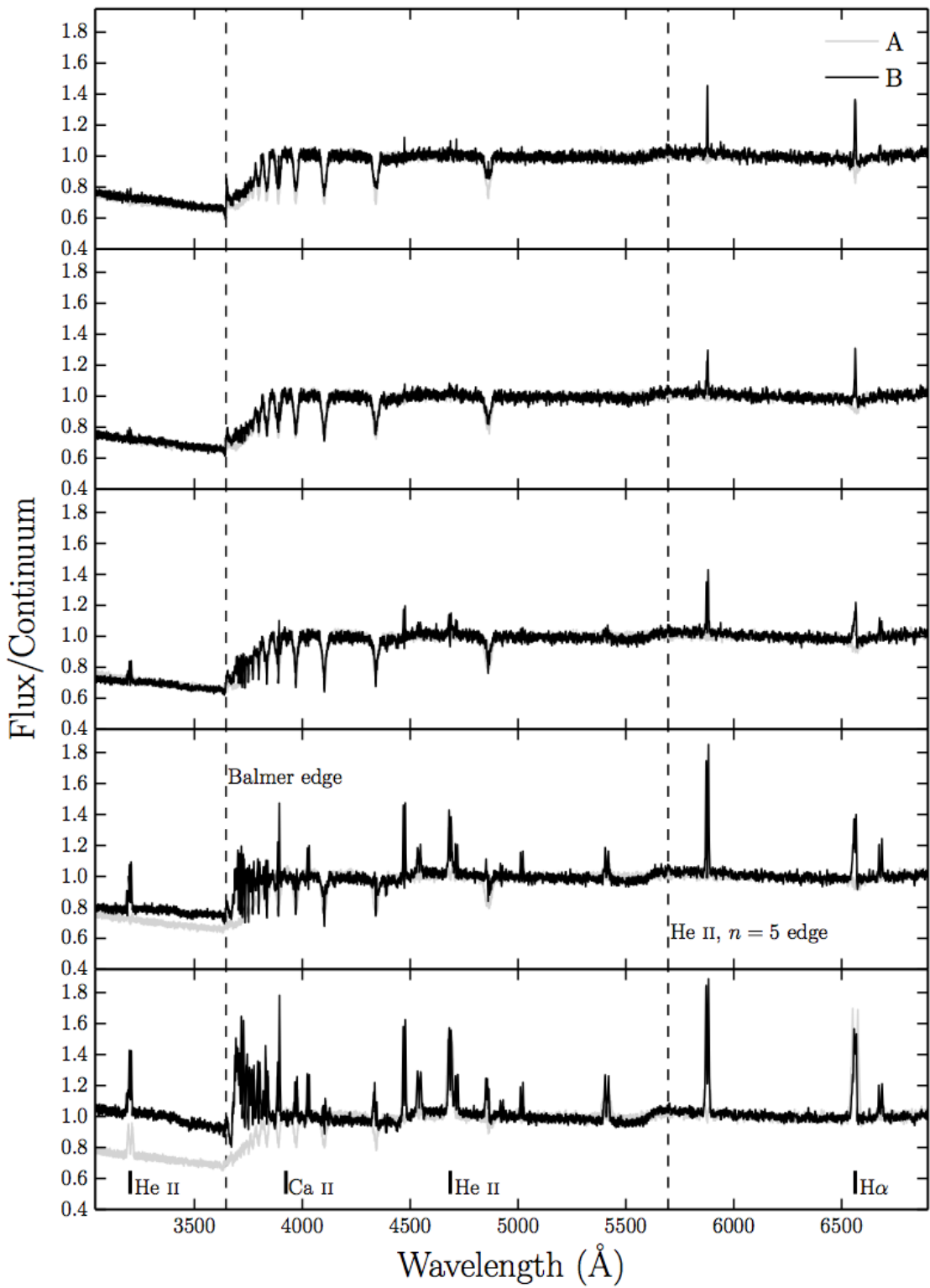


FIGURE 4.8: Synthetic optical spectra from model B computed for sightlines of 10, 27.5, 45, 62.5 and 80 degrees. Model A is shown in grey for comparison. In these plots the flux is divided by a polynomial fit to the underlying continuum redward of the Balmer edge, so that line-to-continuum ratios and the true depth of the Balmer jump can be shown.

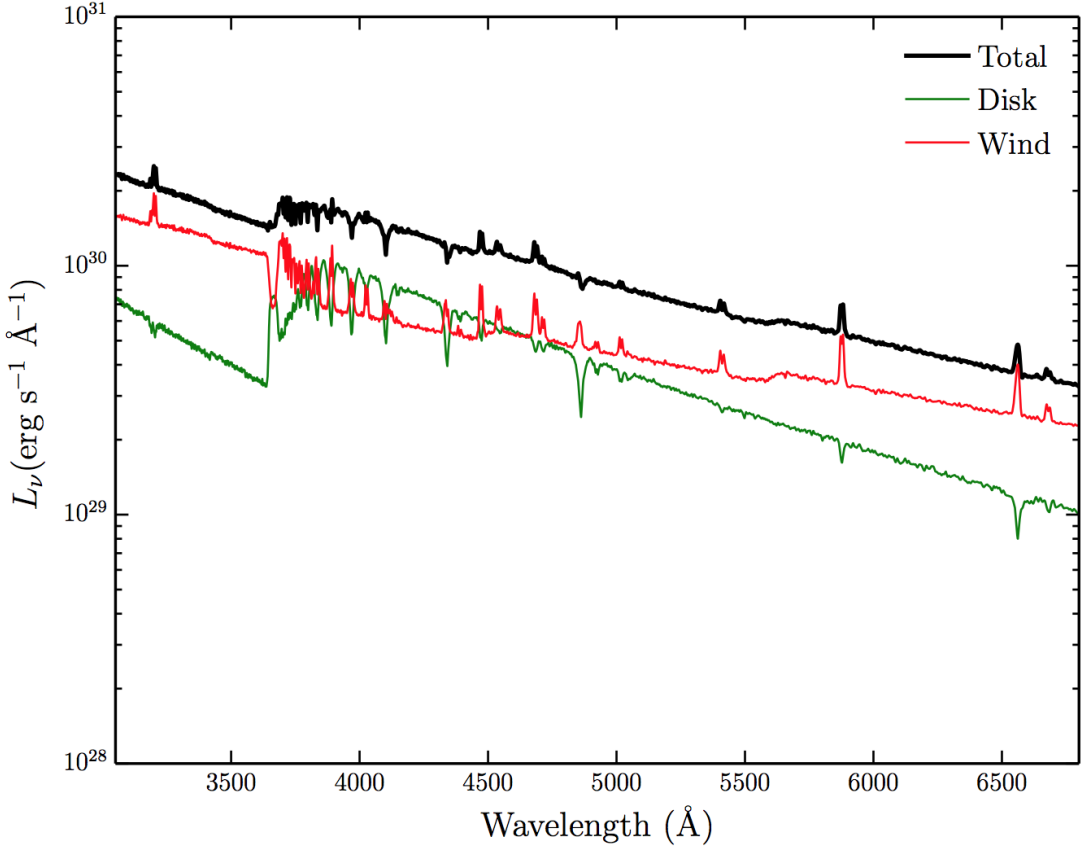


FIGURE 4.9: Total packet-binned spectra across all viewing angles, in units of monochromatic luminosity. The thick black line shows the total integrated escaping spectrum, while the green line shows disc photons which escape without being reprocessed by the wind. The red line show the contributions from reprocessed photons. In this denser model the reprocessed contribution is significant compared to the escaping disc spectrum. The Balmer continuum emission is prominent, and the wind has a clear effect on the overall spectral shape.

4.3.3 Line Profile Shapes: Producing Single-Peaked Emission

Fig. 4.10 shows how the H α profile changes with the kinematics of the wind for an inclination of 80°. The main prediction is that dense, slowly accelerating wind models produce narrower emission lines. This is *not* due to radial velocity shear. As stated by MC96, that mechanism can only work if poloidal and rotational velocity gradients satisfy $(dv_l/dr)/(dv_\phi/dr) \gtrsim 1$; in our models, this ratio is always $\lesssim 0.1$. Instead, the narrow lines predicted by our denser wind models can be traced to the base of the outflow becoming optically thick in the continuum, such that the line emission from the base of the wind cannot escape to the observer. In such models, the ‘line photosphere’ (the $\tau \simeq 1$ surface of the line-forming region) moves outwards, towards larger vertical and cylindrical distances. This reduces the predicted line widths, since the rotational

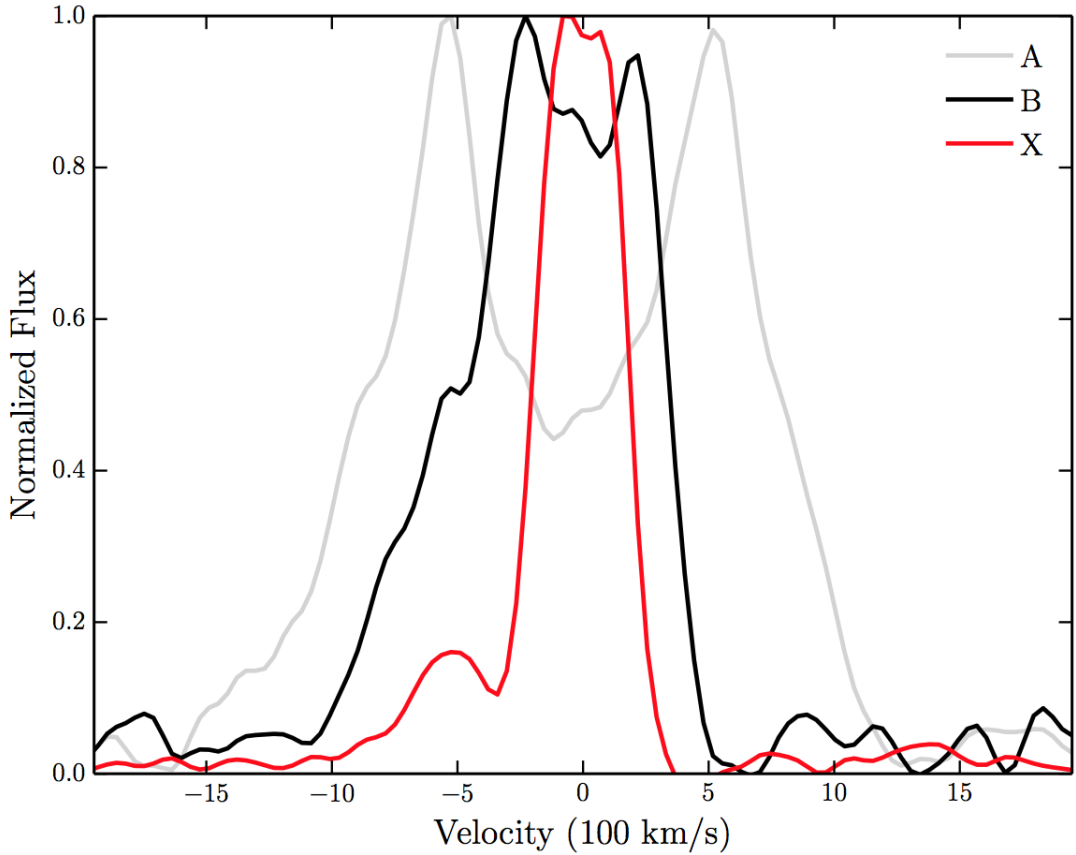


FIGURE 4.10: H α line profiles, normalized to 1, plotted in velocity space for three models with varying kinematic properties, computed at an inclination of 80° . The benchmark model and the improved optical model described in section ?? are labeled as A and B respectively, and a third model (X) which has an increased acceleration length of $R_v = 283.8 R_{WD}$, and $\alpha = 4$ is also shown. The x -axis limits correspond to the Keplerian velocity at $4R_{WD}$, the inner edge of the wind. We observe a narrowing of the lines, and a single-peaked line in model X. This is not due to radial velocity shear (see section 4.3.3).

velocities – which normally provide the main line broadening mechanism at high inclination – drop off as $1/r$. This is not to say that the MC96 mechanism could not be at work in CV winds. For example, it would be worth investigating alternative prescriptions for the wind velocity field, as well as the possibility that the outflows may be clumped. An inhomogeneous flow (which has been predicted in CVs; see section 4.3.1) might allow large radial velocity shears to exist while still maintaining the high densities needed to produce the required level of emission. However, such an investigation is beyond the scope of the present paper.

In our models, single-peaked line profiles are produced once the line forming region has been pushed up to $\sim 10^{11}$ cm ($\sim 150 R_{WD}$) above the disc plane. This number may seem unrealistically large, but the vertical extent of the emission region is actually not

well constrained observationally. In fact, multiple observations of eclipsing NLs show that the H α line is only moderately eclipsed compared to the continuum (e.g. Baptista et al. 2000; Groot et al. 2004; see also section 4.3.5), implying a significant vertical extent for the line-forming region. This type of model should therefore not be ruled out *a priori*, but this specific model was not adopted as our optically optimized model due to its unrealistically high continuum level in eclipse.

4.3.4 Sensitivity to Model Parameters

This revised model demonstrates that one can achieve a more realistic optical spectrum by altering just two kinematic parameters. However, it may also be possible to achieve this by modifying other free parameters such as \dot{M}_{wind} , the opening angles of the wind and the inner and outer launch radii. For example, increasing the mass-loss rate of the wind increases the amount of recombination emission (which scales as ρ^2), as well as lowering the ionization parameter and increasing the optical depth through the wind. Larger launching regions and covering factors tend to lead to a larger emitting volume, but this is moderated by a decrease in density for a fixed mass-loss rate. We also note that the inner radius of $4 R_{WD}$ adopted by SV93 affects the emergent UV spectrum seen at inclinations $< \theta_{min}$ as the inner disc is uncovered. This causes less absorption in the UV resonance lines, but the effect on the optical spectrum is negligible. we have verified this general behaviour, but we suggest that future work should investigate the effect of these parameters in more detail, as well as incorporating a treatment of clumping. If a wind really does produce the line and continuum emission seen in optical spectra of high-state CVs, then understanding the true mass-loss rate and geometry of the outflow is clearly important.

4.3.5 Comparison to RW Tri

Fig. 4.11 shows a comparison of the predicted out-of-eclipse and mid-eclipse spectra against observations of the high-inclination nova-like RW Tri. The inclination of RW Tri is somewhat uncertain, with estimates including 70.5° (Smak 1995), 75° (Groot et al. 2004), 80° (Longmore et al. 1981) and 82° (Frank & King 1981). Here, we adopt $i = 80^\circ$, but our qualitative conclusions are not particularly sensitive to this choice. We follow LK02 is setting the value of r_{disc} (the maximum radius of the accretion disc) to

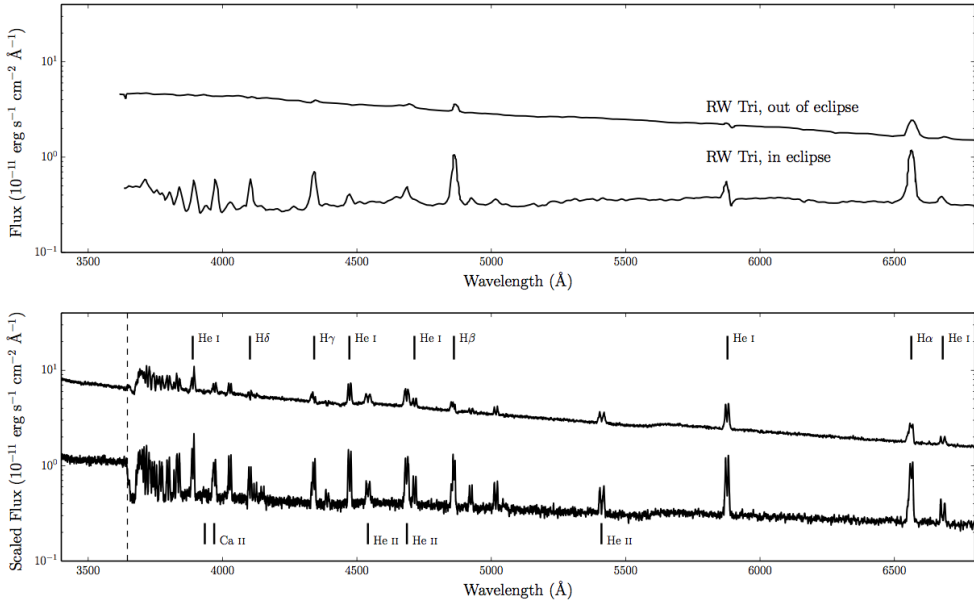


FIGURE 4.11: *Top Panel:* In and out of eclipse spectra of the high inclination NL RW Tri. *Bottom Panel:* In and out of eclipse synthetic spectra from model B. The artificial ‘absorption’ feature just redward of the Balmer jump is caused by the reasons described in section 5.2.

34.3 R_{WD} . When compared to the semi-major axis of RW Tri, this value is perhaps lower than one might typically expect for NLs ([Harrop-Allin & Warner 1996](#)). However, it is consistent with values inferred by [Rutten et al. \(1992\)](#). We emphasize that this model is in no sense a fit to this – or any other – data set.

The similarity between the synthetic and observed spectra is striking. In particular, the revised model produces strong emission in all the Balmer lines, with line-to-continuum ratios comparable to those seen in RW Tri. Moreover, the line-to-continuum contrast increases during eclipse, as expected for emission produced in a disc wind. This trend is in line with the observations of RW Tri, and it has also been seen in other NLs, including members of the SW Sex class ([Neustroev et al. 2011](#)). As noted in section 4.3.1, the majority of the escaping radiation has been reprocessed by the wind in some way (particularly the eclipsed light).

However, there are also interesting differences between the revised model and the RW Tri data set. For example, the model exhibits considerably stronger He II features than the observations, which suggests that the overall ionization state of the model is somewhat too high. As discussed in section 4.3.3, the optical lines are narrow, but double-peaked.

This is in contrast to what is generally seen in observations of NLs, although the relatively low resolution of the RW Tri spectrum makes a specific comparison difficult. In order to demonstrate the double-peaked nature of the narrower lines, we do not smooth the synthesized data to the resolution of the RW Tri dataset. If the data was smoothed, the H α line would appear single-peaked.

4.4 Discussion: Collision Strengths and Boundary Layers

The van Regemorter approximation uses an effective gaunt factor, of order unity. To conduct these simulations a value of $\bar{g} = 1$ was adopted. There are two main concerns when using this approach. The first is related to accuracy, as poorly estimating collision strengths could lead to incorrect heating and cooling balance in the flow, with knock-on effects on the emergent spectrum. The second is that collisions between radiatively forbidden transitions are not taken into account when one splits levels into l - and s -subshells, as well as principal quantum number, n (as we have done with He I; see section ??). Although this approximation is, in general, a poor one, the effect is quantified in section 4.4.1.1.

4.4.1 Model Sensitivity to Collision Strengths

4.4.1.1 Collisions Between Radiatively Forbidden Transitions

4.4.1.2 Line Heating and Cooling

Fig. ?? shows four important heating and cooling mechanisms in the wind for model B.
Line heating and cooling

4.4.2 Improving Collision Strengths

4.4.3 Introducing a Boundary Layer

4.5 Conclusions

I have investigated whether a disc wind model designed to reproduce the UV spectra of high-state CVs would also have a significant effect on the optical spectra of these systems. We find that this is indeed the case. In particular, the model wind produces H and He recombination lines, as well as a recombination continuum blueward of the Balmer edge. We do not produce P-Cygni profiles in the optical H and He lines, which are seen in a small fraction of CV optical spectra. Possible reasons for this are briefly discussed in section 4.3.1.

A revised benchmark model was also constructed to more closely match the optical spectra of high-state CVs. This optically optimized model produces all the prominent optical lines in and out of eclipse, and achieves reasonable verisimilitude with the observed optical spectra of RW Tri. However, this model also has significant shortcomings. In particular, it predicts stronger-than-observed He II lines in the optical region and too much of a collisionally excited contribution to the UV resonance lines. Incorporating more accurate collisional data into PYTHON will help assess this discrepancy in more detail.

Based on these results, I argue that recombination emission from outflows with sufficiently high densities and/or optical depths might produce the optical lines observed in CVs, and may also fill in the Balmer absorption edge in the spectrum of the accretion disc, thus accounting for the absence of a strong edge in observed CV spectra. In section 4.3.3, I demonstrated that although the double peaked lines narrow and single-peaked emission can be formed in our densest models, this is not due to the radial velocity shear mechanism proposed by MC96. I suggest that ‘clumpy’ line-driven winds or a different wind parameterization may nevertheless allow this mechanism to work. We also note the possibility that, as in our denser models, the single-peaked lines are formed well above the disc, where rotational velocities are lower.

It is not yet clear whether a wind model such as this can explain all of the observed optical features of high-state CVs – further effort is required on both the observational and modelling fronts. However, this work demonstrates that disc winds may not just be responsible for creating the blue-shifted absorption and P-Cygni profiles seen in the UV resonance lines of high-state CVs, but can also have a strong effect on the optical appearance of these systems. In fact, most of the optical features characteristic of CVs are likely to be affected – and possibly even dominated – by their disc winds. Given that optical spectroscopy plays the central role in observational studies of CVs, it is critical to know where and how these spectra are actually formed. We believe it is high time for a renewed effort to understand the formation of spectra in accretion discs and associated outflows.

Chapter 5

Testing Quasar Unification: Radiative Transfer In Clumpy Winds

This chapter is based on the publication:

Matthews J. H., Knigge C., Long K. S., Sim S. A., Higginbottom N., Mangham S. W., ‘Testing quasar unification: radiative transfer in clumpy winds’, 2016, MNRAS, 458, 293.

5.1 Introduction

In the earlier chapters I presented the evidence for accretion disc winds in quasars and luminous AGN, and showed how they may be responsible for more than just the broad absorption lines and P-Cygni profiles seen in quasar spectra. In particular, they offer a natural way to *unify* much of the complex phenomenology into one simple picture.

Here, I aim to test that picture using PYTHON, with the specific aim of determining whether it is possible to simulate the properties of the spectra of AGN, including BALQSOs, using simple kinematic prescriptions for biconical disc winds. Past results have been encouraging; H13 produced simulated spectra that resembled that of BALQSOs, as long as the luminosity of the X-ray source was relatively low, of order 10^{43} erg s⁻¹ and the

mass loss rate was relatively high, of order the mass accretion rate. However, at higher X-ray luminosities, the wind was so ionized that UV absorption lines were not produced. In addition, and in part due to limitations inherent in the radiative transfer methods, the model failed to produce spectra with strong emission lines at any inclination angle.

Here I attempt to address both of these issues, by introducing clumping into PYTHON and a more complete treatment of H and He into the radiative transfer calculations. Thus, the simulations presented in this chapter treat H & He as full macro-atoms, and model metals as simple-atoms as described extensively in chapter 3. In order to correctly model the ionizing spectrum for simple-atoms I dispense with the ML93 modified Saha approach and fully solve the ionization balance using the spectral modelling approach described in section 3.4.2.1. Macro-atoms still have their ionization and excitation states calculated from MC estimators.

The kinematic model used once again follows the SV93 prescription, and is described, together with the clumping implementation, in section 5.2. Section 5.3 contains the results from a clumped model, with comparisons to observational data, as well as some discussion. Further discussion and examination of sensitivity to model parameters and viewing angle can be found in section 5.4, which expands somewhat on the work presented in (Matthews et al. 2016). Finally, I summarise the findings in section 5.5.

5.2 A Clumpy Biconical Disk Wind Model for Quasars

Here, I once again adopt the SV93 kinematic prescription for a biconical disc wind model described in section 2.4 LK02, H13 and M15. A schematic is shown in Fig. 6.7, with key aspects marked. The general biconical geometry is similar to that invoked by Murray et al. (1995) and Elvis (2000) to explain the phenomenology of quasars and BALQSOs.

5.2.1 Photon Sources

Two sources of r-packets are included in the model: An accretion disc and a central X-ray source. The accretion disc is assumed to be geometrically thin, but optically thick. Accordingly, the disc is modelled as an ensemble of blackbodies with a Shakura &

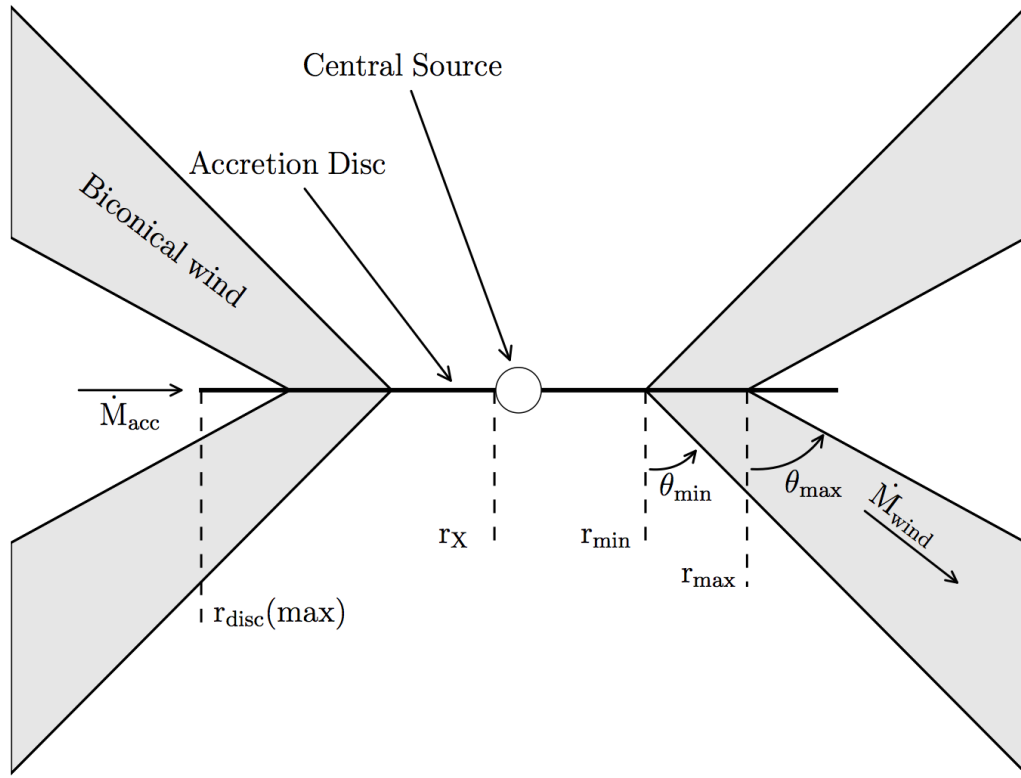


FIGURE 5.1: A cartoon showing the geometry and some key parameters of the biconical quasar wind model.

[Sunyaev \(1973\)](#) effective temperature profile. The emergent SED is then determined by the specified accretion rate (\dot{m}) and central BH mass (M_{BH}). All photon sources in the model are opaque, meaning that r -packets that strike them are destroyed. The inner radius of the disc extends to the innermost stable circular orbit (ISCO) of the BH. I assume a Schwarzschild BH with an ISCO at $6 r_G$, where $r_G = GM_{BH}/c^2$ is the gravitational radius. For a $10^9 M_\odot$ BH, this is equal to 8.85×10^{14} cm or $\sim 10^{-4}$ pc.

The X-ray source is treated as an isotropic sphere at the ISCO, which emits r -packets according to a power law in flux with index α_X , of the form

$$F_X(\nu) = K_X \nu^{\alpha_X}. \quad (5.1)$$

The normalisation, K_X of this power law is such that it produces the specified 2-10 keV luminosity, L_X . The input spectrum for the simulations is therefore a simple combination of a power law X-ray component and accretion disc spectrum; an example input spectrum is shown in Fig. 5.2. In actual fact, this spectrum will be angle dependent due to the

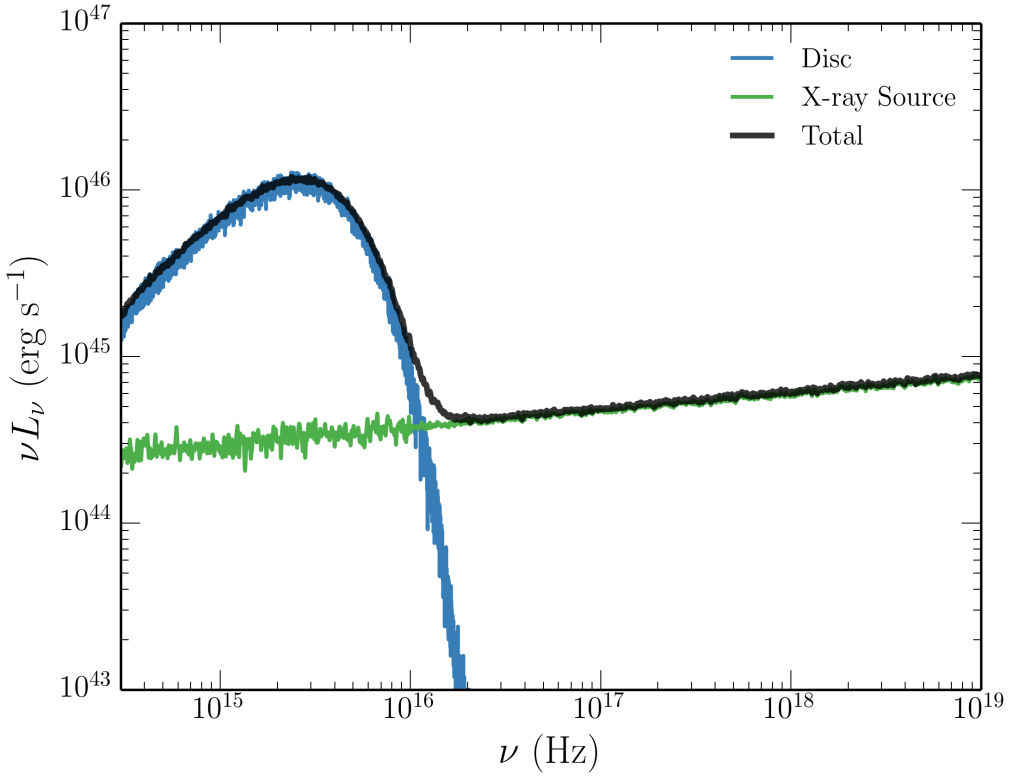


FIGURE 5.2: The input spectrum used for the quasar modelling.

geometry of the system and the angular emissivity profile of the accretion disc (see sections 5.3.3 and 5.4.2. Photons, or r -packets, produced by the accretion disc and central X-ray source are reprocessed by the wind. This reprocessing is dealt with by enforcing strict radiative equilibrium (*modulo* adiabatic cooling; see section 2.3) via an indivisible energy packet constraint (see Lucy 2002, M15).

5.2.2 A Simple Approximation for Clumping

In previous modelling efforts with PYTHON, a smooth outflow was assumed, such that the density at a given point was determined only by the kinematic parameters and mass loss rate. However, as already discussed, AGN winds exhibit significant substructure – the outflow is expected to be *clumpy*, rather than smooth, and probably on a variety of scales. A clumpy outflow offers a possible solution to the so-called ‘over-ionization problem’ in quasar and AGN outflows (e.g. ??Hamann et al. 2013). This is the main motivation for incorporating clumping into the model.

Deciding on how to implement clumping into the existing wind models was not straightforward. First, and most importantly, the physical scale lengths and density contrasts in AGN outflows are not well-constrained from observations or theory. As a result, while one could envision in principle, clouds with a variety of sizes and density contrasts varying perhaps as function of radius, there would have been very little guidance on how to set nominal values of the various parameters of such a model. Second, there are significant computational difficulties associated with adequately resolving and realistically modelling a series of small scale, high density regions with a MCRT – or for that matter, a hydrodynamical – code. Given the lack of knowledge about the actual type of clumping, I have implemented a simple approximation used successfully in stellar wind modelling, known as *microclumping* (e.g. Hamann & Koesterke 1998; Hillier & Miller 1999; Hamann et al. 2008).

The underlying assumption of microclumping is that clump sizes are much smaller than the typical photon mean free path, and thus the clumps are both geometrically and optically thin. This approach allows one to treat clumps only in terms of their volume filling factor, f_V , instead of having to specify separately their size and density distributions. In this model, f_V is independent of position (see section 4.4). The inter-clump medium is modeled as a vacuum, although the outflow is still non-porous and axisymmetric. This approach therefore assumes that the inter-clump medium is unimportant in determining the output spectrum, which is expected to be true only when density constraints are large and the inter-clump medium is both very ionized and of low emissivity and opacity. The density of the clumps is multiplied by the “density enhancement” $D = 1/f_V$. Opacities, κ , and emissivities, ϵ , can then be expressed as

$$\kappa = f_V \kappa_C(D); \quad \epsilon = f_V \epsilon_C(D). \quad (5.2)$$

Here the subscript C denotes that the quantity is calculated using the enhanced density in the clump. The resultant effect is that, *for fixed temperature*, processes that are linear in density, such as electron scattering, are unchanged, as f_V and D will cancel out. However, any quantity that scales with the square of density, such as collisional excitation or recombination, will increase by a factor of D . In PYTHON, the temperature is not fixed, and is instead set by balancing heating and cooling in a given cell. In the presence of an X-ray source, this thermal balance is generally dominated by bound-free heating and line cooling. The main effect of including clumping in this modelling is that

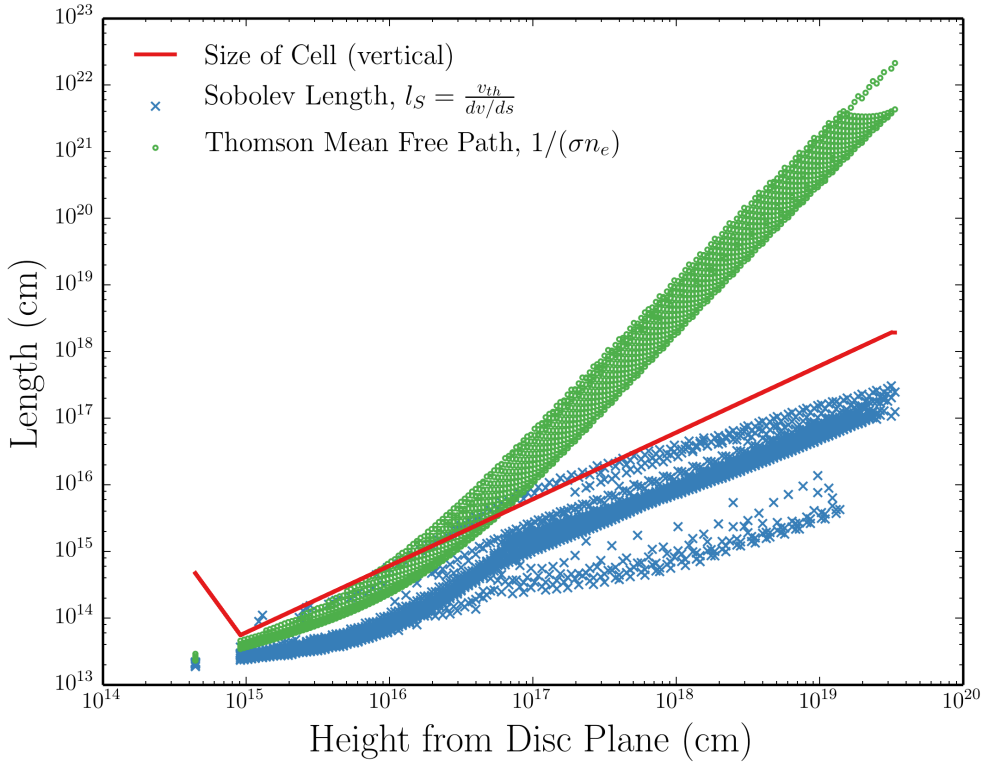


FIGURE 5.3: Some typical length scales for the fiducial model. This places a formal limit of $\sim 10^{12}$ cm on clump sizes in the microclumping framework, and confirms that the cells are sufficiently larger than the Sobolev length in almost all cases.

it moderates the ionization state due to the increased density. This allows an increase in the ionizing luminosity, amplifying the amount of bound-free heating and also increasing the competing line cooling term (thermal line emission).

The shortest length scale in a Sobolev MCRT treatment such as ours is normally the Sobolev length, given by

$$l_S = \frac{v_{th}}{|dv/ds|} \quad (5.3)$$

This is typically $\sim 10^{13}$ cm near the disc plane, increasing outwards. The Sobolev length is shown, together with the size of the cell and Thomson mean free path, in Fig. 5.3. The mean density is used to calculate the Sobolev optical depth, which assumes that l_S is greater than the typical clump size. Thus for the microclumping assumption to be formally correct, clumps should be no larger than $\sim 10^{12}$ cm. This size scale is not unreasonable for quasar outflows, as [de Kool & Begelman \(1995\)](#) suggest that BAL flows may have low filling factors with clump sizes of $\sim 10^{11}$ cm.

Our clumping treatment is necessarily simple; it does not adequately represent the complex substructures and stratifications in ionization state expected in AGN outflows. Nevertheless, this parameterization allows simple estimates of the effect clumping has on the ionization state and emergent line emission.

5.2.3 The Simulation Grid

Using this prescription, I conducted a limited parameter search over a 5-dimensional parameter space involving the variables r_{min} , θ_{min} , f_V , α and R_v . The grid points are shown in Table 1. The aim here was to first fix M_{BH} and \dot{m} to their H13 values, and increase L_X to 10^{45} erg s $^{-1}$ (a more realistic value for a quasar of $10^9 M_\odot$ and an Eddington fraction of 0.2; see section 5.3.3).

These models were then evaluated based on how closely their synthetic spectra reproduced the following properties of quasars and BALQSOs:

- UV absorption lines with $BI > 0$ at $\sim 20\%$ of viewing angles (e.g. Knigge et al. 2010);
- Line emission emerging at low inclinations, with $EW \sim 40\text{\AA}$ in C IV 1550\AA (e.g. Shen et al. 2011);
- H recombination lines with $EW \sim 50\text{\AA}$ in Ly α (e.g. Shen et al. 2011);
- Mg II and Al III (LoBAL) absorption features with $BI > 0$ at a subset of BAL viewing angles;
- Verisimilitude with quasar composite spectra.

Here BI is the ‘Balnicity Index’ (Weymann et al. 1991), given by

$$BI = \int_{3000 \text{ km s}^{-1}}^{25000 \text{ km s}^{-1}} C \left(1 - \frac{f(v)}{0.9} \right) dv. \quad (5.4)$$

The constant $C = 0$ everywhere, unless the normalized flux has satisfied $f(v) < 0.9$ continuously for at least 2000 km s 1 , whereby C is set to 1.

In the next section, I present one of the most promising models, which I refer to as the fiducial model, and discuss the various successes and failures with respect to the

Parameter	Grid Point Values		
r_{min}	$60r_g$	$180r_g$	$300r_g$
θ_{min}	55°	70°	
R_v	10^{18}cm	10^{19}cm	
α	0.5	0.6	0.75
f_V	0.01	0.1	1.5

TABLE 5.1: The grid points used in the parameter search. The sensitivity to some of these parameters is discussed further in section 5.4.1

above criteria. This allows us to gain insight into fundamental geometrical and physical constraints and assess the potential for unification. I then discuss the sensitivity to key parameters in section 5.4.1. The full grid, including output synthetic spectra and plots can be found at jhmatthews.github.io/quasar-wind-grid/.

5.3 Results and Analysis From A Fiducial Model

Here I describe the results from a fiducial model, and discuss these results in the context of the criteria presented in section 3.4. The parameters of this model are shown in Table 2. Parameters differing from the benchmark model of H13 are highlighted with an asterisk. In this section, I examine the physical conditions of the flow, and present the synthetic spectra, before comparing the X-ray properties of this particular model to samples of quasars and luminous AGN.

5.3.1 Physical Conditions and Ionization State

Fig. 5.4 shows the physical properties of the wind. The wind rises slowly from the disc at first, with densities within clumps of $n_H \sim 10^{11} \text{ cm}^{-3}$ close to the disc plane, where n_H is the local number density of H. To illustrate the degree of scale and density ranges in the model I also show n_e in the wind on a linear scale in Fig. 5.5. The flow then accelerates over a scale length of $R_V = 10^{19} \text{ cm}$ up to a terminal velocity equal to the escape velocity at the streamline base ($\sim 10,000 \text{ km s}^{-1}$). This gradual acceleration results in a wind that exhibits a stratified ionization structure, with low ionization material in the base of the wind giving way to highly ionized plasma further out. This is illustrated in Fig. 5.4 by the panels showing the ion fraction $F = n_j/n_{tot}$ of some important ions. The clumped wind produces the range of ionization states observed

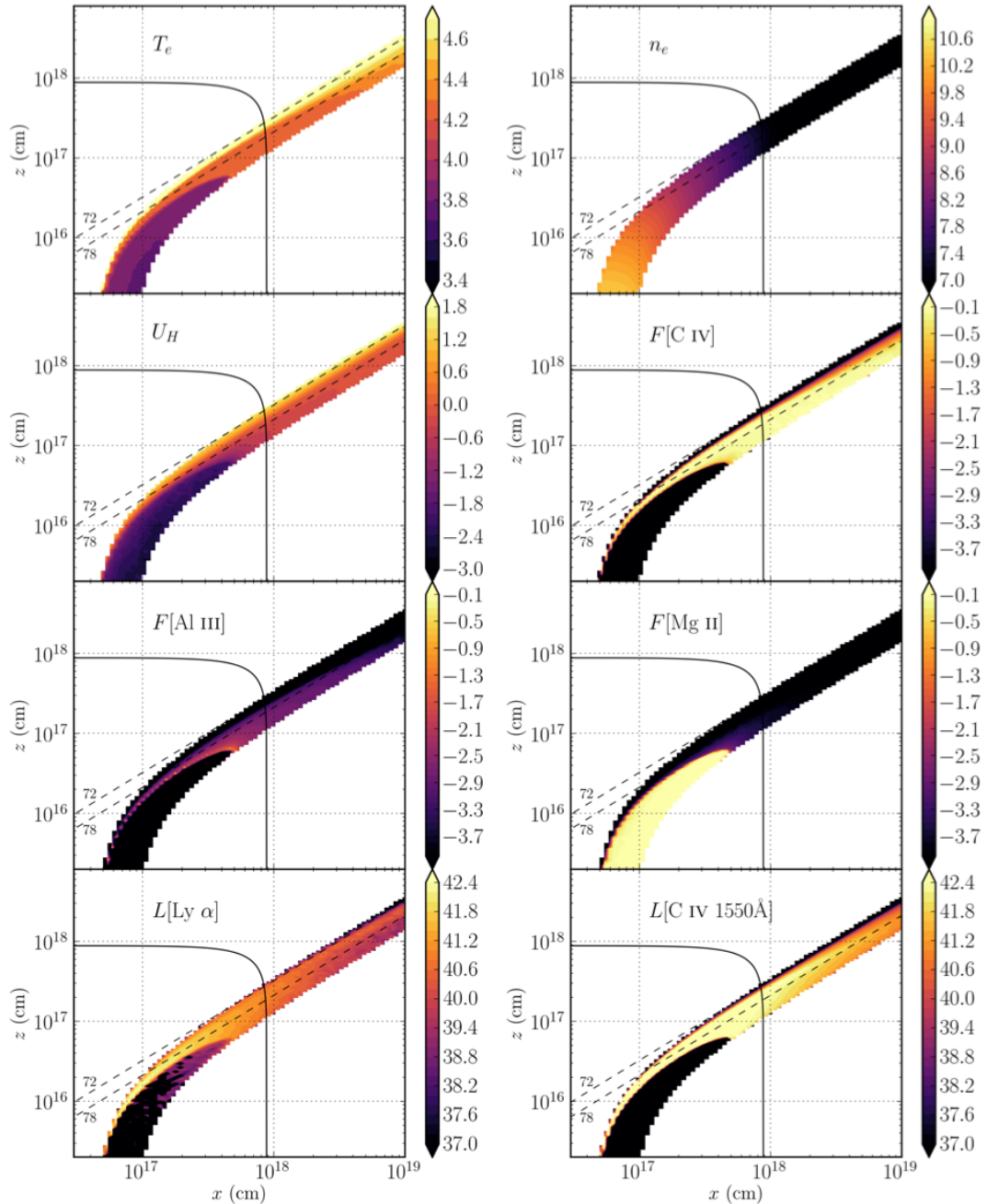


FIGURE 5.4: Contour plots showing the logarithm of some important physical properties of the outflow. The spatial scales are logarithmic and the x and z scales are not the same. Symbols are defined in the text. The solid black line marks a sphere at $1000 r_G$. The dotted lines show the 72° and 78° sightlines to the centre of the system, and illustrate that different sightlines intersect material of different ionization states. The line luminosities, L , represent the luminosity of photons escaping the Sobolev region for each line. These photons do not necessarily escape to infinity.

Fiducial Parameters	Model	Value
M_{BH}		$1 \times 10^9 M_\odot$
\dot{m}_{acc}		$5 M_\odot yr^{-1} \simeq 0.2 \dot{M}_{Edd}$
α_X		-0.9
L_X		$10^{45} \text{ erg s}^{-1}$
$r_{disc}(\min) = r_X$		$6r_g = 8.8 \times 10^{14} \text{ cm}$
$r_{disc}(\max)$		$3400r_g = 5 \times 10^{17} \text{ cm}$
\dot{m}_{wind}		$5 M_\odot yr^{-1}$
r_{min}		$300r_g = 4.4 \times 10^{16} \text{ cm}$
r_{max}		$600r_g = 8.8 \times 10^{16} \text{ cm}$
θ_{min}		70.0°
θ_{max}		82.0°
$v_\infty(r_0)$		$v_{esc}(r_0)$
R_v		10^{19} cm^*
α		0.5*
f_V		0.01*
n_x		100
n_z		200

TABLE 5.2: Wind geometry parameters used in the fiducial model, as defined in the text and figure 1. Parameters differing from the benchmark model of H13 are highlighted with an asterisk.

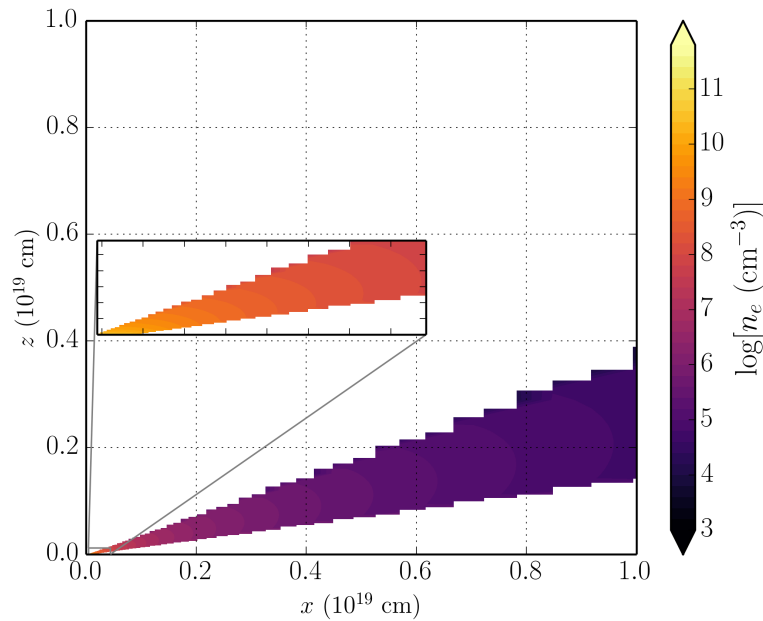


FIGURE 5.5: The electron density in the model, this time on linear axes in order to illustrate the density contrasts and scale of the system. The plot is on the scale of the acceleration length, whereas the inset is a box of $2700 \times 800r_G$, where the bottom left corner corresponds to the base of the innermost streamline.

in quasars and BALQSOs, while adopting a realistic $2 - 10$ keV X-ray luminosity of $L_X = 10^{45}$ erg s $^{-1}$. Without clumping, this wind would be over-ionized to the extent that opacities in e.g., C IV would be entirely negligible (see H13).

One common way to quantify the ionization state of a plasma is through the ionization parameter, U_H , given by equation 3.103. Shown in Fig. 5.4, the ionization parameter is a useful measure of the global ionization state, as it represents the ratio of the number density of H ionizing photons to the local H density. It is, however, a poor representation of the ionization state of species such as C IV as it encodes no information about the shape of the SED. In this case, the X-ray photons are dominant in the photoionization of the UV resonance line ions. This explains why a factor of 100 increase in X-ray luminosity requires a clumping factor of 0.01, even though the value of U_H decreases by only a factor of ~ 10 compared to H13.

The total line luminosity also increases dramatically compared to the unclumped model described by H13. This is because the denser outflow can absorb the increased X-ray luminosity without becoming over-ionized, leading to a hot plasma which produces strong collisionally excited line emission. This line emission typically emerges on the edge of the wind nearest the central source. The location of the line emitting regions is dependent on the ionization state, as well as the incident X-rays. The radii of these emitting regions is important, and can be compared to observations. The line luminosities, L , shown in the figure correspond to the luminosity in erg s $^{-1}$ of photons escaping the Sobolev region for each line. As shown in Fig. 5.4, the C IV 1550Å line in the fiducial model is typically formed between $100 - 1000 r_G$ ($\sim 10^{17} - 10^{18}$ cm). This is in rough agreement with the reverberation mapping results of Kaspi et al. (2007) for the $2.6 \times 10^9 M_\odot$ quasar S5 0836+71, and also compares favourably with microlensing measurements of the size of the C IV 1550Å emission line region in the BALQSO H1413+117 (O'Dowd et al. 2015).

5.3.2 Synthetic Spectra: Comparison to Observations

Fig. 5.6 shows the synthetic spectrum in the UV from the fiducial model. To assess the ability of the synthetic spectra to match real quasar spectra, I also show *Sloan Digital Sky Survey* (SDSS) quasar composites from Reichard et al. (2003), normalised to the flux at 2000Å for low inclinations. Unfortunately, the wide variety of line profile shapes and internal trough structure in BALQSOs tends to ‘wash out’ BAL troughs in composite

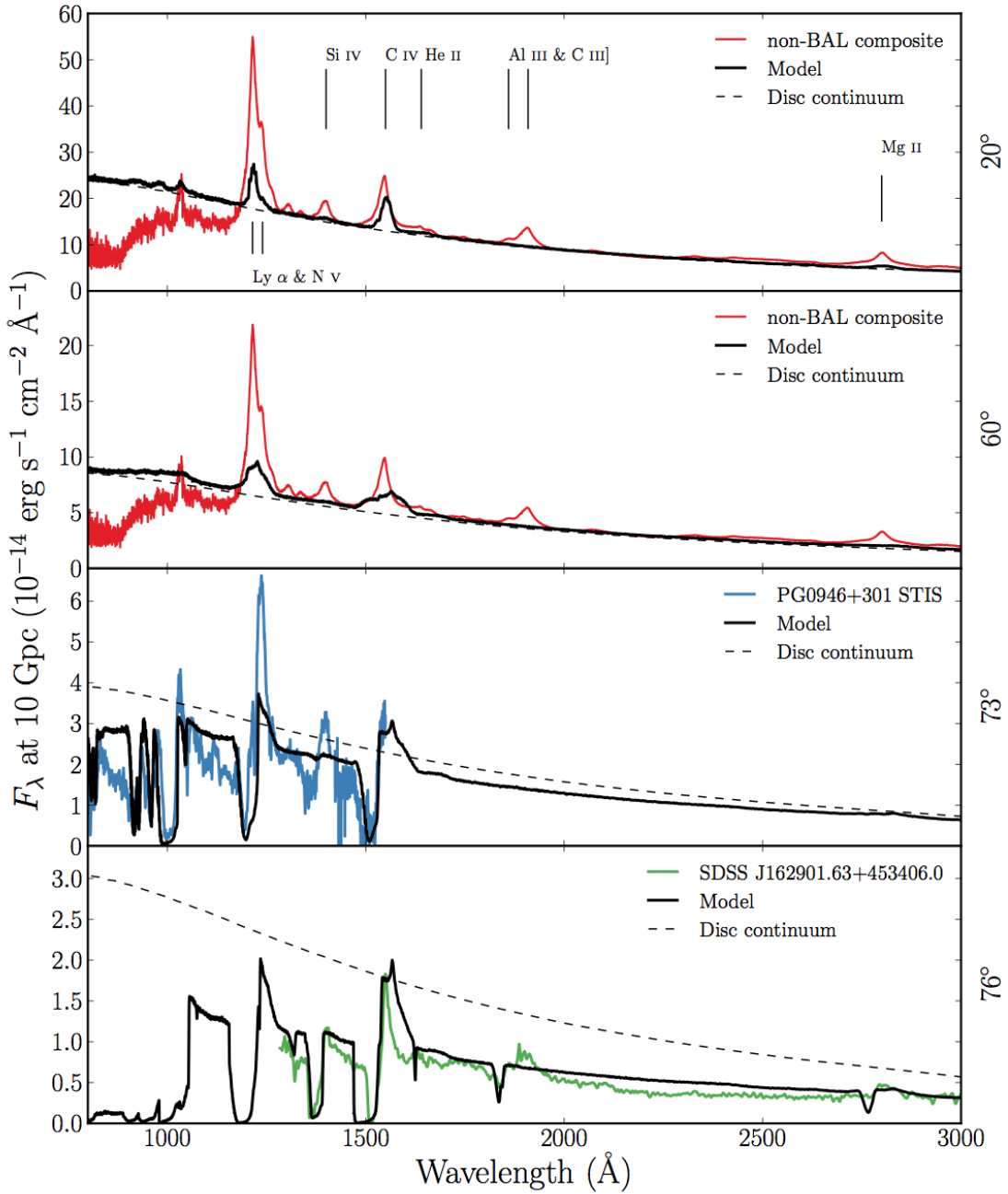


FIGURE 5.6: Synthetic spectra at four viewing angles for the fiducial model. At 20° and 60° I show a comparison to an SDSS quasar composite from Recihard et al. (2003). At 73° and 76° I show a comparison to an *HST* STIS spectrum of the high BALnicity BALQSO PG0946+301 (Arav et al. 2000), and an SDSS spectrum of the LoBAL quasar SDSS J162901.63+453406.0, respectively. The dotted line shows a disc only continuum to show the effect of the outflow on the continuum level. All the spectra are scaled to the model flux at 2000\AA , except for the *HST* STIS spectrum of PG0946+301, which is scaled to 1350\AA due to the incomplete wavelength coverage.

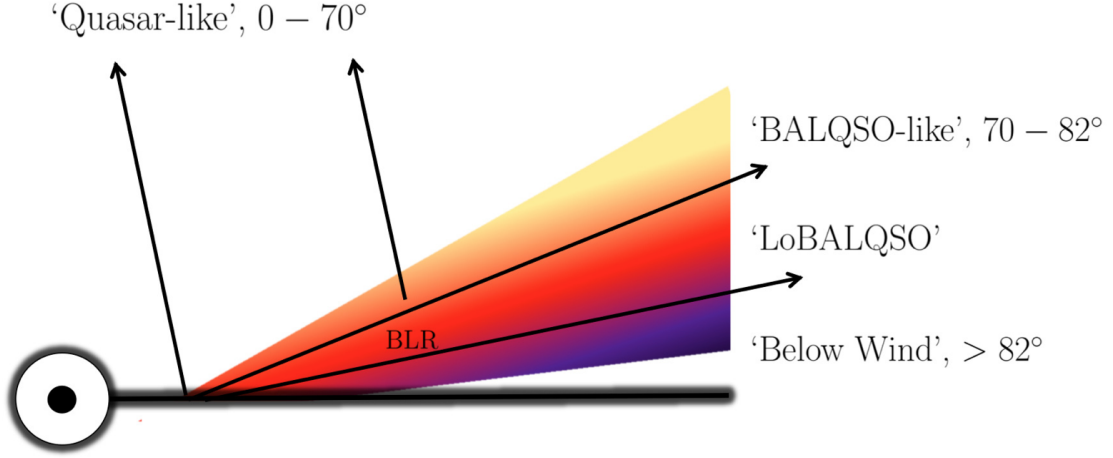


FIGURE 5.7: A cartoon describing the broad classes of sightline in the fiducial model, illustrating how geometric effects lead to the different emergent spectra. The colour gradient is approximate, but indicates the stratified ionization structure, from highly ionized (yellow) to low ionization (purple) material.

spectra to the extent that BALQSO composites do not resemble typical BALQSOs. Because of this, I instead compare to a *Hubble Space Telescope* STIS spectrum of the high BALnicity BALQSO PG0946+301 (Arav et al. 2000), and an SDSS spectrum of the LoBAL quasar SDSS J162901.63+453406.0, for the angles of 73° and 76° , respectively. A cartoon illustrating how geometric effects determine the output spectra is shown in Fig. 5.7.

5.3.2.1 Broad absorption lines ('BALQSO-like' angles)

The UV spectrum is characterised by strong BAL profiles at high inclinations ($> 70^\circ$). This highlights the first success of the model: clumping allows the correct ionization state to be maintained in the presence of strong X-rays, resulting in large resonance line opacities. At the highest inclinations, the cooler, low ionization material at the base of the wind starts to intersect the line of sight. This produces multiple absorption lines in species such as Mg II, Al III and Fe II. The potential links to LoBALQSOs and FeLoBALQSOs are discussed in section 2.4.

The high ionization BAL profiles are often saturated, and the location in velocity space of the strongest absorption in the profile varies with inclination. At the lowest inclination BAL sight lines, the strongest absorption occurs at the red edge, whereas at higher

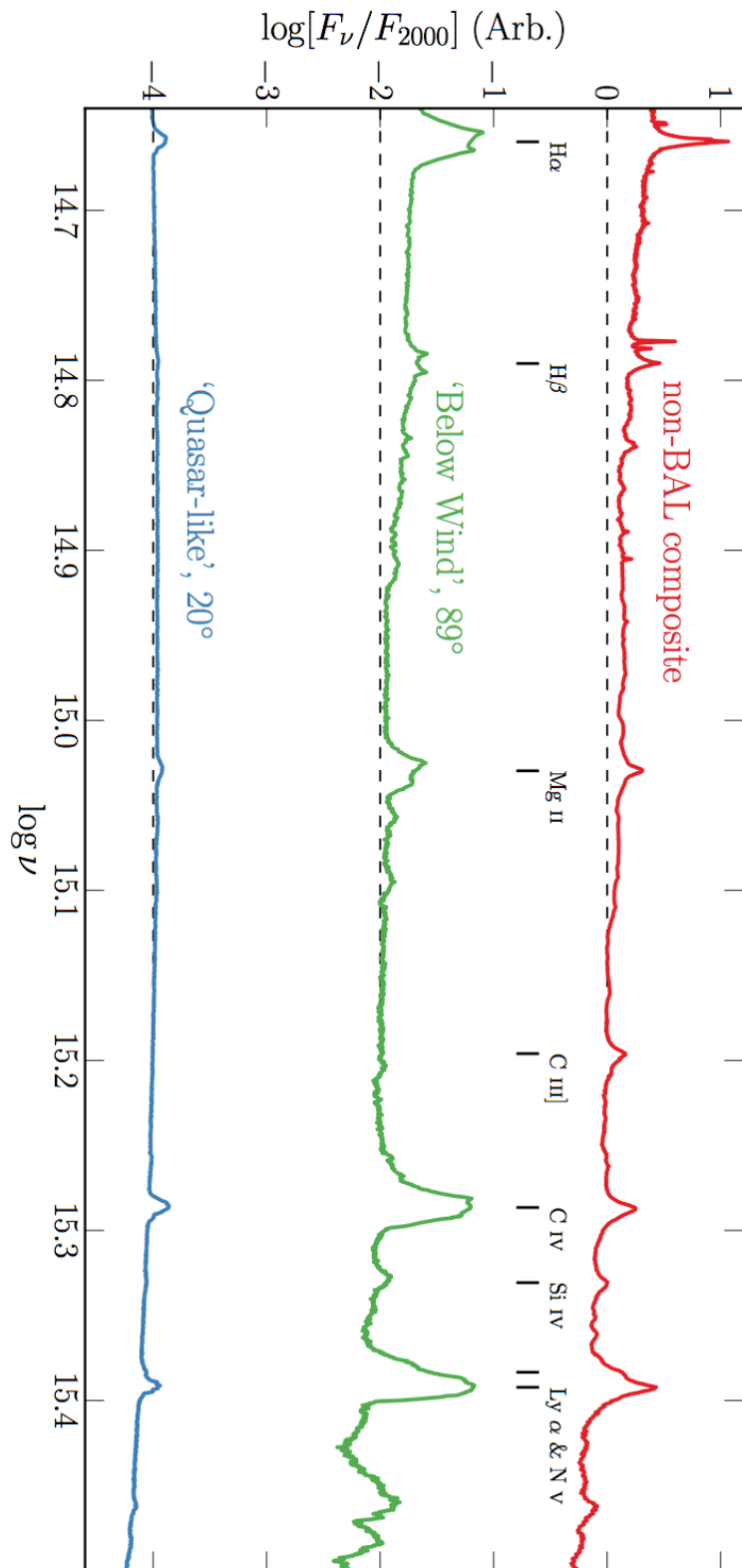


FIGURE 5.8: Synthetic spectra at two viewing angles, this time in frequency space and including the optical band, compared to the non-BAL SDSS quasar composite. The spectra are normalised to the flux at 2000Å, then an offset of 2 is applied per spectrum for clarity – the dotted lines show the zero point of F_ν/F_{2000} in each case.

Property	Synthetic, 20°	Observed (S11)
$\log L[\text{C IV}]$	44.60	44.42 ± 0.32
$\log L[\text{Mg II}]$	43.92	43.54 ± 0.28
$\log(\nu L_\nu)_{1350}$	46.42	46.01 ± 0.30
$\log(\nu L_\nu)_{3000}$	46.18	45.79 ± 0.30

TABLE 5.3: Some derived spectral properties of the fiducial model, at 20°, compared to observations. The observed values are taken from the Shen et al. (2011) SDSS DR7 Quasar catalog, and correspond to mean values with standard deviations in log space from a subsample with $8.5 > \log(M_{BH}) < 9.5$ and $1.5 < \log(L_{bol}/L_{Edd}) < 0$, where the BH mass is a C IV virial estimate. Units are logarithms of values in erg s⁻¹.

inclinations (and for the strongest BALs) the trough has a sharp edge at the terminal velocity. This offers one potential explanation for the wide range of BALQSO absorption line shapes (see e.g. [Trump et al. 2006](#); [Knigge et al. 2008](#); [Filiz Ak et al. 2014](#)).

The absorption profiles seen in BALQSOs are often non-black, but saturated, with flat bases to the absorption troughs ([Arav et al. 1999a,b](#)). This is usually explained either as partial covering of the continuum source or by scattered contributions to the BAL troughs, necessarily from an opacity source not co-spatial with the BAL forming region. The scattered light explanation is supported by spectropolarimetry results ([Lamy & Hutsemékers 2000](#)). Our spectra do not show non-black, saturated profiles. Black, saturated troughs are seen at angles $i > 73^\circ$, and the BALs are non-saturated at lower inclinations. The reasons for this are inherent in the construction of the model. First, the microclumping assumption does not allow for porosity in the wind, meaning that it does not naturally produce a partial covering absorber. To allow this, an alternative approach such as *macroclumping* would be required (e.g. [Hamann et al. 2008](#); [Šurlan et al. 2012](#)). Second, the wind does not have a significant scattering contribution along sightlines which do not pass through the BAL region, meaning that any scattered component to the BAL troughs is absorbed by line opacity. This suggests that either the scattering cross-section of the wind must be increased (with higher mass loss rates or covering factors), or that an additional source of electron opacity is required, potentially in a polar direction above the disc. I note the scattering contribution from plasma in polar regions is significant in some ‘outflow-from-inflow’ simulations ([Kurosawa & Proga 2009](#); [Sim et al. 2012](#)).

5.3.2.2 Broad emission lines ('quasar-like' angles)

Unlike H13, significant collisionally excited line emission now emerges at low inclinations in the synthetic spectra, particular in the C IV and N V lines. Strong Ly α and weak He II 1640Å lines are also observed as a result of the improved treatment of recombination using macro-atoms. In the context of unification, this is a promising result, and shows that a biconical wind can produce significant emission at 'quasar-like' angles. To demonstrate this further, I show line luminosities and monochromatic continuum luminosities from the synthetic spectra in Table 5.3. These are compared to mean values from a subsample of the SDSS DR7 quasar catalog (Shen et al. 2011) with BH mass and Eddington fraction estimates similar to the fiducial model values (see caption). The spectra do not contain the strong C III] 1909Å line seen in the quasar composite spectra, but this is due to a limitation of the current treatment of C; semi-forbidden (intercombination) lines are not included in this modelling.

In Fig. 5.8, I show an F_ν spectrum with broader waveband coverage that includes the optical, showing that the synthetic spectra also exhibit H α and H β emission. In this panel, I include a low inclination and also a very high inclination spectrum, which looks underneath the wind cone. This model shows strong line emission with very similar widths and line ratios to the quasar composites, and the Balmer lines are double peaked, due to velocity projection effects. Such double-peaked lines are seen in so-called 'disc emitter' systems (e.g. Eracleous & Halpern 1994) but not the majority of AGN. The line equivalent widths (EWs) increase at high inclination due to a weakened continuum from wind attenuation, disc foreshortening and limb darkening. This effect also leads to a redder continuum slope, as seen in quasars, which is due to Balmer continuum and Balmer and Fe II line emission. This extreme 89° viewing angle cannot represent a typical quasar within a unified model, but does show that a model such as this can naturally reproduce quasar emission lines if the emissivity of the wind is increased *with respect to the disc continuum*. In addition, it neatly demonstrates how a stratified outflow can naturally reproduce the range of ionization states seen in quasars.

Despite a number of successes, there are some properties of the synthetic spectra that are at odds with the observations. First, the ratios of the EW of the Ly α and Mg II 2800Å lines to the EW of C IV 1550Å are much lower than in the composite spectra. Similar problems have also been seen in simpler photoionization models for

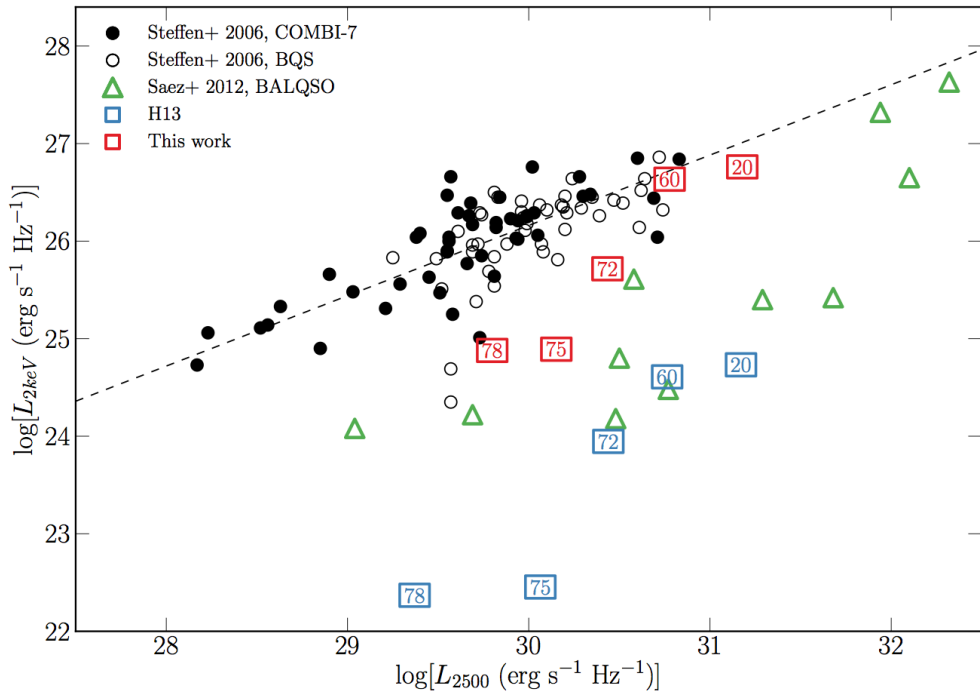


FIGURE 5.9: X-ray (2 keV) luminosity of the clumped model (red squares) and the H13 model (blue squares), plotted against monochromatic luminosity at 2500Å. The points are labeled according to inclination; angles $> 70^\circ$ correspond to BALs in this scheme (see figure 4). Also plotted are measurements from the COMBI-7 AGN and the BQS samples (Steffen et al. 2006) and the Saez et al. (2012) sample of BALQSOs. The dotted line shows the best fit relation for non-BALQSOs from Steffen et al. (2006).

the BLR (Netzer 1990). It may be that a larger region of very dense ($n_e \sim 10^{10} \text{ cm}^{-3}$) material is needed, which could correspond to a disc atmosphere or ‘transition region’ (see e.g. Murray et al. 1995; Knigge et al. 1998a). While modest changes to geometry may permit this, the initial grid search did not find a parameter space in which the Ly α or Mg II EWs were significantly higher (see section 5.4.1). Second, EWs increase with inclination (see Fig. 5.6 and Fig. 5.8; also Fig. 5.10). This is discussed further in section 5.4.2.

5.3.3 X-ray Properties

The main motivation for adding clumping to the model was to avoid over-ionization of the wind in the presence of strong X-rays. Having verified that strong BALs appear in the synthetic spectra, it is also important to assess whether the X-ray properties of this fiducial model agree well with quasar and BALQSO samples for the relevant inclinations.

Fig. 5.9 shows the emergent monochromatic luminosity (L_ν) at 2 keV and plotted against L_ν at 2500Å for a number of different viewing angles in the model. The monochromatic luminosities are calculated from the synthetic spectra and thus include the effects of wind reprocessing and attenuation. In addition to model outputs, I also show the BALQSO sample of Saez et al. (2012) and luminous AGN and quasar samples from Steffen et al. (2006). The best fit relation from Steffen et al. (2006) is also shown. For low inclination, ‘quasar-like’ viewing angles, the model properties are in excellent agreement with AGN samples. The slight gradient from 20° to 60° in the models is caused by a combination of disc foreshortening and limb-darkening (resulting in a lower L_{2500} for higher inclinations), and the fact that the disk is opaque, and thus the X-ray source subtends a smaller solid angle at high inclinations (resulting in a lower L_{2keV} for higher inclinations).

The high inclination, ‘BALQSO-like’ viewing angles show moderate agreement with the data, and are X-ray weak due to bound-free absorption and electron scattering in the wind. Typically, BALQSOs show strong X-ray absorption with columns of $N_H \sim 10^{23} \text{ cm}^{-2}$ (Green & Mathur 1996; Mathur et al. 2000; Green et al. 2001; Grupe et al. 2003b). This is often cited as evidence that the BAL outflow is shielded from the X-ray source, especially as sources with strong X-ray absorption tend to exhibit deep BAL troughs and high outflow velocities (Brandt et al. 2000; Laor & Brandt 2002; Gallagher et al. 2006). Our results imply that the clumpy BAL outflow itself can be responsible for the strong X-ray absorption, and supports Hamann et al.’s (2013) suggestion that geometric effects explain the weaker X-ray absorption in mini-BALs compared to BALQSOs.

5.3.4 LoBALs and Ionization Stratification

At high inclinations, the synthetic spectra exhibit blue-shifted BALs in Al III and Mg II – the absorption lines seen in LoBALQSOs – and even show absorption in Fe II at the highest inclinations. Line profiles in velocity space for C IV, Al III and Mg II, are shown in Fig. 5.10 for a range of BALQSO viewing angles. Ionization stratification of the wind causes lower ionization material to have a smaller covering factor, as demonstrated by figures 5.4 and 5.10. This confirms the behaviour expected from a unification model such as Elvis (2000). LoBALs are only present at viewing angles close to edge-on ($i > 75^\circ$),

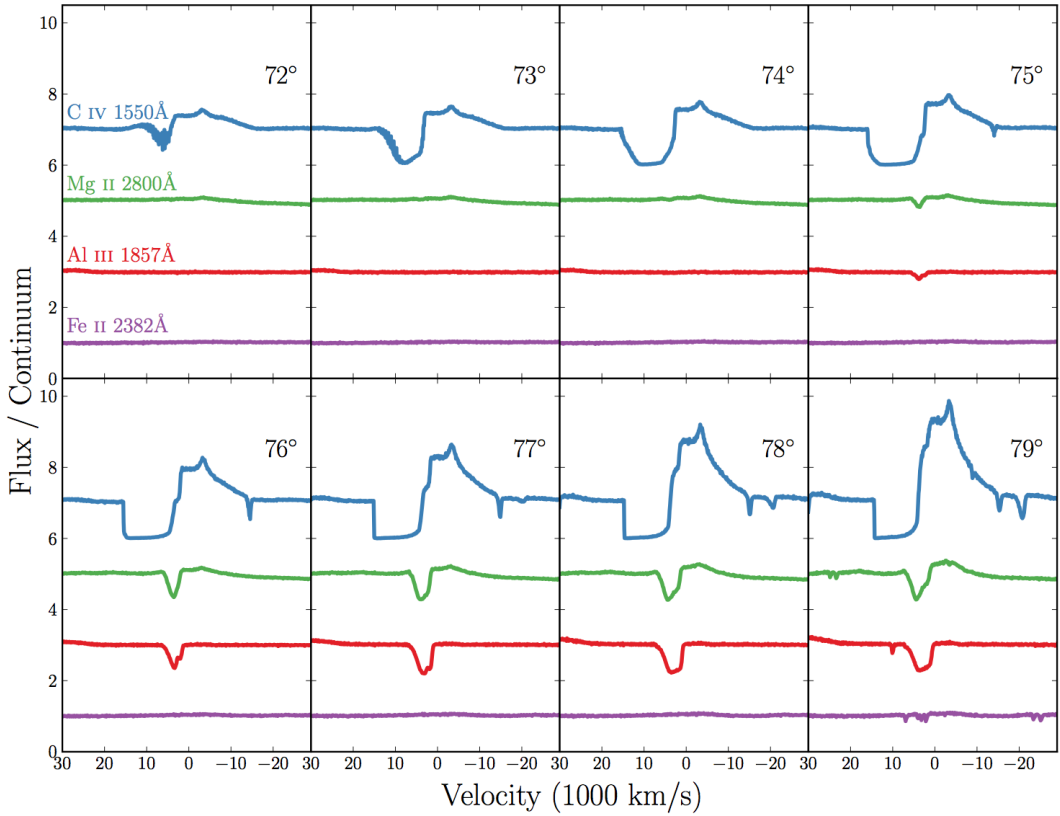


FIGURE 5.10: C IV, Mg II, Al III and Fe II line profiles for viewing angles from 72° – 79° . The profiles are plotted relative to the local continuum with an offset applied for clarity. Lower ionization profiles appear at a subset of high inclinations, compared to the ubiquitous C IV profile.

as predicted by polarisation results (Brotherton et al. 1997). As observed in a BALQSO sample by Filiz Ak et al. (2014), the model BAL troughs are wider and deeper when low ionization absorption features are present, and high ionization lines have higher blue-edge velocities than the low ionization species. There is also a correlation between the strength of LoBAL features and the amount of continuum attenuation at that sightline, particularly blueward of the Lyman edge as the low ionization base intersects the line-of-sight. A model such as this therefore predicts that LoBALQSOs and FeLoBALQSOs have stronger Lyman edge absorption and are more Compton-thick than HiBALQSOs and Type 1 quasars. An edge-on scenario also offers a potential explanation for the rarity of LoBAL and FeLoBAL quasars, due to a foreshortened and attenuated continuum, although BAL fraction inferences are fraught with complex selection effects (Goodrich 1997; Krolik & Voit 1998).

5.4 Discussion

5.4.1 Parameter Sensitivity

Having selected an individual fiducial model from the simulation grid, it is important to briefly explore how specialised this model is, and how small parameter changes can affect the synthetic spectra. Fig. 5.11 shows the EW at a low inclination, and BI at a high inclination for the simulation grid. A few conclusions can be drawn from this plot straight away. First, almost all the models with $f_V = 0.1$ are over-ionized, and fail to produce strong C IV BALs or emission lines. Second, it is difficult to significantly increase line emission while keeping the luminosity and mass loss rate of the system fixed. I show an additional point on figure 7 corresponding to a model with an order of magnitude higher X-ray luminosity and double the mass loss rate. As expected, this results in far higher line EWs, but fails to produce BALs because the collisionally excited emission swamps the BAL profile. In addition, this model would lie well above the expected $L_{2kev} - L_{2500}$ relation in figure 5. Such a high X-ray luminosity could therefore not be the cause of the strong line emission seen in *all* Type 1 quasars.

The parameter search presented here is by no means exhaustive, and conclusions may be limited by the specific parameterisation of the outflow kinematics used. Nevertheless, I suggest that the angular distribution of both the line and continuum emission is perhaps the crucial aspect to understand. With this in mind, obtaining reliable orientation indicators appears to be a crucial observational task if we are to further our understanding of BAL outflows and their connection, or lack thereof, to the broad line region.

5.4.2 Inclination Trends: FWHM and EW

EW increases with inclination in the fiducial model. This trend means that even though significantly denser models can match the line EWs fairly well at low inclinations, they will then possess overly strong red wings to the BAL P-Cygni profiles at high inclinations. The fact that the EW increase in this model are directly related to limb-darkening and foreshortening of the continuum. This appears to contradict observations, which show remarkably uniform emission line properties in quasars and BALQSOs (Weymann et al. 1991; DiPompeo et al. 2012a).

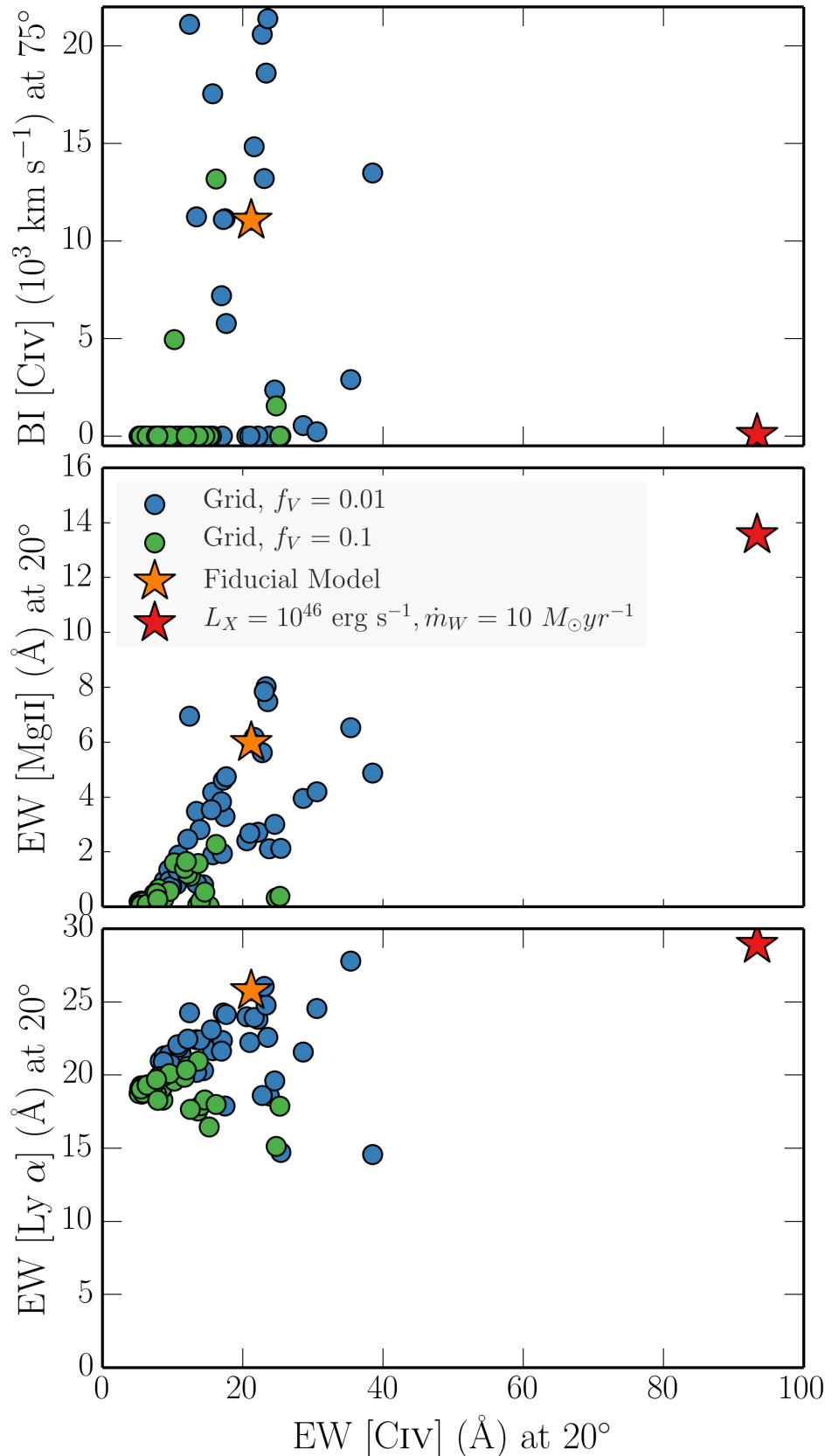


FIGURE 5.11: The EW of the C IV 1550 Å line at 20° plotted against a) the BI of C IV 1550 Å at 75°, b) the EW of the Mg II 2800 Å line at 20° and c) the EW of Ly α at 20°. The circles correspond to the simulation grid for two different values of f_V , and the fiducial model is marked with an orange star. I also show a higher X-ray luminosity model and a higher mass loss rate with a red star.

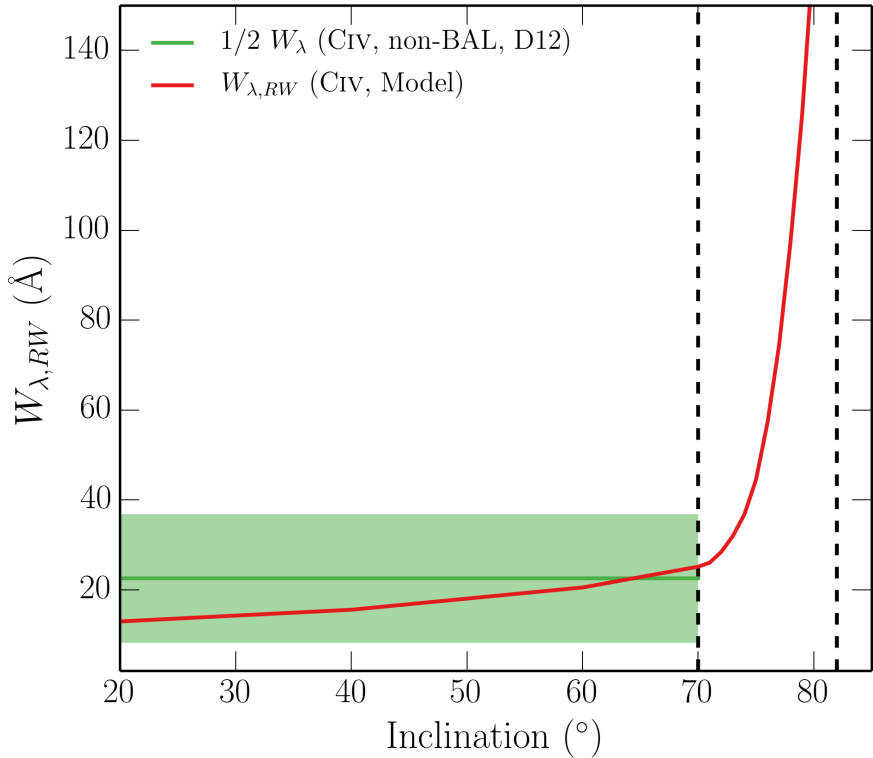


FIGURE 5.12: $W_{\lambda,RW}$ as a function of inclination in the fiducial model, compared to $1/2$ EW from the quasar sample of Di Pompeo et al. (2012; D12).

In order to quantitatively assess how emission lines change with inclination when blue-shifted absorption may affect the line profile, I define the ‘red wing equivalent width’ ($W_{\lambda,RW}$) as

$$W_{\lambda,RW} = \int_{\lambda_0}^{\lambda'} \left(1 - \frac{F_\lambda}{F_0} \right) d\lambda \quad (5.5)$$

where F_0 is the continuum flux and the integral is calculated from λ_0 , line centre, to a wavelength λ' where the flux has returned to the continuum level. This quantity is shown as a function of inclination in Fig. 5.12 for the C IV UV line. The $W_{\lambda,RW}$ expected from isotropic line emission and a foreshortened and limb darkened disc and $1/2$ equivalent widths from DiPompeo et al. (2012a) are also shown.

The variation of EW with inclination is significantly larger than the variation across the quasar population. The angular distribution of the disc continuum and line emission is clearly crucially important in determining the emergent broad line EWs, as suggested by, e.g., the analysis of Risaliti et al. (2011). I shall explore this question further in chapter 6.

5.4.2.1 FWHM and Black Hole Mass Estimates

In a recent study, [Yong et al. \(2016\)](#) used the SV93 wind prescription assess the variation of full-width at half-maximum (FWHM) of H β (and resultant BH mass estimates) with inclination in a disc wind model. Although their model is fairly simple – it does not include, for example, full radiative transfer or ionization physics – this analysis still gives interesting insights into how emission lines from a disc wind might bias BH mass estimates.

If the BLR gas is virialised, as often assumed, then the black hole mass is related to the velocity dispersion, Δv , of the gas by

$$M_{BH} = f \frac{\Delta v^2 R_{BLR}}{G}, \quad (5.6)$$

where R_{BLR} is some appropriate emissivity-weighted radius and is often either assumed, estimated from ionization arguments or calculated from reverberation mapping. When using FWHM to estimate the velocity dispersion the above equation can be rewritten as

$$M_{BH} = f_{FWHM} \left[c \frac{(FWHM)}{\lambda_0} \right]^2 \frac{R_{BLR}}{G}, \quad (5.7)$$

where λ_0 is the central wavelength of the line in question and the FWHM is in the same wavelength units. In a model such as this the BH mass is known, and determines the escape velocities and rotational motions of the outflow. Thus, using a typical radius for line formation in the model it is trivial to calculate f_{FWHM} for each viewing angle. Fig. 5.13 shows f_{FWHM} as a function of inclination for the C IV, Mg II and H α emission lines in the fiducial model, assuming $R_{BLR} = 10^{17}$ cm. For C IV and Mg II the wind angles are not plotted as BAL profiles affect the measurement, and I have compared to H α rather than H β due to the low H β luminosity at some viewing angles. Nevertheless, this value should trace f_{FWHM} from H β fairly well.

The values from the model presented here agree fairly well with the predictions of [Yong et al. \(2016\)](#) from their simpler analysis, suggesting that, at least in this specific set-up, radiative transfer and ionization has a minimal role in determining the emergent FWHM. Instead, the effect is dominated by velocity projection effects. The reason for the significantly lower values for Mg II is that it is actually formed well inside $R_{BLR} =$

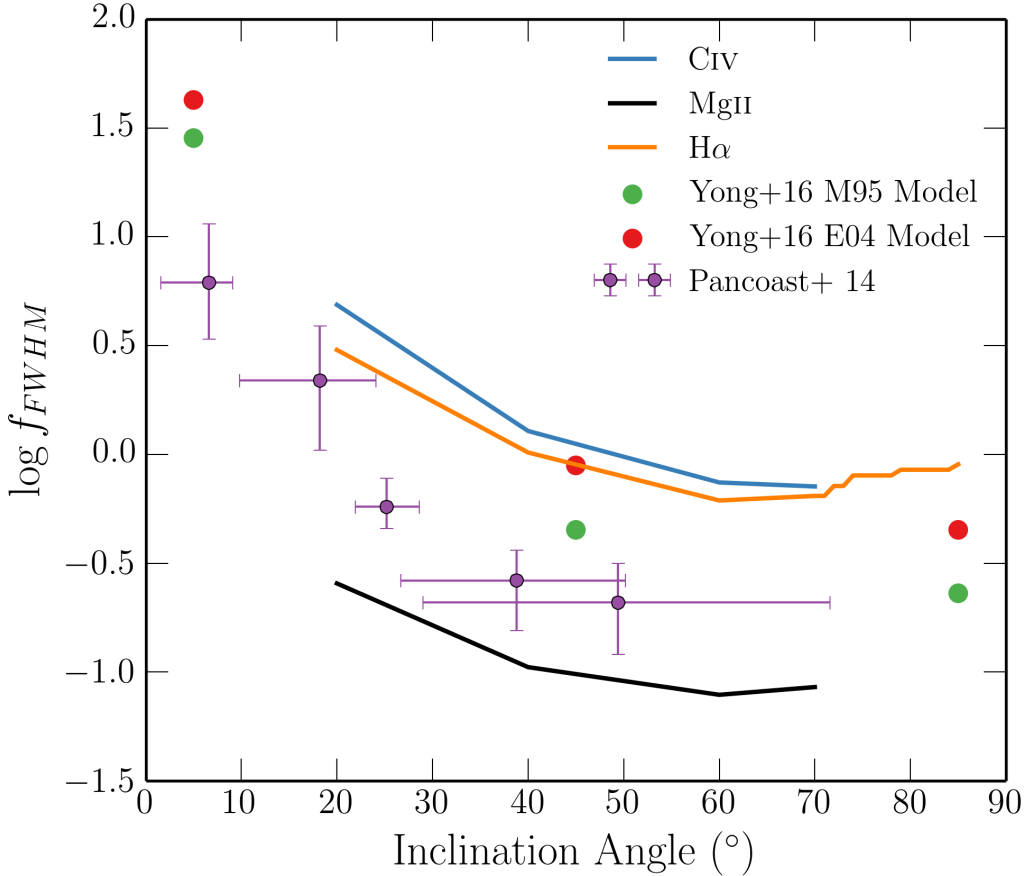


FIGURE 5.13: f_{FWHM} as a function of inclination from the fiducial model for three different lines, compared to values from Yong et al. 2016 and Pancoast et al. 2014.

10^{17} cm, highlighting the dangers of using a single BLR radius for BH mass estimates from different lines.

5.5 Summary And Conclusions

I have carried out MCRT simulations using a simple prescription for a biconical disc wind, with the aim of expanding on the work of H13. To do this, two main improvements were necessary: First, I included a simple treatment of clumping, and second, the modelling of recombination lines was improved by treating H and He as ‘macro-atoms’. Having selected a fiducial model from an initial simulation grid, I assessed the viability of such a model for geometric unification of quasars, and found the following main points:

1. Clumping moderates the ionization state sufficiently to allow for the formation of strong UV BALs while agreeing well with the X-ray properties of luminous AGN and quasars.
2. A clumpy outflow model naturally reproduces the range of ionization states expected in quasars, due to its stratified density and temperature structure. LoBAL line profiles are seen at a subset of viewing angles, and Fe II absorption is seen at particularly high inclinations.
3. The synthetic spectra show Ly α line and weak He II 1640Å line as a result of the improved treatment of recombination using macro-atoms. Balmer emission lines and a Balmer recombination continuum are also seen in the optical spectrum, but this is only really significant at high inclination where the continuum is suppressed.
4. The higher X-ray luminosity causes a significant increase in the strength of the collisionally excited emission lines produced by the model. However, the equivalent-width ratios of the emission lines do not match observations, suggesting that a greater volume of dense ($n_e \sim 10^{10} \text{ cm}^{-3}$) material may be required.
5. The line EWs in the synthetic spectra increase with inclination. BAL and non-BAL quasar composites have comparable EWs, so the fiducial model fails to reproduce this behaviour. If the BLR emits fairly isotropically then for a foreshortened, limb-darkened accretion disc it is not possible to achieve line ratios at low inclinations that are comparable to those at high inclinations. I suggest that understanding the angular distribution of line and continuum emission is a crucial question for theoretical models.

This work confirms a number of expected outcomes from a geometric unification model, and suggests that a simple biconical geometry such as this can come close to explaining much of the phenomenology of quasars. However, these conclusions pose some challenges to a picture in which BALQSOs are explained by an *equatorial* wind rising from a classical thin disc, and suggest the angular distribution of emission is important to understand if this geometry is to be refuted or confirmed. I suggest that obtaining reliable observational orientation indicators and exploring a wider parameter space of outflow geometries in simulations are obvious avenues for future work.

Chapter 6

Quasar Emission Lines as Probes of Orientation and Unification

This chapter is based on a paper in preparation:

Matthews J. H., Knigge C., ‘Quasar Emission Lines as Probes of Orientation and Unification’, to be submitted to MNRAS.

6.1 Introduction

In the previous chapter, I presented tests of geometric unification models using MCRT and photoionization simulations. One of the key results from that analysis is that trends with inclination prohibit models with equatorial outflows matching observations, as the EW of the emission lines tend to increase with inclination. This trend has clear implications for the geometries of BAL outflows; the viewing angle may determine many of the selection effects at work and must therefore be understood before the true covering factor of BAL outflows can be accurately determined. The covering factor and opening angle of the outflow are important quantities to measure in order to calculate the feedback efficiency (e.g. [Borguet et al. 2012](#)), and make inferences about the outflow physics (e.g. [Proga 2005](#)).

Unlike in galactic accretion disc systems, measuring inclinations for quasars and AGN is notoriously difficult, and obtaining reliable orientation indicators is thus an important

observational goal for the community. Perhaps as a result of this problem, directly opposing geometries have been proposed for BAL outflows (see section ??). Here, I use observational data from the Sloan Digital Sky Survey to constrain the inclinations of BAL quasars. Similar attempts have been made previously with different diagnostics; for example, by considering radio measurements (Zhou et al. 2006; DiPompeo et al. 2012b), polarisation (Brotherton et al. 2006) and emission line properties (DiPompeo et al. 2012a).

This chapter is structured as follows. First, I describe the data sample and selection criteria being used. I begin by simply examining the distributions of the EW of the O III 5007Å emission line, EW[O III], and comparing the BAL and non-BAL quasar distributions. In section 6.3 I review the angular distribution of continuum emission one would expect from simple α -disc models, as well as exploring more advanced disc models computed with AGNSPEC. I then use these theoretical angular distributions applied to a simple toy model in section 6.4, and conduct MC simulations in an attempt to fit the observed LoBAL and non-BAL quasar distributions of EW[O III], using a similar approach to Risaliti et al. (2011). I also discuss the broad emission line distribution in HiBAL quasars more detail in this section. In section 6.5 I discuss the results in the context of radio and polarisation measurements of AGN, as well as exploring the location of BAL quasars in ‘Eigenvector 1’ parameter space. Finally, in section 6.6, I summarise the results.

6.2 Data Sample

The data sample is based upon the Shen et al. (2011, hereafter S11) catalog of 105,783 quasars from the The Sloan Digital Sky Survey (SDSS) Data Release 7 (DR7). As I will use emission line diagnostics in this study, this sample must be further divided according to which emission lines are present in the SDSS wavelength range at a given redshift. Sample A contains all quasars within the redshift range $0.35 < z < 0.83$, such that the Mg II 2800Å and O III 5007Å line EWs are both measured, and Mg II BAL identification is possible. Sample B contains all quasars within the redshift range $1.45 < z < 2.28$, such that the EWs and presence of BALs in Mg II 2800A and CIV 1550A are both measurable. The details of these samples are shown in table 1. The

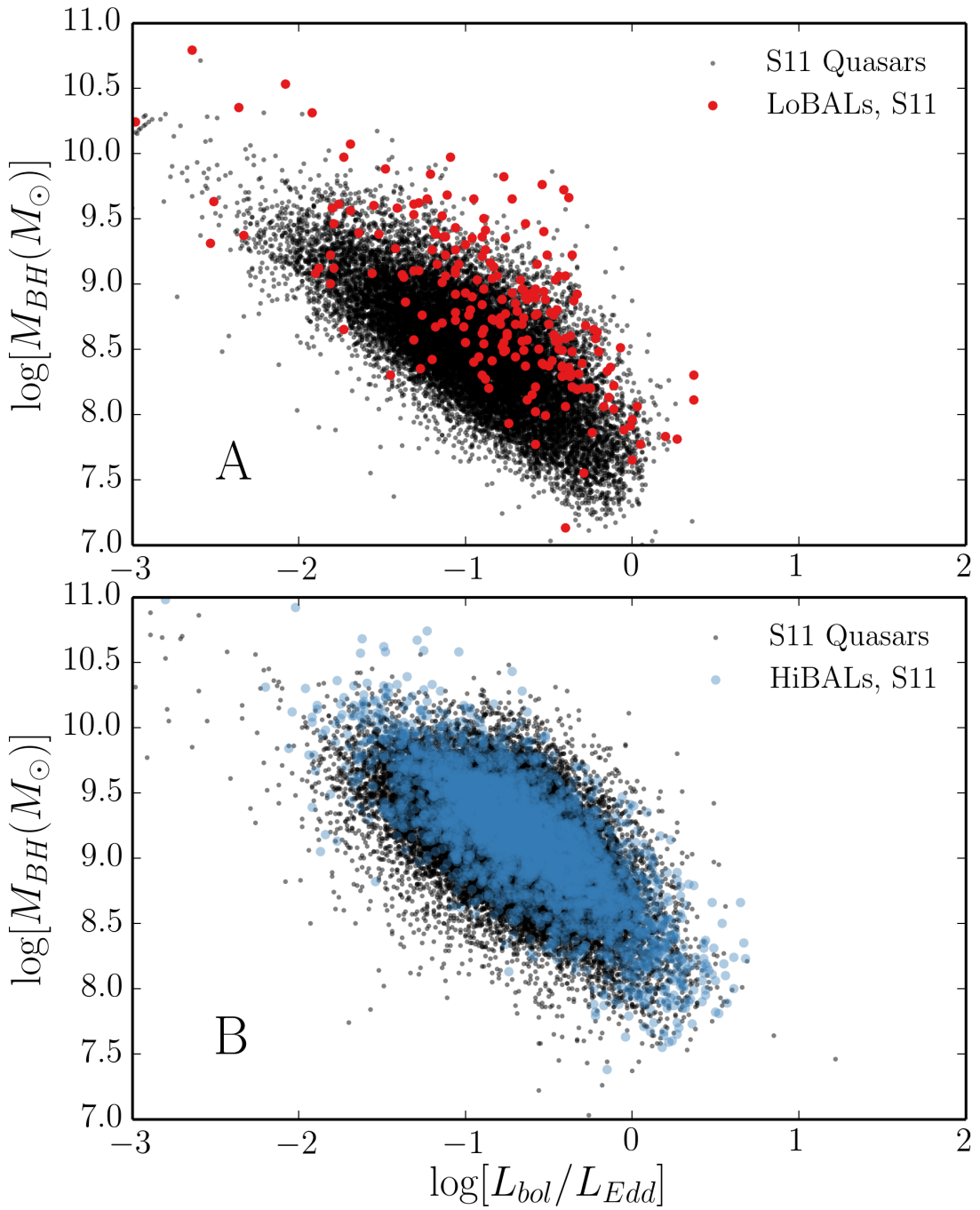


FIGURE 6.1: BH mass and Eddington fraction for the BAL samples plotted over the overall quasar sample from S11.

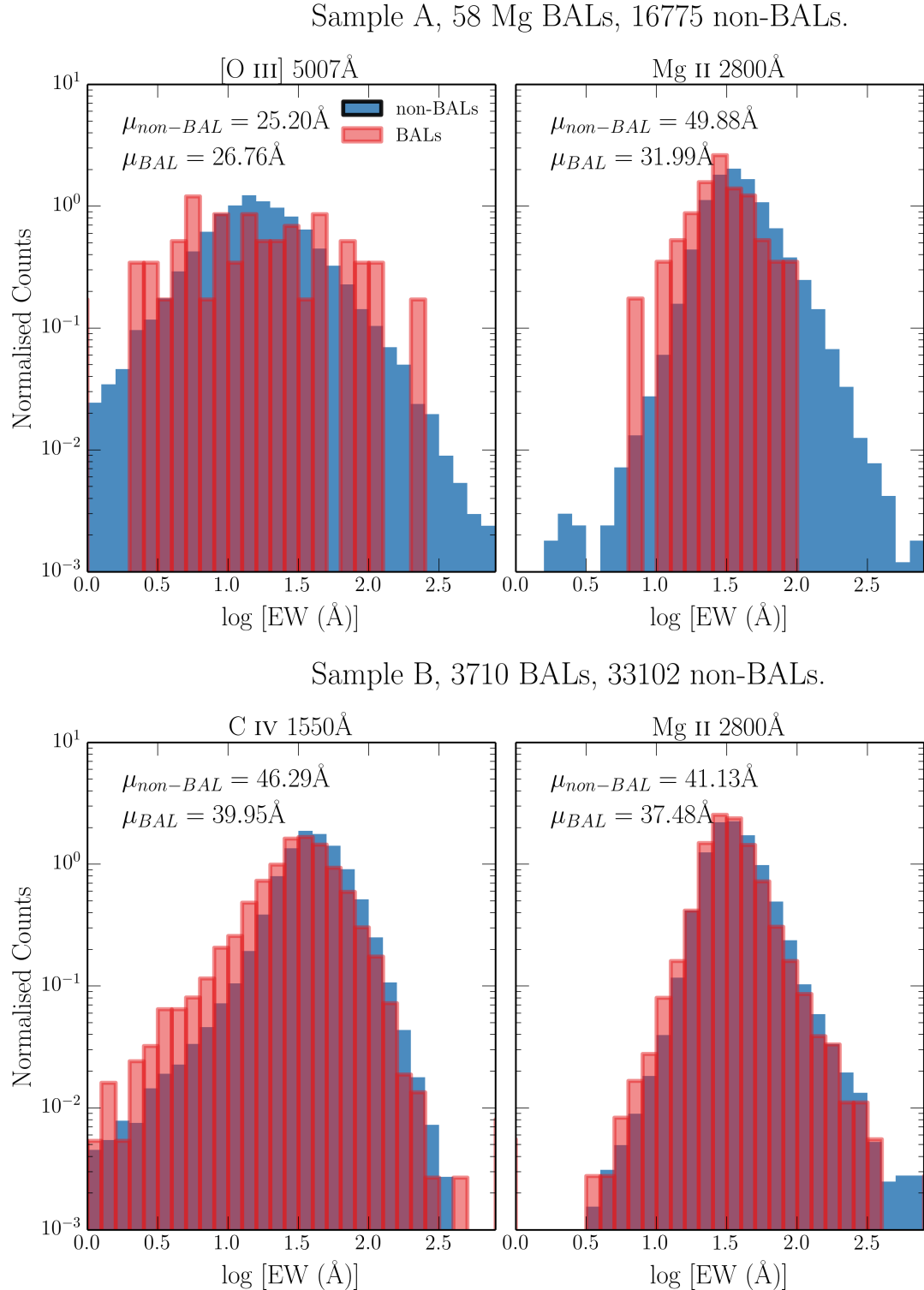


FIGURE 6.2: Histograms of equivalent widths for three emission lines from the two different samples.

mass and Eddington fraction measurements from S11 of the two samples, are shown in Fig. 6.1 against the background distribution of all S11 quasars.

S11 are careful to take into account traditional problems with quasar line fitting, such as narrow line or Fe pseudocontinuum contamination, in their fits to emission line profiles and resultant EW measurements. For Mg II 2800Å this includes careful subtraction of the Fe emission using the templates of (Vestergaard & Wilkes 2001). This subtraction is not included for C IV 1550Å, as the Fe emission is less prominent and harder to model. This may lead to a systematic overestimate by ~ 0.05 dex in the C IV line EW. The O III 5007Å line is fitted with a Gaussian and the flux ratio with the sister component of the doublet, O III 4959Å, is found to agree well with the theoretical expectation of around 3, implying a reliable subtraction of broad H β . To mask out the effects of e.g., absorption, on C IV, S11 ignore 3σ outliers in the fit to the profile. Based on these considerations, the S11 catalog makes for a reliable set of EW measurements. This is especially true when making inferences from multiple emission lines, as systematics inherent to individual lines or spectral windows are less likely to affect the analysis as a whole.

In attempting to draw broad conclusions about unification models as a whole, I would ideally construct a large, homogenous dataset of *HiBAL* and non-BAL quasars, both with O III 5007Å EWs. Unfortunately, the wavelength limits of SDSS do not allow this, and only LoBAL quasars have both BALs and EW[O III] measurements. One of the problems with using just LoBAL quasars as tests of unification is that there is evidence that they are drawn from a different population than normal quasars, perhaps suggesting an *evolutionary* origin. Examples include anomalously high LoBAL fractions in dust-reddened quasar samples (Urrutia et al. 2009) and infra-red selected samples (Dai et al. 2012); although see also Lazarova et al. (2012).

Fig. 2 shows histograms of a number of different emission line properties for samples A and B. As discussed by previous authors (e.g. Weymann et al. 1991), I find that BAL and non-BAL quasars really do seem to possess very similar emission line properties. The EW is related to the ‘face-on’ equivalent width, EW_0 by the equation

$$EW = EW_0 / \epsilon(\theta) \quad (6.1)$$

where θ is the viewing angle with respect to the symmetry axis and $\epsilon(\theta)$ is the ‘angular emissivity function’, which describes how the continuum luminosity from the disc varies as a function of viewing angle. For a foreshortened disc this is simply $\epsilon(\theta) = \cos \theta$.

Thus, if BAL quasars are viewed from a larger viewing angle on average then one would expect them to possess higher EWs, with a broader distribution. It is already apparent from figure 1 that the BAL distribution mean is not significantly higher than the non-BAL mean – in fact, in many cases it is lower. This is not expected from a model in which the continuum is foreshortened and BAL outflows are at all equatorial. This problem is examined further in section 6.4. First, I will examine the motivations for different forms of $\epsilon(\theta)$ in AGN and quasars.

6.3 The Angular Distribution of Emission from an Accretion Disc

As introduced in chapter 1, the most widely-used theoretical model for an accretion disc is the so-called ‘ α -disc’ model of SS73. There are a number of well-documented problems when fitting AGN SEDs with SS73 accretion disc models (see section 1.4). Despite these problems, Capellupo et al. (2015) recently had some success fitting spectra of AGN when the effects of GR, mass-loss and comptonisation were included. In this section, I start by discussing the angular distribution of emission from an SS73 disc, before exploring opacity and GR effects. In order to do so, I use AGNSPEC (Hubeny et al. 2000; Davis & Hubeny 2006; Davis et al. 2007). I stress that the discussion here is not limited to SS73 discs; the only real condition for the angular distributions derived here is that the disc is geometrically thin and optically thick.

6.3.1 Standard Thin Disc Models

Any geometrically thin, optically thick disc will appear foreshortened and limb darkened (if temperature decreases with height from the central disc plane). Foreshortening is a simple $\cos \theta$ geometric effect, where θ is the inclination with respect to the vertical z axis, which is perpendicular to the disc plane. Limb darkening, $\eta(\theta)$, is given by

$$\eta(\theta) = a(1 + b \cos \theta), \quad (6.2)$$

where a is a normalisation constant and b governs the strength of the limb darkening. $b = 3/2$, known as the Eddington approximation tends to give good agreement with solar observations (e.g. [Mihalas 1978](#)). The two effects can be combined to give an angular emissivity function, of

$$\epsilon(\theta) = a \cos \theta \left(1 + \frac{3}{2} \cos \theta \right). \quad (6.3)$$

6.3.2 Including GR, Comptonisation and Opacity Effects

In reality, limb darkening is not frequency independent and depends on the bound-free and bound-bound opacities in the disc. In addition, it has been shown that GR can ‘isotropize’ the radiation field in XRBs ([Zhang et al. 1997](#); [Muñoz-Darias et al. 2013](#)), in some cases overcoming foreshortening effects. To assess the impact of GR and disc opacities on $\epsilon(\theta)$ I use AGNSPEC models, which uses stellar atmosphere calculations to calculate the SED in a series of annuli, before using the KERRTRANS code to calculate the emergent SED by ray-tracing along Kerr geodesics. Fig. 6.3 shows $\epsilon(\theta)$ as a function of θ for AGNSPEC models for minimally and maximally spinning BHs, compared to foreshortened and limb-darkened predictions for SS73 models. Clearly, there is very little effect; the accretion disc is still strongly anisotropic in the relevant wavebands.

6.4 Predicted EW Distributions Compared to Observations

6.4.1 Fitting the Quasar Distribution

[Risaliti et al. \(2011\)](#), hereafter R11) analysed the EW[O III] distribution of 6029 quasars in SDSS DR5. They demonstrated that a foreshortened disc and isotropic O III 5007Å line produces a high EW tail to the distribution with a characteristic slope of $\Gamma_{EW} = -3.5$. In order to first reproduce their result and discuss its implications, I have created a sample according to their selection criteria. The criteria are that the object in question lies in the redshift range 0.01 to 0.8, have an absolute magnitude $M_i > 22$, an apparent magnitude $m_i > 19.1$, and signal to noise per pixel of greater than 5. Using the updated SDSS quasar sample of S11, this defines a sample of 14,424 quasars.

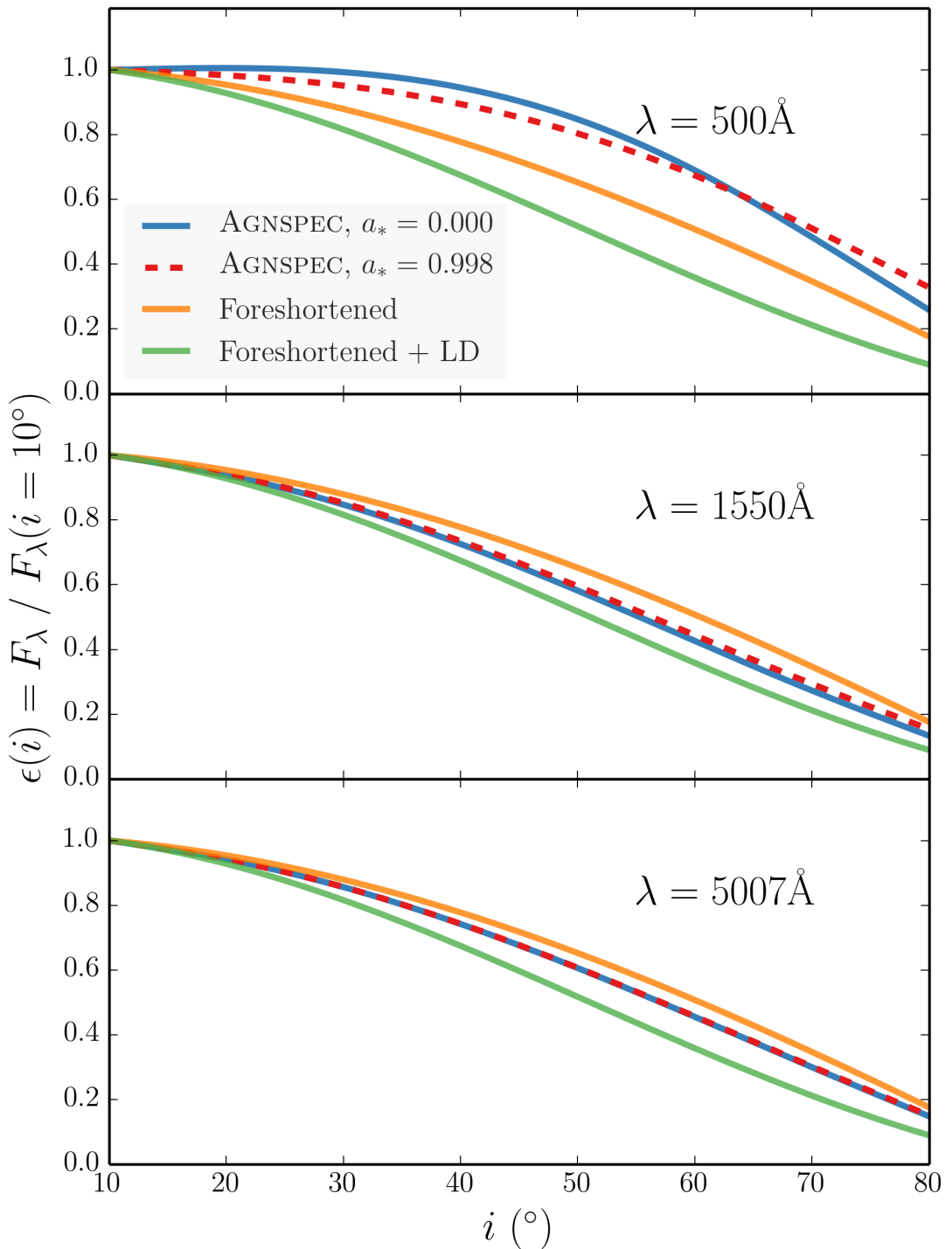


FIGURE 6.3: Monochromatic continuum luminosities from AGNSPEC and classical thin disc models.

To fit the distribution, I conduct the following procedure, which is similar to the method R11 use to demonstrate that the power law tail is expected.

1. A set of isotropic angles is chosen such that $P(\theta) \propto d\Omega(\theta)$. If $\theta < \theta_1$ then the fake object is designated as unobsured, and otherwise the object is ignored.
2. To be included in the sample, the object also has to survive a selection test to simulate the distribution of angles in a flux-limited sample. This is done by drawing a random sample from the real quasar sample, and calculating a ‘doubly observed continuum flux’, F_O at 5100Å (rest frame), such that $F_O = F_{5100} \epsilon(\theta)$. The flux limit is set at 5×10^{-13} erg s⁻¹ cm⁻¹ Å⁻¹, but the results are fairly insensitive to the limit chosen.
3. For each mock sample, an EW_* is drawn from an intrinsic (i.e. ‘face-on’) EW distribution for quasars. This is assumed to be a gaussian. The mean, μ_* , and width, σ_* , of this Gaussian can either be set arbitrarily – for example, to demonstrate trends in mock data – or obtained from a χ^2 fit to the observed EW distribution.
4. A mock EW is estimated such that $EW = EW_0/\epsilon(\theta)$, and this process is repeated to build up a mock sample of 10^6 objects.

The result of this numerical experiment is, as found by R11, a distribution with a high EW tail of slope -3.5 . I can now vary the maximum angle, θ_1 , and examine how this tail changes. Mock data for a series of maximum angles is shown in Fig. 6.4, for two different intrinsic Gaussians. The power law behaviour is only seen when the maximum angle is sufficiently large, and a rapid decay in the distribution is observed at a characteristic EW related to both the width and mean of the intrinsic distribution as well as the cosine of the maximum angle. The top panel has μ_* and σ_* of the R11 Model 1, whereas the bottom panel shows a narrower distribution to illustrate the earlier onset of the high EW cutoff. In principle, this cutoff could be used to infer information about the viewing angle distribution of quasars, but this is complicated by poor statistics in the tail, selection effects and lack of knowledge about the true face-on distribution.

Fig. 6.5 shows the result of a χ^2 minimization fit to the R11 sample. The best fit is achieved with a maximum angle of $\theta_1 = 84^\circ$ and a narrower intrinsic distribution than

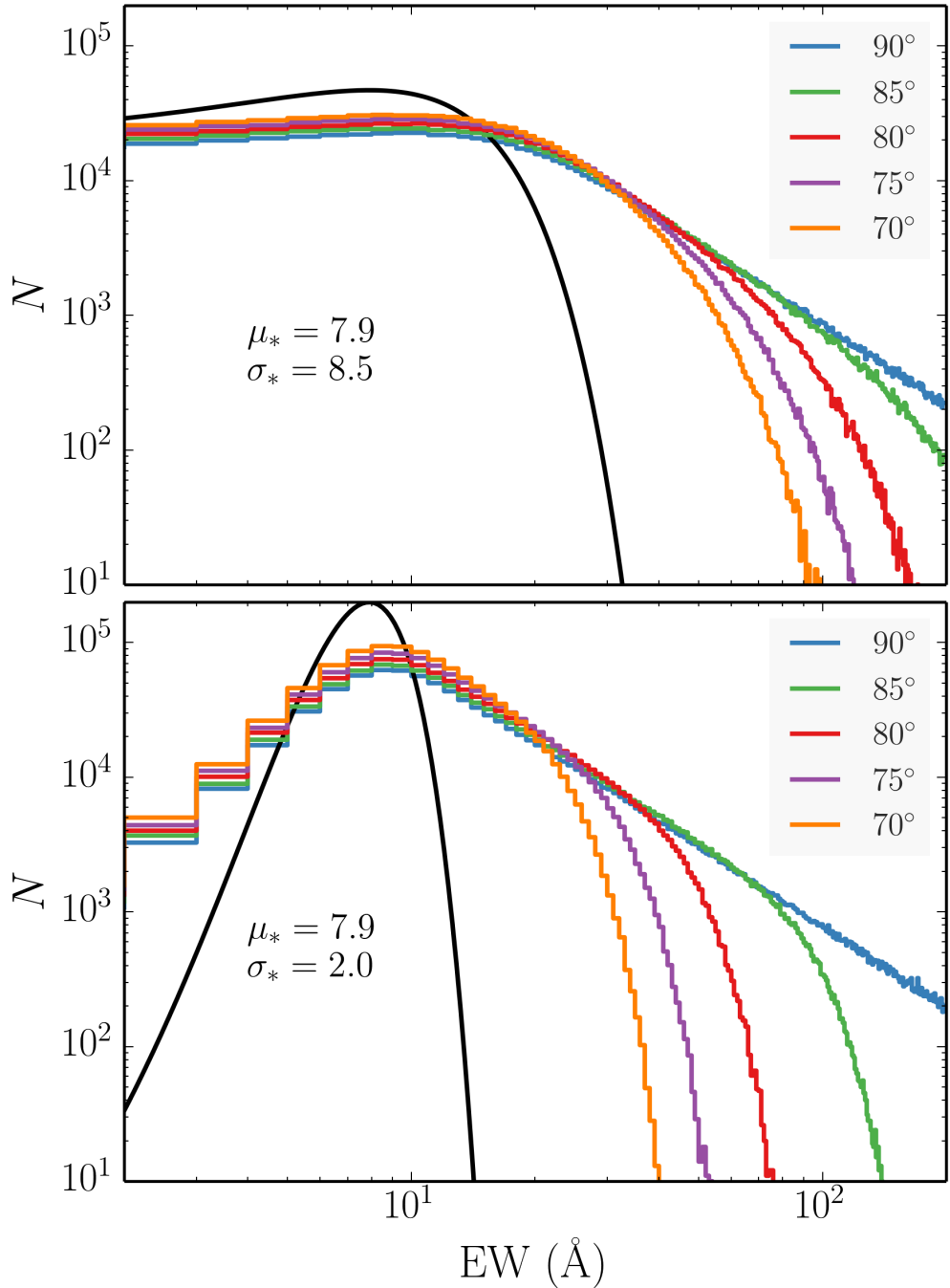


FIGURE 6.4: Theoretical Ew distributions from the numerical experiment described in section 6.4.1 for a few different maximum angles. The results in the top panel use the same intrinsic distribution as Model 1 from R11 (shown in black), whereas the bottom panel shows the distributions obtained from a narrower intrinsic Gaussian. By the time the maximum angle is limited to around 70° the cutoff is clear even at moderate values of EW.

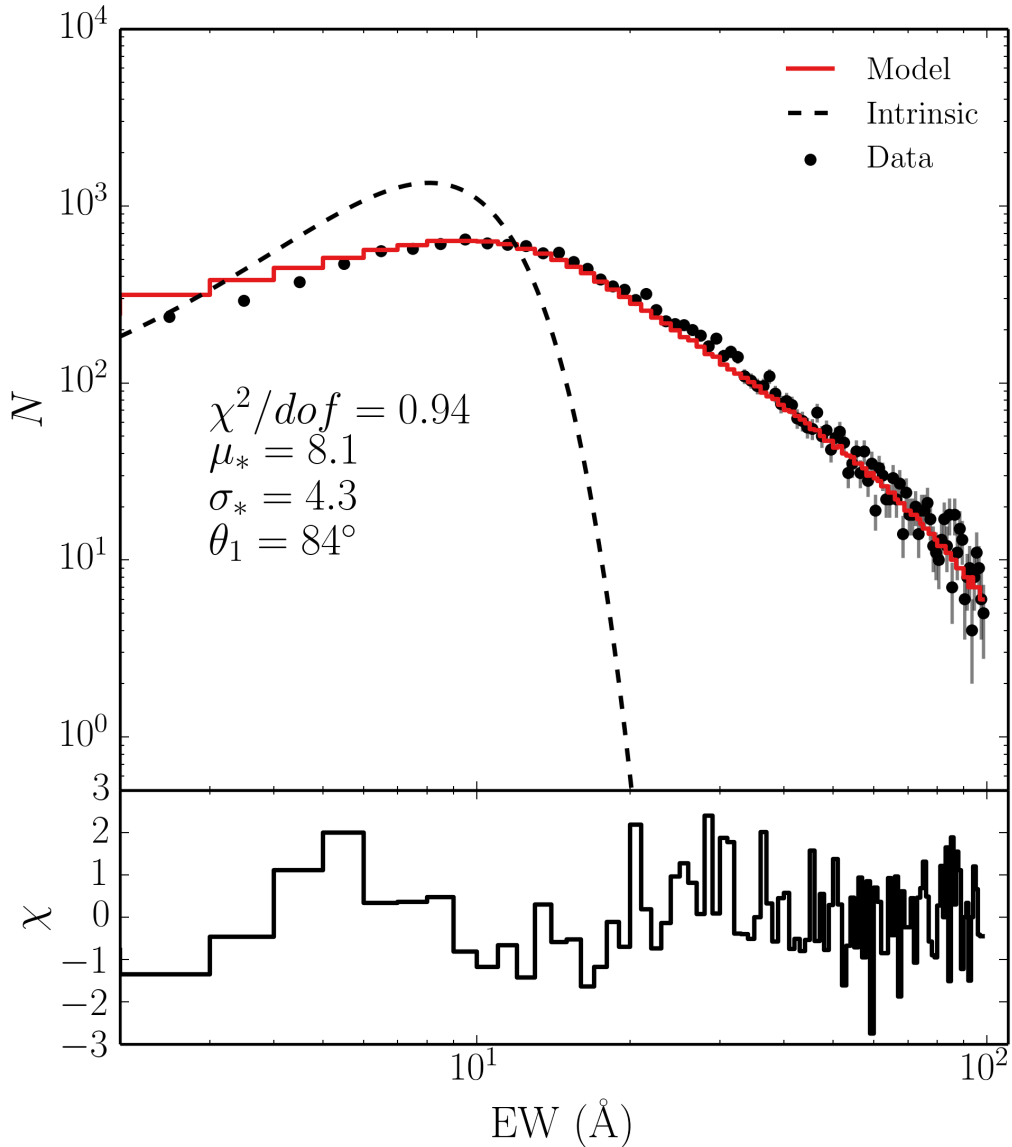


FIGURE 6.5: The EW distribution of quasars in the R11 sample (red errorbars) and the best fit model with a maximum viewing angle of 84° .

model 1 of R11. The run of reduced χ^2 with maximum angle is shown in Fig. 6.6, where the choice for μ_* and σ_* is left free in each case. Maximum angles below $\sim 80^\circ$ are strongly disfavoured by this model. I adopt linear binning to facilitate easy comparison with R11, and only fit up $EW = 100\text{\AA}$ due to poor statistics above that limit. Unfortunately, this makes inferring any information about a potential high EW cutoff difficult as a more complete sample at high EW is required.

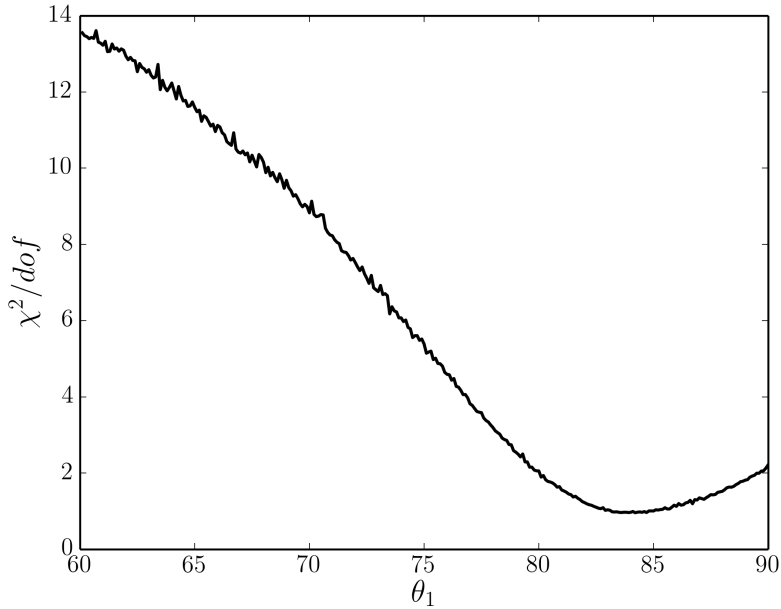


FIGURE 6.6: χ^2/dof as a function of maximum angle, θ_1 , calculated in steps of 0.1° . The choice for μ_* and σ_* is left free in each case.

6.4.2 Comparing non-BAL and LoBAL Distributions

In order to compare the observed distributions to those expected for BALs and non-BALs I conduct a Monte Carlo simulation similar to the process described in section 6.4.1, but with a few key differences. I once again assume $\epsilon(\theta) = \cos \theta$. The geometry of the toy model used in this simulation is shown in Fig. 6.7.

First, A set of isotropic angles is generated. If $\theta_{min} < \theta < \theta_{max}$ then the fake object is flagged as a mock BAL. If $\theta < \theta_{min}$ then the fake object is designated a non-BAL, and otherwise the object is ignored. Once again, the object also has to survive a selection test based on a arbitrary flux selection limit. I then fit the non-BAL distribution using the method described previously. For each mock sample, a EW_* is drawn from the intrinsic gaussian, and a mock EW is estimated such that $EW = EW_*/\epsilon(\theta)$. This process is repeated to build up a mock sample of objects, and carried out for a series of pairs of θ_{min} and θ_{max} . This allows theoretical distributions for BAL and non-BAL quasars for a series of different outflow geometries to be derived.

The diagnostics recorded from the simulation are the following four quantities:

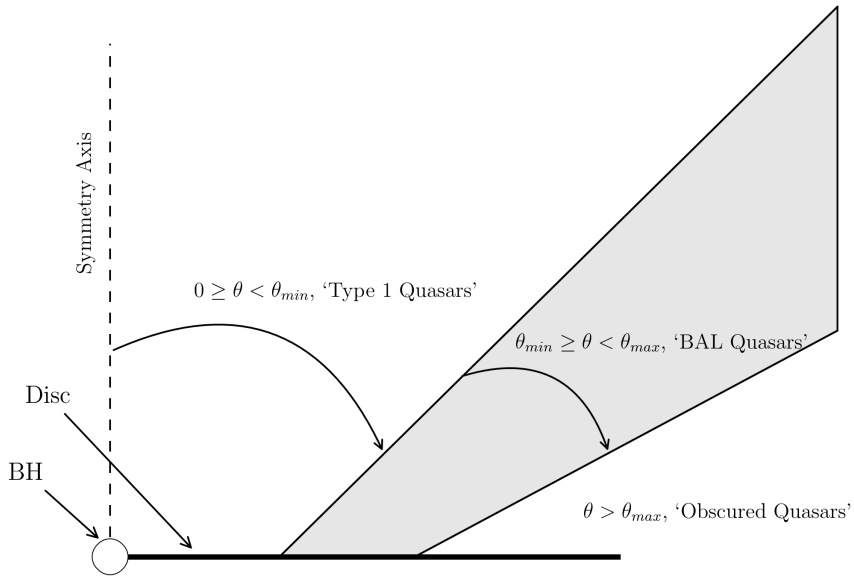


FIGURE 6.7: The geometry of the toy model used to carry out the Monte Carlo simulations

- The p -value associated with the Kolgomorov-Smirnov (K-S) test statistic, p_{KS} , in which the mock BAL sample is compared to the real LoBAL sample.
- The BAL fraction, f_{BAL} , is calculated from the number of objects in the mock sample with $\theta_{min} < \theta < \theta_{max}$.
- The χ^2/dof from the fit to the non-BAL quasar distribution.
- $\Delta\mu$, the difference between the mean value of the mock BAL distribution and the mean value of the mock non-BAL distribution.

The simulation results are shown in figure 6.8, in which the four diagnostics are plotted as a function of θ_{min} and θ_{max} .

As expected, equatorial viewing angles for BAL quasars are disfavoured, and furthermore, it is only possible to fit the tail to the EW[O III] distribution if non-BAL quasars are allowed to be viewed from high inclinations. However, any conclusions are somewhat limited by the lack of knowledge about the intrinsic face-on distribution of EW[O III], or equivalently, the orientations of the quasars themselves. If either of these quantities were known then the results of the K-S test and χ^2 minimization could be used to place

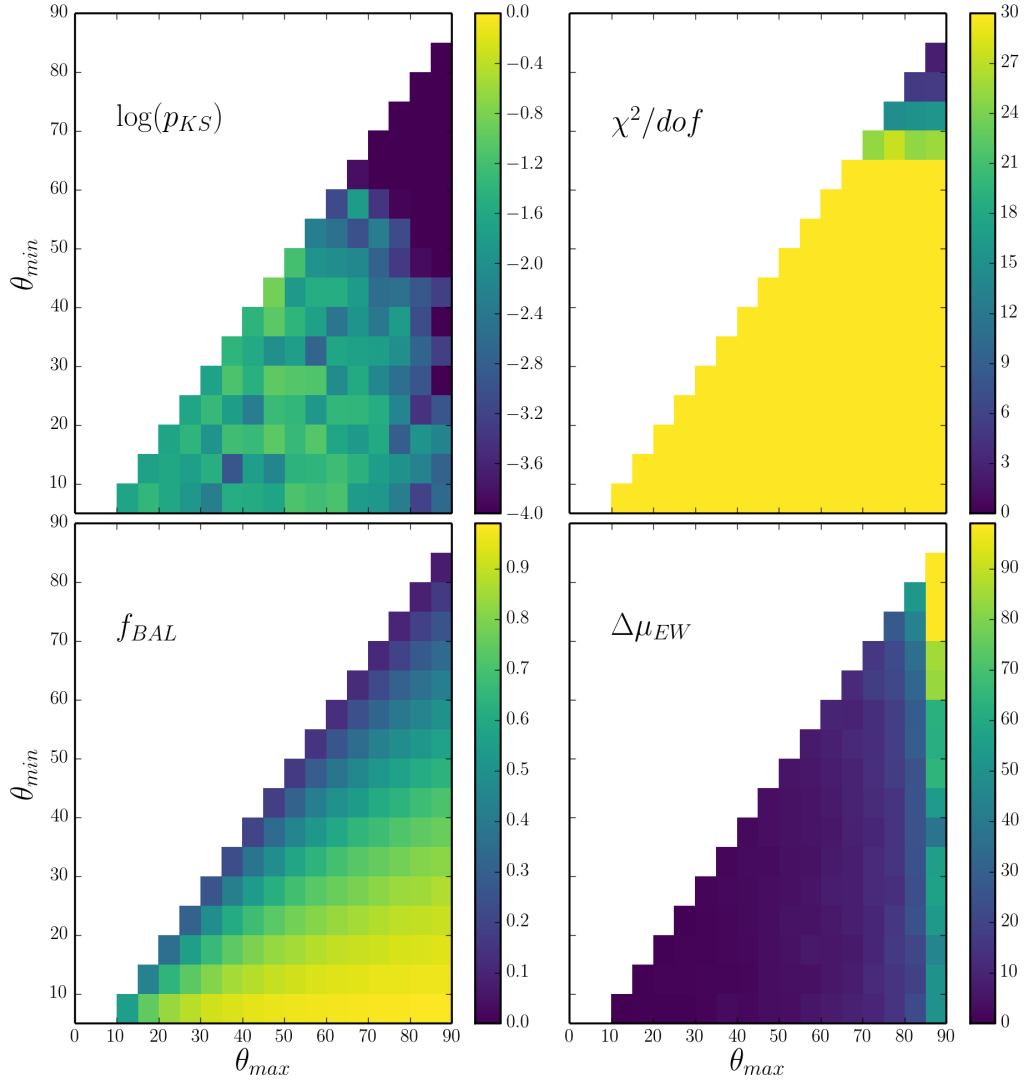


FIGURE 6.8: Heat map showing the results of the MC simulation described in section 6.4.2. The quantities shown are discussed further in the text, but correspond to (clockwise from top left): the p_{KS} value from a comparison between the mock BAL dataset and the observed BAL dataset, the reduced χ^2 from the fit to the non-BAL EW distribution, the difference in mean EW between the mock BAL and mock non-BAL datasets, and the BAL fraction expected for the geometry in question.

more robust constraints on BAL and non-BAL viewing angles and the associated covering factor of the outflow. Furthermore, the distribution of C IV quasar EW cannot be fit by the same model as the EW[O III] distribution.

An additional limitation is due to the SDSS wavelength coverage and means that only LoBALs can be used when EW[O III] is present (sample A). I would suggest that future observational programs might look to build up a large sample of EW[O III] measurements for HiBAL quasars. In the mean time, I will turn to the UV broad emission lines to

Par. A	Par. B	$r_{corr,AB}$ (non- BALs)	$r_{corr,AB}$ (BALs)
$\log[\text{EW}[\text{O III}]]$	$\text{FWHM}[\text{H}\beta]$	0.14	0.18
$\log[\text{EW}[\text{O III}]]$	R_{FeII}	-0.51	-0.67
$\text{FWHM}[\text{H}\beta]$	R_{FeII}	-0.26	-0.42

TABLE 6.1: Eigenvector 1 correlation coefficients

examine if the above conclusions also hold when examining the properties of the HiBAL quasars in sample B.

6.4.3 Broad Emission Lines in HiBAL quasars

The situation involving broad emission lines is somewhat different, as the lines are dipole permitted transitions and can thus be optically thick. An additional complication is that they are formed much closer to the accretion disc, and so may be subject to the same absorption effects as the continuum.

6.5 Discussion

I have demonstrated that the EW distributions of the O III 5007Å emission line in quasars is not consistent with a model in which BAL quasars are viewed from equatorial angles and the continuum emission originates from a foreshortened accretion disc. This conclusion would be strengthened were I to include limb darkening. This conclusion is extendible to the broad emission lines, with the caveat that those lines are dipole transitions and so opacity effects can change the angular distribution of emission. I will now explore how the above results compare to other observations of quasars that are expected to probe system orientation.

6.5.1 Eigenvector 1

Eigenvector 1 (EV1) is a fundamental parameter space for AGN and quasars ([Boroson & Green 1992](#); [Sulentic et al. 2000](#); [Marziani et al. 2001](#); [Shen & Ho 2014](#)). It relates the FWHM of H β , FWHM[H β], the relative iron strength, R_{FeII} and the EW[O III]. Both

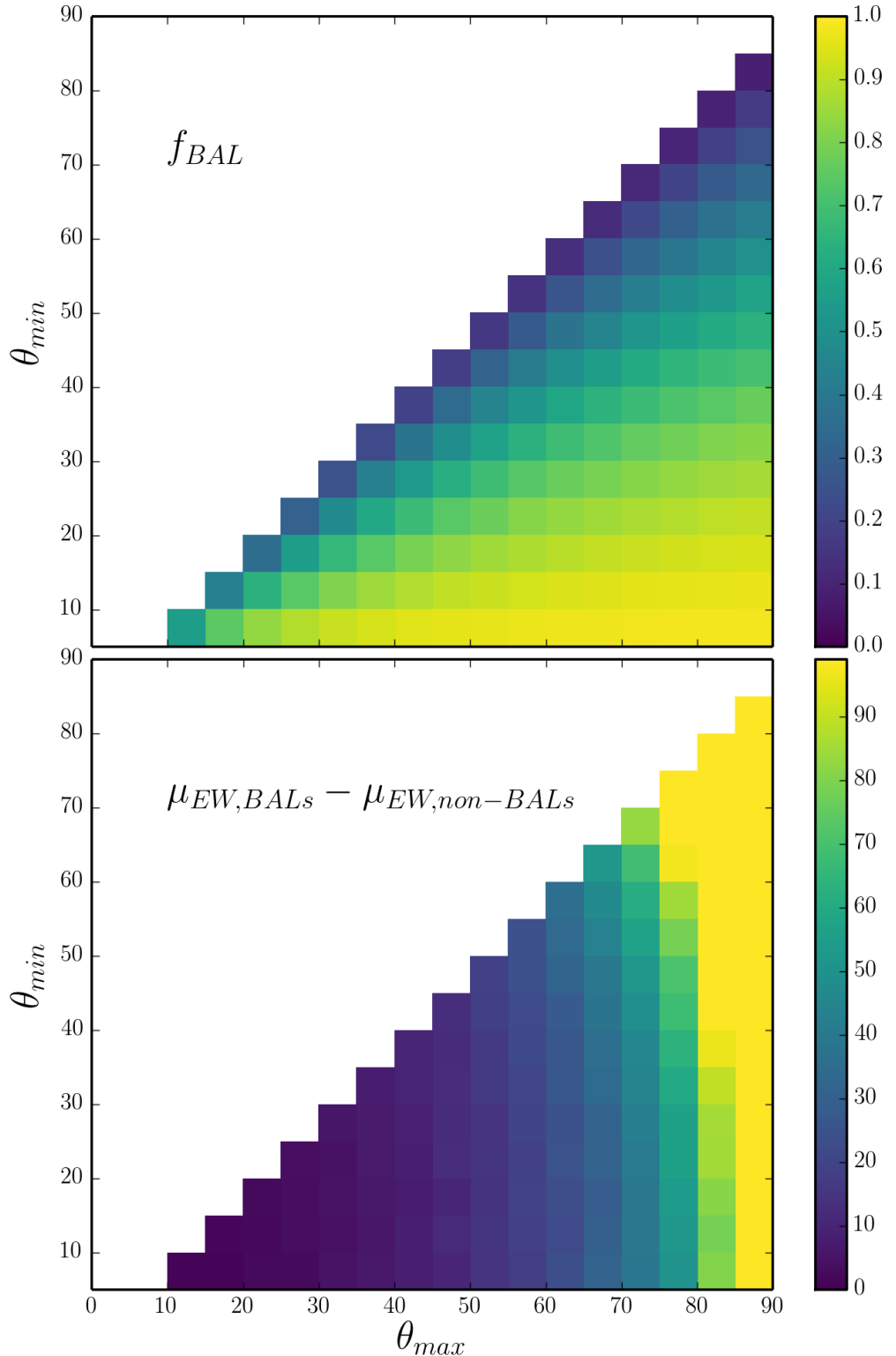


FIGURE 6.9: Heat map showing the results of the MC simulation described in section 6.4.3. The top panel shows the expected BAL fraction for the geometry in question, and the

$\text{EW}[\text{O III}]$ and $\text{FWHM}[\text{H}\beta]$ have been used as orientation indicators, and so comparing the BAL EV1 distribution to the non-BAL EV1 distribution is particularly interesting.

Fig. 6.10 shows the quasar distribution from sample A in EV1 parameter space, with BAL quasars from samples A and B overplotted. (Shen & Ho 2014, hereafter SH14) propose that the main inclination driver in the parameter space is $\text{FWHM}[\text{H}\beta]$, and that high inclination sources should thus cluster around a diagonal line from the lower right to upper left quadrants. Conversely, R11's analysis instead suggests that high inclination sources should cluster around high EW OIII widths. As $\text{EW}[\text{O III}]$ and $\text{FWHM}[\text{H}\beta]$ are very weakly correlated (Spearman's rank coefficient of 0.13), this means they should lie to the left of the parameter space. Inspection of the figure clearly shows that BAL quasars are not only found in one region of the EV1 parameter space.

In order to assess this more quantitatively, I have shown contours of quasar counts overlaid on the scatter plot. The contours correspond to the number of objects in each bin, where the bins are of size $\Delta R_{\text{FeII}} = 0.2$ and $\Delta \text{FWHM}[\text{H}\beta] = 500 \text{ km s}^{-1}$. The percentage of quasars falling within the inner contour is 45%, whereas only 18% of BAL quasars fall in the space. Conversely, 24% of BAL quasars fall outside the outermost contour compared to 10% of non-BAL quasars. It would therefore appear that BAL quasars are preferentially clustered towards the high-mass and high-inclination end of EV1 space (under the interpretation of SH14). This is further illustrated by Fig. 6.11, which shows the LoBAL fraction in the same bins, compared to the mean LoBAL fraction. This is again suggestive of an overdensity towards the upper right of the parameter space. It is also clear that a unification picture in which BAL quasars are viewed exclusively from high inclinations is ruled out, under both the R11 and SH14 interpretations.

Larger datasets, preferably including HiBAL quasars with EV1 measurements, are needed in order to properly constrain the EV1 behaviour of BAL quasars. However, overall, the behaviour of $\text{FWHM}[\text{H}\beta]$ strengthens the above conclusion that BAL quasars are not always viewed from extreme inclinations.

6.5.2 Radio Observations

Fig. ? shows the equivalent width distributions in radio-loud quasars, split into core or lobe dominated. This designation is commonly used as an orientation indicator (Orr &

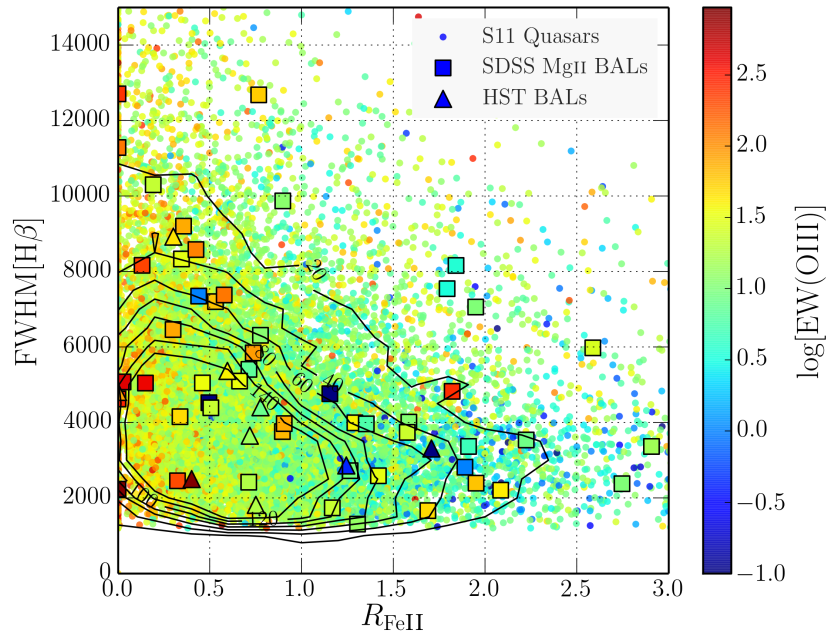


FIGURE 6.10: Eigenvector 1 for BAL and non-BAL quasars. FWHM of the H β line plotted against the relative iron strength, R_{FeII} . The colour coding corresponds to the EW of OIII. The dots mark all quasars from sample A, while the squares mark those with Mg II BALs. The triangles show the HST BAL quasars from sample B.

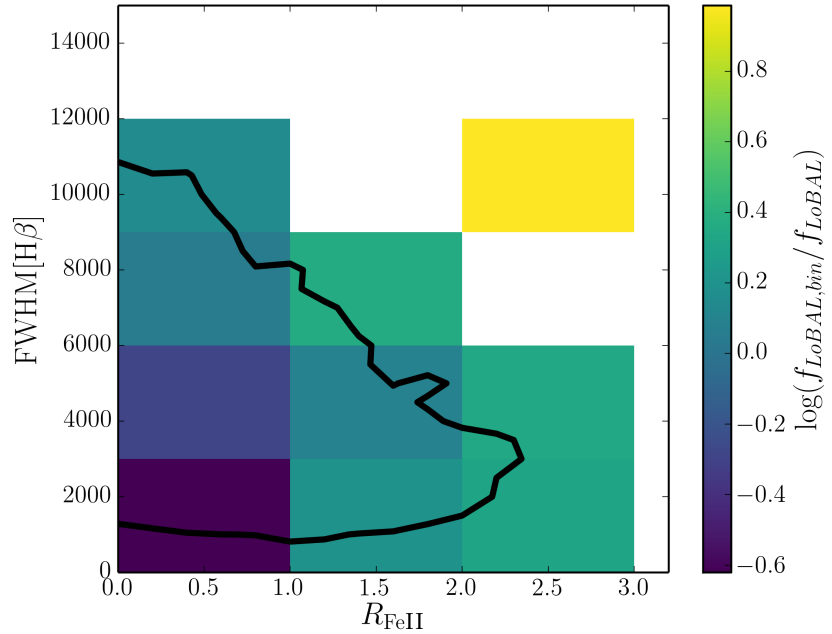


FIGURE 6.11: LoBAL fraction compared to mean LoBAL fraction in Eigenvector 1 space. The contour shows the outermost contour from Fig. 6.10 for reference.

Browne 1982; Wills & Brotherton 1995). Although th

In this case, we can see that A full investigation of this is beyond the scope

6.5.3 Polarisation

Polarisation measurements of BAL quasars tend to show two properties. The first is a polarisation angle of $\gtrsim 60^\circ$ with respect to the radio jet axis in RL source (Brotherton et al. 2006). The second is a polarisation percentage of around 2.4 times greater, on average, than the non-BAL population. The polarisation percentages of a sample of BAL quasars from REF are compared to the Type I and Type II AGN populations from REF in Fig. 6.12.

The polarisation properties of BAL quasars offer some of the best insights into the geometries of BAL outflows, some of which appear to be in contrast with the conclusions drawn from emission line and radio properties.

6.5.4 Theoretical Considerations

Discuss Proga models: They tend to rise fairly equatorially (see eg. PK04) Talk to Nick?

6.6 Conclusions

I have explored the emission line properties of BAL and non-BAL quasars and found that they are inconsistent with a unification picture in which BAL outflows rise equatorially from a foreshortened or limb darkened accretion disc. Based on these findings, it is possible to construct a few possible scenarios that are not ruled out by the above results. these conclusions have the caveat that I have assumed that conclusions drawn about LoBAL quasars can be extended to BAL quasars in general.

- *Scenario 1:* The quasar continuum is roughly isotropic, which is not expected from a geometrically thin, optically thick accretion disc. I have demonstrated that general relativistic effects cannot account for this discrepancy in the UV. Reprocessing by surrounding dense plasma with a large covering factor or limb brightening in

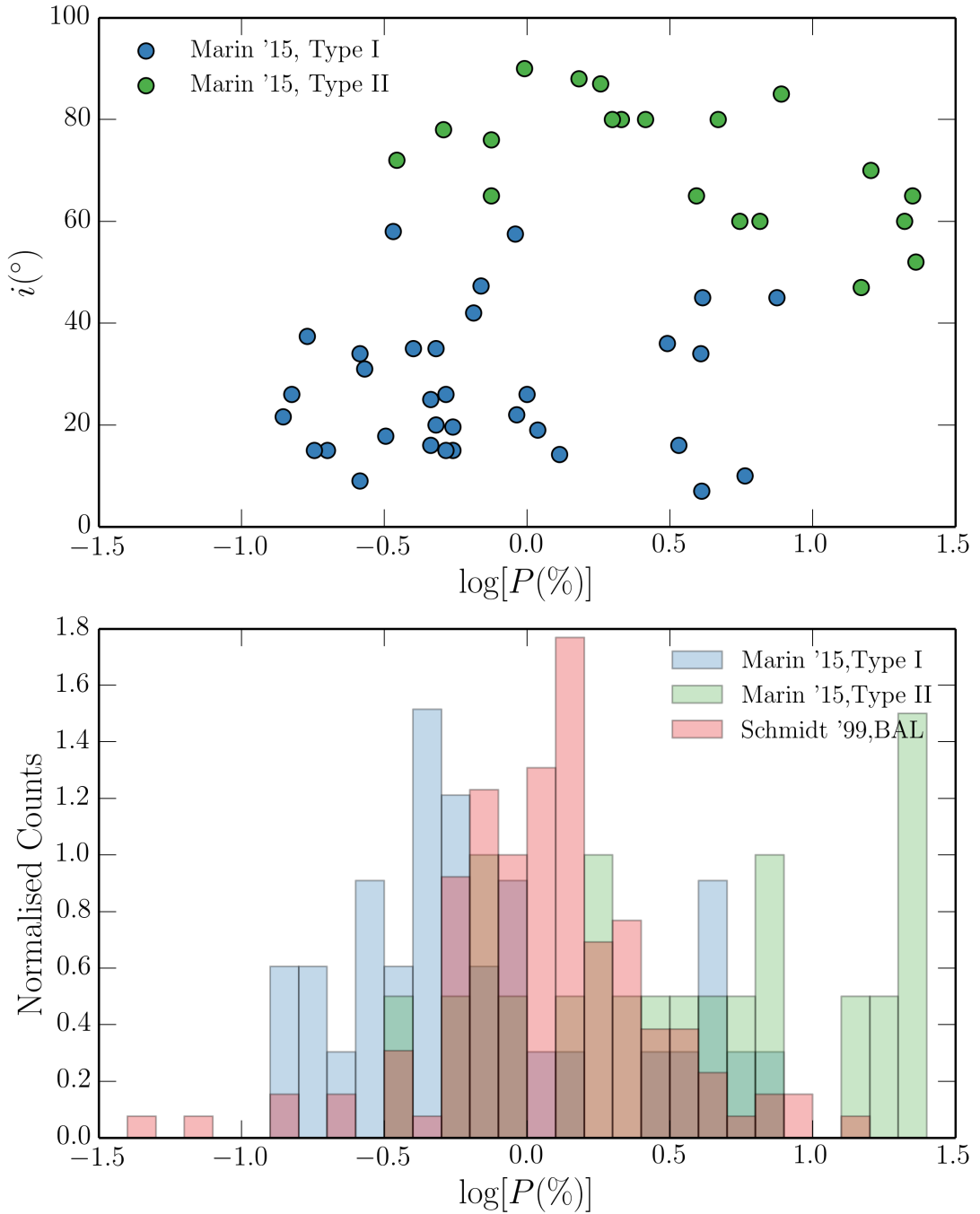


FIGURE 6.12: *Top:* Polarisation percentages as a function of measured inclination from Marin et al. (2015) for Type I and Type II AGN. *Bottom:* Histograms of polarisation percentages for BAL quasars from Schmidt et al. (1999) together with the Marin et al. (2015) AGN sample.

the disc may provide possible explanations which this analysis cannot yet confirm or refute.

- **Scenario 2:** Quasar discs are strongly anisotropic, as expected from a geometrically thin, optically thick accretion disc. In this case, BAL outflows cannot only emerge at extreme inclinations and should instead be seen at very similar angles to non-BAL quasars. Polarisation measurements need to be reconciled with this hypothesis. I recommend that future RT modelling efforts explore different outflow geometries and that detailed polarisation modelling is undertaken to constrain the outflow opening angles.
- **Scenario 3:** The geometric unification model does not explain the incidence of BALs in quasars, or requires an additional component which is *time-dependent*, such as an evolutionary or accretion state origin for BAL outflows. In this scenario, BAL quasars would be seen from very similar angles to non-BAL quasars. However, the evidence for this is limited and there is no good model for why outflows would exist only for $\sim 20\%$ of a quasar's lifetime. Even if this is the case, then the covering factor of the outflow still needs to be constrained in order to estimate the BAL duty cycle.

Regardless of the conclusions about BAL quasars and their outflow geometries, this analysis allows conclusions to be drawn about the *overall* quasar population. In scenario 1, the EW[O III] distribution of quasars cannot be driven by inclination as suggested by (Risaliti et al. 2011). It is also clear from the work presented here that $\log R$, EW[O III] and FWHM H β are *cannot all* be reliable orientation indicators. Furthermore, if a geometric unification does explain BAL quasars, then absorption effects cannot be responsible for the observed EW[O III] distribution. The above conclusions each pose a different challenge to the current understanding of, respectively, accretion physics, polarisation measurements and geometric unification models. This work therefore adds to the growing evidence that our simplest models are not sufficient to describe the overall quasars and that alternatives should be sought.

Chapter 7

Conclusions and Future Work

“...and the credits rave as the critics roll.”

Mike Vennart, Silent/Transparent

I began this thesis with the fundamental tenet that accreting systems and their associated outflows are astrophysically important. However, I also demonstrated that much of the diverse phenomenology associated with such systems, as well as the underlying *physics*, is not well understood. Having attempted to address some of the issues raised in the introductory chapters, I will provide some concluding remarks. First, I will summarise my findings, before commenting on how future research can help unveil the true nature of accretion discs and their winds.

A large portion of this PhD has been spent maintaining, testing and developing the MCRT and ionization code, PYTHON. The first step in this project was to understand the macro-atom scheme developed by Lucy (2002, 2003), and its specific integration into PYTHON. I described the scheme and the operation of PYTHON in detail in chapter 3, partly in the hope that it will prove a useful document for future efforts involving this powerful, but complex, piece of software. The latter parts of the same chapter focused on the series of tests I conducted to robustly verify that the code worked as expected and that it could reproduce the analytical and computational results in the right physical limits. Near the start of the project many of these tests would fail, either because PYTHON did not possess the relevant atomic data, or because the necessary integration between the macro-atom and simple-atom portions of the code was not yet

in place. Thus, while time consuming, progressing to the point where all the tests shown in chapter 3 could be passed was an important milestone, and enabled the techniques in question to be applied to astrophysical problems with confidence.

The first of these astrophysical problems involved CVs, and in particular those accreting at a relatively high rate, such as DNe or NLs. Having improved the radiative transfer techniques from previous CV modelling efforts involving PYTHON (LK02, [Noebauer et al. 2010](#)), it was now possible to see if the outflows that are responsible for the P-Cygni profiles seen in UV resonance lines could also affect the *optical* line and continuum emission. The results are unambiguous. By simply taking the SV93/LK02 models – designed to reproduce the UV spectra of high-state CVs – and ‘turning on’ the improved radiative transfer mode, the wind has a significant effect on the optical spectrum, producing strong H α , He II 4686Å and He II 3202Å lines, among others, at high inclinations.

I then conducted a small parameter search over just two kinematic parameters, to see if a model could produce *all* of the optical H and He lines observed in high-state CVs. Synthetic spectra from a model with a more slowly accelerating outflow show the full sequence of H and He recombination lines, with the observed trend from strong emission at high inclination to weaker lines at low inclination. Furthermore, the dense outflow now produces strong Balmer recombination emission that is sufficient to ‘fill in’ the Balmer absorption edge intrinsic to the disc atmosphere input spectrum. The optimised model is not without issues; the red wing to the C IV line is now overly strong, particularly at high inclinations, and He II emission is stronger than that observed. Nevertheless, the synthetic spectra exhibit reasonable verisimilitude with observations of the high inclination NL RW Tri, and the results indicate that disc winds may have a much broader impact, especially in wavelength terms, than is traditionally expected. Furthermore, the large vertical extent of the line emitting region has implications for techniques that assume planar line emission, such as Doppler tomography (e.g. [Marsh & Horne 1988](#)) and eclipse mapping (e.g. [Horne et al. 1994](#)).

In chapter 5, I applied similar techniques to the question of quasar unification, but with one additional adaptation. In order to simultaneously increase the emission measure of the wind, as well as moderate the ionization state in the presence of strong X-rays, I incorporated a simple treatment of clumping into PYTHON. The technique – known as *microclumping* – is prevalent in the stellar wind community, but this was the first

time it had been applied to quasar winds in this context. Although the motivation for including clumping was in some sense empirical, in that H13 could not produce a model with strong C IV BALs without severely limiting the X-ray luminosity, the validity of this approach is strengthened by the theoretical and observational evidence for clumping in line-driven hot star winds (see sections 2.1.4.1 and 2.2.3).

Once again, I conducted a parameter search, this time in 5 dimensions. A broad family of models produce strong UV emission lines at low inclinations and UV BALs at high inclinations. Thus, the first success of the clumpy quasar wind model is that, for clumping factors comparable to those required in stellar wind modelling (Hamann et al. 2008), the ionization state of the wind matches well with observations despite the presence of strong X-ray radiation. Indeed, the X-ray properties of the model now agree well with observed non-BAL and BAL quasar values for L_X , suggesting that the partially self-shielding BAL outflow itself might be responsible for the observed X-ray weakness of BAL quasars. Perhaps the most compelling attribute of the wind model is that it naturally reproduces the broad range of ionization states observed in AGN such that the wind emission has very similar characteristics to the observed BLR spectrum (see, e.g., Fig. 5.8). The primary limitation of the fiducial quasar model is a geometric one; it is not possible to produce comparable line EWs at low inclination to those at high inclination, due to the foreshortened, limb-darkened, and absorbed disc emission. Thus, even if the low inclination line emission could be matched to the observed quasar EWs, the model would then over-predict the line emission emerging at high inclination ‘BALQSO-like’ angles. This suggests an issue with an equatorial unification model, and provides the motivation for exploring the observational characteristics of emission lines in BAL and non-BAL quasars.

The final project in this PhD saw a switch in philosophy, as, informed by the radiative transfer modelling, I turned to observations and in particular the invaluable dataset that is the *Sloan Digital Sky Survey*. The aim of this exercise was to more quantitatively assess the apparent similarity in emission line properties in BAL and non-BAL quasars. I first reproduced the results of Risaliti et al. (2011) using the updated dataset by fitting the distribution of the EW of the O III 5007Å emission line with a simple geometric model, in which an intrinsic Gaussian distribution was convolved with the expected angular distribution of quasars expected in a flux-limited sample. I then constructed a toy model for geometric unification, and showed that predictions from the simplest

quasar wind models – those where an equatorial outflow rises from a geometrically thin, optically thick accretion disc – are not consistent with the observed EW distributions of quasar emission lines. The results also suggest that obscuration is not the key driver of the EW[O III] distribution – albeit under the assumption that LoBAL quasars are drawn from the same population as non-BAL quasars.

The overall conclusions of this final study are striking, and extend beyond just constraining BAL outflow parameters. They suggest a few possible scenarios; perhaps quasar discs are much more isotropic than one might expect. If this is the case, how is it reconciled with the *theory* of accretion? Alternatively, BAL and non-BAL quasars may be viewed from a similar range of angles, in which case their differences in polarisation properties must be understood. The final possibility is of course that geometric unification does not explain the incidence of BALs in the UV spectra of quasars. This final scenario is not a solution to the problem, *per se*. After all, BAL outflows *must* emerge at some range of angles, and this range of angles is important to constrain in order to understand the outflow physics.

Perhaps unsurprisingly, the work presented in this thesis has raised many questions, some of which are fundamental to our understanding of CVs, quasars and accreting systems generally. I will therefore devote some time to discussing what I believe are natural next steps in furthering our understanding of accretion and outflow on all scales.

7.1 Suggestions for Future Work

7.1.1 CVs as Accretion and Outflow Laboratories

CVs are the closest and best understood laboratories for our understanding of accretion physics. In particular, the NL variables make excellent testbeds for the α -disc model, as they are one of the few accreting systems known to lie in a relatively constant accretion rate state – fulfilling an explicit assumption of the SS73 prescription. I suggest that two observational programs relating to NLs are pursued. The first is to take broadband, simultaneous spectroscopy of a number of NL variables. This will allow the impact of winds on the spectrum to be assessed more carefully as modelling of the entire wavelength range can be undertaken, possibly including fits to the observed spectrum. It

will also allow the broadband SED to be fitted with confidence, and inferences made about the temperature profile of the disc. The second is to take measurements of the depth of the Balmer jump in a relatively large sample of NLs, either through narrow band spectroscopy or two-band photometry. Together with inclination measurements the predictions of disc and outflow models can be tested directly by exploring how the depth of the Balmer absorption edge varies with viewing angle and accretion rate.

7.1.2 Improving the Treatment of Clumping

One of the limitations of the work presented in chapter 5 is that the treatment of clumping is fairly simple, and does not adequately capture the physics of potential dense substructures in AGN outflows. Indeed, it is considered a ‘first step’ towards accurately including clumpiness in PYTHON. So, what is the next step? One fairly simple way of including some degree of porosity in the treatment would be to relax the assumption that the Sobolev length is larger than the clump size. The Sobolev optical depth can then be calculated either or in or out of a clump, based on a random number choice proportional to the clump filling factor. This would mean that there is a chance that photons will not interact with clumps, possibly leading to the non-black saturation that is observed in BAL troughs ([Arav et al. 1999a,b](#), see also section 5.3.2.1). More generally, an approach similar to *macroclumping*, as used in stellar wind modelling (e.g. [Hamann et al. 2008](#); [Šurlan et al. 2012](#)), would allow the inclusion of porosity.

More complex approaches could also be considered here, such as the ‘two-phase’ ideas used in clumpy torus models ([Stalevski et al. 2013](#)) and suggested for the BLR (e.g. [Netzer 1990](#); [de Kool & Begelman 1995](#); [Elvis 2000](#)). However, the general problem here is that, while introducing more freedom into the wind model would certainly allow one to fit quasar spectra more effectively, the question is whether this provides useful physical insight. This is somewhat open to interpretation, as the filling factors and origins of clumps in BLR and outflow models are not well constrained. I would therefore suggest that some of the above techniques are implemented, and experimented with, but would urge caution with regards to the interpretation of the overall results.

7.1.3 Improving Atomic Models

In chapter 4, the dominant source of heating in the benchmark CV model is line heating. This means that accurate collision strengths are needed in order

Fig. ??

7.1.4 Using Radiative Transfer to Test

7.1.5 Obtaining Reliable Orientation Indicators

A wide variety of quantities have been used as AGN orientation indicators. However, many of these indicators are *model-dependent*, which is concerning given the lack of knowledge about the true origins of the multi-wavelength AGN SED. Furthermore, I showed in chapter 6 that it is not possible for EW[O III], FWHM[H β] and radio-core dominance to *all* be reliable orientation indicators due to the lack of the expected correlations between these measurements.

In order to distinguish between geometric unification, obscuration and evolutionary scenarios for the diversity of AGN it is critical to constrain their inclinations.

7.1.6 Placing BAL Quasars on the Eigenvector 1 Parameter Space

In chapter 6 it was only possible to

7.2 Closing Remarks

Disc winds are ubiquitous in accreting systems and have a profound connection with the accretion process. I have demonstrated, through state-of-the-art MCRT simulations, that disc winds extend their influence beyond the blue-shifted BALs and P-Cygni profiles traditionally associated with outflow. They may produce the optical line and continuum emission in CVs, possibly even dominating the observed spectrum. Simple clumpy biconical wind models also naturally exhibit the range of ionization states and emission lines seen in type 1 AGN and quasars, and once again may significantly alter

the continuum shape. Regardless of their true impact, the influence of disc winds on the spectra of accreting systems must be understood, and the outflow covering factors and opening angles accurately estimated, for three main reasons. First, so that the feedback efficiency of BAL outflows, and mass-loss rates in CVs, can be calculated. Second, so that the true intrinsic continuum can be unveiled, and the viability of the current ‘best-bet’ accretion disc models can be assessed. Third, so that the orientations of AGN and quasars can be properly constrained, allowing us to unify their diverse phenomenology. These questions are still unanswered, but I hope that in this thesis I have demonstrated that *disc winds matter*, and are fundamental to our understanding of accreting compact objects.

Bibliography

- Abbott D. C., 1982, ApJ 259, 282
- Abbott D. C., Lucy L. B., 1985, ApJ 288, 679
- Adams F. C., Graff D. S., Richstone D. O., 2001, ApJ Letters 551, L31
- Alexander D. M., Bauer F. E., Brandt W. N., Daddi E. et al., 2011, ApJ 738, 44
- Allen J. T., Hewett P. C., Maddox N., Richards G. T., Belokurov V., 2011, MNRAS 410, 860
- Antonucci R., 1988, in M. Kafatos (ed.), Supermassive Black Holes, p. 26
- Antonucci R., 2013, Nature 495, 165
- Antonucci R., Geller R., Goodrich R. W., Miller J. S., 1996, ApJ 472, 502
- Antonucci R. R. J., Miller J. S., 1985, ApJ 297, 621
- Arav N., 1996, ApJ 465, 617
- Arav N., Becker R. H., Laurent-Muehleisen S. A., Gregg M. D. et al., 1999a, ApJ 524, 566
- Arav N., Korista K. T., Barlow T. A., Begelman, 1995, Nature 376, 576
- Arav N., Korista K. T., de Kool M., Junkkarinen V. T., Begelman M. C., 1999b, ApJ 516, 27
- Arévalo P., Uttley P., 2006, MNRAS 367, 801
- Badnell N. R., 2006, ApJs 167, 334
- Balbus S. A., Hawley J. F., 1991, ApJ 376, 214

- Baldi R. D., Capetti A., Robinson A., Laor A., Behar E., 2016, MNRAS
- Baldry I. K., Glazebrook K., Brinkmann J., Ivezić Ž. et al., 2004, ApJ 600, 681
- Baptista R., Silveira C., Steiner J. E., Horne K., 2000, MNRAS 314, 713
- Bartlett E., 2013, Ph.D. thesis, University of Southampton
- Becker R. H., White R. L., Gregg M. D., Brotherton M. S. et al., 2000, ApJ 538, 72
- Begelman M. C., McKee C. F., Shields G. A., 1983, ApJ 271, 70
- Bell E. F., McIntosh D. H., Katz N., Weinberg M. D., 2003, ApJs 149, 289
- Belloni T. (ed.), 2010, The Jet Paradigm, Vol. 794 of *Lecture Notes in Physics, Berlin Springer Verlag*
- Benz A. O., Fuerst E., Kiplinger A. L., 1983, Nature 302, 45
- Beuermann K., Stasiewski U., Schwope A. D., 1992, A&A 256, 433
- Beuermann K., Thomas H.-C., 1990, A&A 230, 326
- Bîrzan L., McNamara B. R., Nulsen P. E. J., Carilli C. L., Wise M. W., 2008, ApJ 686, 859
- Blandford R. D., Payne D. G., 1982, MNRAS 199, 883
- Blandford R. D., Znajek R. L., 1977, MNRAS 179, 433
- Bondi H., 1952, MNRAS 112, 195
- Bondi H., Hoyle F., 1944, MNRAS 104, 273
- Bongiorno A., Schulze A., Merloni A., Zamorani G. et al., 2016, A&A 588, A78
- Bonning E. W., Cheng L., Shields G. A., Salviander S., Gebhardt K., 2007, ApJ 659, 211
- Borguet B., Hutsemékers D., 2010, A&A 515, A22
- Borguet B. C. J., Arav N., Edmonds D., Chamberlain C., Benn C., 2013, ApJ 762, 49
- Borguet B. C. J., Edmonds D., Arav N., Dunn J., Kriss G. A., 2012, ApJ 751, 107
- Boroson T. A., Green R. F., 1992, ApJs 80, 109

- Boroson T. A., Meyers K. A., 1992, ApJ 397, 442
- Bowler R. A. A., Hewett P. C., Allen J. T., Ferland G. J., 2014, MNRAS 445, 359
- Braito V., Reeves J. N., Dewangan G. C., George I. et al., 2007, ApJ 670, 978
- Brandt W. N., Laor A., Wills B. J., 2000, ApJ 528, 637
- Brotherton M. S., De Breuck C., Schaefer J. J., 2006, MNRAS 372, L58
- Brotherton M. S., Tran H. D., van Breugel W., Dey A., Antonucci R., 1997, ApJ Letters 487, L113
- Brown J. C., Richardson L. L., Antokhin I., Robert C. et al., 1995, A&A 295, 725
- Burkert A., Silk J., 2001, ApJ Letters 554, L151
- Capellupo D. M., Hamann F., Barlow T. A., 2014, MNRAS 444, 1893
- Capellupo D. M., Hamann F., Shields J. C., Rodríguez Hidalgo P., Barlow T. A., 2011, MNRAS 413, 908
- Capellupo D. M., Hamann F., Shields J. C., Rodríguez Hidalgo P., Barlow T. A., 2012, MNRAS 422, 3249
- Capellupo D. M., Netzer H., Lira P., Trakhtenbrot B., Mejía-Restrepo J., 2015, MNRAS 446, 3427
- Cappi M., Mihara T., Matsuoka M., Hayashida K. et al., 1996, ApJ 458, 149
- Cassinelli J. P., 1979, ARAA 17, 275
- Castor J. I., Abbott D. C., Klein R. I., 1975, ApJ 195, 157
- Castor J. L., 1974, MNRAS 169, 279
- Cavagnolo K. W., McNamara B. R., Wise M. W., Nulsen P. E. J. et al., 2011, ApJ 732, 71
- Chamberlain C., Arav N., Benn C., 2015, MNRAS 450, 1085
- Chartas G., Kochanek C. S., Dai X., Poindexter S., Garmire G., 2009, ApJ 693, 174
- Chen B., Dai X., Baron E., 2013a, ApJ 762, 122

- Chen B., Dai X., Baron E., Kantowski R., 2013b, ApJ 769, 131
- Clavel J., Schartel N., Tomas L., 2006, A&A 446, 439
- Cohen M. H., Ogle P. M., Tran H. D., Vermeulen R. C. et al., 1995, ApJ Letters 448, L77
- Cohen R. D., Puetter R. C., Rudy R. J., Ake T. B., Foltz C. B., 1986, ApJ 311, 135
- Connolly S. D., McHardy I. M., Dwelly T., 2014, MNRAS 440, 3503
- Connolly S. D., McHardy I. M., Skipper C. J., Emmanoulopoulos D., 2016, MNRAS
- Coppejans D. L., Körding E. G., Miller-Jones J. C. A., Rupen M. P. et al., 2015, MNRAS 451, 3801
- Cordova F. A., Mason K. O., 1982, ApJ 260, 716
- Cottis C. E., Goad M. R., Knigge C., Scaringi S., 2010, MNRAS 406, 2094
- Crenshaw D. M., Rodriguez-Pascual P. M., Penton S. V., Edelson R. A. et al., 1996, ApJ 470, 322
- Croton D. J., Springel V., White S. D. M., De Lucia G. et al., 2006, MNRAS 365, 11
- Crummy J., Fabian A. C., Gallo L., Ross R. R., 2006, MNRAS 365, 1067
- Cunto W., Mendoza C., Ochsenbein F., Zeippen C. J., 1993, A&A 275, L5
- Dabrowski Y., Fabian A. C., Iwasawa K., Lasenby A. N., Reynolds C. S., 1997, MNRAS 288, L11
- Dai X., Kochanek C. S., Chartas G., Kozłowski S. et al., 2010, ApJ 709, 278
- Dai X., Shankar F., Sivakoff G. R., 2008, ApJ 672, 108
- Dai X., Shankar F., Sivakoff G. R., 2012, ApJ 757, 180
- Davis S. W., Hubeny I., 2006, ApJs 164, 530
- Davis S. W., Woo J.-H., Blaes O. M., 2007, ApJ 668, 682
- de Kool M., Begelman M. C., 1995, ApJ 455, 448
- Denney K. D., De Rosa G., Croxall K., Gupta A. et al., 2014, ApJ 796, 134

- Dere K. P., Landi E., Mason H. E., Monsignori Fossi B. C., Young P. R., 1997,
A&As 125, 149
- Dexter J., Agol E., 2011, ApJ Letters 727, L24
- Dhillon V. S., 1996, in A. Evans, J. H. Wood (eds.), IAU Colloq. 158: Cataclysmic
Variables and Related Objects, Vol. 208 of *Astrophysics and Space Science Library*,
3
- Dhillon V. S., Rutten R. G. M., 1995, MNRAS 277, 777
- Díaz Trigo M., Boirin L., 2015, ArXiv e-prints
- DiPompeo M. A., Brotherton M. S., Cales S. L., Runnoe J. C., 2012a, MNRAS 427,
1135
- DiPompeo M. A., Brotherton M. S., De Breuck C., 2012b, ApJ 752, 6
- Done C., Davis S. W., Jin C., Blaes O., Ward M., 2012, MNRAS 420, 1848
- Done C., Jin C., 2015, ArXiv e-prints
- Drew J., Verbunt F., 1985, MNRAS 213, 191
- Echevarria J., 1988, MNRAS 233, 513
- Edelson R., Gelbord J. M., Horne K., McHardy I. M. et al., 2015, ApJ 806, 129
- Edge D. O., Shakeshaft J. R., McAdam W. B., Baldwin J. E., Archer S., 1959,
MmRA 68, 37
- Eggleton P. P., 1983, ApJ 268, 368
- Ehman J. R., Dixon R. S., Kraus J. D., 1970, AJ 75, 351
- Ekers J. A., 1969, Australian Journal of Physics Astrophysical Supplement 7
- Elitzur M., 2012, ApJ Letters 747, L33
- Elitzur M., Ho L. C., Trump J. R., 2014, MNRAS 438, 3340
- Elvis M., 2000, ApJ 545, 63
- Elvis M., Wilkes B. J., McDowell J. C., Green R. F. et al., 1994, ApJs 95, 1

- Emmanoulopoulos D., Papadakis I. E., Dovčiak M., McHardy I. M., 2014, MNRAS 439, 3931
- Emmanoulopoulos D., Papadakis I. E., McHardy I. M., Arévalo P. et al., 2012, MNRAS 424, 1327
- Eracleous M., Halpern J. P., 1994, ApJs 90, 1
- Fabian A. C., 2012, ARAA 50, 455
- Fabian A. C., Kunieda H., Inoue S., Matsuoka M. et al., 1994, PASJ 46, L59
- Fabian A. C., Nandra K., Reynolds C. S., Brandt W. N. et al., 1995, MNRAS 277, L11
- Fath E. A., 1909, Lick Observatory Bulletin 5, 71
- Feldmeier A., 1995, A&A 299, 523
- Fender R. P., 2001, MNRAS 322, 31
- Fender R. P., Belloni T. M., Gallo E., 2004, MNRAS 355, 1105
- Fender R. P., Gallo E., Russell D., 2010, MNRAS 406, 1425
- Ferland G. J., Porter R. L., van Hoof P. A. M., Williams R. J. R. et al., 2013, RMXAA 49, 137
- Ferrarese L., Merritt D., 2000, ApJ Letters 539, L9
- Filiz Ak N., Brandt W. N., Hall P. B., Schneider D. P. et al., 2012, ApJ 757, 114
- Filiz Ak N., Brandt W. N., Hall P. B., Schneider D. P. et al., 2014, ApJ 791, 88
- Flohic H. M. L. G., Eracleous M., Bogdanović T., 2012, ApJ 753, 133
- Foltz C. B., Weymann R. J., Morris S. L., Turnshek D. A., 1987, ApJ 317, 450
- Frank J., King A., Raine D., 1992, Accretion power in astrophysics.
- Frank J., King A. R., 1981, MNRAS 195, 227
- Friend D. B., Abbott D. C., 1986, ApJ 311, 701
- Fukumura K., Tombesi F., Kazanas D., Shrader C. et al., 2015, ApJ 805, 17

- Gabriel E., Fagg G. E., Bosilca G., Angskun T. et al., 2004, in Proceedings, 11th European PVM/MPI Users' Group Meeting, Budapest, Hungary, p. 97
- Gallagher S. C., Brandt W. N., Chartas G., Garmire G. P., 2002, ApJ 567, 37
- Gallagher S. C., Brandt W. N., Chartas G., Priddey R. et al., 2006, ApJ 644, 709
- Gallagher S. C., Brandt W. N., Sambruna R. M., Mathur S., Yamasaki N., 1999, ApJ 519, 549
- Gallo E., Fender R. P., Pooley G. G., 2003, MNRAS 344, 60
- Gandhi P., Hönig S. F., Kishimoto M., 2015, ApJ 812, 113
- Gandhi P., Terashima Y., Yamada S., Mushotzky R. F. et al., 2013, ApJ 773, 51
- Ganguly R., Bond N. A., Charlton J. C., Eracleous M. et al., 2001, ApJ 549, 133
- Ganguly R., Sembach K. R., Tripp T. M., Savage B. D., Wakker B. P., 2006, ApJ 645, 868
- Gardner E., Done C., 2016, ArXiv e-prints
- Gayet R., 1970, A&A 9, 312
- Gebhardt K., Bender R., Bower G., Dressler A. et al., 2000, ApJ Letters 539, L13
- Ghosh K. K., Punsly B., 2007, ApJ Letters 661, L139
- Gibson R. R., Jiang L., Brandt W. N., Hall P. B. et al., 2009, ApJ 692, 758
- Gierliński M., Done C., 2004, MNRAS 349, L7
- Gierliński M., Done C., 2006, MNRAS 371, L16
- Giustini M., Cappi M., Chartas G., Dadina M. et al., 2011, A&A 536, A49
- Gofford J., Reeves J. N., Braito V., Nardini E. et al., 2014, ApJ 784, 77
- Gofford J., Reeves J. N., McLaughlin D. E., Braito V. et al., 2015, MNRAS 451, 4169
- Gofford J., Reeves J. N., Tombesi F., Braito V. et al., 2013, MNRAS 430, 60
- Goodrich R. W., 1997, ApJ 474, 606
- Goodrich R. W., Miller J. S., 1995, ApJ Letters 448, L73

- Gough B., 2009, GNU Scientific Library Reference Manual - Third Edition, Network Theory Ltd., 3rd edition
- Green A. R., McHardy I. M., Lehto H. J., 1993, MNRAS 265, 664
- Green P. J., Aldcroft T. L., Mathur S., Wilkes B. J., Elvis M., 2001, ApJ 558, 109
- Green P. J., Mathur S., 1996, ApJ 462, 637
- Greenstein J. L., Oke J. B., 1982, ApJ 258, 209
- Groot P. J., Rutten R. G. M., van Paradijs J., 2004, A&A 417, 283
- Grupe D., Mathur S., Elvis M., 2003a, AJ 126, 1159
- Grupe D., Mathur S., Elvis M., 2003b, AJ 126, 1159
- Grupe D., Nousek J. A., 2015, AJ 149, 85
- Gu M., Cao X., 2009, MNRAS 399, 349
- Gültekin K., Richstone D. O., Gebhardt K., Lauer T. R. et al., 2009, ApJ 698, 198
- Haardt F., Maraschi L., 1991, ApJ Letters 380, L51
- Hall P. B., Anderson S. F., Strauss M. A., York D. G. et al., 2002, ApJs 141, 267
- Hall P. B., Anosov K., White R. L., Brandt W. N. et al., 2011, MNRAS 411, 2653
- Halpern J. P., 1984, ApJ 281, 90
- Hamann F., Chartas G., McGraw S., Rodriguez Hidalgo P. et al., 2013, MNRAS 435, 133
- Hamann W.-R., Koesterke L., 1998, A&A 335, 1003
- Hamann W.-R., Leuenhagen U., Koesterke L., Wessolowski U., 1992, A&A 255, 200
- Hamann W.-R., Oskinova L. M., Feldmeier A., 2008, in W.-R. Hamann, A. Feldmeier, L. M. Oskinova (eds.), Clumping in Hot-Star Winds, 75
- Hamann W.-R., Wessolowski U., Koesterke L., 1994, A&A 281, 184
- Häring N., Rix H.-W., 2004, ApJ Letters 604, L89
- Harrop-Allin M. K., Warner B., 1996, MNRAS 279, 219

- Hartley L. E., Murray J. R., Drew J. E., Long K. S., 2005, MNRAS 363, 285
- Hassall B. J. M., 1985, MNRAS 216, 335
- Haug K., 1987, AP&SS 130, 91
- Hazard C., Mackey M. B., Shimmins A. J., 1963, Nature 197, 1037
- Hazard C., Morton D. C., Terlevich R., McMahon R., 1984, ApJ 282, 33
- Heap S. R., Boggess A., Holm A., Klinglesmith D. A. et al., 1978, Nature 275, 385
- Heil L. M., Vaughan S., Uttley P., 2012, MNRAS 422, 2620
- Hessman F. V., Robinson E. L., Nather R. E., Zhang E.-H., 1984, ApJ 286, 747
- Higginbottom N., Knigge C., Long K. S., Sim S. A., Matthews J. H., 2013, MNRAS 436, 1390
- Higginbottom N., Proga D., Knigge C., Long K. S. et al., 2014, ApJ 789, 19
- Hillier D. J., 1984, ApJ 280, 744
- Hillier D. J., 1991, A&A 247, 455
- Hillier D. J., Miller D. L., 1999, ApJ 519, 354
- Hoare M. G., Drew J. E., 1991, MNRAS 249, 452
- Hoare M. G., Drew J. E., 1993, MNRAS 260, 647
- Hogg J. D., Reynolds C., 2015, ArXiv e-prints
- Honeycutt R. K., Schlegel E. M., Kaitchuck R. H., 1986, ApJ 302, 388
- Hönig S. F., Kishimoto M., Tristram K. R. W., Prieto M. A. et al., 2013, ApJ 771, 87
- Horne K., 1993, Eclipse Mapping of Accretion Disks: The First Decade, 117
- Horne K., Marsh T. R., 1986, MNRAS 218, 761
- Horne K., Marsh T. R., Cheng F. H., Hubeny I., Lanz T., 1994, ApJ 426, 294
- Hoyle F., Lyttleton R. A., 1939, Proceedings of the Cambridge Philosophical Society 35, 405

- Hubeny I., 2001, in G. Ferland, D. W. Savin (eds.), Spectroscopic Challenges of Photoionized Plasmas, Vol. 247 of *Astronomical Society of the Pacific Conference Series*, 197
- Hubeny I., Agol E., Blaes O., Krolik J. H., 2000, ApJ 533, 710
- Hubeny I., Lanz T., 1995, ApJ 439, 875
- Humphrey A., Binette L., 2014, MNRAS 442, 753
- Idan I., Lasota J.-P., Hameury J.-M., Shaviv G., 2010, A&A 519, A117
- Ioannou Z., van Zyl L., Naylor T., Charles P. A. et al., 2003, A&A 399, 211
- Iwasawa K., Fabian A. C., Mushotzky R. F., Brandt W. N. et al., 1996a, MNRAS 279, 837
- Iwasawa K., Fabian A. C., Reynolds C. S., Nandra K. et al., 1996b, MNRAS 282, 1038
- Janiuk A., Czerny B., Madejski G. M., 2001, ApJ 557, 408
- Ju W., Stone J. M., Zhu Z., 2016, ArXiv e-prints
- Kaastra J. S., Kriss G. A., Cappi M., Mehdiour M. et al., 2014, Science 345, 64
- Kaastra J. S., Mewe R., Liedahl D. A., Komossa S., Brinkman A. C., 2000, A&A 354, L83
- Kafka S., Honeycutt R. K., 2004, AJ 128, 2420
- Kaspi S., Brandt W. N., Maoz D., Netzer H. et al., 2007, ApJ 659, 997
- Kerzendorf W. E., Sim S. A., 2014, MNRAS 440, 387
- King A., 2003, ApJ Letters 596, L27
- Klein O., Nishina T., 1929, Zeitschrift fur Physik 52, 853
- Knigge C., Baraffe I., Patterson J., 2011, ApJs 194, 28
- Knigge C., Drew J. E., 1997, ApJ 486, 445
- Knigge C., Long K. S., Blair W. P., Wade R. A., 1997, ApJ 476, 291
- Knigge C., Long K. S., Wade R. A., Baptista R. et al., 1998a, ApJ 499, 414

- Knigge C., Long K. S., Wade R. A., Baptista R. et al., 1998b, ApJ 499, 414
- Knigge C., Scaringi S., Goad M. R., Cottis C. E., 2008, MNRAS 386, 1426
- Knigge C., Woods J. A., Drew J. E., 1995, MNRAS 273, 225
- Konigl A., Kartje J. F., 1994, ApJ 434, 446
- Koratkar A., Blaes O., 1999, PASP 111, 1
- Körding E., Rupen M., Knigge C., Fender R. et al., 2008, Science 320, 1318
- Körding E. G., Jester S., Fender R., 2006, MNRAS 372, 1366
- Kormendy J., Ho L. C., 2013, ARAA 51, 511
- Kotani T., Ebisawa K., Dotani T., Inoue H. et al., 2000, ApJ 539, 413
- Kotov O., Churazov E., Gilfanov M., 2001, MNRAS 327, 799
- Kraft R. P., Mathews J., Greenstein J. L., 1962, ApJ 136, 312
- Kriss G. A., Krolik J. H., Otani C., Espey B. R. et al., 1996, ApJ 467, 629
- Krolik J. H., Begelman M. C., 1986, in Bulletin of the American Astronomical Society, Vol. 18 of *BAAS*, 903
- Krolik J. H., Kriss G. A., 2001, ApJ 561, 684
- Krolik J. H., Voit G. M., 1998, ApJ Letters 497, L5
- Kromer M., Sim S. A., 2009, MNRAS 398, 1809
- Kudoh T., Shibata K., 1997, ApJ 474, 362
- Kurosawa R., Proga D., 2009, ApJ 693, 1929
- Kurucz R. L., 1991, in L. Crivellari, I. Hubeny, D. G. Hummer (eds.), NATO ASIC Proc. 341: Stellar Atmospheres - Beyond Classical Models, 441
- Kurucz R. L., Bell B., 1995, Atomic line list
- Kusterer D.-J., Nagel T., Hartmann S., Werner K., Feldmeier A., 2014, A&A 561, A14
- Kuulkers E., Motta S., Kajava J., Homan J. et al., 2015, The Astronomer's Telegram 7647

- La Dous C., 1989a, MNRAS 238, 935
- La Dous C., 1989b, A&A 211, 131
- Lamy H., Hutsemékers D., 2000, A&A 356, L9
- Landi E., Del Zanna G., Young P. R., Dere K. P., Mason H. E., 2012, ApJ 744, 99
- Laor A., 1991, ApJ 376, 90
- Laor A., Brandt W. N., 2002, ApJ 569, 641
- Laor A., Davis S. W., 2014, MNRAS 438, 3024
- Lasota J.-P., 2001, NAR 45, 449
- Lazarova M. S., Canalizo G., Lacy M., Sajina A., 2012, ApJ 755, 29
- Liebert J., Stockman H. S., 1985, in D. Q. Lamb, J. Patterson (eds.), *Cataclysmic Variables and Low-Mass X-ray Binaries*, Vol. 113 of *Astrophysics and Space Science Library*, p. 151
- Long K. S., Blair W. P., Davidsen A. F., Bowers C. W. et al., 1991, ApJ Letters 381, L25
- Long K. S., Knigge C., 2002, ApJ 579, 725
- Long K. S., Wade R. A., Blair W. P., Davidsen A. F., Hubeny I., 1994, ApJ 426, 704
- Longmore A. J., Lee T. J., Allen D. A., Adams D. J., 1981, MNRAS 195, 825
- Lucy L. B., 1999a, A&A 344, 282
- Lucy L. B., 1999b, A&A 345, 211
- Lucy L. B., 2002, A&A 384, 725
- Lucy L. B., 2003, A&A 403, 261
- Lucy L. B., Solomon P. M., 1970, ApJ 159, 879
- Lusso E., Worseck G., Hennawi J. F., Prochaska J. X. et al., 2015, MNRAS 449, 4204
- Lynden-Bell D., 1969, Nature 223, 690
- Lyubarskii Y. E., 1997, MNRAS 292, 679

- MacGregor K. B., Hartmann L., Raymond J. C., 1979, ApJ 231, 514
- Madau P., Ghisellini G., Fabian A. C., 1994, MNRAS 270, L17
- Magdziarz P., Blaes O. M., Zdziarski A. A., Johnson W. N., Smith D. A., 1998, MNRAS 301, 179
- Magorrian J., Tremaine S., Richstone D., Bender R. et al., 1998, AJ 115, 2285
- Mangham S. W., Knigge C., Matthews J. H., Long K. S. et al., 2016, in prep.
- Marinucci A., Bianchi S., Matt G., Alexander D. M. et al., 2016, MNRAS 456, L94
- Marscher A. P., 2006, in P. A. Hughes, J. N. Bregman (eds.), Relativistic Jets: The Common Physics of AGN, Microquasars, and Gamma-Ray Bursts, Vol. 856 of *American Institute of Physics Conference Series*, p. 1
- Marsh T. R., Horne K., 1988, MNRAS 235, 269
- Marsh T. R., Horne K., 1990, ApJ 349, 593
- Marziani P., Sulentic J. W., Zwitter T., Dultzin-Hacyan D., Calvani M., 2001, ApJ 558, 553
- Mathur S., Green P. J., Arav N., Brotherton M. et al., 2000, ApJ Letters 533, L79
- Matt G., Guainazzi M., Maiolino R., 2003, MNRAS 342, 422
- Matthews J. H., Knigge C., Long K. S., Sim S. A., Higginbottom N., 2015, MNRAS 450, 3331
- Matthews J. H., Knigge C., Long K. S., Sim S. A. et al., 2016, MNRAS
- Matzeu G. A., Reeves J. N., Nardini E., Braito V. et al., 2016, MNRAS 458, 1311
- Mauche C. W., 1996, ArXiv Astrophysics e-prints
- Mauche C. W., Raymond J. C., 1987, ApJ 323, 690
- Mazzali P. A., Lucy L. B., 1993, A&A 279, 447
- McConnell N. J., Ma C.-P., 2013, ApJ 764, 184
- McHardy I. M., Koerding E., Knigge C., Uttley P., Fender R. P., 2006, Nature 444, 730

- McHardy I. M., Papadakis I. E., Uttley P., 1999, Nuclear Physics B Proceedings Supplements 69, 509
- Menzel D. H., Pekeris C. L., 1935, MNRAS 96, 77
- Merloni A., Heinz S., di Matteo T., 2003, MNRAS 345, 1057
- Mihalas D., 1978, Stellar atmospheres /2nd edition/
- Miller L., Turner T. J., 2013, ApJ Letters 773, L5
- Miller L., Turner T. J., Reeves J. N., 2008, A&A 483, 437
- Misawa T., Charlton J. C., Eracleous M., Ganguly R. et al., 2007, ApJs 171, 1
- Misawa T., Eracleous M., Chartas G., Charlton J. C., 2008, ApJ 677, 863
- Misra R., Kembhavi A. K., 1998, ApJ 499, 205
- Mitsuda K., Inoue H., Nakamura N., Tanaka Y., 1989, PASJ 41, 97
- Morabito L. K., Dai X., Leighly K. M., Sivakoff G. R., Shankar F., 2013, ArXiv e-prints
- Morgan C. W., Kochanek C. S., Morgan N. D., Falco E. E., 2010, ApJ 712, 1129
- Motta S., Beardmore A., Oates S., Sanna N. P. M. K. A. et al., 2015, The Astronomer's Telegram 7665
- Muñoz-Darias T., Coriat M., Plant D. S., Ponti G. et al., 2013, MNRAS 432, 1330
- Murray N., Chiang J., 1996, Nature 382, 789
- Murray N., Chiang J., 1997, ApJ 474, 91
- Murray N., Chiang J., Grossman S. A., Voit G. M., 1995, ApJ 451, 498
- Nandra K., Pounds K. A., 1994, MNRAS 268, 405
- Narayan R., McClintock J. E., 2012, MNRAS 419, L69
- Narayan R., McClintock J. E., Tchekhovskoy A., 2014, Energy Extraction from Spinning Black Holes Via Relativistic Jets, 523
- Narayan R., Yi I., 1994, ApJ Letters 428, L13
- Narayan R., Yi I., 1995, ApJ 452, 710

- Nardini E., Reeves J. N., Gofford J., Harrison F. A. et al., 2015, *Science* 347, 860
- Nestor D., Hamann F., Rodriguez Hidalgo P., 2008, *MNRAS* 386, 2055
- Netzer H., 1990, in R. D. Blandford, H. Netzer, L. Woltjer, T. J.-L. Courvoisier, M. Mayor (eds.), *Active Galactic Nuclei*, p. 57
- Neugebauer G., Oke J. B., Becklin E. E., Matthews K., 1979, *ApJ* 230, 79
- Neustroev V. V., Suleimanov V. F., Borisov N. V., Belyakov K. V., Shearer A., 2011, *MNRAS* 410, 963
- Noebauer U. M., Long K. S., Sim S. A., Knigge C., 2010, *ApJ* 719, 1932
- North M., Knigge C., Goad M., 2006, *MNRAS* 365, 1057
- O'Dowd M. J., Bate N. F., Webster R. L., Labrie K., Rogers J., 2015, ArXiv e-prints
- Orr A., Molendi S., Fiore F., Grandi P. et al., 1997, *A&A* 324, L77
- Orr M. J. L., Browne I. W. A., 1982, *MNRAS* 200, 1067
- Osaki Y., 1974, *PASJ* 26, 429
- Osterbrock D. E., 1989, *Astrophysics of gaseous nebulae and active galactic nuclei*
- Otani C., Kii T., Reynolds C. S., Fabian A. C. et al., 1996, *PASJ* 48, 211
- Ouyed R., Pudritz R. E., 1997, *ApJ* 482, 712
- Owocki S., 2014, ArXiv e-prints
- Owocki S. P., Castor J. I., Rybicki G. B., 1988, *ApJ* 335, 914
- Owocki S. P., Rybicki G. B., 1984, *ApJ* 284, 337
- Owocki S. P., Rybicki G. B., 1985, *ApJ* 299, 265
- Parmar A. N., Oosterbroek T., Boirin L., Lumb D., 2002, *A&A* 386, 910
- Patterson J., 1984, *ApJs* 54, 443
- Patterson J., 1994, *PASP* 106, 209
- Patterson J., Patino R., Thorstensen J. R., Harvey D. et al., 1996, *AJ* 111, 2422

- Pauldrach A., Puls J., Kudritzki R. P., 1986, A&A 164, 86
- Pauldrach A. W. A., Kudritzki R. P., Puls J., Butler K., Hunsinger J., 1994, A&A 283, 525
- Pelletier G., Pudritz R. E., 1992, ApJ 394, 117
- Penrose R., Floyd R. M., 1971, Nature Physical Science 229, 177
- Pereyra N. A., Kallman T. R., Blondin J. M., 1997, ApJ 477, 368
- Perley R. A., Dreher J. W., Cowan J. J., 1984, ApJ Letters 285, L35
- Ponti G., Fender R. P., Begelman M. C., Dunn R. J. H. et al., 2012, MNRAS 422, L11
- Potash R. I., Wardle J. F. C., 1980, ApJ 239, 42
- Pounds K., Lobban A., Reeves J., Vaughan S., 2016, MNRAS 457, 2951
- Pounds K. A., Nandra K., Stewart G. C., Leighly K., 1989, MNRAS 240, 769
- Pounds K. A., Reeves J. N., 2009, MNRAS 397, 249
- Prinja R. K., Ringwald F. A., Wade R. A., Knigge C., 2000, MNRAS 312, 316
- Prinja R. K., Smith L. J., 1992, A&A 266, 377
- Proga D., 2003, ApJ 585, 406
- Proga D., 2005, in J.-M. Hameury, J.-P. Lasota (eds.), *The Astrophysics of Cataclysmic Variables and Related Objects*, Vol. 330 of *Astronomical Society of the Pacific Conference Series*, 103
- Proga D., Kallman T. R., 2004, ApJ 616, 688
- Proga D., Kallman T. R., Drew J. E., Hartley L. E., 2002a, ApJ 572, 382
- Proga D., Kallman T. R., Drew J. E., Hartley L. E., 2002b, ApJ 572, 382
- Proga D., Stone J. M., Drew J. E., 1998, MNRAS 295, 595
- Proga D., Stone J. M., Kallman T. R., 2000, ApJ 543, 686
- Puccetti S., Fiore F., Risaliti G., Capalbi M. et al., 2007, MNRAS 377, 607
- Puebla R. E., Diaz M. P., Hillier D. J., Hubeny I., 2011, ApJ 736, 17

- Randall S. W., Forman W. R., Giacintucci S., Nulsen P. E. J. et al., 2011, ApJ 726, 86
- Read J. I., Trentham N., 2005, Philosophical Transactions of the Royal Society of London Series A 363
- Reeves J. N., O'Brien P. T., Ward M. J., 2003, ApJ Letters 593, L65
- Reeves J. N., Wynn G., O'Brien P. T., Pounds K. A., 2002, MNRAS 336, L56
- Reichard T. A., Richards G. T., Hall P. B., Schneider D. P. et al., 2003, AJ 126, 2594
- Reynolds C. S., 1999, in J. Poutanen, R. Svensson (eds.), High Energy Processes in Accreting Black Holes, Vol. 161 of *Astronomical Society of the Pacific Conference Series*, 178
- Reynolds C. S., Fabian A. C., 1995, MNRAS 273, 1167
- Ringwald F. A., Naylor T., 1998, AJ 115, 286
- Risaliti G., Elvis M., Fabbiano G., Baldi A. et al., 2007, ApJ Letters 659, L111
- Risaliti G., Elvis M., Nicastro F., 2002, ApJ 571, 234
- Risaliti G., Salvati M., Marconi A., 2011, MNRAS 411, 2223
- Romanova M. M., Ustyugova G. V., Koldoba A. V., Chechetkin V. M., Lovelace R. V. E., 1997, ApJ 482, 708
- Ross R. R., Fabian A. C., 2005, MNRAS 358, 211
- Rottenberg J. A., 1952, MNRAS 112, 125
- Rupke D. S. N., Veilleux S., 2011, ApJ Letters 729, L27
- Rutten R. G. M., van Paradijs J., Tinbergen J., 1992, A&A 260, 213
- Rybicki G., 1970, in H. G. Groth, P. Wellmann (eds.), IAU Colloq. 2: Spectrum Formation in Stars with Steady-State Extended Atmospheres, 87
- Rybicki G. B., Hummer D. G., 1978, ApJ 219, 654
- Sabra B. M., Hamann F., 2001, ApJ 563, 555
- Scaringi S., Körding E., Uttley P., Knigge C. et al., 2012, MNRAS 421, 2854

- Scaringi S., Maccarone T. J., Koerding E., Knigge C. et al., 2015, ArXiv e-prints
- Schechter P., 1976, ApJ 203, 297
- Schmidt M., 1963, Nature 197, 1040
- Schmidt M., 1965a, ApJ 141, 1295
- Schmidt M., 1965b, ApJ 141, 1
- Schmutz W., 1997, A&A 321, 268
- Seaton M. J., 1959, MNRAS 119, 90
- Setti G., Woltjer L., 1989, A&A 224, L21
- Seyfert C. K., 1943, ApJ 97, 28
- Shakura N. I., Sunyaev R. A., 1973, A&A 24, 337
- Shankar F., Calderone G., Knigge C., Matthews J. et al., 2016, ApJ Letters 818, L1
- Shaviv G., Wehrse R., 1991, A&A 251, 117
- Shen Y., Ho L. C., 2014, Nature 513, 210
- Shen Y., Richards G. T., Strauss M. A., Hall P. B. et al., 2011, ApJs 194, 45
- Shlosman I., Vitello P., 1993, ApJ 409, 372
- Silk J., Rees M. J., 1998, A&A 331, L1
- Silva C., Uttley P., Costantini E., 2015, in The Extremes of Black Hole Accretion, 63
- Sim S. A., 2004, MNRAS 349, 899
- Sim S. A., Drew J. E., Long K. S., 2005, MNRAS 363, 615
- Sim S. A., Long K. S., Miller L., Turner T. J., 2008, MNRAS 388, 611
- Sim S. A., Miller L., Long K. S., Turner T. J., Reeves J. N., 2010a, MNRAS 404, 1369
- Sim S. A., Proga D., Kurosawa R., Long K. S. et al., 2012, MNRAS 426, 2859
- Sim S. A., Proga D., Miller L., Long K. S., Turner T. J., 2010b, MNRAS 408, 1396

- Simon L. E., Hamann F., 2010, MNRAS 409, 269
- Sluse D., Hutsemékers D., Anguita T., Braibant L., Riaud P., 2015, ArXiv e-prints
- Smak J., 1981, ACTAA 31, 395
- Smak J., 1995, ACTAA 45, 259
- Sobolev V. V., 1957, SvA 1, 678
- Sobolev V. V., 1960, Moving envelopes of stars
- Sobolewska M. A., Siemiginowska A., Gierliński M., 2011, MNRAS 413, 2259
- Soltan A., 1982, MNRAS 200, 115
- Somerville R. S., Primack J. R., Faber S. M., 2001, MNRAS 320, 504
- Springel V., Di Matteo T., Hernquist L., 2005, ApJ Letters 620, L79
- Stalevski M., Fritz J., Baes M., Popovic L. C., 2013, ArXiv e-prints
- Stalin C. S., Srianand R., Petitjean P., 2011, MNRAS 413, 1013
- Stockman H. S., Angel J. R. P., Miley G. K., 1979, ApJ Letters 227, L55
- Strateva I., Ivezić Ž., Knapp G. R., Narayanan V. K. et al., 2001, AJ 122, 1861
- Struve O., 1935, ApJ 81, 66
- Suleimanov V., Hertfelder M., Werner K., Kley W., 2014, ArXiv e-prints
- Sulentic J. W., Zwitter T., Marziani P., Dultzin-Hacyan D., 2000, ApJ Letters 536, L5
- Surdej J., Hutsemekers D., 1987, A&A 177, 42
- Sutherland R. S., 1998, MNRAS 300, 321
- Tatum M. M., Turner T. J., Sim S. A., Miller L. et al., 2012, ApJ 752, 94
- Thorne K. S., 1974, ApJ 191, 507
- Tohline J. E., Osterbrock D. E., 1976, ApJ Letters 210, L117
- Tombesi F., Cappi M., Reeves J. N., Palumbo G. G. C. et al., 2010, A&A 521, A57
- Tombesi F., Meléndez M., Veilleux S., Reeves J. N. et al., 2015, Nature 519, 436

- Tran H. D., 2001, ApJ Letters 554, L19
- Trump J. R., Hall P. B., Reichard T. A., Richards G. T. et al., 2006, ApJs 165, 1
- Turing A. M., 1948, QJMAM 1(1), 287
- Ueda Y., Inoue H., Tanaka Y., Ebisawa K. et al., 1998, ApJ 492, 782
- Urrutia T., Becker R. H., White R. L., Glikman E. et al., 2009, ApJ 698, 1095
- Urry C. M., Padovani P., 1995, PASP 107, 803
- Ustyugova G. V., Koldoba A. V., Romanova M. M., Chechetkin V. M., Lovelace R. V. E., 1999, ApJ 516, 221
- Uttley P., Cackett E. M., Fabian A. C., Kara E., Wilkins D. R., 2014, AAPR 22, 72
- Uttley P., McHardy I. M., 2001, MNRAS 323, L26
- Uttley P., McHardy I. M., Vaughan S., 2005, MNRAS 359, 345
- Šurlan B., Hamann W.-R., Kubát J., Osokinova L. M., Feldmeier A., 2012, A&A 541, A37
- Van de Sande M., Scaringi S., Knigge C., 2015, MNRAS 448, 2430
- van Regemorter H., 1962, ApJ 136, 906
- Verner D. A., Barthel P. D., Tytler D., 1994, A&As 108, 287
- Verner D. A., Ferland G. J., Korista K. T., Yakovlev D. G., 1996a, ApJ 465, 487
- Verner D. A., Verner E. M., Ferland G. J., 1996b, Atomic Data and Nuclear Data Tables 64, 1
- Vestergaard M., Wilkes B. J., 2001, ApJs 134, 1
- Voit G. M., Weymann R. J., Korista K. T., 1993, ApJ 413, 95
- Wade R. A., 1984, MNRAS 208, 381
- Wade R. A., 1988, ApJ 335, 394
- Walker M. F., 1963, ApJ 137, 485

- Walton D. J., Miller J. M., Harrison F. A., Fabian A. C. et al., 2013, ApJ Letters 773, L9
- Wang B., Han Z., 2012, NAR 56, 122
- Warner B., 2003, Cataclysmic Variable Stars
- Weymann R. J., Morris S. L., Foltz C. B., Hewett P. C., 1991, ApJ 373, 23
- White N. E., Stella L., Parmar A. N., 1988, ApJ 324, 363
- Wills B. J., Brotherton M. S., 1995, ApJ Letters 448, L81
- Woltjer L., 1959, ApJ 130, 38
- Woods D. T., Klein R. I., Castor J. I., McKee C. F., Bell J. B., 1996, ApJ 461, 767
- Woods J. A., 1991, Ph.D. thesis, D. Phil thesis, Univ. Oxford , (1991)
- Yong S. Y., Webster R. L., King A. L., 2016, PASA 33, e009
- Zakamska N. L., Strauss M. A., Krolik J. H., Collinge M. J. et al., 2003, AJ 126, 2125
- Zanstra H., 1929, Publications of the Dominion Astrophysical Observatory Victoria 4, 209
- Zhang S. N., Cui W., Chen W., 1997, ApJ Letters 482, L155
- Zhou H., Wang T., Wang H., Wang J. et al., 2006, ApJ 639, 716
- Zubovas K., King A., 2013, ApJ 769, 51